

Spring 2010

## Exclusive $\pi^-$ - Electro-Production From the Neutron in the Resonance Region

Jixie Zhang  
*Old Dominion University*

Follow this and additional works at: [https://digitalcommons.odu.edu/physics\\_etds](https://digitalcommons.odu.edu/physics_etds)



Part of the [Elementary Particles and Fields and String Theory Commons](#), and the [Nuclear Commons](#)

---

### Recommended Citation

Zhang, Jixie. "Exclusive  $\pi^-$ - Electro-Production From the Neutron in the Resonance Region" (2010). Doctor of Philosophy (PhD), Dissertation, Physics, Old Dominion University, DOI: 10.25777/40k3-b091  
[https://digitalcommons.odu.edu/physics\\_etds/92](https://digitalcommons.odu.edu/physics_etds/92)

This Dissertation is brought to you for free and open access by the Physics at ODU Digital Commons. It has been accepted for inclusion in Physics Theses & Dissertations by an authorized administrator of ODU Digital Commons. For more information, please contact [digitalcommons@odu.edu](mailto:digitalcommons@odu.edu).

**EXCLUSIVE  $\pi^-$  ELECTRO-PRODUCTION FROM THE  
NEUTRON IN THE RESONANCE REGION**

by

Jixie Zhang  
B.S. July 2001, Tsinghua University, China  
M.S. June 2005, Old Dominion University

A Dissertation Submitted to the Faculty of  
Old Dominion University in Partial Fulfillment of the  
Requirement for the Degree of

DOCTOR OF PHILOSOPHY

PHYSICS

OLD DOMINION UNIVERSITY  
May 2010

Approved by:

---

Gail E. Dodge (Director)

---

Sebastian E. Kuhn

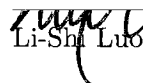
---

Anatoly Radyushkin

---

Charles I. Sukenik

---

  
Li-Shi Luo

## ABSTRACT

### EXCLUSIVE $\pi^-$ ELECTRO-PRODUCTION FROM THE NEUTRON IN THE RESONANCE REGION

Jixie Zhang

Old Dominion University, 2010

Director: Dr. Gail E. Dodge

The study of baryon resonances is crucial to our understanding of nucleon structure. Although the excited states of the proton have been studied in great detail, there are very few data available for the neutron resonances because of the difficulty inherent in obtaining a free neutron target. To overcome this limitation, the spectator tagging technique was used in one of the CEBAF Large Acceptance Spectrometer (CLAS) collaboration experiments, *Barely off-shell Nuclear Structure (BoNuS)*, in Hall-B at Jefferson Lab. We have constructed a radial time projection chamber (RTPC) based on the gaseous electron multiplier (GEM) technology to detect low momentum recoil protons. Electron scattering data were taken in Fall 2005 with beam energies of 2.1, 4.2 and 5.3 GeV using a 7 atmosphere gaseous deuterium target in conjunction with the RTPC and CLAS detectors. We have studied the exclusive reactions  $D(e, e' \pi^- p_{\text{CLAS}})p$  and  $D(e, e' \pi^- p_{\text{RTPC}})p$ , in which the proton was detected either in CLAS or in the RTPC. Measurements of the absolute differential cross section over a large kinematic range are reported.



©Copyright, 2010, by Jixie Zhang, All Rights Reserved



## ACKNOWLEDGMENTS

This dissertation would not have been possible without the help from many. I would like to thank everyone who has helped me complete this work.

First and foremost, I would like to express my profound gratitude to my advisor, Professor Gail Dodge, for providing me inspiration and guidance. She has invested so much time and energy in helping me during this research, which will be appreciated and remembered always. I cannot thank Gail enough for her kindness beyond supporting me in education and research, which has made my life at ODU an enjoyable experience.

I would also like to thank Professors Sebastian Kuhn, Charles Sukenik, Anatoly Radyushkin, and Li-Shi Luo for serving on my thesis committee and providing numerous helpful suggestions. I am particularly grateful to Professor Kuhn for his guidance, help, and sense of humor, which cheered me up so often. Professor Kuhn is the best knowledge resource I can hope for — he knows everything there is to know about the CLAS detector and data analysis, which are crucial to my research. I am very grateful to Lawrence Weinstein, who is one of the outstanding teachers I have ever met. Larry can always explain difficult things in a simple and straight way and he always help me out from analysis dilemmas whenever I turn to him throughout my school years. I am also in debt to Professors Stephen Bueltmann, Moskov Amarian, Charles Hyde and Gagik Gavalian for many helpful discussions.

I would like to thank Stepan Stepanyan for his help about the CLAS detector and its peripheral devices and the FSGEN. This work would not be possible without his help. I would also like to thank Igor Strakovsky, J. M. Laget, and Mher Aghasyan for their help and stimulating discussions.

I would like to thank Henry Juengst, Rustam Niyazov, Kijun Park and Hovannes Egiyan for their many productive discussions which have greatly improved the quality of this work. I would like to thank Klaus Grimm for his patience in helping me with the GEANT4 simulation when I was struggling.

Thanks to my fellow graduate students and postdocs in BoNuS Group, Nathan Baillie, Svyatoslav Tkachenko, Narbe Kalantarians, Michael Ispiryan, Vlas Tvaskis and for their valuable work and useful discussions. I certainly would not have been able to finish this without their contributions.

I also want to thank my fellow ODU graduate students Megh Niroula, Nevzat Guler, Serkan Golge, Mustafa Canan, Dereth Drake, Giovanni Chirilli, Saori Pastore, Marija Raskovic, Krishna Adhikari, Careccia Sharon, Hovhannes Baghdasaryan and Michael Mayer for their help and useful discussions during so many long long work days.

Finally, I would like to express my most profound gratitude to my wife, Ruicui Liu, for her selfless support and her dedication to our family with all her heart and soul. My son, Ian, is a constant source of joy during this endeavor, and I am thankful to him.



## TABLE OF CONTENTS

	Page
List of Tables . . . . .	ix
List of Figures . . . . .	xiv
 Chapter	
I Introduction . . . . .	1
II Theoretical Background . . . . .	4
II.1 Motivation . . . . .	4
II.2 Electron Scattering . . . . .	6
II.3 Resonances . . . . .	7
II.4 Pion Production . . . . .	9
II.5 Fits to Existing Data . . . . .	12
II.6 Extracting the Cross Section . . . . .	12
II.6.1 Off-shell Effects . . . . .	12
II.6.2 Final State Interactions . . . . .	14
III Experimental Setup . . . . .	19
III.1 Continuous Electron Beam Accelerator Facility . . . . .	19
III.2 The Beam Line of Hall B . . . . .	20
III.3 CEBAF Large Acceptance Spectrometer . . . . .	21
III.3.1 Drift Chambers . . . . .	24
III.3.2 Cherenkov Counters . . . . .	27
III.3.3 Time of Flight System . . . . .	27
III.3.4 Electromagnetic Calorimeter . . . . .	29
III.3.5 Event Trigger and Data Acquisition System . . . . .	31
III.3.6 Target . . . . .	33
III.4 Radial Time Projection Chamber . . . . .	34
IV Simulation . . . . .	43
IV.1 Introduction . . . . .	43
IV.2 The Simulation of the RTPC Detector . . . . .	44
IV.2.1 Material . . . . .	44
IV.2.2 Geometry . . . . .	46
IV.2.3 Physics Processes . . . . .	51
IV.2.4 Electric and Magnetic Fields . . . . .	53
IV.2.5 Electron Drift Path . . . . .	53
IV.2.6 Signal Digitization . . . . .	56
IV.2.7 Event Reconstruction . . . . .	57
IV.3 The Simulation of the CLAS Detector . . . . .	57
IV.4 GSIM Post Processing . . . . .	59
IV.5 Event Generators . . . . .	66
IV.5.1 Inclusive Event Generator . . . . .	66
IV.5.2 Exclusive Event Generator . . . . .	67

V	Data Analysis . . . . .	74
V.1	Data Processing . . . . .	74
V.2	Detector Calibrations . . . . .	77
V.2.1	Time of Flight Calibration . . . . .	77
V.2.2	Drift Chamber Calibration . . . . .	77
V.2.3	Electromagnetic Calorimeter Time Calibration . . . . .	78
V.2.4	Electromagnetic Calorimeter Energy Calibration . . . . .	81
V.2.5	Cherenkov Counter Calibration . . . . .	81
V.2.6	RTPC Calibration . . . . .	84
V.3	Quality Checks . . . . .	84
V.4	Corrections and Cuts . . . . .	87
V.4.1	Trigger Particle Identification . . . . .	87
V.4.2	Electron Identification for Exclusive Analysis . . . . .	91
V.4.3	Fiducial Cut for Electrons . . . . .	92
V.4.4	Fiducial Cut for Hadrons . . . . .	94
V.4.5	Solenoid geometry $\theta$ - $z$ cut . . . . .	98
V.4.6	Beam Line and Vertex Correction . . . . .	98
V.4.7	Energy Loss corrections . . . . .	106
V.4.8	$D(e, e'\pi^-p)p$ Event Selection . . . . .	112
V.5	Kinematic Coverage and Data Binning . . . . .	114
V.6	Acceptance Correction . . . . .	114
V.7	Particle Detection Efficiency . . . . .	121
V.7.1	Trigger Efficiency . . . . .	121
V.7.2	Proton Detection Efficiency in CLAS . . . . .	127
V.7.3	Proton Detection Efficiency in the RTPC . . . . .	127
V.7.4	$\pi^-$ Detection Efficiency . . . . .	131
V.8	Background Subtraction . . . . .	131
V.9	Luminosity . . . . .	141
V.9.1	Charge Calculation . . . . .	141
V.9.2	Target Pressure Calculation . . . . .	143
V.9.3	Time Integrated Luminosity . . . . .	149
V.10	Cross Section Calculations . . . . .	149
V.11	Radiative Corrections . . . . .	151
V.12	Systematic Error Evaluation . . . . .	151
VI	Physics Results . . . . .	153
VI.1	Differential Cross Section . . . . .	153
VI.2	Structure Functions . . . . .	165
VI.3	Result with Low-momentum Spectator Protons . . . . .	185
VII	Summary . . . . .	204
APPENDICES		
A	Materials defined in the RTPC GEANT4 simulation . . . . .	211

B	Physics processes in the RTPC GEANT4 simulation . . . . .	216
VITA	. . . . .	219



**LIST OF TABLES**

	Page
1 Quarks and their properties . . . . .	1
2 Preamplifier chip elements . . . . .	45
3 RTPC geometry and materials . . . . .	49
4 RTPC geometry and materials (Cont.) . . . . .	50
5 GPP parameters for the BoNuS simulation . . . . .	61
6 List of BoNuS runs . . . . .	75
7 Binning information . . . . .	114
8 Effective target pressure . . . . .	149
9 Time integrated luminosity . . . . .	150
10 Summary of the systematic errors . . . . .	152



## LIST OF FIGURES

		Page
1	Inclusive electron scattering from the proton and deuteron . . . . .	5
2	Diagram of electron scattering . . . . .	6
3	Example of $\Delta$ resonance production and decay . . . . .	8
4	Kinematics of $\pi^-$ Electro-production from the Neutron . . . . .	11
5	Calculated ratio of bound to free neutron structure function . . . . .	13
6	Feynman diagrams for the $\gamma^*d \rightarrow \pi^-pp$ reaction . . . . .	14
7	Spectator momentum dependence of the final state interactions . . . . .	15
8	Spectator momentum dependence of the final state interactions . . . . .	16
9	Final State Interaction . . . . .	17
10	Schematic view of the accelerator . . . . .	19
11	Schematic view of the hall B beam line . . . . .	22
12	Cutaway view of CLAS detector . . . . .	23
13	Configuration of the CLAS torus coils . . . . .	23
14	CLAS magnetic field strength . . . . .	25
15	Drift chamber section showing two super-layers . . . . .	25
16	CLAS drift chamber layout . . . . .	26
17	CC optical modules in one of the six sectors . . . . .	27
18	One optical module of the CLAS cherenkov detector . . . . .	28
19	TOF scintillator counters in one of the six sectors . . . . .	29
20	CLAS electromagnetic calorimeter modules . . . . .	30
21	Side view of the fiber-optic readout unit of the EC . . . . .	31
22	CLAS data acquisition system . . . . .	32
23	Mechanical drawing of the BoNuS target . . . . .	35
24	The assembly drawing of the BoNuS target system . . . . .	36
25	RTPC assembly drawing . . . . .	37
26	Electrical field map of a GEM foil . . . . .	38
27	Pad layout of the RTPC . . . . .	38
28	Magnetic field map of at the RTPC position . . . . .	39
29	Schematic of the BoNuS RTPC . . . . .	41
30	Helix fitting in the RTPC . . . . .	42
31	Side view of the RTPC detector . . . . .	47
32	Diagram of the RTPC geometry and materials . . . . .	48
33	Diagram of the RTPC and ionization electrons in the GEANT4 simulation . . . . .	52
34	Drift path of ionization electrons in the RTPC . . . . .	54
35	The azimuthal angle and radial position as a function of the drift time in the RTPC . . . . .	55
36	GPP SC smearing scale value determination . . . . .	60
37	CLAS timing resolution for electrons . . . . .	61
38	GPP DC smearing scale value determination for the 1 GeV simulation . . . . .	62
39	CLAS $W$ resolution for the 1 GeV data . . . . .	62

40	GPP DC smearing scale value determination for the 2 GeV simulation	63
41	CLAS $W$ resolution for the 2 GeV data . . . . .	63
42	GPP DC smearing scale value determination for the 4 GeV simulation	64
43	CLAS $W$ resolution for the 4 GeV data . . . . .	64
44	GPP DC smearing scale value determination for the 5 GeV simulation	65
45	CLAS $W$ resolution for the 5 GeV data . . . . .	65
46	Ratio of the $D(e, e'\pi^- p_{\text{CLAS}})p$ events for the 5 GeV real data to the simulated data as a function of $W'$ . . . . .	70
47	Ratio of the $D(e, e'\pi^- p_{\text{CLAS}})p$ events for the 5 GeV real data to the simulated data as a function of $Q^2$ . . . . .	70
48	Ratio of the $D(e, e'\pi^- p_{\text{CLAS}})p$ events for the 5 GeV real data to the simulated data as a function of $\cos\theta_\pi^*$ . . . . .	71
49	Ratio of the $D(e, e'\pi^- p_{\text{CLAS}})p$ events for the 5 GeV real data to the simulated data as a function of $\phi_\pi^*$ . . . . .	71
50	Ratio of the $D(e, e'\pi^- p_{\text{RTPC}})p$ events for the 5 GeV real data to the simulated data as a function of $W'$ . . . . .	72
51	Ratio of the $D(e, e'\pi^- p_{\text{RTPC}})p$ events for the 5 GeV real data to the simulated data as a function of $Q^2$ . . . . .	72
52	Ratio of the $D(e, e'\pi^- p_{\text{RTPC}})p$ events for the 5 GeV real data to the simulated data as a function of $\cos\theta_\pi^*$ . . . . .	73
53	Ratio of the $D(e, e'\pi^- p_{\text{RTPC}})p$ events for the 5 GeV real data to the simulated data as a function of $\phi_\pi^*$ . . . . .	73
54	Sample event reconstructed by RECSIS . . . . .	76
55	DC residuals before calibration for each layers in sectors 1 to 6. . . . .	79
56	DC residuals after calibration for each layer in sectors 1 to 6. . . . .	80
57	$\Delta t_{\text{ECSC}}$ before the EC time calibration . . . . .	82
58	$\Delta t_{\text{ECSC}}$ after the EC time calibration . . . . .	83
59	Ratio of good trigger electrons to the accumulated charge in the FC without stopper correction. . . . .	85
60	Ratio of the good trigger electrons to the accumulated charge (in arbitrary units) for runs 49692 $\sim$ 49798 . . . . .	86
61	Distribution of photoelectrons in the CC for electrons . . . . .	88
62	Momentum distribution for electrons and negative pions. . . . .	88
63	$nphe$ vs. $cc.c2$ for electrons . . . . .	89
64	Energy deposited in the EC. . . . .	90
65	Electrons with and without $E_{\text{tot}}/p$ cut . . . . .	91
66	Missing mass distribution for the 5 GeV $D(e, e'\pi^- p_{\text{CLAS}})X$ events with and without the EC total energy cut . . . . .	93
67	Sample of $\phi_{\text{dc1}}^s$ vs. $\theta_{\text{dc1}}$ for electrons . . . . .	94
68	$\phi_{\text{dc1}}^s$ distribution for electrons in narrow $\theta_{\text{dc1}}$ bin . . . . .	95
69	Fiducial region for electrons with momenta $p \leq 2.0$ GeV/c . . . . .	96
70	Fiducial region for electrons with momenta $p > 2.0$ GeV/c . . . . .	97
71	Fiducial region for $\pi^-$ with momenta $p \leq 2.0$ GeV/c . . . . .	99
72	Fiducial region for $\pi^-$ with momenta $p > 2.0$ GeV/c . . . . .	100



73	Fiducial region for protons with momenta $p \leq 2.0$ GeV/c . . . . .	101
74	Fiducial region for protons with momenta $p > 2.0$ GeV/c . . . . .	102
75	Side view of the solenoid . . . . .	103
76	RTPC target system . . . . .	104
77	Vertex $z$ cut . . . . .	104
78	Vertex $z$ distribution for the end cap before and after the beam line correction . . . . .	105
79	Electron energy loss correction . . . . .	109
80	Pion energy loss correction . . . . .	110
81	kaon energy loss correction . . . . .	110
82	Proton energy loss correction . . . . .	111
83	$\delta$ vs. $p$ for electrons before and after the energy loss corrections	111
84	Missing mass Cut for the 5 GeV data . . . . .	113
85	Binning in $W'$ and $Q^2$ for the 5 GeV data . . . . .	115
86	Binning in $W'$ and $Q^2$ for the 4 GeV data . . . . .	116
87	Binning in $W'$ and $Q^2$ for the 2 GeV data . . . . .	117
88	Binning in $\cos \theta_\pi^*$ and $\phi_\pi^*$ for the 5 GeV data . . . . .	118
89	Binning in $\cos \theta_\pi^*$ and $\phi_\pi^*$ for the 5 GeV data . . . . .	119
90	Binning in $\cos \theta_\pi^*$ and $\phi_\pi^*$ for the 5 GeV data . . . . .	120
91	Acceptance as a function of $W'$ for the 5 GeV data . . . . .	122
92	Acceptance as a function of $Q^2$ for the 5 GeV data . . . . .	123
93	Acceptance as a function of $\cos \theta_\pi^*$ for the 5 GeV data . . . . .	124
94	Acceptance as a function of $\phi_\pi^*$ for the 5 GeV data . . . . .	125
95	CLAS trigger efficiency for the 5 GeV data . . . . .	126
96	CLAS proton detection efficiency for the 5 GeV data . . . . .	128
97	Super ratio (real to simulation) of the CLAS proton detection efficiency	129
98	The RTPC proton detection efficiency . . . . .	130
99	Super ratio (real to simulation) of the RTPC proton detection efficiency	131
100	Real data: Background for all $W'$ bins . . . . .	133
101	Real data: Background dependence on $W'$ . . . . .	133
102	Real data: Background for all $Q^2$ bins . . . . .	134
103	Real data: Background dependence on $Q^2$ . . . . .	134
104	Real data: Background for all $\cos \theta_\pi^*$ bins . . . . .	135
105	Real data: Background dependence on $\cos \theta_\pi^*$ . . . . .	135
106	Real data: Background for all $\phi_\pi^*$ bins . . . . .	136
107	Real data: Background dependence on $\phi_\pi^*$ . . . . .	136
108	Simulated data: Background of all $W'$ bins . . . . .	137
109	Simulated data: Background dependence on $W'$ . . . . .	137
110	Simulated data: Background of all $Q^2$ bins . . . . .	138
111	Simulated data: Background dependence on $Q^2$ . . . . .	138
112	Simulated data: Background of all $\cos \theta_\pi^*$ bins . . . . .	139
113	Simulated data: Background dependence on $\cos \theta_\pi^*$ . . . . .	139
114	Simulated data: Background of all $\phi_\pi^*$ bins . . . . .	140
115	Simulated data: Background dependence on $\phi_\pi^*$ . . . . .	140

116	Ratio of Faraday cup to BPM current . . . . .	142
117	Ratio of Faraday cup to BPM for run 49566 (no stopper) . . . . .	144
118	Ratio of Faraday cup to BPM for 49935 (with stopper) . . . . .	145
119	The fitted penetration efficiency for runs from 49664 to 49691 . . . . .	146
120	The fitted penetration efficiency for runs from 49692 to 49796 . . . . .	146
121	Charge for each run after the penetration efficiency correction . . . . .	147
122	Ratio of the number of electrons to the total charge after the penetra- tion efficiency correction . . . . .	147
123	BoNuS Target Pressure for Each Run . . . . .	148
124	Differential cross section vs. $\phi_\pi^*$ at $W' = 1.230$ , for the 2 GeV data set	156
125	Differential cross section vs. $\phi_\pi^*$ at $W' = 1.525$ , for the 2 GeV data set	157
126	Differential cross section vs. $\phi_\pi^*$ at $W' = 1.675$ , for the 2 GeV data set	158
127	Differential cross section vs. $\phi_\pi^*$ at $W' = 1.230$ , for the 4 GeV data set	159
128	Differential cross section vs. $\phi_\pi^*$ at $W' = 1.525$ , for the 4 GeV data set	160
129	Differential cross section vs. $\phi_\pi^*$ at $W' = 1.675$ , for the 4 GeV data set	161
130	Differential cross section vs. $\phi_\pi^*$ at $W' = 1.230$ , for the 5 GeV data set	162
131	Differential cross section vs. $\phi_\pi^*$ at $W' = 1.525$ , for the 5 GeV data set	163
132	Differential cross section vs. $\phi_\pi^*$ at $W' = 1.675$ , for the 5 GeV data set	164
133	4D Cross Section Fitting Sample . . . . .	166
134	Structure functions vs. $\cos\theta_\pi^*$ at $W' = 1.230$ GeV/c, for the 2 GeV data set . . . . .	167
135	Structure functions vs. $\cos\theta_\pi^*$ at $W' = 1.375$ , for the 2 GeV data set .	168
136	Structure functions vs. $\cos\theta_\pi^*$ at $W' = 1.525$ , for the 2 GeV data set .	168
137	Structure functions vs. $\cos\theta_\pi^*$ at $W' = 1.675$ , for the 2 GeV data set .	169
138	Structure functions vs. $\cos\theta_\pi^*$ at $W' = 1.230$ , for the 4 GeV data set .	169
139	Structure functions vs. $\cos\theta_\pi^*$ at $W' = 1.375$ , for the 4 GeV data set .	170
140	Structure functions vs. $\cos\theta_\pi^*$ at $W' = 1.525$ , for the 4 GeV data set .	170
141	Structure functions vs. $\cos\theta_\pi^*$ at $W' = 1.675$ , for the 4 GeV data set .	171
142	Structure functions vs. $\cos\theta_\pi^*$ at $W' = 1.825$ , for the 4 GeV data set .	171
143	Structure functions vs. $\cos\theta_\pi^*$ at $W' = 1.975$ , for the 4 GeV data set .	172
144	Structure functions vs. $\cos\theta_\pi^*$ at $W' = 1.230$ , for the 5 GeV data set .	172
145	Structure functions vs. $\cos\theta_\pi^*$ at $W' = 1.375$ , for the 5 GeV data set .	173
146	Structure functions vs. $\cos\theta_\pi^*$ at $W' = 1.525$ , for the 5 GeV data set .	173
147	Structure functions vs. $\cos\theta_\pi^*$ at $W' = 1.675$ , for the 5 GeV data set .	174
148	Structure functions vs. $\cos\theta_\pi^*$ at $W' = 1.825$ , for the 5 GeV data set .	174
149	Structure functions vs. $\cos\theta_\pi^*$ at $W' = 1.975$ , for the 5 GeV data set .	175
150	$\sigma_T + \varepsilon\sigma_L$ vs. $W'$ for the 2 GeV data set . . . . .	176
151	$\sigma_{LT}$ vs. $W'$ for the 2 GeV data set . . . . .	177
152	$\sigma_{TT}$ vs. $W'$ for the 2 GeV data set . . . . .	178
153	$\sigma_T + \varepsilon\sigma_L$ vs. $W'$ for the 4 GeV data set . . . . .	179
154	$\sigma_{LT}$ vs. $W'$ for the 4 GeV data set . . . . .	180
155	$\sigma_{TT}$ vs. $W'$ for the 4 GeV data set . . . . .	181
156	$\sigma_T + \varepsilon\sigma_L$ vs. $W'$ for the 5 GeV data set . . . . .	182
157	$\sigma_{LT}$ vs. $W'$ for the 5 GeV data set . . . . .	183

158	$\sigma_{\text{TT}}$ vs. $W'$ for the 5 GeV data set . . . . .	184
159	$\sigma_{\text{T}} + \varepsilon\sigma_{\text{L}}$ vs. $\cos\theta_{\pi}^*$ for the 2 GeV data set, VIP cuts applied . . . . .	186
160	$\sigma_{\text{LT}}$ vs. $\cos\theta_{\pi}^*$ for the 2 GeV data set, VIP cuts applied . . . . .	187
161	$\sigma_{\text{TT}}$ vs. $\cos\theta_{\pi}^*$ for the 2 GeV data set, VIP cuts applied . . . . .	188
162	$\sigma_{\text{T}} + \varepsilon\sigma_{\text{L}}$ vs. $\cos\theta_{\pi}^*$ for the 4 GeV data set, VIP cuts applied . . . . .	189
163	$\sigma_{\text{LT}}$ vs. $\cos\theta_{\pi}^*$ for the 4 GeV data set, VIP cuts applied . . . . .	190
164	$\sigma_{\text{TT}}$ vs. $\cos\theta_{\pi}^*$ for the 4 GeV data set, VIP cuts applied . . . . .	191
165	$\sigma_{\text{T}} + \varepsilon\sigma_{\text{L}}$ vs. $\cos\theta_{\pi}^*$ for the 5 GeV data set, VIP cuts applied . . . . .	192
166	$\sigma_{\text{LT}}$ vs. $\cos\theta_{\pi}^*$ for the 5 GeV data set, VIP cuts applied . . . . .	193
167	$\sigma_{\text{TT}}$ vs. $\cos\theta_{\pi}^*$ for the 5 GeV data set, VIP cuts applied . . . . .	194
168	$\sigma_{\text{T}} + \varepsilon\sigma_{\text{L}}$ vs. $W'$ for the 2 GeV data set, VIP cuts applied . . . . .	195
169	$\sigma_{\text{LT}}$ vs. $W'$ for the 2 GeV data set, VIP cuts applied . . . . .	196
170	$\sigma_{\text{TT}}$ vs. $W'$ for the 2 GeV data set, VIP cuts applied . . . . .	197
171	$\sigma_{\text{T}} + \varepsilon\sigma_{\text{L}}$ vs. $W'$ for the 4 GeV data set, VIP cuts applied . . . . .	198
172	$\sigma_{\text{LT}}$ vs. $W'$ for the 4 GeV data set, VIP cuts applied . . . . .	199
173	$\sigma_{\text{TT}}$ vs. $W'$ for the 4 GeV data set, VIP cuts applied . . . . .	200
174	$\sigma_{\text{T}} + \varepsilon\sigma_{\text{L}}$ vs. $W'$ for the 5 GeV data set, VIP cuts applied . . . . .	201
175	$\sigma_{\text{LT}}$ vs. $W'$ for the 5 GeV data set, VIP cuts applied . . . . .	202
176	$\sigma_{\text{TT}}$ vs. $W'$ for the 5 GeV data set, VIP cuts applied . . . . .	203



# CHAPTER I

## INTRODUCTION

It is well known that matter is composed of atoms and that atoms have a nucleus and electrons that move around it. A nucleus is made up of nucleons, which is a collective name for protons and neutrons. Since the discovery of the neutron by J. Chadwick in 1932, protons and neutrons were assumed to be the elemental particles of matter, until the 1960s. As time went on, more and more evidence that the proton and neutron had internal structure was discovered. In 1964, the constituent quark model (CQM) was proposed by Gell-Mann and Zweig to explain particles and their strong interactions in the language of quarks [1] [2] [3]. In the CQM, particles made from quarks fall into one of two groups: mesons and baryons. Mesons are composed of quark and anti-quark pairs, while baryons are composed of three quarks. Mesons and baryons together form the family of hadrons. The quantum numbers of a hadron can be formed by considering the quark components, which are shown in Table 1.

TABLE 1: Quarks and their properties

Symbol	Name	Mass (GeV/c <sup>2</sup> )	Charge (e)	Isospin
d	Down	0.0015 – 0.005	–1/3	1/2
u	Up	0.003 – 0.009	2/3	1/2
s	Strange	0.06 – 0.17	–1/3	0
c	Charm	1.1 – 1.4	2/3	0
b	Bottom	4.1 – 4.4	–1/3	0
t	Top	168.6 – 179.0	2/3	0

Although this model succeeded in explaining most hadrons, it violated Fermi-Dirac statistics, which was discovered by Fermi in 1952 [4], when trying to describe the  $\Delta^{++}$  hadron. The  $\Delta^{++}$  has spin  $\frac{3}{2}$  and charge +2, and is interpreted as a  $uuu$  bound state with zero orbital angular momentum and three parallel spins. In that case the wave function is completely symmetric, which would violate the Pauli exclusion principal. In order to explain this dilemma, in 1965 and 1966, Han and Nambu [5] and Greenberg [6] independently introduced another quantum number

---

This dissertation follows the style of *Physical Review C*.

into the CQM. It was proposed that quarks have another quantum number with three possible states which can change from one to the other. This quantum number was later named “color”, and its three states are known as red, green and blue. This “color charge” provides an additional  $SU(3)$  gauge degree of freedom to the CQM. In the 1970s, Politzer [8] [9] and Wilczek and Gross [7] realized that quarks and gluons couple to the color change in a theory named Quantum Chromodynamics (QCD). QCD has two unique properties, asymptotic freedom and confinement. Asymptotic freedom means that in very high-energy reactions, quarks and gluons interact very weakly. Asymptotic freedom tells us that if the quarks are close enough to each other, the strong interaction between them is so weak that they behave almost like free particles. Confinement means that the force between quarks does not diminish as they are separated. Because of this, it would take an infinite amount of energy to separate two quarks. Although not analytically proven yet, confinement seems to be true because it explains the consistent failure to find a free quark despite many searches.

Despite the highly nonlinear nature of the strong force, asymptotic freedom means that one can use the perturbative approximation accurately at high energy since quarks and gluons can be treated as nearly free. This technique is known as perturbative QCD (pQCD) and enables us to calculate many aspect of experiments at high energy. Unfortunately, many processes at low energy can not be calculated directly with pQCD because free quarks and gluons are not allowed by confinement. Therefore physicists separate strong interactions into two parts: the short-distance part (for which pQCD is available) and the long-distance part (non-perturbative). The long-distance parts can be measured with a global fit to experiments. In such a way, scientists obtain a partly calculable prediction of particle reaction processes. The universal long-distance functions include the parton distribution functions (PDF), generalized parton distributions (GPD), and many kinds of form factors and structure functions.

Since 1932, the structure of nucleons and their excited states, known as resonances, has been an active area of experimental investigation. Electron scattering as a probe of the internal structure of nucleons has been widely used. Large and successful efforts have been dedicated to obtain accurate measurements of the inclusive electron scattering cross section. Unfortunately, the nucleon resonances are wide and overlapping, so inclusive measurements are not capable of distinguishing and

studying all of them. More information can be available by measuring the other outgoing particles together with the scattered electron. Such measurements are known as “exclusive” because the final state of the reaction is completely determined.

In this dissertation we will describe an experiment, *Barely off-shell Nuclear Structure* (BoNuS), which was carried out in Hall B of the Thomas Jefferson National Accelerator Facility (TJNAF) in the Fall of 2005. Electrons with beam energies of 1.1005, 2.1426, 4.2262 and 5.2681 GeV were used to bombard a gaseous deuterium target. A Radial Time Projection Chamber (RTPC) was built to measure low energy spectator protons to study the  $D(e, e'p_s)X$  reaction. With this detector, protons with momentum as low as 67 MeV/c were measured. We analyzed these experimental data to study the  $D(e, e'\pi^-p)p$  reaction, in order to investigate neutron resonance structure. This thesis is dedicated to the analysis of exclusive negative pion production from the deuteron for the purpose of studying the neutron resonances.

## CHAPTER II

### THEORETICAL BACKGROUND

#### II.1 MOTIVATION

The objective of this analysis is to study the resonances of the neutron. The proton ( $uud$  quarks) and neutron ( $udd$  quarks) are isospin partners of each other. The electromagnetic force on a proton and neutron is different, since their electric charge is different. There is also a slight difference between the mass of an up and down quark. However, these differences are negligible compared to the magnitude of the strong force. Since the strong force on an up quark and a down quark are the same, the quark model does not predict important differences between proton structure and neutron structure. From the view of the strong force, it can even be assumed that the proton and the neutron are the same particle but in different states. The difference between these two states can be characterized by the  $\hat{z}$  component ( $I_z$ ) of their isospin ( $I$ ). For the proton  $I_z = \frac{1}{2}$  while for the neutron  $I_z = -\frac{1}{2}$ . Of course protons and neutrons are more complicated in reality because their structures include  $q\bar{q}$  pairs (the sea) and gluons.

Many electron-proton scattering experiments have been carried out in the past 60 years and a lot of useful data have been measured, both inclusive and exclusive, for the proton. However, due to the fact that there is no free neutron target, very few neutron data are available. The free neutron  $\beta$ -decays with a half life of about 10.3 minutes, but some bound states of the neutron are remarkably stable. Deuterium, an isotope of hydrogen, whose nucleus consists of one proton and one neutron, is the best alternate target for neutrons, because it is the simplest and most loosely bound state that includes a neutron. However, because the neutron and the proton in a deuteron are still bound, a few corrections must be considered in order to extract the neutron information. For example, binding effects, off-shell effects and the Fermi motion of the nucleon play important roles.

Figure 1 shows the cross section in the resonance region for both the proton and deuteron measured by Jefferson Laboratory (JLab) as well as the fit to the Stanford Linear Accelerator Center (SLAC) data. In the case of the proton the three main resonance structures, known as  $\Delta(1232)$  and the 2nd and 3rd resonance regions,



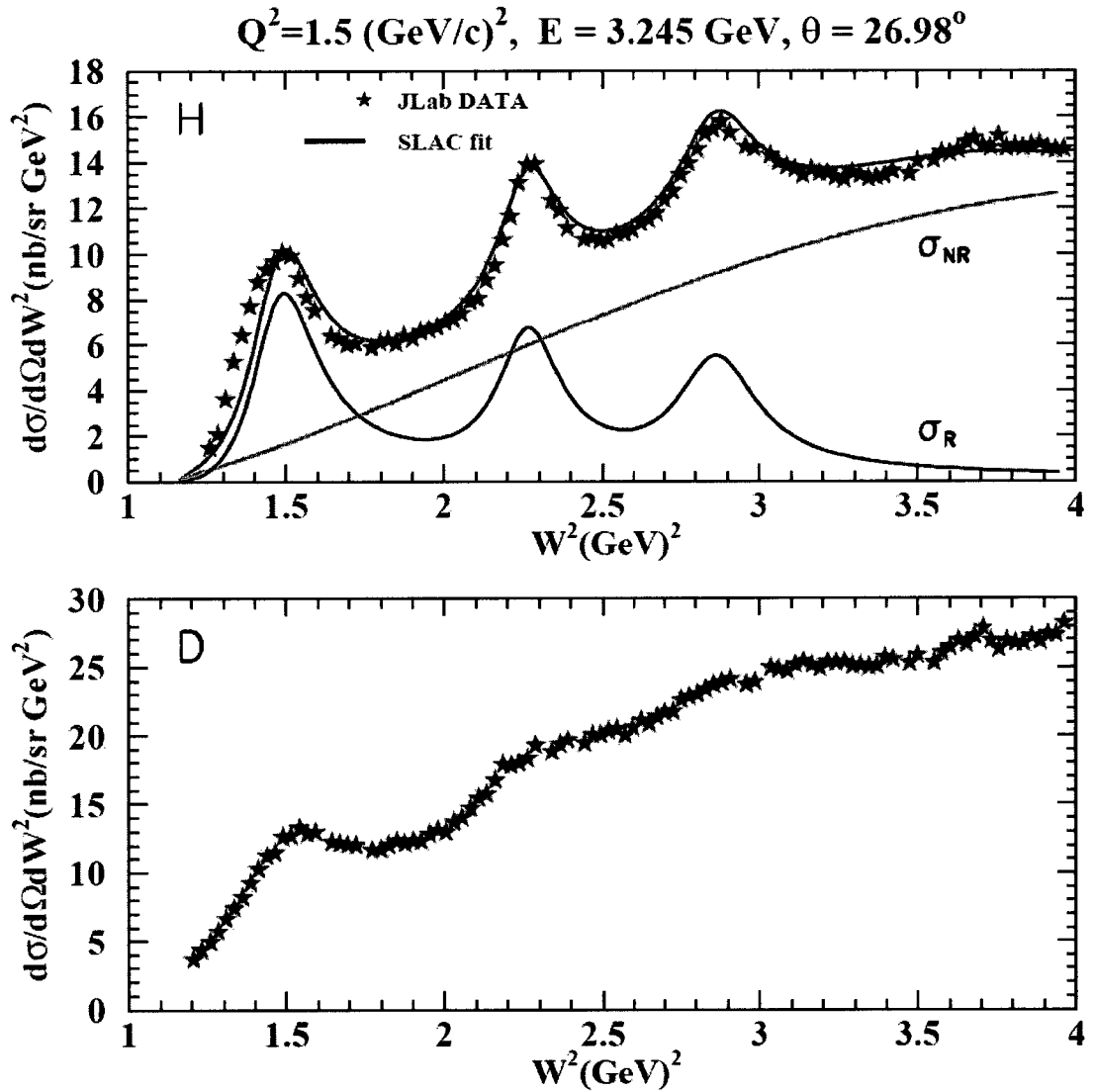


FIG. 1: Inclusive electron scattering cross section for the proton (top) and deuteron (bottom) measured by Jefferson Lab (JLab) at  $Q^2 = 1.5 \text{ GeV}^2$  and  $\theta = 26.98^\circ$ . The red points are JLab data and the blue curve is a fit to the Stanford Linear Accelerator Center (SLAC) data. The  $\sigma_R$  (black curve) and  $\sigma_{NR}$  (green curve) in the top figure are the resonance fit and non-resonance background fit, respectively.

can be seen clearly. However, the deuteron spectrum has been smeared out for the reasons mentioned above. New theoretical models and new technology are needed to deal with binding effects, off-shell effects and the Fermi motion in order to extract more detailed information about the resonances of the neutron.

## II.2 ELECTRON SCATTERING

Electron scattering is a powerful tool to study the internal structure of hadrons. While elastic scattering can be used only to study the ground state of the particle, inelastic scattering can be employed to investigate the complicated excited states of the particle.

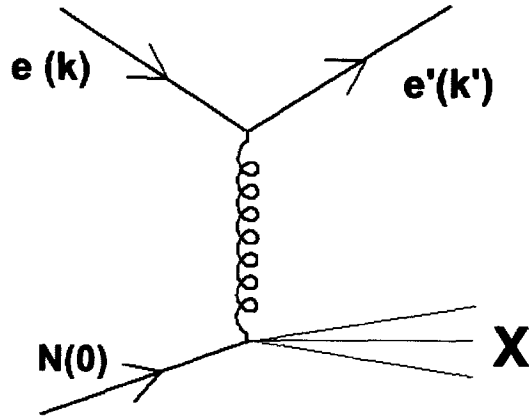


FIG. 2: Diagram of electron scattering in the one (virtual) photon exchange approximation.

Fig. 2 shows a diagram of electron scattering. In this picture, the electron comes in with initial four-momentum  $(E, \mathbf{k})$  and goes out with final four-momentum  $(E', \mathbf{k}')$  and with an angle  $\theta_e$  with respect to the incident direction. A virtual photon is emitted that interacts with a target nucleon  $N$  at rest, whose four-momentum is characterized as  $N(M, \mathbf{0})$ . The four-momentum of the virtual photon here can be characterized as  $q(\nu, \mathbf{q})$ , where  $\nu = E - E'$  and  $\mathbf{q} = \mathbf{k} - \mathbf{k}'$ . The squared four-momentum transfer  $Q^2$  is defined as the negative mass square of the virtual photon

$$Q^2 \equiv -q^2 = 4EE' \sin^2 \frac{\theta_e}{2}, \quad (1)$$

and the invariant mass of the photon-nucleon system is given by

$$W = \sqrt{(q + N)^2} = \sqrt{M^2 + 2M\nu - Q^2}. \quad (2)$$

The cross section for inelastic electron scattering from a nucleon target can be written as

$$\frac{d^2\sigma}{dE'd\Omega} = \sigma_{\text{Mott}}(2W_1(\nu, Q^2) \tan^2 \frac{\theta_e}{2} + W_2(\nu, Q^2)). \quad (3)$$

Here  $\sigma_{\text{Mott}} = \frac{4\alpha^2 E'^2}{Q^4} \cos^2 \frac{\theta_e}{2}$  is the so called Mott cross section, which is the cross section for electron scattering from a point like particle in a Coulomb field and  $\alpha = 1/137$  is the electromagnetic coupling constant.  $W_1$  and  $W_2$  are inelastic structure functions. For convenience, we introduce the transverse and longitudinal component cross sections  $\sigma_T$  and  $\sigma_L$ ,

$$\sigma_T = \frac{4\pi^2\alpha}{K_\gamma} W_1(\nu, Q^2), \quad (4)$$

$$\sigma_L = \frac{4\pi^2\alpha}{K_\gamma} \left( W_1(\nu, Q^2) + \left(1 + \frac{\nu^2}{Q^2}\right) W_2(\nu, Q^2) \right). \quad (5)$$

In the equation above,

$$K_\gamma = \frac{W^2 - M^2}{2M}, \quad (6)$$

is introduced as the photon equivalent energy, the laboratory energy necessary for a real photon to excite a hadronic system with center of mass  $W$ . Using Eqs. (4) and (5), Eq. (3) then can be written as

$$\frac{d^2\sigma}{dE'd\Omega} = \Gamma_v(\sigma_T + \varepsilon\sigma_L), \quad (7)$$

where  $\Gamma_v$  is the flux of the virtual photon, which is given by

$$\Gamma_v = \frac{\alpha}{2\pi^2} \frac{E' K_\gamma}{E Q^2} \frac{1}{1 - \varepsilon}, \quad (8)$$

and  $\varepsilon$  is the degree of virtual photon polarization defined by

$$\varepsilon = \left(1 + 2 \frac{\mathbf{q}^2}{Q^2} \tan^2 \frac{\theta_e}{2}\right)^{-1} = \left(1 + 2\left(1 + \frac{\nu^2}{Q^2}\right) \tan^2 \frac{\theta_e}{2}\right)^{-1}. \quad (9)$$

### II.3 RESONANCES

The ground states of most hadrons are relatively stable and they decay by the weak or electromagnetic interaction. There also exists many excited states, which

are usually highly unstable particles, called *resonances*. Excited states usually decay through the strong interaction with a very short life-time of about  $10^{-23}$  seconds [10], so they are very difficult to detect directly. However, the existence of resonances can be inferred from the observation of the more stable hadrons to which they decay. For example, in an electron neutron inelastic scattering, a neutron may absorb a virtual photon and turn into  $\Delta$  resonance:

$$\gamma^* + n \rightarrow \Delta, \quad (10)$$

which then decays by the reaction

$$\Delta \rightarrow \pi^- + p. \quad (11)$$

This reaction has been illustrated in Fig. 3, where the time between when the  $\Delta$  is

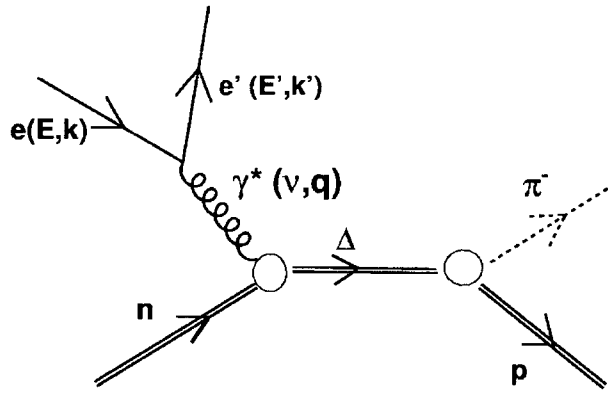


FIG. 3: In an electron neutron inelastic scattering event, a neutron absorbs the virtual photon and turns into a resonance state  $\Delta$  which then decays to a  $\pi^-$  and proton.

produced and when it decays is too short to be measured. The observation of this reaction therefore is written as

$$e + n \rightarrow e' + \pi^- + p, \quad (12)$$

but the same final state may be produced from many other resonant or non-resonant reactions.

Basically a resonance is considered to be a “particle” since it has all the characteristics that a particle has, i.e. mass (energy), charge, spin, isospin and other quantum

numbers. However, we still use the term “resonance” because its life time is short and its energy spans a large range. Therefore the resonance energy, width and half life are usually used to describe a resonance. For example, if one plots the probability of finding a  $\pi^-p$  final state as a function of the invariant mass,  $W = \sqrt{(p^\mu + \pi^\mu)^2}$ , where  $p^\mu$  and  $\pi^\mu$  are the four-momentum of the proton and  $\pi^-$  respectively, one sees a broad peak centered at 1.232 GeV for the lowest lying  $\Delta$  resonance.

The notation that we use to characterize a particular resonance depends on its quantum numbers. There are currently 6 families of resonances:  $N$  ( $I = \frac{1}{2}$ ),  $\Delta$  ( $I = \frac{3}{2}$ ),  $\Lambda$  ( $I = 0$ ),  $\Sigma$  ( $I = 1$ ),  $\Xi$  ( $I = \frac{1}{2}$ ) and  $\Omega$  ( $I = 0$ ). The numbers inside the parenthesis is the isospin of this type of resonances. These families are organized in the following way:

- $N$  are the resonances with  $I = \frac{1}{2}$  that consist of  $u$  and  $d$  quarks only.
- $\Delta$  are the resonances with  $I = \frac{3}{2}$  that consist of  $u$  and  $d$  quarks only.
- $\Lambda$  are the resonances with  $I = 0$  that consist of both  $u$  and  $d$  quarks plus at least one quark from  $s$ ,  $c$  and  $b$ . The  $c$  or  $b$  quarks must be included in the name as a subscript.
- $\Sigma$  are the resonances with  $I = 1$  that consist of both  $u$  and  $d$  quarks plus at least one quark from  $s$ ,  $c$  and  $b$ . The  $c$  or  $b$  quark must be included in the name as a subscript.
- $\Xi$  are the resonances with  $I = \frac{1}{2}$  that consist of one quark from  $u$  or  $d$  plus two quarks from  $s$ ,  $c$  and  $b$ . The  $c$  or  $b$  quark must be included in the name as a subscript. For example the  $dsc$  and  $dcc$  bound states are written as  $\Xi_c^0$  and  $\Xi_{cc}^+$ , respectively.
- $\Omega$  are the resonances with  $I = 0$  that have no  $u$  or  $d$  quarks. Again, the  $c$  or  $b$  quarks must be included in the name as a subscript.

## II.4 PION PRODUCTION

As mentioned above, resonances usually decay via the strong interaction, so the decay products must be a baryon (three quarks state) accompanied by one or more mesons (two quarks state). Referring back to the masses of quarks in Table 1, one

can see that a meson that is a bound state of an up and a down quark must be the lightest one in the hadron family. There are three combinations of  $u$  and  $d$  quark and anti-quark pairs:  $\pi^+(u\bar{d})$ ,  $\pi^0(\frac{u\bar{u}-d\bar{d}}{\sqrt{2}})$  and  $\pi^-(\bar{u}d)$ . These three bound states are also known as pions. A pion production process is a reaction whose decay products contain at least one of these three pions. Since the pions are the lightest hadrons, the pion production process is one of the most common ways to study the nucleon resonances. The four simplest pion production reactions from proton and neutron targets in electron scattering can be summarized as

$$\gamma^* + p \rightarrow \pi^+ + n, \quad (13)$$

$$\gamma^* + p \rightarrow \pi^0 + p, \quad (14)$$

$$\gamma^* + n \rightarrow \pi^- + p, \quad (15)$$

$$\gamma^* + n \rightarrow \pi^0 + n. \quad (16)$$

Reaction (16) is very difficult to study because there are two neutral particles in the final state. Reaction (15) is problematic due to the lack of a free neutron target, as mentioned above, but it is the channel on which we are focused in this analysis.

The kinematics of  $\pi^-$  electro-production from the neutron is shown in Fig. 4. The kinematic variables  $\nu$ ,  $\mathbf{q}$ ,  $Q^2$  and  $W$  are the same as described in Section II.2. The leptonic plane is formed by vector  $\mathbf{q}$  and the direction of the beam line. The hadronic plane is formed by the momentum vector of the emitted  $\pi^-$  and the momentum of the center of mass (CM) system (the virtual photon plus the moving neutron target:  $\mathbf{q} + \mathbf{n}$ ). The three axes of the CM frame can be defined as:

$$\begin{aligned} \hat{z} &= \frac{\mathbf{q} + \mathbf{n}}{|\mathbf{q} + \mathbf{n}|}; \\ \hat{y} &= \mathbf{q} \times \mathbf{n}; \\ \hat{x} &= \hat{y} \times \hat{z}. \end{aligned}$$

$\theta^*$  and  $\phi^*$  are the polar angle and azimuthal angle of the outgoing  $\pi^-$  in the CM frame. The invariant mass  $W$  defined in Eq. (2) was derived assuming that the target nucleon is at rest. In the BoNuS experiment our target neutron has Fermi motion inside the deuteron, so the invariant mass of the virtual photon plus neutron system becomes

$$W' = \sqrt{(q^\mu + n^\mu)^2}. \quad (17)$$

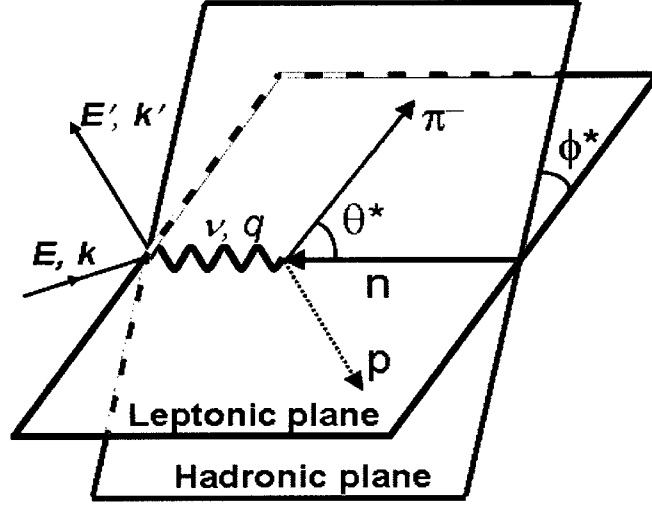


FIG. 4: Kinematics of  $\pi^-$  electro-production from a moving neutron. The leptonic plane is formed by vector  $\mathbf{q}$  and the direction of the beam line. The hadronic plane is formed by the momentum vector of the emitted  $\pi^-$  and the center of mass momentum of the virtual photon and the moving neutron.  $\theta^*$  and  $\phi^*$  are the polar angle and azimuthal angle of the outgoing  $\pi^-$  in the C.M. frame.

Since we are using an electron beam and a deuterium target, reaction (15) can be rewritten as

$$e + D \rightarrow e' + \pi^- + p + p_s, \quad (18)$$

where  $p_s$  stands for the spectator proton, which is not involved in the reaction. The cross section for this exclusive reaction with unpolarized electron beam and unpolarized deuteron target is given by

$$\frac{\partial^5 \sigma}{\partial E' \partial \Omega_e \partial \Omega_\pi^*} = \Gamma_v \frac{\partial^2 \sigma}{\partial \Omega_\pi^*}, \quad (19)$$

where  $\Gamma_v$  is the virtual photon flux given by Eq. (8) and  $\frac{\partial^2 \sigma}{\partial \Omega_\pi^*}$  is the differential pion photo-absorption cross section:

$$\frac{\partial^2 \sigma}{\partial \Omega_\pi^*} = \sigma_T + \varepsilon \sigma_L + \sqrt{2\varepsilon(1+\varepsilon)} \sigma_{LT} \cos \phi_\pi^* + \varepsilon \sigma_{TT} \cos 2\phi_\pi^*. \quad (20)$$

In this equation,  $\sigma_T$  and  $\sigma_L$  are the transverse and longitudinal components of the differential pion photo-absorption cross section,  $\sigma_{LT}$  is the longitudinal-transverse interference term and  $\sigma_{TT}$  is the transverse-transverse interference term. All of them are

functions of  $W'$ ,  $Q^2$  and  $\theta_\pi^*$ . In this analysis, we have measured  $\frac{\partial^2 \sigma}{\partial \Omega_\pi^*} (W', Q^2, \cos \theta_\pi^*, \phi_\pi^*)$  and have extracted the structure functions  $\sigma_T + \varepsilon \sigma_L$ ,  $\sigma_{LT}$  and  $\sigma_{TT}$  for comparison with existing phenomenological models in the resonance region.

## II.5 FITS TO EXISTING DATA

There exist several phenomenological models which describe the pion production cross section in the resonance region. Two of the widely used models are MAID and SAID. The MAID model is a unitary isobar model for pion photo- and electro-production on the nucleon, which was developed in Mainz, Germany [11] [12] [13]. The SAID model is another similar database provided by the nuclear physics group at George Washington University (GWU) [14]. Both of these models are phenomenological fits to previous photo- and electro-production data, covering the center of mass energy  $W$  up to 2.0 GeV and  $Q^2$  up to 4.0 GeV<sup>2</sup>. Most of the data points fitted by these two models came from proton measurements. A very small fraction of the data came from deuteron target experiments in which the ratio of  $\pi^-$  production to  $\pi^+$  production was measured [16, 17, 18, 19, 20, 21, 22, 23]. For example, in the SAID database, there are in total about 100,000 pion electro-production data points, but only 890 of them belong to deuteron or helium measurements.

## II.6 EXTRACTING THE CROSS SECTION

The goal of this analysis is to provide  $\pi^-$  electro-production cross sections over a large kinematic range to the phenomenological models mentioned above. These cross sections will be added to the database and should improve the fits, such as MAID and SAID, for the neutron. However, as mentioned previously, using a neutron in a deuteron target is not the same as a free neutron target, even if the spectator proton is detected. Although the momentum of the spectator proton is measured, we still need to deal with the off-shell effects and final state interactions.

### II.6.1 Off-shell Effects



One way to investigate the effects of the neutron being off-shell is to consider the ratio of the off-shell to on-shell neutron structure function  $F_2$ :

$$R_n \equiv \frac{F_2^{n\text{bound}}}{F_2^{n\text{free}}}. \quad (21)$$

The ratio  $R_n$  calculated by Melnitchouk and Schreiber [24, 25] is plotted in Fig. 5 as a function of spectator proton momentum  $p_s$  for different values of Bjoken  $x$ , which is defined as

$$x \equiv \frac{Q^2}{2q^\mu N^\mu}, \quad (22)$$

where  $q^\mu$  is the four-momentum of the virtual photon and  $N^\mu$  is that of the target with mass  $M$ . If the target is at rest then the Bjoken  $x$  can be reduced to  $x = \frac{Q^2}{2M\nu}$ .

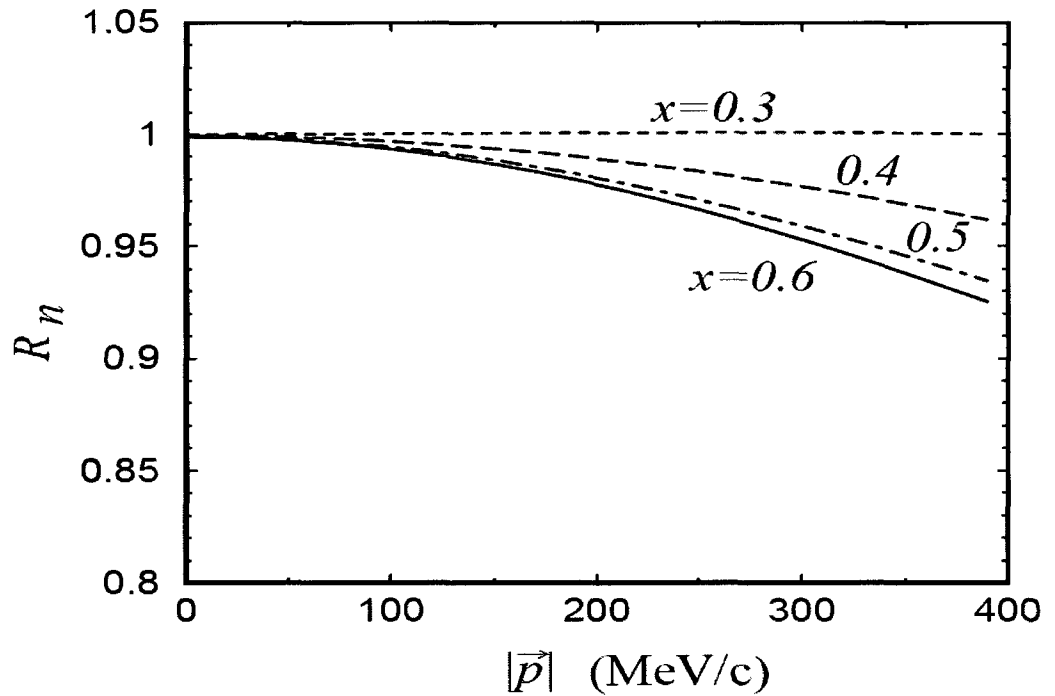


FIG. 5: Calculation of the ratio of bound to free neutron structure function as a function of the spectator proton momentum. Predictions for various Bjoken  $x$  values are shown [24, 25].

One can see that the off-shell effects are small (less than 5%) when  $p_s$  is below 300 MeV/c, regardless of the value of  $x$ .

## II.6.2 Final State Interactions

Final state interactions (FSI) play a critical role in the reaction  $D(e, e'\pi^-p)p$ . Of course the motivation to study  $\pi^-$  production from the deuteron is that it is primarily sensitive to the neutron. We hope to study the process shown in Fig. 6 (I). However, also shown in Fig. 6 are the main two source of final state interactions in which the final state  $\pi^-$  (Fig. 6 (II)) or proton (Fig. 6 (III)) interact with the spectator proton. One can define an FSI correction factor,  $R_{\text{FSI}}$ , which is the ratio of the amplitude associated with the diagram in Fig. 6 (I) to the full calculation for all diagrams in Fig. 6.

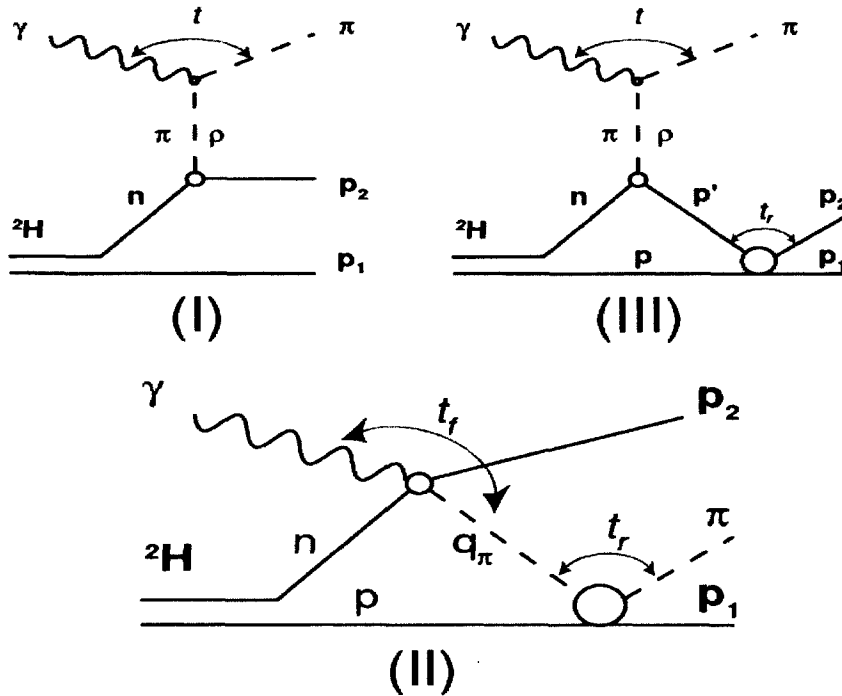


FIG. 6: Feynman diagrams for the three leading terms in  $\gamma^*d \rightarrow \pi^-pp$  [27]: (I) quasi-free; (II)  $\pi p$  rescattering; (III)  $pp$  rescattering. Diagrams (II) and (III) are the main source of final state interactions.

I. Strakovsky *et al.* are working on a calculation of the FSI for real photons ( $Q^2 = 0$ ),  $\gamma d \rightarrow \pi^-pp$ . For  $E_\gamma = 0.8$  GeV or  $W = 1.545$  GeV and with the spectator proton momentum below 200 MeV/c, the FSI correction factor varies from 0.4 to 1.3 [26]. Strakovsky and collaborators plan to expand this calculation to include

virtual photons ( $Q^2 > 0$ ).

J.M. Laget has also calculated the  $\gamma d \rightarrow \pi^- pp$  process [27]. Laget considered the same two processes ( $\pi p$  and  $pp$  rescattering) in Fig. 6. The ratio of the full cross

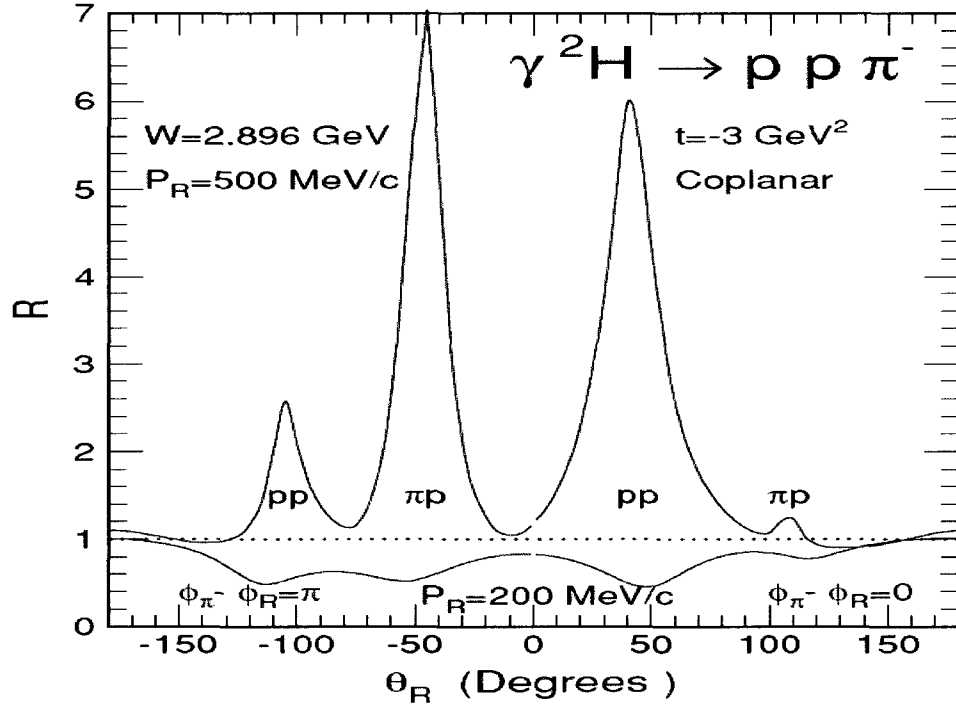


FIG. 7: The ratio of the total to the quasi-free cross section for the reaction  $D(\gamma, \pi^- p)p$  as a function of the polar angle of the recoiling proton, whose momentum is kept constant at 500 MeV/c (top) and 200 MeV/c (bottom) [27]. The peaks labeled  $\pi p$  and  $pp$  correspond, respectively, to  $\pi p$  and  $pp$  on-shell rescattering. The dotted line corresponds to the quasi-free process. The kinematics is coplanar, and positive angles correspond to the emission of the pion and the recoiling proton on the same side of the photon.

section to the quasi-free cross section at  $W = 2.896$  GeV and momentum transfer  $t = -3.0$  GeV<sup>2</sup> for spectator momenta  $P_R = 500$  MeV/c and  $P_R = 200$  MeV/c are shown as a function of the angle between the spectator proton and the photon (*cf.* Fig. 7), where  $t$  is defined as the momentum transfer between the photon and the outgoing  $\pi^-$ :

$$t \equiv (q^\nu - p_i^\nu)^2.$$

The  $\pi p$  and  $pp$  rescattering peaks are extremely prominent, which means that FSI has a very strong dependence on the angle  $\theta_R$ . In addition to that, by comparing

these two ratios one can see that FSI at  $P_R = 500$  MeV/c can be as large as a factor of 7 while FSI at  $P_R = 200$  MeV/c is no more than a factor of 0.5, which means that FSI has strong dependence on spectator momentum too. Note that the ratio calculated by Laget is the inverse of  $R_{\text{FSI}}$  defined previously.

In order to study the spectator momentum dependence, Laget selected the  $\pi p$  rescattering peak region and plotted the ratio of the total to the quasi-free cross section in that same kinematic region as a function of the spectator momentum (*cf.* Fig. 8). This result shows that the ratio decreases as  $P_R$  increases when  $P_R < 250$

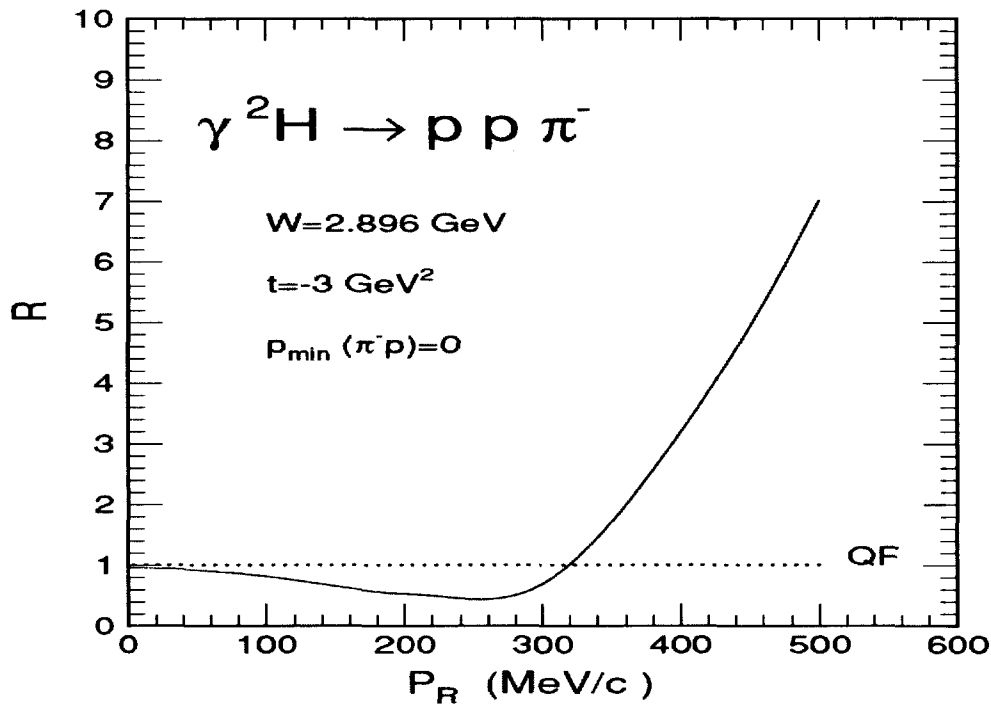


FIG. 8: The ratio of the total to the quasi-free cross section at  $W = 2.896$  GeV and  $t = -3.0$  GeV<sup>2</sup> against the spectator proton momentum at the  $\pi p$  rescattering peak region. The solid curve includes both  $\pi p$  and  $pp$  scattering (small effect). The dotted line corresponds to the quasi-free process.

MeV/c, while the ratio increases sharply as  $P_R$  increases when  $P_R > 250$  MeV/c. If one keeps  $P_R < 120$  MeV/c, the FSI correction factor can be held at a level below 20%.

A very similar result had been achieved by C. Ciofi degli Atti, L.P. Kaptari and B.Z. Kopeliovich [28]. Ciofi degli Atti and his collaborators were trying to study FSI in semi-exclusive deep inelastic scattering (DIS) of electrons off the deuteron,

$D(e, e'p_s)X$ . Their calculation demonstrated that when the recoiling spectator nucleon is detected in the backward hemisphere with low momentum, the effects from the FSI are negligible, whereas at large transverse momenta of the spectator, FSI effects are rather large [28]. Figure 9 shows the ratio of the DIS cross section with and without FSI corrections as a function of spectator proton momentum  $p_s$  (left) and  $\theta_s$  (right).  $\theta_s$  defined by Ciofi is the same as  $\theta_{pq}$  defined in the BoNuS analysis. One

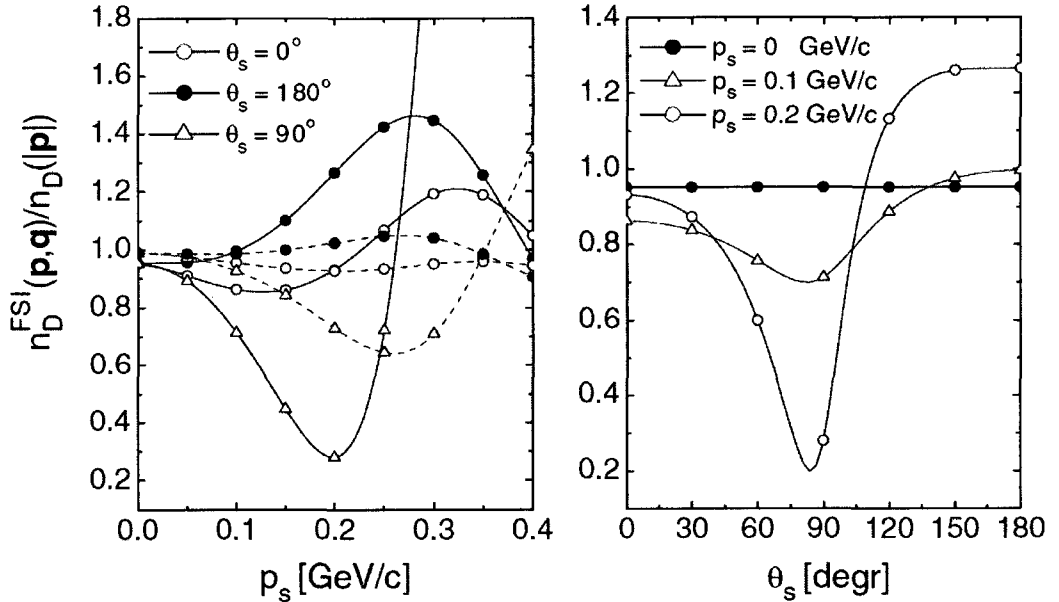


FIG. 9: The ratio of the deep inelastic scattering cross section with and without FSI corrections from [28], at  $Q^2 = 5 \text{ GeV}^2$  and  $x = 0.2$ , as a function of spectator momentum  $p_s$  (left) and  $\theta_s$  (right), which is the angle between spectator proton and the virtual photon). In the left panel, the full lines correspond to the  $Q^2$ - and  $z$ -dependent debris-nucleon effective cross section ( $\sigma_{\text{eff}}$ ), whereas the dashed lines correspond to a constant cross section  $\sigma_{\text{eff}} = 20 \text{ mb}$ .

can see that FSI effects can be held at a level below 20% by requiring the spectator momentum less than 120 MeV/c and  $\theta_s$  larger than  $100^\circ$ .

All three of the calculations described above show that the effects of FSI are not trivial. Although no predictions for  $D(e, e'\pi^-p)p$  are available yet, both the DIS model (from Ciofi degli Atti) and the exclusive photo-production model (from Laget) show that the effects of FSI can be held to the 20% level by requiring  $p_s < 120$  MeV/c and  $\theta_{pq} > 100^\circ$ . In order to study this, a special cut named ‘‘Very Important spectator Protons (VIP)’’ is introduced in this analysis. For convenience, the VIP

cut is defined as  $70 \text{ MeV}/c \leq p_s < 120 \text{ MeV}/c$  and  $\theta_{pq} > 100^\circ$ . The differential cross section and the structure functions  $\sigma_T + \varepsilon\sigma_L$ ,  $\sigma_{LT}$  and  $\sigma_{TT}$  with and without this VIP cut will be extracted and compared. Details will be given in the following chapters.

In this thesis we describe an experiment to measure the differential cross sections for the  $D(e, e'\pi^-p)$  reaction. In Chapter 3 we describe the BoNuS experiment in some detail, including both the CLAS and the RTPC detectors. The simulation of BoNuS will be described in Chapter 4 and the data analysis procedure will be described in Chapter 5. Chapter 6 shows the physics results and chapter 7 will summarize this work and give an outlook for the future.

## CHAPTER III

### EXPERIMENTAL SETUP

#### III.1 CONTINUOUS ELECTRON BEAM ACCELERATOR FACILITY

The BoNuS experiment was performed using the electron beam provided by the Continuous Electron Beam Accelerator Facility (CEBAF) at Jefferson Lab (TJNAF). The electron accelerator uses 338 superconducting radio frequency accelerating cavities to boost the electron and provides a continuous high luminosity electron beam with energy up to almost 6 GeV after five turns [29, 30, 31]. These accelerating cavities are made of the metallic element niobium, which is a superconductor when cooled down to 2 Kelvin by liquid helium produced at the Lab's Central Helium Refrigerator. The cavities are operating at a frequency of 1.497 GHz to produce an electric field that accelerates a charged particle beam. A schematic of the accelerator is shown in Fig. 10. The electron injector delivers polarized electrons from a strained

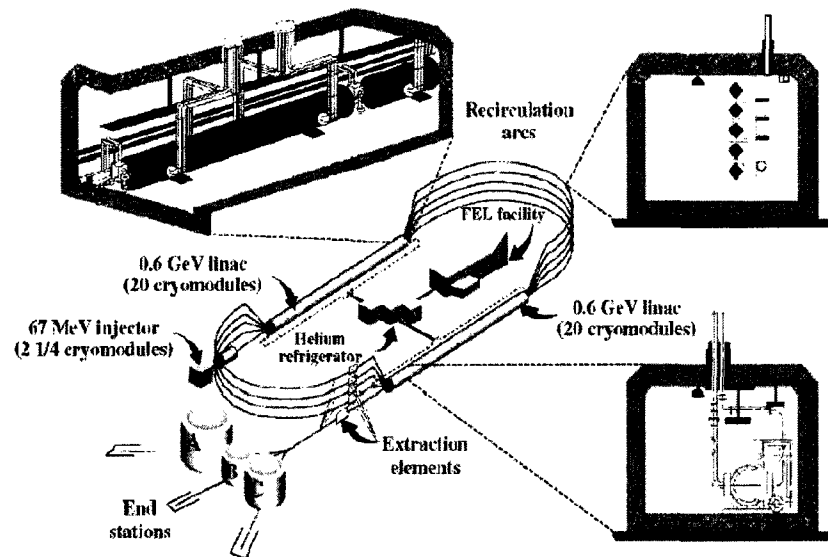


FIG. 10: Schematic view of the accelerator. One of the cryomodules is shown in the upper left corner. A vertical cross section of a cryomodule is shown in the lower right corner. A cross section of the five recirculation arcs is shown in the upper right corner.

GaAs photocathode source [32]. Electrons leaving the injector can have energy up to

about 70 MeV, but the electron source can only give electrons about 100 KeV. The main portion of the injector contains 18 cavities and each cavity can give an electron 2.5 MeV energy. The beam from the injector is accelerated through a unique recirculating beam line consisting of two linear accelerators joined by two 180° arcs with a radius of 80 meters. A cryostat is a thermos-bottle-like tank that contains a pair of cavities and filled with liquid helium needed to cool them to two Kelvin. Four of the cryostats are assembled together to form one cryomodule, which weighs about six tons and measures 8.3 meters in length. The accelerator contains 40 cryomodules. Both the north linear accelerator and the south linear accelerator are lined up end to end with 20 cryomodules. The two parallel linacs recirculate the beam up to five times boosting the beam energy up to 1.2 GeV for each turn. Many quadrupole and dipole magnets are used in the tunnel to focus and steer the beam as it passes through each arc. More than 2,000 conventional magnets, powered by an elaborate direct-current (dc) power system to guide and focus the beam through its orbits. The energy spread of the beam is  $\delta E/E < 10^{-4}$  [31][33]. The beam is directed into each experimental hall's transport channel using magnetic or RF extraction. The RF scheme uses 499 MHz cavities, which kick every third bunch out of the machine. Beam is delivered into three experimental areas (Halls A, B and C) with one beam "bucket" every 2 ns. The accelerator is able to deliver beam currents sufficient to reach luminosities of  $10^{38} \text{ cm}^{-2}\text{s}^{-1}$  in Halls A and C. The maximum luminosity of Hall B is limited to about  $10^{34} \text{ cm}^{-2}\text{s}^{-1}$  by detector occupancy in the CEBAF Large Acceptance Spectrometer (CLAS) [35].

### III.2 THE BEAM LINE OF HALL B

The electron beam delivered to Hall B is monitored by three beam position monitors (BPMs) located at 36.0, 24.6 and 8.2 m upstream of the CLAS center [35]. These BPMs measure the current and position of the beam in real-time with resolution better than 100  $\mu\text{m}$ . The current and position of the beam from each BPM is written into the data stream every 20 seconds. The beam profile is determined whenever any significant changes are made to the beam, such as the beam current. There are a total of three profilers, called harps, placed at 36.7, 22.1 and 15.5 m upstream from the center of CLAS [35]. Each harp is a set of wires (20 and 50  $\mu\text{m}$  tungsten and 100  $\mu\text{m}$  iron) orientated along the horizontal axis ( $x$ ) and vertical axis ( $y$ ). To



measure the beam distribution, the harps are slid into the beam line and moved at  $45^\circ$  with respect to the horizontal axis using a computer-controlled stepping motor. A small fraction of the electrons are scattered by the wire and the signal is collected by PMTs located about 6.8 m upstream of the CLAS center [35]. The acceptable width of the beam is typically less than  $200 \mu\text{m}$ .

The Faraday cup (FC) is located at the very end of the beam line, 29.0 m downstream of the center of CLAS. The FC is used to measure the accumulated beam charge. It is made of 4 tons of lead and has a depth of 75 radiation lengths. The electron beam usually ends up in the FC and part of its energy turns into heat. In front of the FC, there are some pieces of lead shielding that can be moved in, if necessary, to protect it from over heating. During experiments, the beam charge is measured through a current-to-voltage converter followed by a voltage-to-frequency converter. Once the voltage or frequency reach the preset threshold the FC will be reset by an electrical signal. Under the typical operating gain, a pulse can accumulate 0.11 pC of charge. The gain and offset can be checked, calibrated and operated remotely. In the BoNuS experiment, this gain was changed to 10% of the typical value since high beam current was requested (see entry 20126 in CLAS electronic log database for detail). The FC measurement is necessary for determining the cross sections and beam charge asymmetry correction and is written into the output data with a frequency of 30 Hz. A schematic view of the Hall B beam line and the FC is shown in Fig. 11.

### III.3 CEBAF LARGE ACCEPTANCE SPECTROMETER

The CEBAF Large Acceptance Spectrometer (CLAS), a nearly  $4\pi$  detector (*cf.* Fig. 12), is located in Hall B of Jefferson Lab. It provides a unique facility to investigate nucleon reactions with multi-particle final states.

The magnetic field in the CLAS is generated by six superconducting coils arranged around the beam line to produce a field oriented primarily in the azimuthal direction around the beam axis, with maximum magnitude of about 2 Tesla. CLAS is divided into six independent sectors by the superconducting coils (*cf.* Fig. 13). Each sector essentially acts as an independent spectrometer. The size and shape of the coils (about 5 m long and 2.5 m wide) were chosen to optimize measurements with fixed targets. Each sector of the CLAS consists of three separate Drift

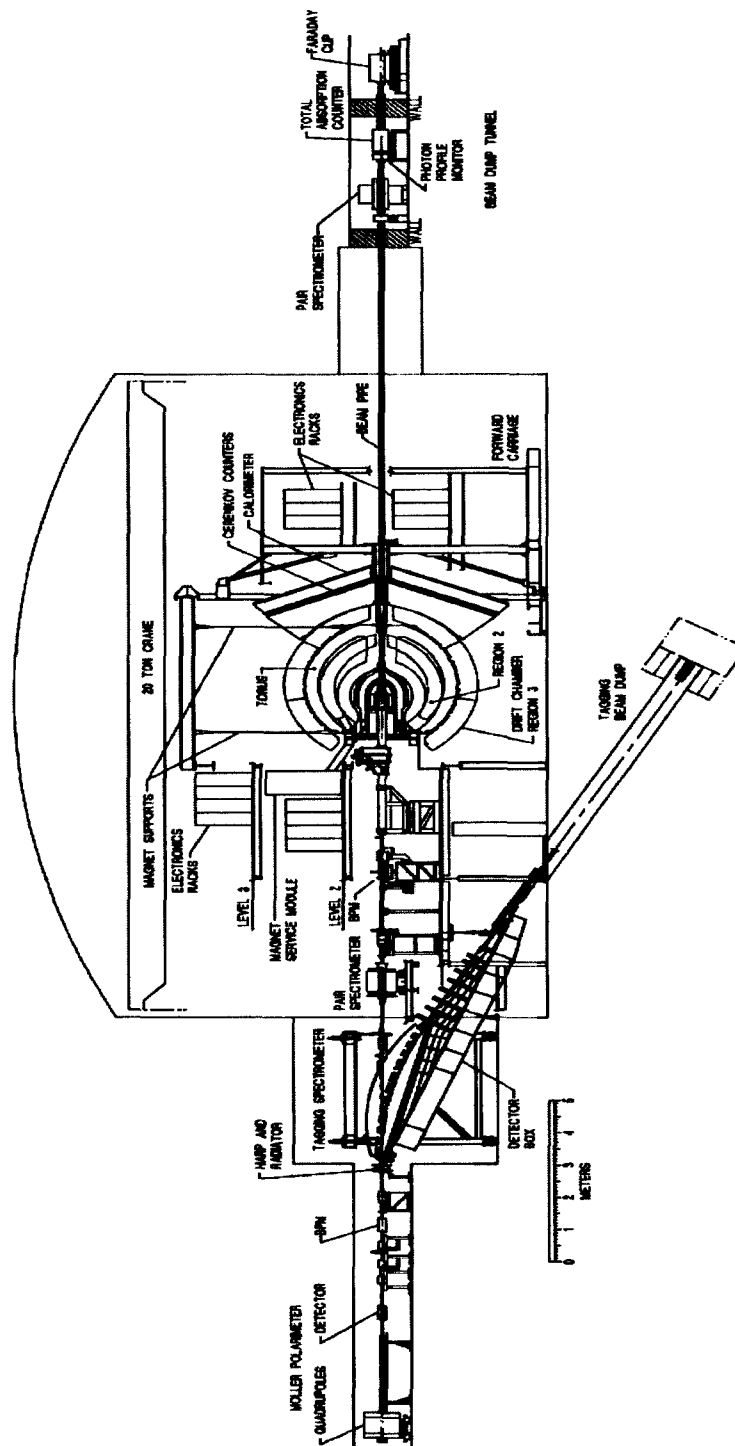


FIG. 11: Schematic view of the Hall B beam line and CLAS detector and its associated equipment. Items used for electron beam experiments are described in the text.

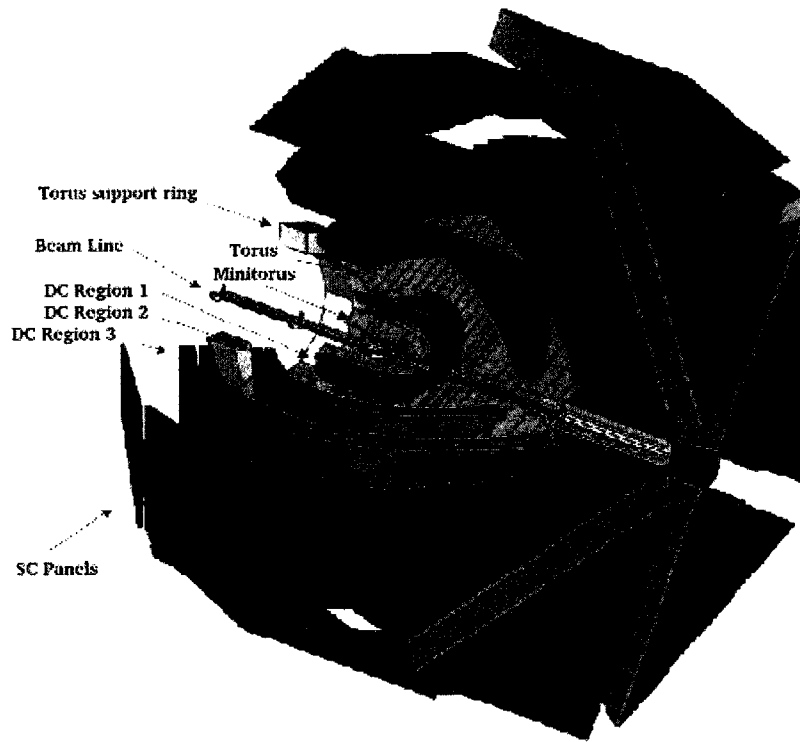


FIG. 12: Cutaway view of CLAS detector. The Drift Chamber (DC) are shown in purple, the Cherenkov Counters (CC) are in dark blue, the Scintillator Counters (SC) are in red and the Electromagnetic Calorimeters (EC) are in green.

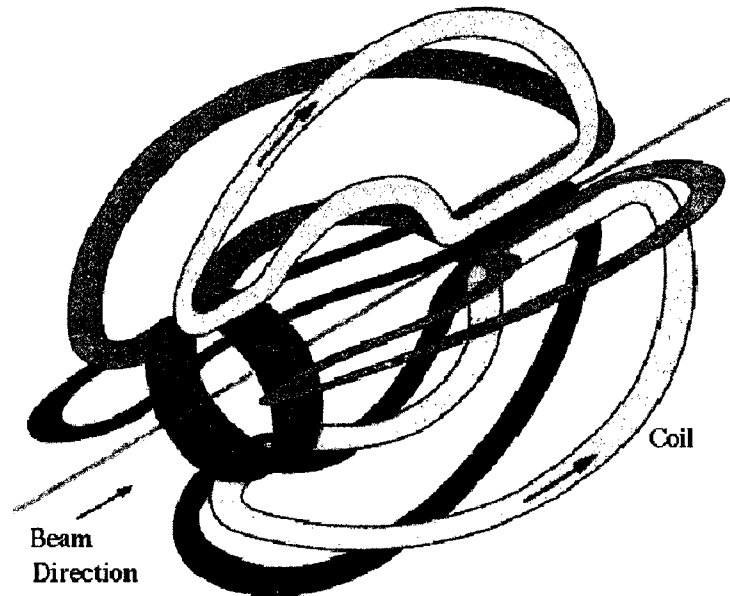


FIG. 13: Configuration of the CLAS torus coils.

Chambers (DC) assembled to determine the trajectories and momenta of charged particles, Cherenkov Counters (CC) for electron identification, Scintillation Counters (SC) for time-of-flight (TOF) measurements, and Electromagnetic Calorimeters (EC) to identify showering particles such as electrons and photons and also to detect neutral particles (i.e. neutrons). All detectors may be used to build the trigger configuration for the reaction of interest. The EC system coverage is extended by the Large Angle Calorimeter (LAC) in sectors 2 and 5. The polar angle coverage ranges from  $8^\circ$  to  $140^\circ$  for the DC,  $9^\circ$  to  $143^\circ$  for the SC, and  $8^\circ$  to  $45^\circ$  for the CC and EC. The LAC accepts particles from  $45^\circ$  to  $75^\circ$ . The next sections describe the individual detectors.

### III.3.1 Drift Chambers

The drift chamber system is divided into six sectors by the six superconducting coils. Each sector consists of three separate regions: Region 1 is closest to the target, Region 2 is between the coils and Region 3 is outside of the coils (*cf.* Figs. 12 and 13). A toroidal magnetic field with magnitude up to 2 Tesla and pointing in the azimuthal direction (*cf.* Fig. 14), which is produced by the coils, is mainly distributed in the 2nd region and has a negligible influence in Regions 1 and 3 or in the target area. This magnetic field will kick charged particles in the  $\theta$  direction while keeping the  $\phi$  angle essentially unchanged. Measurement of the bending of charged particles in Region 2 enables us to determine the momenta of the charged particles.

Each region of the drift chambers consists of axial and stereo layers of wires. Axial wires are strung parallel to the direction of the magnetic field (perpendicular to the beam direction). Stereo wires are strung at an angle of  $6^\circ$  with respect to the axial wires. The sense wires are surrounded by field wires in hexagonal cells (*cf.* Fig. 15). The axial-stereo combination in each region allows us to determine the azimuthal information for particle trajectories. Each region contains 2 superlayers (*cf.* Fig. 16) and each superlayer contains four or six layers of drift cells. The first superlayer of Region 1 contains only four layers due to the limited space while all other superlayers (the 2nd superlayer of Region 1 and all other superlayers in Regions 2 and 3) consist of six layers of sense wires.

The drift chamber system uses a non-flammable Ar/CO<sub>2</sub> gas mixture, 88/12 by volume, which has an ionization gain of  $\approx 10^4$ . This mixture provides drift velocities

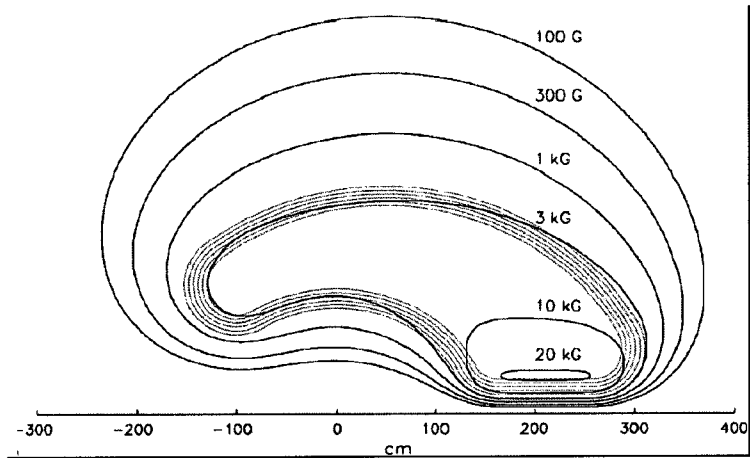


FIG. 14: CLAS magnetic field strength in the center of the area between two torus coils.

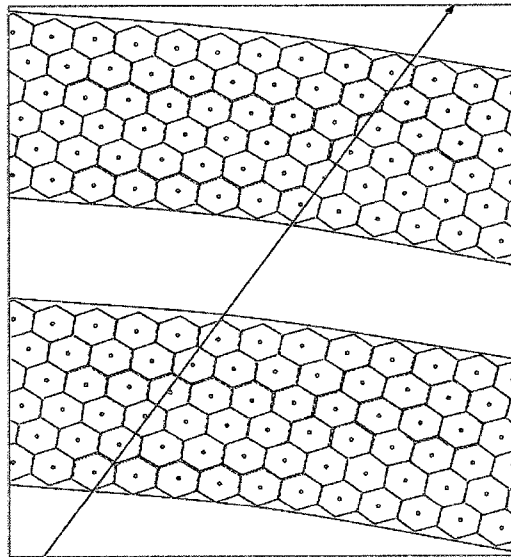


FIG. 15: Drift chamber section showing two super-layers. The wires are arranged in hexagonal patterns (cells). The sense wires are located in the center and field wires are located at each corner of each cell. The arrow shows a charged particle passing through the drift chamber and the shaded hexagons represent the hit cells.

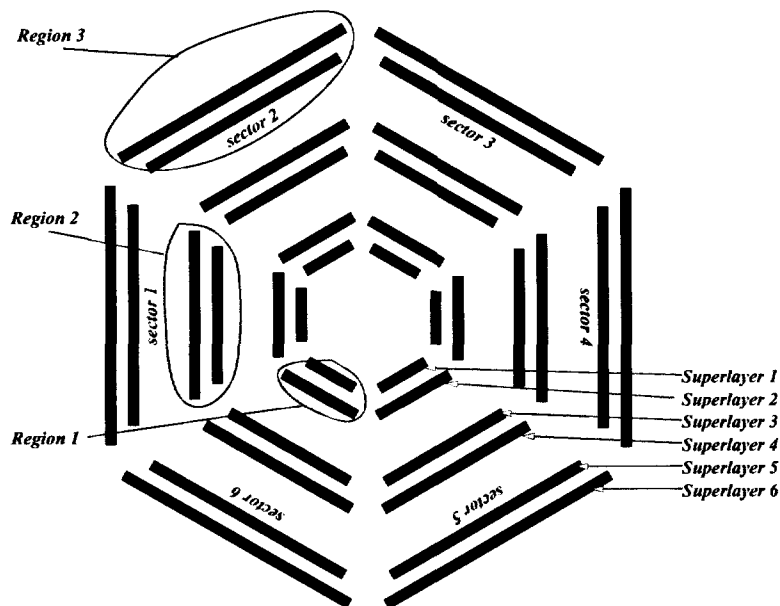


FIG. 16: CLAS drift chamber layout. This view represents a vertical slice through the drift chambers at the target position looking downstream. The schematic shows how the regions and superlayers are placed and named.

of typically  $4 \text{ cm}/\mu\text{sec}$  and an operational voltage plateau of several hundred volts before breakdown. The intrinsic resolution provided by this gas is  $\approx 100 \mu\text{m}$  [37]. The final spatial resolution is  $\approx 400 \mu\text{m}$ , mostly limited by the knowledge of the wire position and the quality of the drift velocity parametrization.

The charged particles ionize gas molecules in the drift chamber while they are traversing through. The gas is maintained in an electric field so that the electrons and ions created in the ionization process drift toward the anode and cathode wires, respectively. In the high field region near the anode wires, drifting electrons collide with gas atoms and produce secondary ionization resulting in a multiplication of collected electrons and ions. Detected electric signals on the sensor wire carry information about the particle's drift time which translates to the hit position of the original charged particle going through the detector. The electric signal passes through a preamplifier, an amplifier, a discriminator, and a 2:1 multiplexer and then starts a time-to-digital converter (TDC), which is written into the output data stream. More details on the DC are given in [36].

### III.3.2 Cherenkov Counters

The Cherenkov Counters (CC) are designed to discriminate between electrons and pions at the trigger level [38]. A charged particle will emit electromagnetic radiation while traveling through a medium with a speed exceeding the local phase velocity of light. The velocity threshold for Cherenkov light emission is  $\beta = 1/n$  where  $n$  is the refraction index of the medium. The Cherenkov material used in CLAS is perfluorobutane,  $C_4F_{10}$ , which has refraction index of 1.00153. That corresponds to an energy threshold for the particle:

$$E = \frac{M}{\sqrt{1 - \beta^2}} = \frac{nM}{\sqrt{n^2 - 1}} = 18.10 M,$$

where  $M$  is the mass of the particle. This provides an acceptably high pion momentum threshold of 2.5 GeV/c.

The CLAS Cherenkov detector consists of six independent identical Cherenkov detectors (one per sector) and each detector covers a scattering angle  $\theta$  from  $8^\circ$  to  $45^\circ$ . Each detector consists of 36 optical modules (*cf.* Fig. 17) to cover 18 regions of  $\theta$ , with two modules per  $\theta$  region. Each module has three mirrors, elliptical, hyperbolic

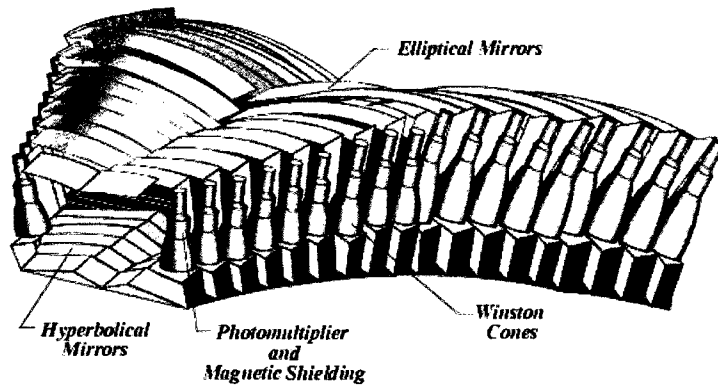


FIG. 17: CC optical modules in one of the six sectors.

and cylindrical, to direct the light into a light collecting Winston cone (*cf.* Fig. 18). The mirrors are aligned to optimize the light collection by the photomultiplier tubes (PMT).

### III.3.3 Time of Flight System

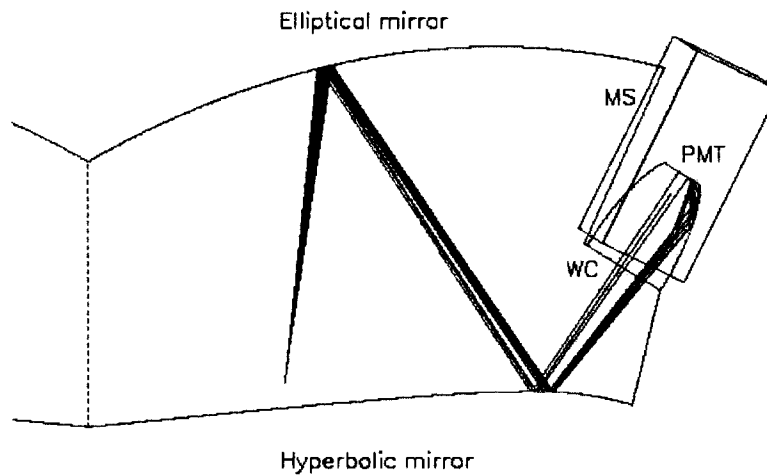


FIG. 18: One optical module of the CLAS cherenkov detector. Optical and light collection components are also shown. Cherenkov light from electrons is reflected from the hyperbolic and elliptical mirrors into the Winston Cone (WC), surrounded by a Magnetic Shield (MS), and is collected by a Photomultiplier Tubes (PMT).

The CLAS Time-of-Flight (TOF) system was designed to measure the travel time for charged particles from the target to the scintillator counter [40]. Knowing the path length, the TOF system allows us to determine the velocity of the particle ( $\beta$ ), which can determine the particle's mass in conjunction with the momentum as measured by the DC:

$$M = \frac{p\sqrt{1 - \beta^2}}{\beta}. \quad (23)$$

In each sector, the TOF system consists of 57 scintillator paddles (BC-408) mounted as four panels combined together (*cf.* Fig. 19). The scintillator paddles are uniformly 5.08 cm thick and vary in length from 32 cm to 445 cm depending on their location in the array. Their width is 15 cm in the forward region ( $\theta < 45^\circ$ ) and 22 cm at larger polar angles. These scintillator paddles are located perpendicularly to the beam direction with angular coverage of  $2^\circ$  each. The light signals are collected by the PMTs connected to light guides attached to both ends of each paddle. Signals from the PMTs are read out by TDCs and analogue-to-digital converters (ADCs). The last 18 scintillators in the back angles are grouped into 9 pairs each connected to a single TDC and a single ADC channel. Because of that pairing, each sector comprises 48 electronic channels. The timing resolution for scintillator counters varies



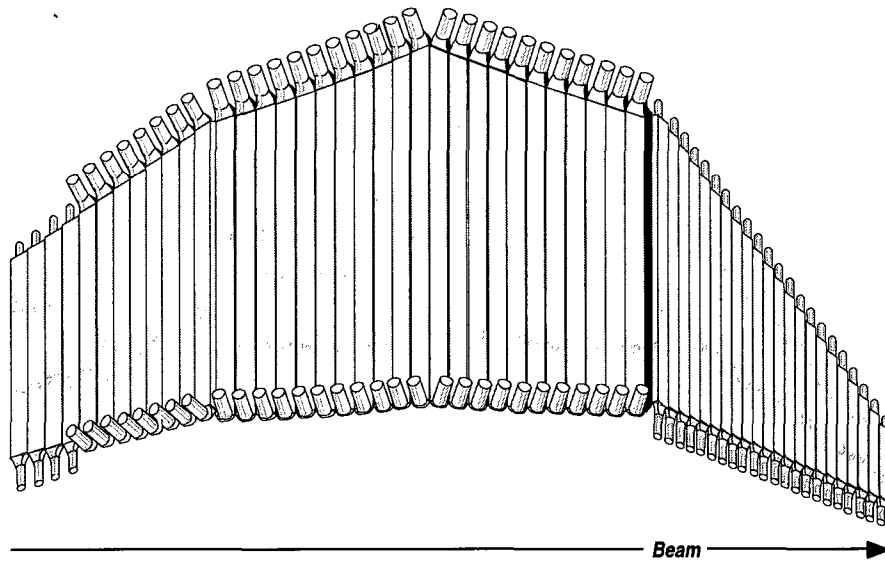


FIG. 19: TOF scintillator counters in one of the six sectors.

with the length and width of the strip. The time resolution is about 150 ps for the shortest paddle and about 250 ps for the longest paddles 19), which allows us to separate reliably pions and protons up to a momentum of 2.5 GeV/c.

### III.3.4 Electromagnetic Calorimeter

The CLAS Electromagnetic Calorimeter (EC) is designed to identify electrons and neutral particles like the neutron and photon. Mostly it is used for detection and triggering of electrons at energies above 0.5 GeV, detection of photons at energies above 0.2 GeV, and detection of neutrons, assuming their separation from photons based on time information [41].

The EC system consists of alternating layers of scintillator strips and lead sheets with a total thickness of 16 radiation lengths. The lead sheets are used to produce electro-magnetic showers, and the scintillator layers are used to measure the timing, location and energy of the charged particles in the resulting showers. The calorimeter covers the region  $8^\circ - 45^\circ$  in the polar angle and consists of six modules, one for each sector, with the cross-section of an equilateral triangle (cf. Fig. 20). Each

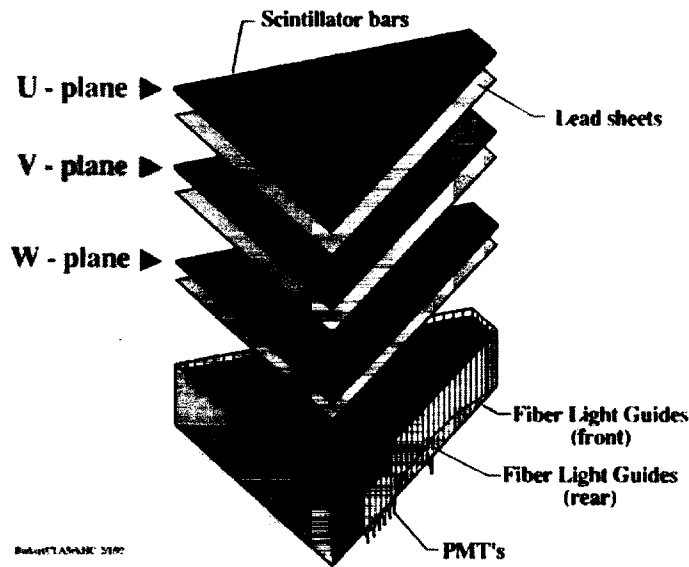


FIG. 20: CLAS electromagnetic calorimeter modules in one of the six sectors.

module has a total of 39 lead-scintillator layers, each consisting of a 2.2 mm thick lead sheet followed by a layer of 10 mm thick BC-412 scintillator. The calorimeter utilizes a “projective” geometry, in which the area of each successive layer increases. This minimizes shower leakage at the edges of the active volume and minimizes the dispersion in arrival times of signals originating in different scintillator layers. Each scintillator layer is made of 36 strips parallel to one side of the triangle, with the orientation of the strips rotated by  $120^\circ$  in each successive layer (*cf.* Fig. 20). Thus there are three orientations or views (labeled U, V and W), each containing 13 layers, which provide stereo information on the location of energy deposition. The 13 layers of each view are combined into an inner (5 layers) and outer (8 layers) stack, to provide longitudinal sampling of the shower for improved hadron identification.

A fiber-optic light readout system is used to transmit the scintillator light to the PMTs. Figure 21 displays a schematic side view of the fiber-optic readout unit of the calorimeter module. These fibers were bent in a controlled way to form semi-rigid bundles originating at the ends of the scintillator strips and terminating at a plastic mixing light-guide adapter coupled to a PMT. The PMTs have been chosen to behave linearly over a very large dynamical range and for a typical signal from a 1 GeV electron have an amplitude resolution of 4% and time resolution of about 100–150 ps.

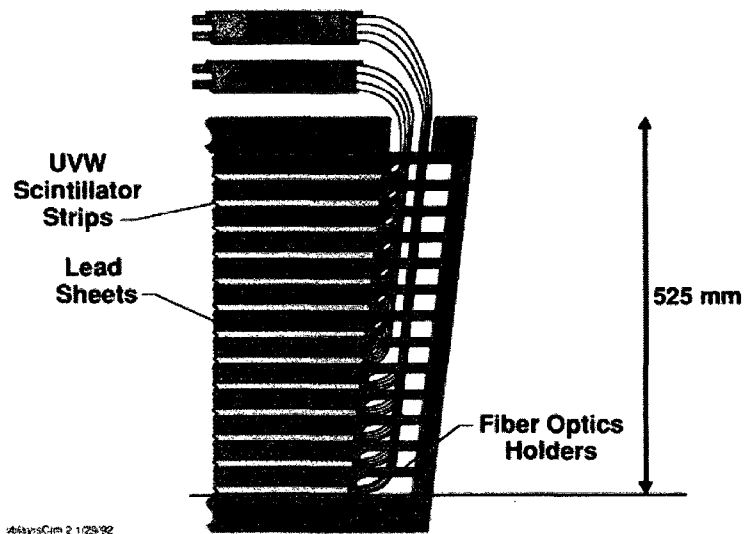


FIG. 21: Side view of the fiber-optic readout unit of the calorimeter module.

The total energy deposited in the calorimeter is available at the trigger level to reject minimum ionizing particles or to select a particular range of scattered electron energy. Pion events are heavily suppressed by setting the EC total energy threshold  $E_{total}$  in the CLAS hardware trigger.

### III.3.5 Event Trigger and Data Acquisition System

A schematic of the data acquisition system (DAQ) is shown in Fig. 22. The trigger requires that signals from the detectors (*e.g.* CC, SC and EC) are sent to a pretrigger logic module. If the pretrigger conditions are satisfied, the signal is submitted to the Level-1 trigger. If there is a trigger in the event, then the signal is passed to the trigger supervisor (TS) which communicates with the read out controllers (ROCs). The Level 2 trigger selects events by DC track hits and by identifying a primary track. It is implemented between the trigger supervisor and the read out controller. A level 2 trigger is passed to the ROC from the TS by a different channel. If the Level 2 trigger is satisfied, then the data are read out, digitized and transferred to the Event Builder (EB). In the BoNuS experiment, we used only the Level 1 trigger, which required a coincident signal in the CC,  $EC_{inner}$  and  $EC_{total}$ . Finally the Event Recorder (ER) receives the information from the Event Builder through the Data

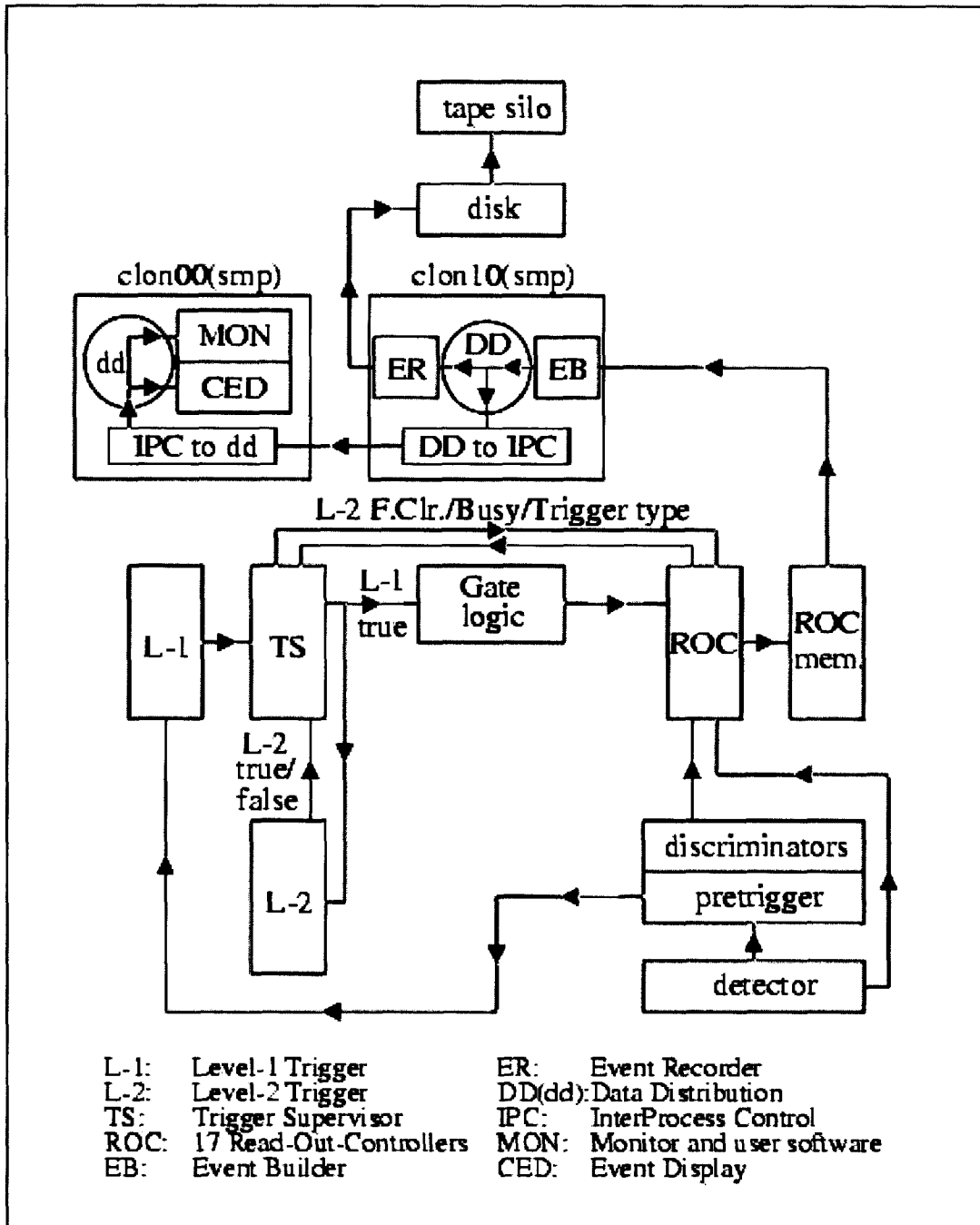


FIG. 22: CLAS data acquisition system.

Distribution (DD) shared memory. The data then are written to the disk and later transferred to the tape SILO for permanent storage. The typical CLAS DAQ rates are about 2.0–4.0 kHz with a live time of about 90% [35]. However, the RTPC DAQ rate was about 0.7 KHz, so the DAQ rate for BoNuS experiment was just 0.7 KHz with a live time of about 74% [42].

The event trigger is formed from a combination of signals from the CLAS detector components that pass pretrigger discriminators. The configuration of the event trigger and the pretrigger discriminator thresholds are set to satisfy the requirements of each experiment. The threshold on the CC is normally set to minimize  $\pi^-$  contamination in the trigger particle. Similarly the threshold on  $EC_{\text{inner}}$  is usually set to exclude minimum ionizing particles. The threshold on the total deposited energy in the calorimeter,  $EC_{\text{total}}$ , is chosen to reduce the background of low energy electrons and photons.

In the BoNuS experiment, an electron trigger was used. The hardware thresholds were 75 mV for the CC (corresponding to 1.5 photoelectrons), and 72 mV for the  $EC_{\text{inner}}$ . We used three thresholds for  $EC_{\text{total}}$ : 150 mV, 200 mV and 260 mV, depending on the beam energy. A complete set of the trigger thresholds used in the BoNuS experiment can be found in [43]. Our trigger thresholds were much higher than typical experiments. For example the CC threshold is typically set to 20 mV and  $EC_{\text{total}}$  is usually set to 100 mV. We set these thresholds so high based on the following considerations: 1) the DAQ rate and live time are seriously encumbered by the RTPC DAQ rate; the CLAS could have accepted more events; 2) high thresholds provide much higher quality triggers and much smaller data stream size. The high thresholds in the BoNuS experiment resulted in a high energy requirement for the trigger electrons. The relation of  $EC_{\text{total}}$  threshold to the trigger electron energy is given by [44]:

$$E_{el}^{\text{EC}}(\text{MeV}) \approx 214 + 2.47 \times EC_{\text{threshold}}(\text{mV}). \quad (24)$$

### III.3.6 Target

In order to meet the goal of the BoNuS experiment it is necessary to detect low energy spectator protons. A Radial Time Projection Chamber (RTPC) with a gaseous deuterium target was built for that purpose. Most of the spectator protons have a momentum less than 150 MeV/c. We had to avoid using a solid or liquid

target because the spectator proton would not have enough energy to escape. The target wall had to be made of material with a small radiation length and that was strong enough to enable us to reduce the thickness as much as possible. For these reasons we finally used a gaseous deuterium target at about 7 atmospheres and room temperature. We used kapton with a thickness of 50 micrometers to make the target “straw” (tube), which had an inner diameter of 6 mm. The total length of the target “straw” is 280 mm but only 210 mm was covered by the RTPC. At both ends of the target window there is a 15 micrometers thick aluminum cap. On the upstream end there is an aluminum collar (*cf.* Fig. 23) to limit forward going particles from causing a signal in the RTPC. Therefore the valid target length is about 160 mm. In order to minimize the background, the down stream part of the target “straw” was surrounded by a helium gas tube with a diameter of 25.4 mm. Some details of this target design can be seen from its assembly drawing in Fig. 24.

Although deuterium was the production target for BoNuS, we also used gaseous hydrogen and helium targets for calibration purposes. The details of the RTPC are described below.

### III.4 RADIAL TIME PROJECTION CHAMBER

The addition of a custom-built Radial Time Projection Chamber (RTPC) using Gas Electron Multipliers (GEM) technology [46] is the key feature of the BoNuS experiment that makes it different from other CLAS experiments.

The major purpose of the RTPC is to detect low energy backward protons. There are two important features of this detector: radial time projection and low energy threshold. The time projection was chosen due to its fast response. In order to have a low energy threshold, we need to minimize the energy loss of the particle before it reaches the drift region. Therefore we chose a gaseous target with a kapton target wall of only 50  $\mu\text{m}$  thickness. A detailed picture of the RTPC detector design is shown in Fig. 25

Our RTPC was divided into two identical halves by their supporting bed plates, each covering  $180^\circ$  in azimuthal angle and 20 cm in length. Looking at the RTPC from the downstream end, one sees that the RTPC is composed of six coaxial cylinders (Cf. 25, panel a). The first cylinder is the inner window located at  $r = 2$  cm, which is made out of aluminized mylar ( $\text{C}_{10}\text{H}_8$ ) foil (6.4  $\mu\text{m}$  thick mylar with 0.035  $\mu\text{m}$  thick

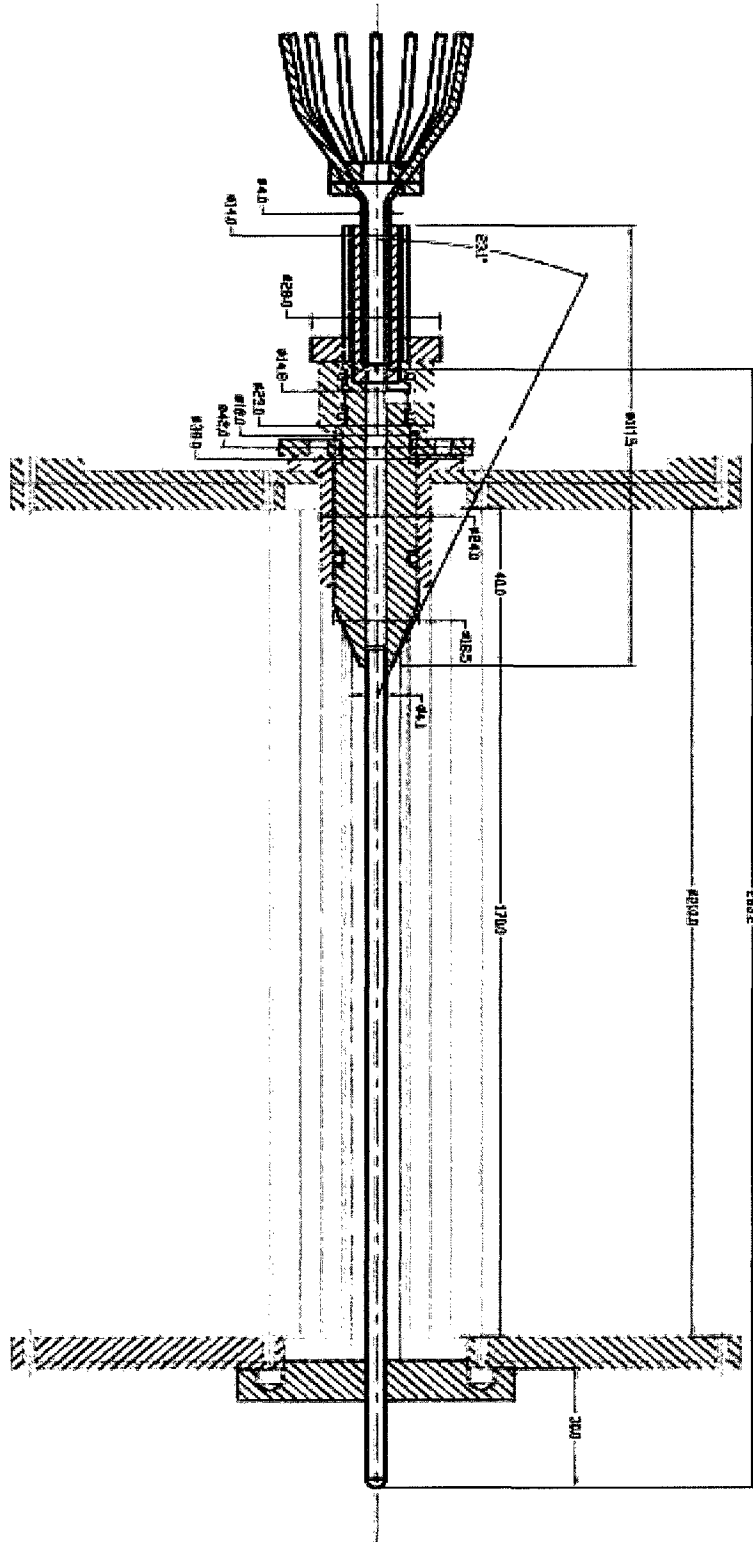


FIG. 23: Mechanical drawing of the BoNuS target.

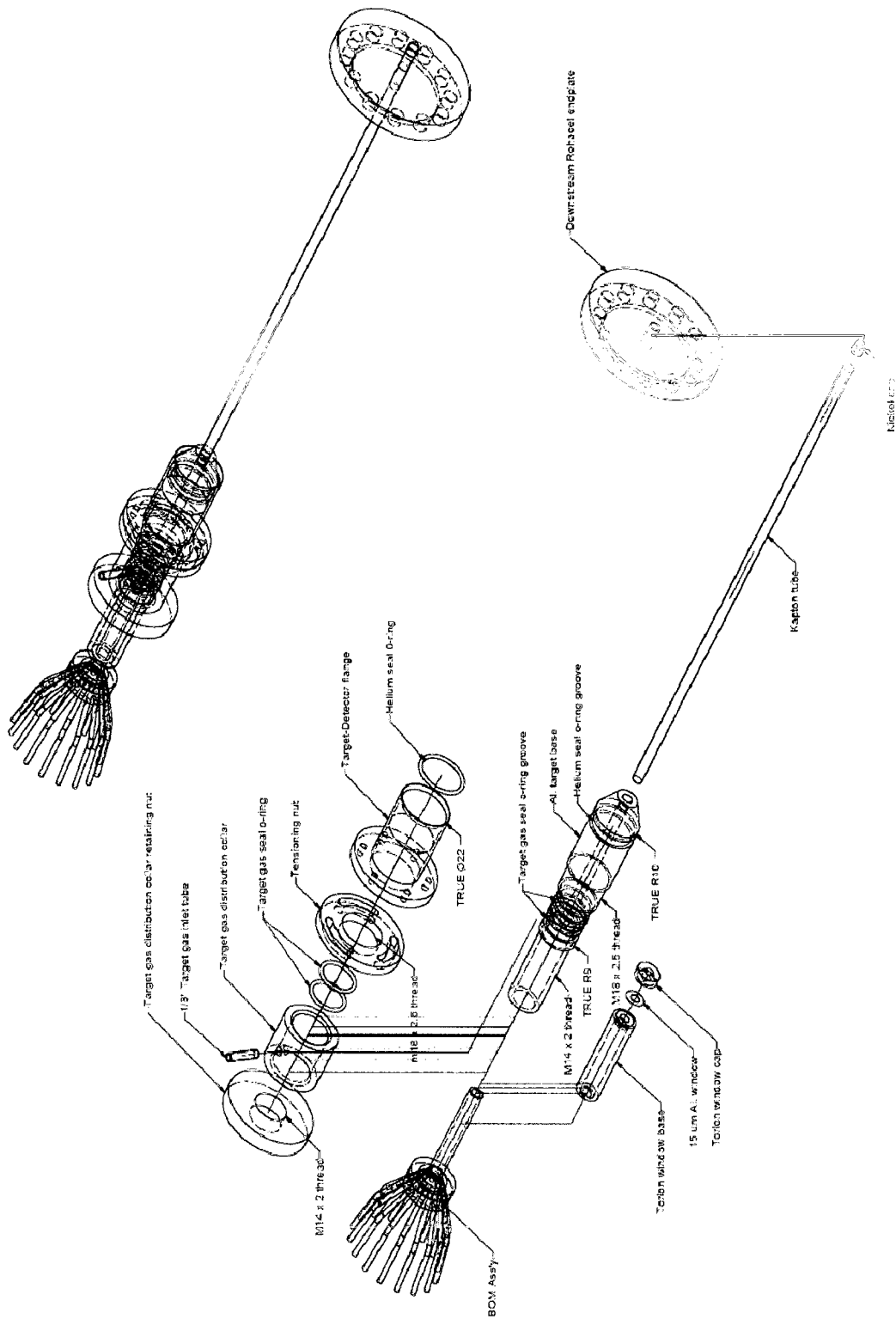


FIG. 24: The BoNuS target system.



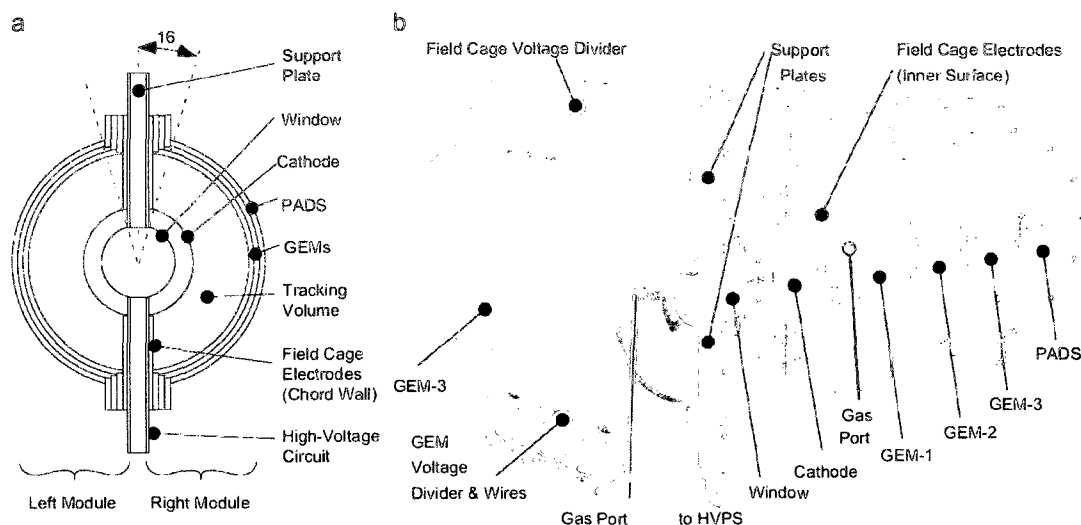


FIG. 25: a) Cross section of the RTPC detector as viewed from down stream; b) A picture of the RTPC's left section without the read out pad board layer and an exploded diagram of the right section.

aluminum on both sides). This layer was connected to ground during data taking in order to shield the target straw from the electric field. The second cylinder layer is located at  $r = 3$  cm. It is also made of the same aluminized mylar foil. This layer also serves as the cathode of the drift region. The 3rd, 4th and 5th cylinders are the Gas Electron Multiplier sheets, which are attached at  $r = 6.0$ ,  $6.3$  and  $6.6$  cm, respectively. These GEM sheets are made from copper-surfaced kapton ( $C_{22}H_{10}N_2O_5$ ) foil ( $50 \mu\text{m}$  thick kapton with  $5 \mu\text{m}$  thick copper on both sides). Figure 26 shows the electric field in a single layer of GEM computed using GARFIELD [47][48]. The holes in the foil have a diameter of  $50 \mu\text{m}$ , a pitch of  $100 \mu\text{m}$  and a double-conical cross section. Drift electrons enter the hole (region 2) and are multiplied in the high electric fields. The resulting avalanche of electrons provides a gain per foil on the order of 100 [57]. The 6th cylinder layer, located at  $r = 7.0$  cm is the readout board, which is also the anode layer of the drift region. 3200 readout pads were attached to the outside surface of this layer, 40 rows  $\times$  40 columns for each half of the detector. Each pad covers a rectangle of  $5.0(z) \times 4.45(\phi)$  mm. Every 16 pads were grouped and connected to one preamplifier chip. The shaded region of Fig. 27 shows an example group of pads read out by the same preamplifier. Electron signals were collected by these pads then passed to the preamplifier chips and eventually passed to the Data Acquisition

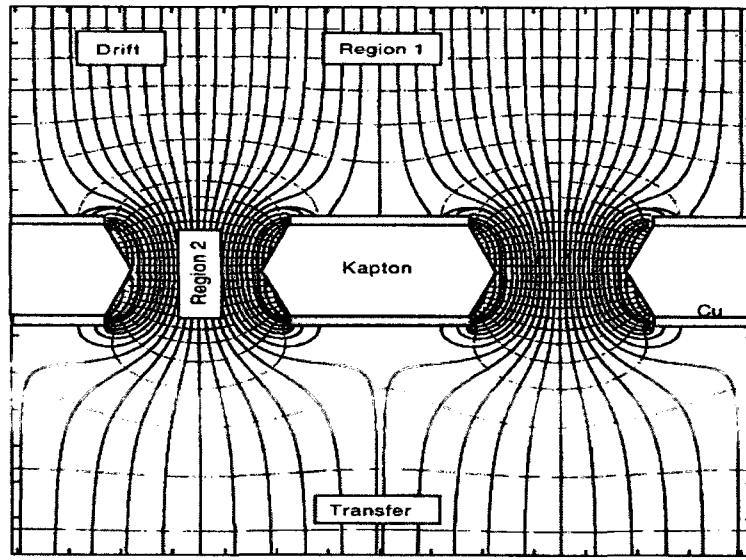


FIG. 26: Electric field map of a GEM foil. Shown are the electric field lines and their equipotential lines.

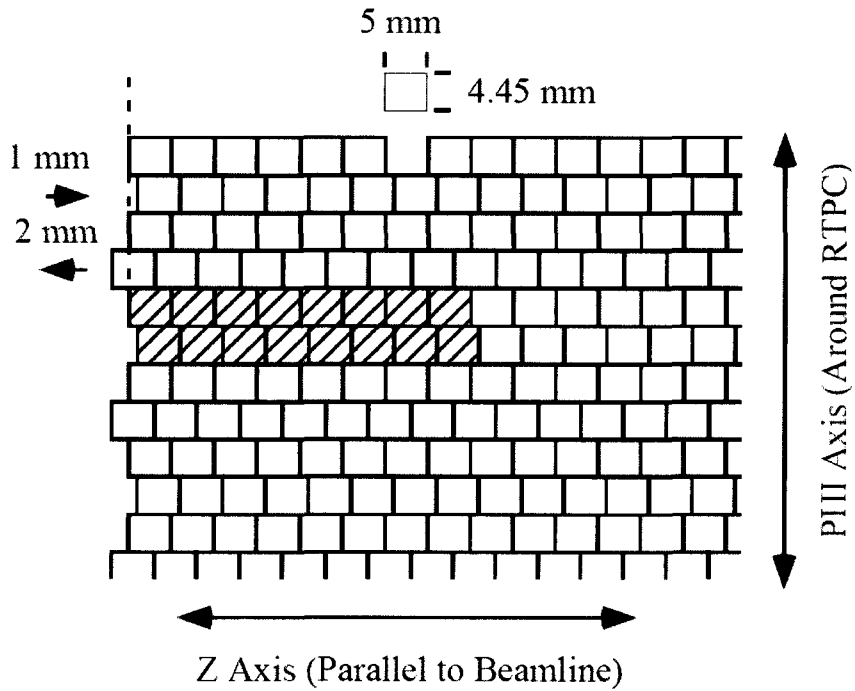


FIG. 27: Pad layout of the RTPC.

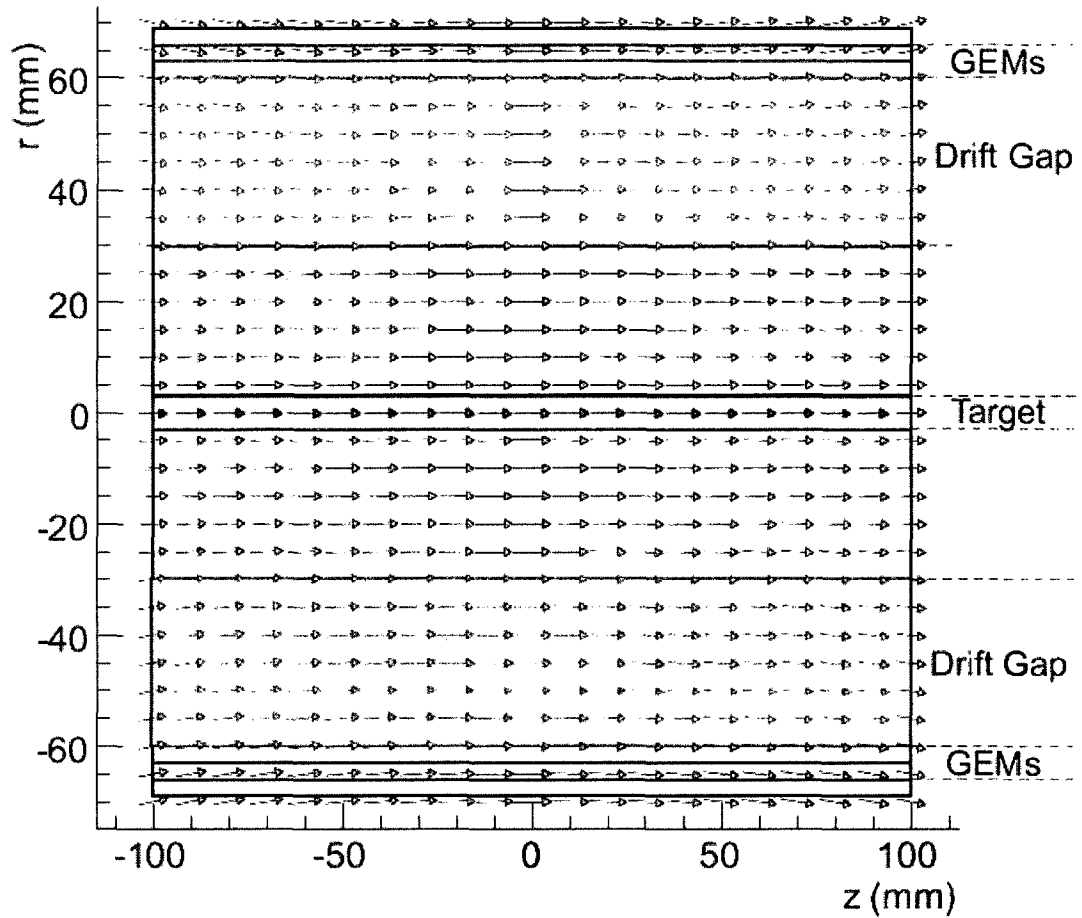


FIG. 28: Magnetic field map in the vicinity of the RTPC.

(DAQ) system.

The RTPC detector and the BoNuS target were placed at 58 cm upstream of the CLAS center, which is the center of a superconducting solenoid. Operating with an electric current of 450 A, this solenoid can produce a magnetic field of 4 Tesla at its center, and pointing in the opposite direction of the beam. The magnetic field map is shown in Fig. 28. One can see that this magnetic field has a non-negligible  $\phi$  component at either end of the RTPC. A He/DME gas mixture at normal atmospheric pressure with volume ratio of 80/20 was filled into the inner gap (between the inner window and the cathode) and the drift region. When a proton

goes through the drift region, it ionizes the gas and creates ionization electrons along its trajectory. Due to the magnetic field the proton trajectory will bend in the  $\phi$  direction but not in  $\theta$ . The ionization electrons drift toward the anode driven by the electric field. Electron avalanche happens when they go through the GEM layers and finally they are collected by the read out pads. The electronic signals are then chopped into 114 ns intervals and written into the output data stream. Each 114 ns interval signal for each pad here is called a hit. The trajectory of drift electrons also bends due to the the magnetic field. Using the drift time one can calculate the initial  $r$  position (the distance from the  $z$  axis) of the drift electron and its change in  $\phi$  angle. Since the pad position  $(r_0, \phi_0, z_0)$  is known, one can calculate the initial position  $(r_0, \phi_0, z_0)$  for each hit. By linking those reconstructed positions to form a train, one can reconstruct the trajectory of the proton. A schematic picture of this reconstruction is shown in Fig. 29. Fitting the proton trajectory with a helix, one can obtain the radius of the track and the initial angles  $\theta$  and  $\phi$ . Figure 30 shows an example of the helix fitting to the reconstructed positions in the drift region of the RTPC.

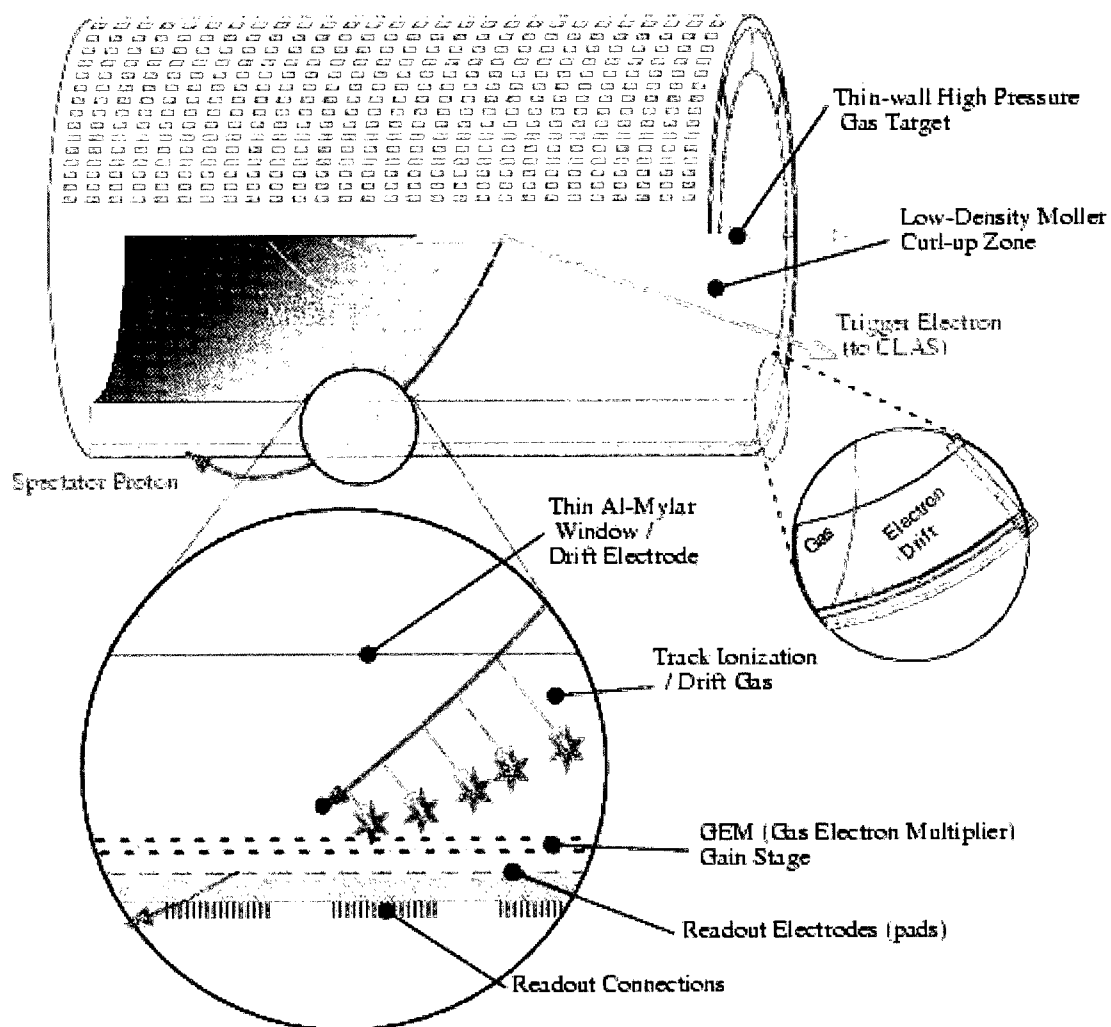


FIG. 29: Schematic of the BoNuS RTPC.

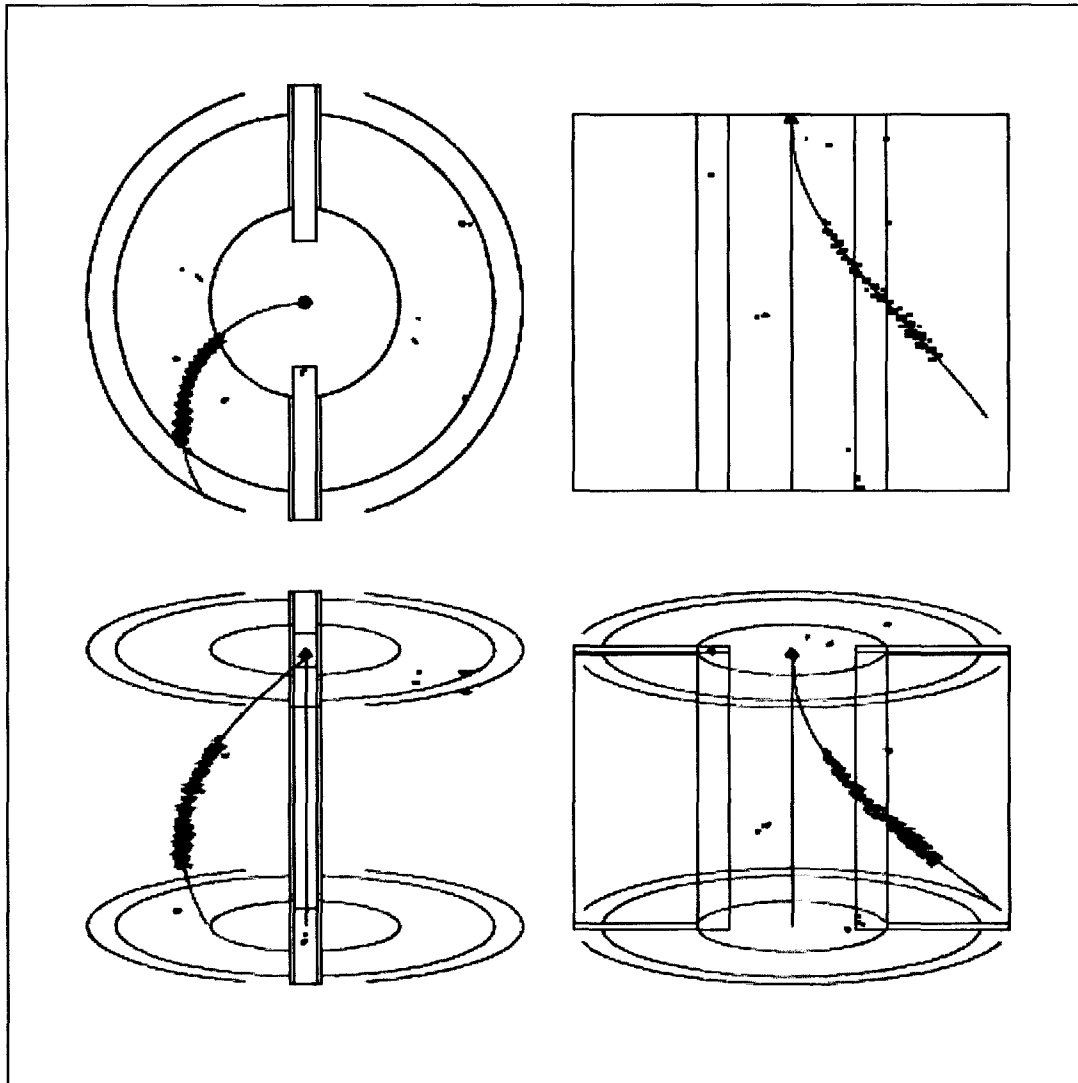


FIG. 30: An example of helix fitting to the reconstructed positions in the drift region. The box size for each hit is proportional to the pulse amplitude (the deposited energy). The four panels represent different views of the same event. The figure in the top left is viewed from the down stream of the beam line. The top right figure is viewed from the side along  $x$  axis, and the arrow in the center of the RTPC points along the direction of the electron beam. The two figures in the bottom are viewed from side but with a small  $\theta$  angle. The bottom left is viewed with  $\phi = 90^\circ$  and the bottom right is viewed with  $\phi = 0^\circ$ .

## CHAPTER IV

### SIMULATION

#### IV.1 INTRODUCTION

Simulation is very important for experiments, especially for nuclear experiments that are time consuming and require a huge amount of manpower and financial support. In the stage of preparing the experiment, simulation is very useful in designing a detector and developing the reconstruction software. For instance, in the case of the RTPC there are so many possible configurations of drift gas that can be used, such as Ar/CO<sub>2</sub> with various volume ratios, or He/DME (Dimethyl ether gas, CH<sub>3</sub>OCH<sub>3</sub>) with various volume ratios, or some other gas mixture. The designers have to know which configuration is the best, but they may not have enough time, manpower or resources to test all of these configurations. Simulation can be a useful tool to find out the answer. At the data analysis stage, simulation can be used to study the acceptance and efficiency of the detector, determine the energy loss corrections and model the background.

Compared with other CLAS experiments in the past, BoNuS has a new target system and a new Radial Time Projection Chamber (RTPC). We had to develop our simulation and reconstruction software packages for the RTPC. Our simulation includes a program sequence including the following:

- The simulation of the RTPC (named BONUS),
- The simulation of the CLAS (GSIM), and
- GSIM Post Processing (GPP).

At the end of the GPP, the simulated data are in the identical format as the real experimental data and are ready to use. We then use the reconstruction and analysis framework (RECSIS) to reconstruct and analyze both the simulated and the real data. The details of the simulation we developed for the BoNuS experiment will be described in the following sections.

## IV.2 THE SIMULATION OF THE RTPC DETECTOR

Our Radial Time Projection Chamber was constructed to detect the low energy backward protons. Because the RTPC was newly built for the BoNuS experiment, the simulation of the RTPC was very crucial. Our RTPC uses three layers of Gaseous Electron Multipliers (GEMs) to amplify the ionization electron signal. Although the GEM technology with parallel Time Projection Chamber (TPC) has been used in other laboratories, such as CERN, our Radial Time Projection Chamber with GEMs was the first of its kind [45]. The simulation of the RTPC was developed by N. Baillie and J. Zhang. Baillie ran a Magboltz simulation program [49] to determine the drift path and drift velocity for low energy electrons (less than 3 keV) within the drift region under various configurations of drift gas, high voltages and magnetic fields. MAGBOLTZ is a Monte Carlo simulation package of electron drift and diffusion in counting gases under the influence of electric and magnetic fields. I was responsible for developing a full simulation of particles traveling inside the RTPC using the GEANT4 software [50][51], version 8.01. GEANT4 is a toolkit to simulate the interaction of particles with matter [54]. It is widely used in the simulation of high energy, nuclear physics, accelerator physics, as well as in medical physics and space science. Because GEANT4 cannot simulate the thermal electrons' behavior very well [55][56], we used a parameterized result for the drift path and drift velocity in the RTPC simulation. The following sections will explain the GEANT4 RTPC simulation program, BONUS, in detail.

### IV.2.1 Material

To “build” a detector in GEANT4, one first needs to create/define all used elements and materials. To define an element, the atomic index  $Z$  and density must be provided. To create a material one usually needs to provide the following information: density, components, state (solid or gas), temperature and pressure. This means that no material can be made without the molecular formula.

The molecular formula for most materials used in this simulation were already known, for example, Kapton with the molecular formula  $C_{22}H_{10}N_2O_5$ . However, the molecular formula for some mixtures were unknown, for instance, the flat cable and



the preamplifier chips embedded with two connectors. We were not able to find their densities and molecular formula in any books. Therefore we had to make a careful investigation to determine these quantities. A large portion of the credit for this work should be granted to M. Ispiryan for his contribution.

### The Flat Cable

According to our measurements, the flat cable used for the RTPC readout has a rectangular cross-section of  $21.5 \times 0.4$  mm. Its linear density is 0.03027 kg/m. Within these cables there are 34 copper conductors and copper constitutes 57% of the mass. The insulator is made of polyvinyl chloride (PVC) with molecular formula  $C_2H_3Cl$ . If we assume that a molecule of the cable has the formula  $Cu_xC_2H_3Cl$ , then, in order for the copper to have the same mass fraction (0.57) in the molecule,  $x$  must be 1.316. This brings us to the following “molecular formula” of the flat cable as  $Cu_{1.316}C_2H_3Cl$  or  $Cu_4C_6H_9Cl_3$ .

### The Preamplifier Chip Plus Two Embedded Connectors

We already know the density and the molecular formula for a standard Printed Circuit Board (PCB) without electronic elements embedded. The preamplifier chip connected to the readout PCB has two embedded connectors and some small electronic elements. In order to get a good approximation we took one of the preamplifier chips and measured its weight and dimensions. The equivalent size of the board is  $35 \times 31 \times 2.5$  mm<sup>3</sup>. Its mass is 6.27 g. Hence its density is 2.31 g/cm<sup>3</sup>. The edges of the parallelepiped that are 31 mm in length are parallel to the  $z$  axis. The 35 mm edges are almost parallel to the radius direction. Its chemical components have been listed in Table 2.

TABLE 2: Preamplifier chip elements

Component		Mass (g)	Mass Fraction
Epoxy	$C_{20}H_{22}O_6$	5.77	0.920
Copper	Cu	0.4	0.064
Silicon	Si	0.1	0.016

Fig. 31 shows the geometry and position of the preamplifier chips and the connected flat cables for the RTPC detector. The “molecular formula” of this chip with connectors is  $\text{Cu}_{0.39}\text{Si}_{0.22}\text{C}_{20}\text{H}_{22}\text{O}_6$  or  $\text{Cu}_9\text{Si}_5\text{C}_{460}\text{H}_{506}\text{O}_{138}$ . A list of all materials used in the RTPC simulation can be found in Appendix A.

#### IV.2.2 Geometry

The geometry in the RTPC simulation module was built based on the mechanical drawing for each piece of the detector. We tried to make the simulated detector as similar as possible to the real one, while also considering the speed of the simulation. For those components within the RTPC read out boards and for most of the downstream part, the shape, position, material and thickness of each piece of material was built exactly the same as the real detector. For those components outside (at greater radius) the RTPC read out boards and for the upstream part, some approximations have been used. Materials outside the read out board are not as important as those inside. That is because 1) the spectator protons do not need to be simulated any longer once they hit the read out board and 2) the CLAS particles mostly go forward and penetrate the downstream end-plate and very few of them penetrate the preamplifier chips and cables; 3) furthermore, the CLAS particles usually have high energy such that the deviation between their behaviors in the real geometry and in an approximation geometry is negligible.

The geometry of the RTPC detector is shown in Fig. 32. This diagram represents the design of the prototype RTPC. Some of the thicknesses shown in this diagram were changed for the final RTPC detector. The corrected values have been listed in Tables 3 and 4. A beam view of the RTPC geometry in the GEANT4 simulation is shown in Fig. 33.

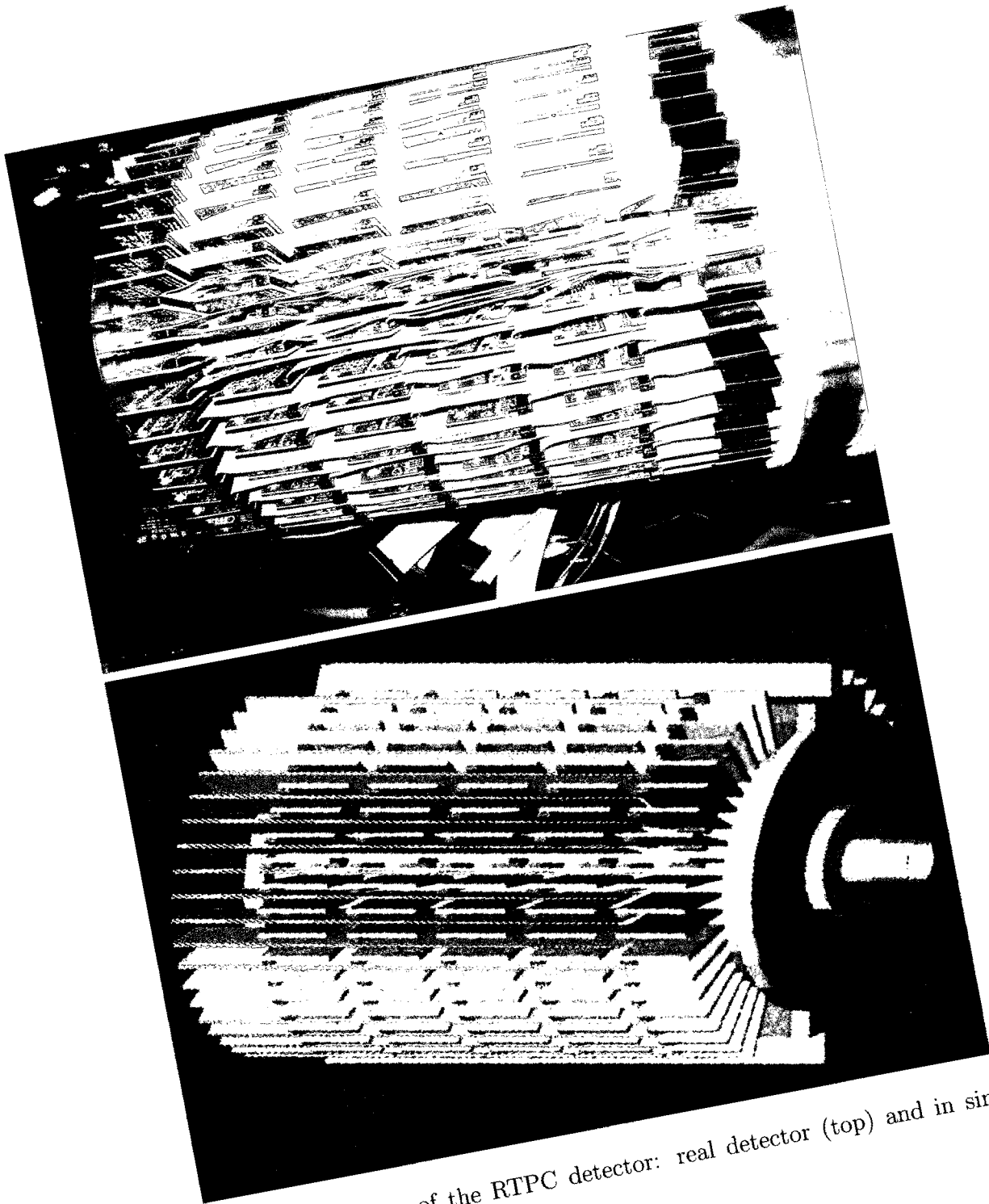


FIG. 31: Side view of the RTPC detector: real detector (top) and in simulation (bottom).

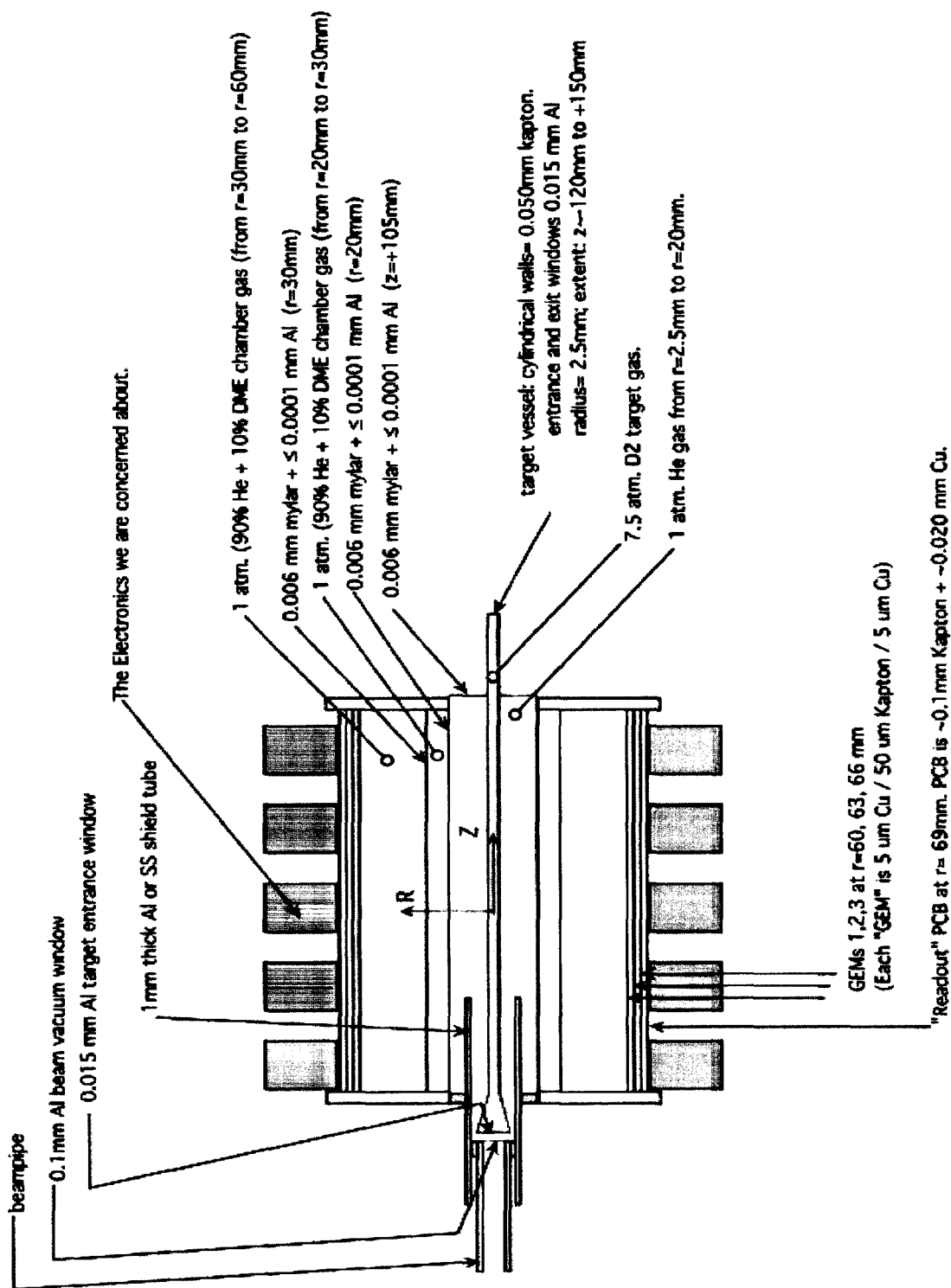


FIG. 32: Diagram of the RTPC geometry and materials. The exact thicknesses of some components may be different from the real detector.

Name	Shape	Size and Position(mm)	Material	Density(mg/cm <sup>3</sup> for gas or g/cm <sup>3</sup> for others)
Target tube	cylinder	$0 \leq R < 3$	D <sub>2</sub> gas, 7.5 atm, 300K	1.227
Target wall	tube	$3 \leq R < 3.05$	kapton(C <sub>22</sub> H <sub>10</sub> N <sub>2</sub> O <sub>5</sub> )	1.42
Helium tube	tube	$3.05 \leq R < 20$	He gas, 1 atm, 300K	0.163
Inner layers (3 layers)	tube	$20 \leq R < 20.00607$	Al/mylar(C <sub>10</sub> H <sub>8</sub> )/Al thickness: 0.035/6.4/0.035 $\mu$ m	aluminum: 2.7 mylar: 1.39
Inner gap	tube	$20.00607 \leq R < 30$	He/DME(C <sub>2</sub> H <sub>6</sub> O) mixture volume ratio 80/20, 1 atm, 300K	helium: 0.163 DME: 1.871
Cathode (3 layers)	tube	$30 \leq R < 30.00607$	Al/mylar(C <sub>10</sub> H <sub>8</sub> )/Al thickness:0.035/6.4/0.035 $\mu$ m	aluminum: 2.7 mylar: 1.39
Drift region	tube	$30.00607 \leq R < 60$	He/DME(C <sub>2</sub> H <sub>6</sub> O) mixture volume ratio 80/20, 1 atm, 300K	helium: 0.163 DME: 1.871
GEM 1 (3 layers)	tube	$60 \leq R < 60.06$	Cu/kapton(C <sub>22</sub> H <sub>10</sub> N <sub>2</sub> O <sub>5</sub> )/Cu thickness: 5/50/5 $\mu$ m	Cu: 8.96 kapton: 1.42
GEM gap 1	tube	$60.06 \leq R < 63$	He/DME(C <sub>2</sub> H <sub>6</sub> O) mixture volume ratio 80/20, 1 atm, 300K	helium: 0.163 DME: 1.871
GEM 2 (3 layers)	tube	$63 \leq R < 63.06$	Cu/kapton(C <sub>22</sub> H <sub>10</sub> N <sub>2</sub> O <sub>5</sub> )/Cu thickness: 5/50/5 $\mu$ m	Cu: 8.96 kapton: 1.42
GEM gap 2	tube	$63.06 \leq R < 66$	He/DME(C <sub>2</sub> H <sub>6</sub> O) mixture volume ratio 80/20, 1 atm, 300K	helium: 0.163 DME: 1.871
GEM 3 (3 layers)	tube	$66 \leq R < 66.06$	Cu/kapton(C <sub>22</sub> H <sub>10</sub> N <sub>2</sub> O <sub>5</sub> )/Cu thickness: 5/50/5 $\mu$ m	Cu: 8.96 kapton: 1.42
GEM gap 3	tube	$66.06 \leq R < 70$	He/DME(C <sub>2</sub> H <sub>6</sub> O) mixture volume ratio 80/20, 1 atm, 300K	helium: 0.163 DME: 1.871

TABLE 3: RTPC geometry and materials

Name	Shape	Size and Position(mm)	Material	Density(mg/cm <sup>3</sup> for gas or g/cm <sup>3</sup> for others)
Readout Board	tube	$70 \leq R < 71.5748$	G10FR4: ( 60% SiO <sub>2</sub> and 40% C <sub>11</sub> H <sub>12</sub> O <sub>3</sub> )	SiO <sub>2</sub> : 2.2 C <sub>11</sub> H <sub>12</sub> O <sub>3</sub> : 1.268
Support Spikes (bed-plates)	box	R = 20 to 108 7.1628 × 88 × 200	ultem (C <sub>37</sub> H <sub>24</sub> N <sub>2</sub> O <sub>6</sub> )	1.27
Support spike PCB	box	R = 30 to 108 1.5748 × 88 × 200	1.5748 mm thick G10FR4	SiO <sub>2</sub> : 2.2 C <sub>11</sub> H <sub>12</sub> O <sub>3</sub> : 1.268
Support of GEM1	box	locate at R = 60.06 to 90 2.1084 × 29.94 × 200	ultem (C <sub>37</sub> H <sub>24</sub> N <sub>2</sub> O <sub>6</sub> )	1.27
Support of GEM2	box	locate at R = 63.06 to 90 4.6228 × 29.94 × 200	ultem (C <sub>37</sub> H <sub>24</sub> N <sub>2</sub> O <sub>6</sub> )	1.27
Support of GEM3	box	locate at R = 66.06 to 90 4.6228 × 29.94 × 200	ultem (C <sub>37</sub> H <sub>24</sub> N <sub>2</sub> O <sub>6</sub> )	1.27
Entrance cover	poly-cone	locate at z = -58.7 to -145	aluminum	2.7
End plates	box + tube	locate at z = ± 108.1736	6.3 mm thick ultem	1.27
Up end plate cover	box + tubes	z = -117.6236	6.3 mm thick stainless steel	7.8
Down end plate cover	box + tubes	z = 115.2737	1.6002 mm thick G10FR4	SiO <sub>2</sub> : 2.2 C <sub>11</sub> H <sub>12</sub> O <sub>3</sub> : 1.268
Pre-amplifier chip with 2 connectors	boxes union	200 chips 35 × 31 × 2.5	effective molecular formula: Cu <sub>9</sub> Si <sub>5</sub> C <sub>460</sub> H <sub>506</sub> O <sub>138</sub>	2.31
Flat cable	boxes union	40 groups, along z direction	effective molecular formula: Cu <sub>4</sub> C <sub>6</sub> H <sub>9</sub> C <sub>13</sub>	3.520

TABLE 4: RTPC geometry and materials (Cont.)

### IV.2.3 Physics Processes

In a GEANT4 simulation, one needs to link the relevant physics processes to each particle. If no physics process is registered, the particle may not be simulated properly. In this RTPC simulation program, BONUS, the following physics processes from the GEANT4 packages had been registered:

- Penetration,
- Decay,
- Multiple Scattering,
- Low Energy Elastic Scattering,
- Low Energy Inelastic Scattering,
- High Energy Inelastic Scattering,
- Low Energy Ionization,
- Ionization,
- Low Energy Gamma Conversion,
- Gamma Conversion,
- Low Energy Compton Scattering,
- Compton Scattering,
- Low Energy Photo-Electric Effect,
- Photo-Electric Effect,
- Low Energy Rayleigh Scattering,
- Low Energy Bremsstrahlung,
- Bremsstrahlung,
- Annihilation,

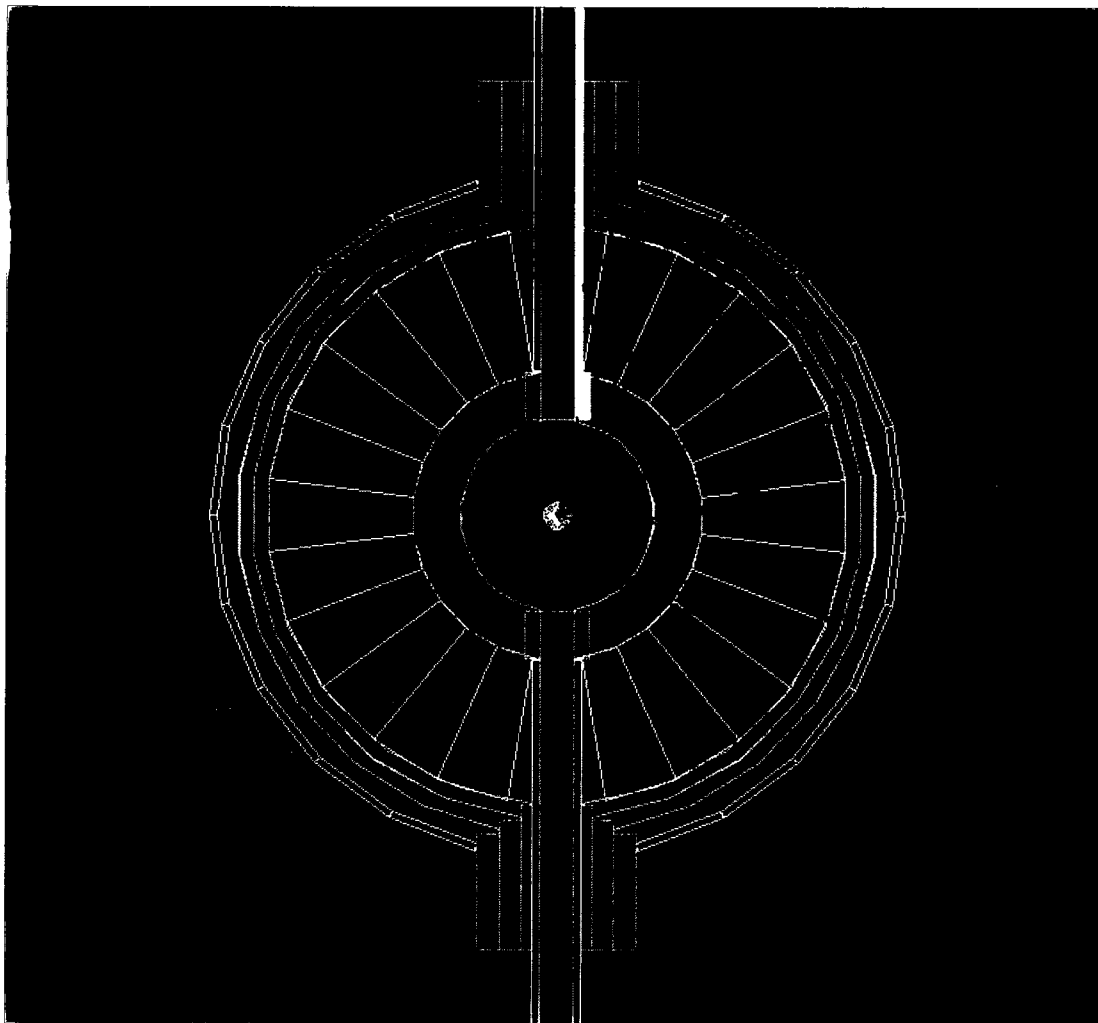


FIG. 33: Diagram of the RTPC and ionization electrons in the GEANT4 simulation without the end plates and elements outside the readout board. This view is looking from the downstream. Blue curves are the trajectories of protons and red points along them are secondary electrons created from the ionization of the gas. Light blue materials indicate that energy depositions (hits) occur inside them.



- Pair Production.

Note that the above physics processes were not all registered for each particle. For example, we only associated decay, low energy elastic and inelastic scattering, high energy inelastic scattering, multiple scattering and ionization with protons. For details about the physics processes used in BONUS, please refer to the Appendix B.

#### IV.2.4 Electric and Magnetic Fields

Our RTPC detector was immersed in a magnetic field which was parallel to the negative  $z$  direction. This magnetic field was produced by a superconducting solenoid which was originally designed for the Inner-electromagnetic Calorimeter (IC) in the CLAS. When running with full current (534 A) it can provide a field up to 4.5 T. In order to accurately simulate the tracks for the protons in the RTPC, it is important to introduce the magnetic field into the detector. The electric fields in both halves were very weak since the potentials between the anode and cathode of both halves were only about 2.5 KV. Compared with the typical kinetic energy of a spectator proton (about  $1 \sim 5$  MeV), the influence caused by this electric field is negligible. Therefore we introduced a simplified electric field in the simulation. The simplified electric field is calculated assuming that there are two coaxial infinitely long cylinders with inner radius  $a = 30$  mm and outer radius  $b = 70$  mm and their potential difference is  $V$ , the electric field for an arbitrary point in between these two cylinders is given as

$$E(r) = \frac{V}{r \ln \frac{b}{a}}. \quad (25)$$

#### IV.2.5 Electron Drift Path

The drift path for electrons from ionization were simulated by N. Baillie using the Magboltz program. This program used an electric and magnetic field to study the Lorentz angle (the deflection of a moving charged particle affected by the magnetic field), the drift velocity and the trajectory of the electron [57]. He parameterized these results in an analytical form and provided the following functions:

- A function  $f_\phi(r, \phi, z)$  that can calculate the  $\phi$  angle change,  $\delta\phi$ , of a track which starts from position  $(r, \phi, z)$  and ends up on the read out board  $(r_f, \phi_f, z_f)$ , where  $r_f = 70$  cm.

- A function  $f_t(r, \phi, z)$  that can calculate the drift time,  $t$ , of an electron which starts from position  $(r, \phi, z)$  and ends up on the read out board.
- A function  $f_r(t, \phi_f, z_f)$  that is the inverse function of  $f_t(r_0, \phi_0, z_0)$ . This function was used to reconstruct a position  $(r_0, \phi_0, z_0)$  using the  $\phi$  angle on the readout board and the drift time.

This drift path package was used to propagate electrons from the ionization location  $(r_0, \phi_0, z_0)$  until it then hit the readout board  $(r_f, \phi_f, z_f)$  at which time the position, drift time and deposited energy was converted into (ID, TDC, ADC) signals. On the other hand, it was also used in the reconstruction to convert (ID, TDC, ADC) signals back to position  $(r_0, \phi_0, z_0)$ . The digitization and reconstruction will be described later.

Figure 34 shows a typical path of an electron from ionization moving in the drift region of the RTPC. Figure 35 shows the azimuthal angle (top) and the radial position (bottom) of the electron as a function of the drift time for various high voltage settings. More information about the drift path package can be found in [57].

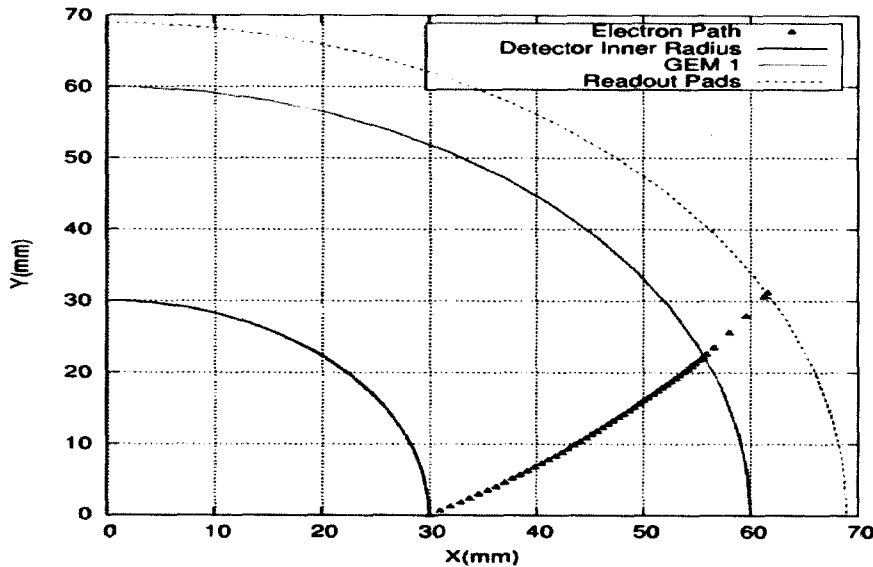


FIG. 34: Drift path of ionization electrons in the drift region of the RTPC.

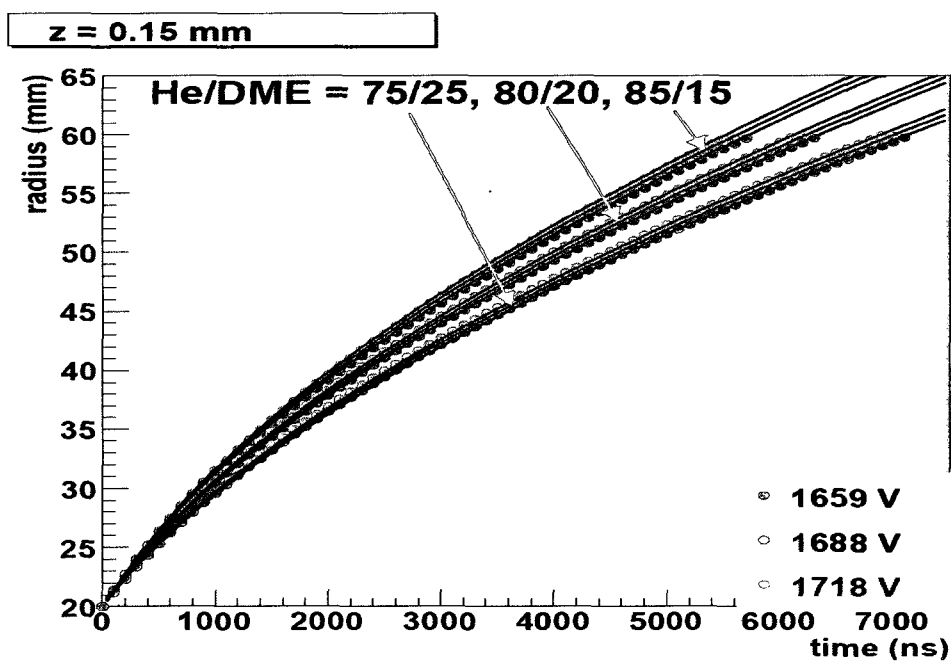
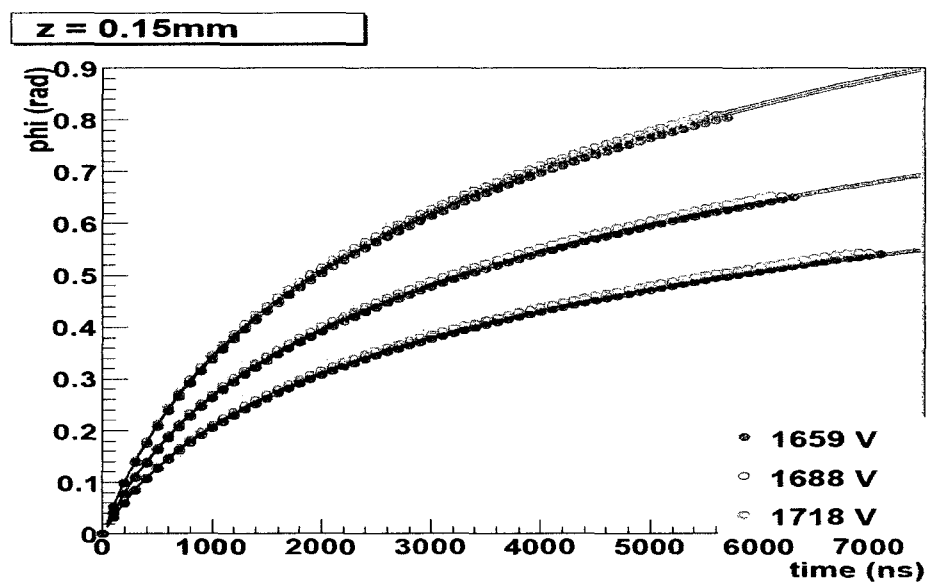


FIG. 35: The azimuthal angle (top) and radial position (bottom) of electrons as a function of the drift time for various high voltage settings.

### IV.2.6 Signal Digitization

Generally speaking, the RTPC simulation can simulate the behaviors of all particles traveling inside it. According to our goal, the drift region was designed to be sensitive to heavy ionization particles only, *i.e.* proton, deuteron, triton and alpha particles. When a proton travels through the drift region, the physics processes like low energy elastic and inelastic scattering, high energy inelastic scattering, multiple scattering and ionization will take effect according to the GEANT4 physics models. Ionization is very likely to happen for a proton along its trajectory, so ions and electrons are created from the He/DME drift gas. The number of ion-electron pairs is proportional to the deposited energy,  $\delta E$ . From the simulation point of view, an ionization is a hit, which contains information on the position  $(r, \phi, z)$  and deposited energy,  $\delta E$ . The analytic functions for the drift path will be used to 1) propagate the ionization electrons from the ionization position  $(r, \phi, z)$  to the readout board  $(r_f, \phi_f, z_f)$  and 2) calculate the drift time  $t$ . Eventually the position  $(r_f, \phi_f, z_f)$  will be converted to channel  $ID$ , the drift time  $t$  will be converted to  $TDC$  using the 114 ns time window and the deposited energy  $\delta E$  will be converted into  $ADC$  in units of 10 eV. This unit was chosen such that the simulated  $ADC$  distribution match that of the real data.

One important issue I must point out here is that the digitization described above does not represent the real electronics signal very well. In the real detector, an electron will cause avalanches in the GEMs, hence producing a pulse in the readout electronics. This pulse may last for more than one TDC window (114 ns) and have signal on several channels. If taking electrical inductance into account, there may be some induced signal in the adjoining channels too. Unfortunately, we do not have an analytical solution for this pulse and electrical inductance. It requires more effort on testing the real detector and the read out electronics. Due to the lack of knowledge of these, one simulated hit  $(r, \phi, z, \delta E)$  in the current RTPC simulation was digitized to only one set of digital signals of  $(ID, TDC, ADC)$ . As a result, the number of simulated hits and the number of simulated fired channels are much smaller than in the real data. Our experimental data show that the average number of hits in a proton track is about 50. In order to make the simulation generate an equivalent number of hits as the real detector, a step length limit of 0.6 mm was applied in the drift region of the RTPC. In other words, with this 0.6 mm step length limit

GEANT4 would force particles to create a step within each 0.6 mm path length. This step length limit cut “0.6 mm” was set in the configuration file “Detector.ini” of the simulation program (BONUS) and could be changed to any positive values. Noting that if this value is set too large, the simulation may not generate enough hits. If it is set too low, the simulation would create too many overlapped hits which may cause longer CPU time and a larger output data size.

#### IV.2.7 Event Reconstruction

As part of the simulation code, I have developed a simple and quick reconstruction module to analyze the simulated data and write the output into the data stream. This reconstruction module uses the inverse drift path function to reconstruct all simulation hits, and then links them to build a track. A helix fitting routine is then applied to the track, which returns the necessary parameters of this track, for example the vertex position  $(x_0, y_0, z_0)$  and the initial polar angle  $\theta$  and azimuthal angle  $\phi$ , the radius of the helix curvature  $R$  (which will be converted to momentum later), the  $\chi^2$  of the fit, etc. Compared to the full RTPC reconstruction module in RECSIS, which was developed to reconstruct the experimental data, my module did not contain the sophisticated track finder which selects only those hits likely to be a track to form a chain while rejecting background hits. However, this module can provide a result as good as the full reconstruction one for the simulated data because there are no background hits in the simulation. This module is very helpful for the RTPC simulation in some cases because we can get the result much quicker than running the slow and complicated RECSIS program.

### IV.3 THE SIMULATION OF THE CLAS DETECTOR

There is already a simulation program based on GEANT3 for CLAS named GSIM. This program uses an input file called “ffread card” to configure what kind of modules (i.e. DC, CC, SC, EC and so on) will be used in the simulation. For example, we turned off all devices except torus, DC, CC, SC, EC and the solenoid. Basically each CLAS experiment will have a custom-built target system and this part must be customized before running GSIM. In our case, we developed the RTPC and target

system using the GEANT4 package, BONUS. There is no way to link the GEANT4 code with a GEANT3 code. My solution for running the full BoNuS simulation is described next.

In the RTPC simulation program, BONUS, we defined a virtual boundary as a barrel with radius of 114 mm, length of 290 mm and thickness of 1 mm. This virtual boundary is made of air and the whole RTPC was placed within it. We made it a sensitive volume therefore it can record all the information (i.e. time, particle type, momentum and position) of a particle which impinges on it. This information, together with the original particle information is written into the output in a format called “bos” [52] [53], which can be read by GSIM. This bos format output file contains only the initial (thrown) information (momentum, position, and particle id) at the vertex and the final information (at the RTPC virtual boundary). Then we ran GSIM to read this file and continue simulating these particles as they propagate in the CLAS detector. In order to let GSIM read this information and process it correctly, we had to modify a few places in the existing GSIM and the RECSIS code. First, GSIM usually takes only one set of input as the thrown parameters and these thrown parameters can be recognized by the reconstruction program, RECSIS, and finally written into the output data stream. Since the BONUS output file contains two sets of information (one at the vertex and another at the virtual boundary), by default GSIM can take the latter only. We had to modify GSIM such that it copied the original information set at the vertex and finally wrote it into GSIM’s output. In order to implement this we introduced a new BOS bank named TRUE into GSIM and RECSIS. This bank has a structure similar to the PART bank, which is one of the bos format data streams that GSIM can read, and contains all information on the BONUS output. Secondly, GSIM usually treats the input information as if it is generated at the vertex of the CLAS and therefore it smears the position in a default way. In the BoNuS situation we had to turn off these smearings. Third, the BONUS TRUE bank we introduced could not be recognized and processed by RECSIS unless we modified it to do that. Therefore we added a reconstruction module for the TRUE bank into the RECSIS code.

After all the above modifications, the new GSIM copies the TRUE bank into its output file without smearing the positions provided by BONUS, and the new RECSIS processes both the RTPC signals and the TRUE bank.

#### IV.4 GSIM POST PROCESSING

The detection efficiency of a real detector can be affected by a lot of sources, such as temperature, alignment or malfunction of electronics. The efficiency of the detector, hence, is always less than 100%. In simulation, these kinds of issues are very difficult to take into account, so the efficiency of the detector in the simulation is always ideal. In order to achieve a simulation result that can match the real data, we ran another program called GSIM Post Processing (GPP), which is used to change the simulation output such that it agrees with real data, for example, by accounting for the dead wires in DC and by smearing the timing and distance resolution.

The GPP is an existing program developed by previous CLAS collaborators. It can be used to change the simulation signals for the DC, SC, CC and EC detectors. For DC signals, the GPP can 1) knock out the dead wires according to the DC calibration database and 2) shift the DOCA mean value and 3) smear the hit signals according to the resolution determined by the DC calibration procedure using the real experimental data. For the SC signal, GPP can smear the signal to change the time resolution. For the CC and EC signals, GPP can take the hardware thresholds into account.

The resolution and detector constants may vary from experiment to experiment since the experimental conditions may change. We therefore had to find a new set of calibration constants for each experimental based on the experiment data. For the same reason one needs to have a unique set of optional parameters to run one's own GPP, such as the run number ( $R$ ), the DC smearing scale values for regions 1, 2 and 3 ( $a$ ,  $b$ ,  $c$ ) and the SC smearing scale value ( $f$ ). The value for  $R$  can be any run number that belongs to the BoNuS experimental data set. This number was used to determine which entry of the calibration constants in the calibration database would be used. In order to simplify the job, we chose only one single value for the DC smearing, namely we used the same value for  $a$ ,  $b$  and  $c$ , assuming DC Regions 1, 2 and 3 had identical resolutions. In order to determine a value for  $a$ ,  $b$  and  $c$ , we generated about 1 million electron-proton elastic events distributed according to the elastic cross section and then ran them through BONUS and GSIM.

To find a value for  $f$  such that the simulated resolution matches the real resolution, we scanned  $f$  from 0.8 to 1.4 with the GPP. These GPP outputs were reconstructed by RECSIS and then analyzed to plot the SC time resolution for the

trigger electrons as a function of  $f$ . Figure 36 shows the scan result, namely the simulated SC time resolution for electrons as a function of  $f$ . Figure 37 shows the SC time resolution for electrons in the real data. By matching the resolution from the simulation to that of the real data we determined that the  $f$  value for BoNuS simulation is 1.01.

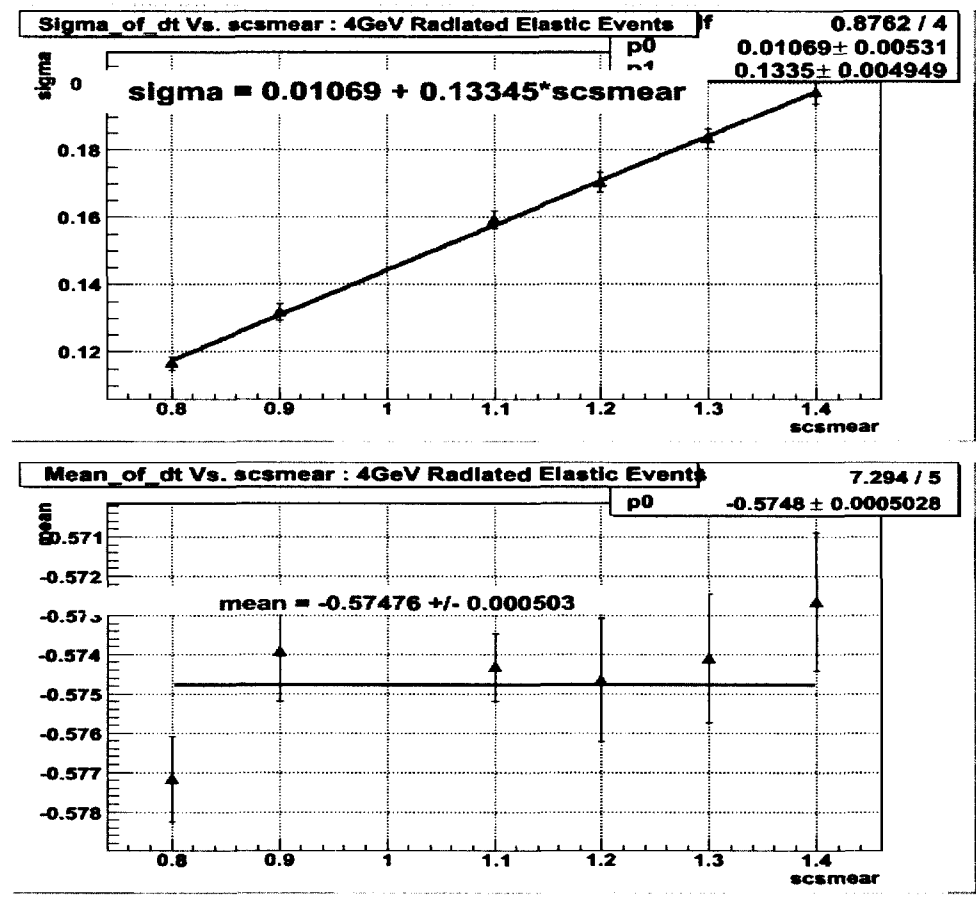


FIG. 36: The SC timing resolution for the simulation as a function of the GPP SC smearing scale value.

To find a value for  $a$ , we scanned  $a$  from 1.0 to 4.0 with the GPP, then reconstructed and analyzed the simulated data to plot the invariant mass ( $W$ ) as a function of  $a$ . Finally we compared the resolution of  $W$  in simulation with that in real data to determine the best value for DC smearing. Since  $W$  resolution is beam energy dependent, we had to find a value for  $a$  for each beam energy separately. Figure 38 shows the resolution in  $W$  as a function of  $a$  for the 1 GeV simulated data. Figure 39



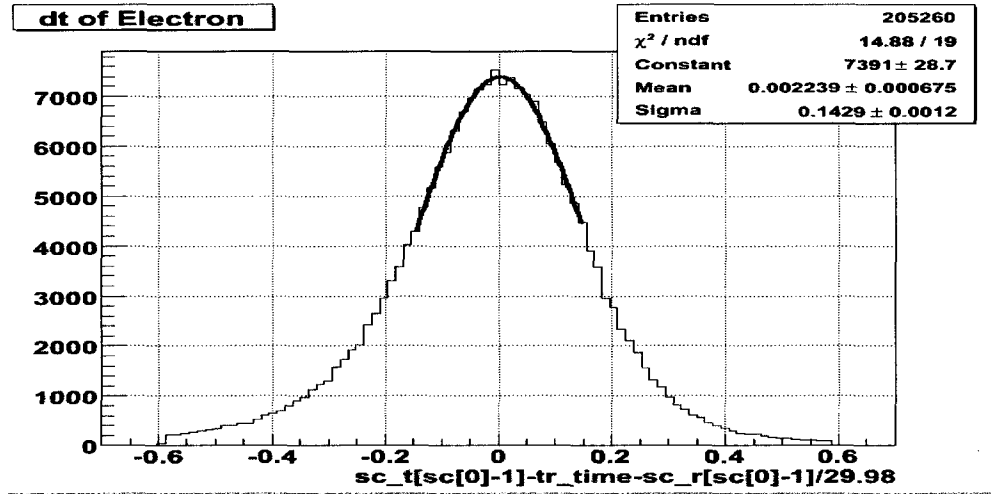


FIG. 37: Timing resolution for electrons in the BoNuS experimental data.

shows the resolution in  $W$  for the 1 GeV real data. Again, by matching the simulated resolution to the that of the real data we determined that  $a = 2.76$  for the 1 GeV data set. Repeating the same procedure for the other beam energy data sets, we finally obtained the DC smearing scale values of 1.89, 1.69 and 1.56 for the 2, 4, and 5 GeV data sets, respectively. Figures 40 to 45 show these scanning results. These GPP optional parameters for the BoNuS simulation are summarized in Table 5.

TABLE 5: GPP parameters for the BoNuS simulation

invoke option	values	description
-RR	any run number	To select the corresponding database
-Y	N/A	Knock out dead DC wires based on the database
-ff	1.01	SC smearing scale value, for all data sets
-aa -ba -ca	2.76	DC smearing scale value, for the 1 GeV data set
-aa -ba -ca	1.89	DC smearing scale value, for the 2 GeV data set
-aa -ba -ca	1.69	DC smearing scale value, for the 4 GeV data set
-aa -ba -ca	1.56	DC smearing scale value, for the 5 GeV data set

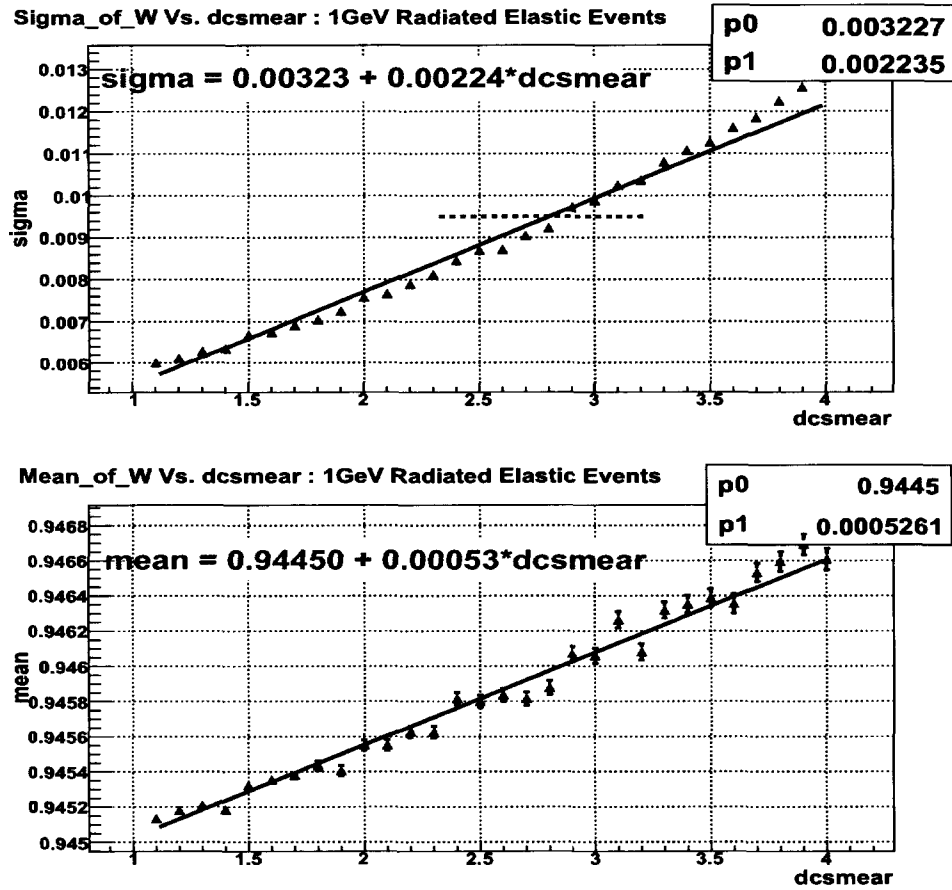


FIG. 38:  $W$  resolution for the 1 GeV simulated data as a function of the DC smearing scale value.

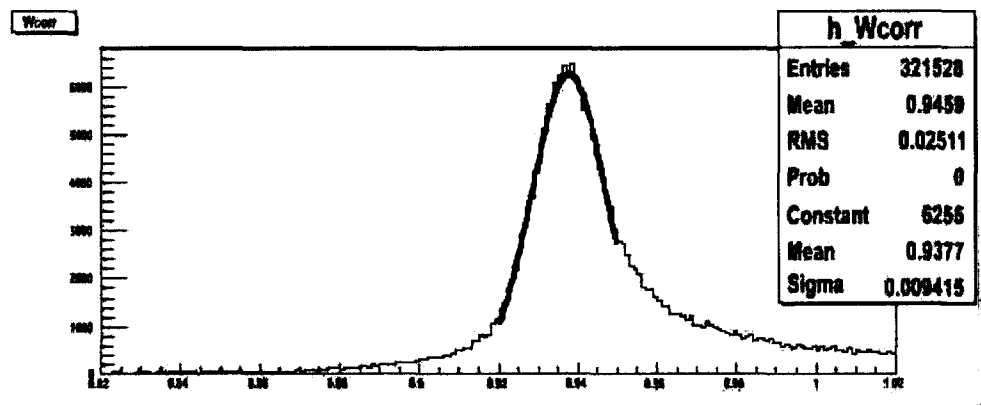


FIG. 39:  $W$  resolution for the 1 GeV real data after momentum correction.

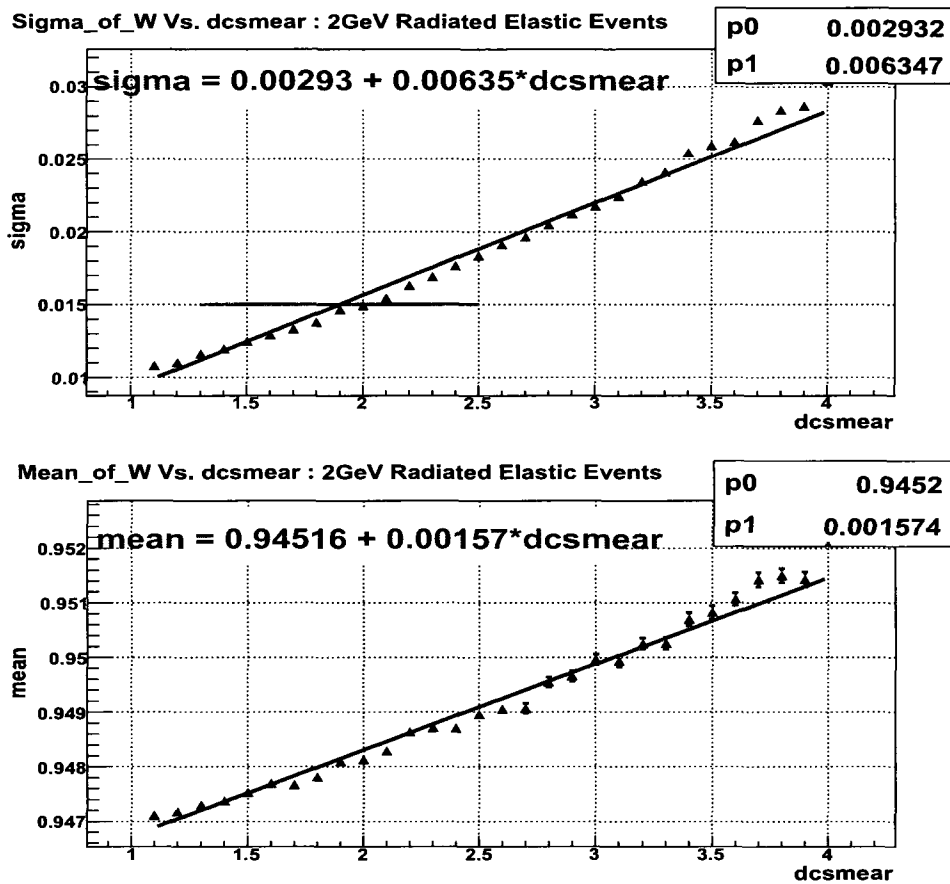


FIG. 40: The  $W$  resolution for the 2 GeV simulation as a function of  $a$ .

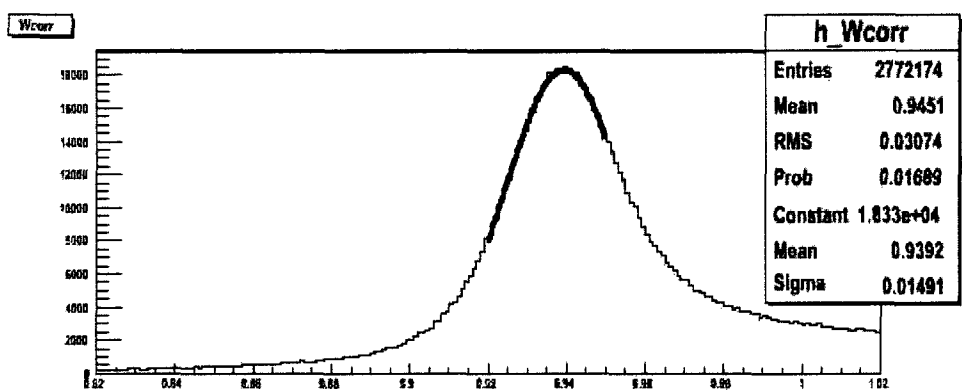


FIG. 41: The  $W$  resolution for the 2 GeV real data after momentum correction.

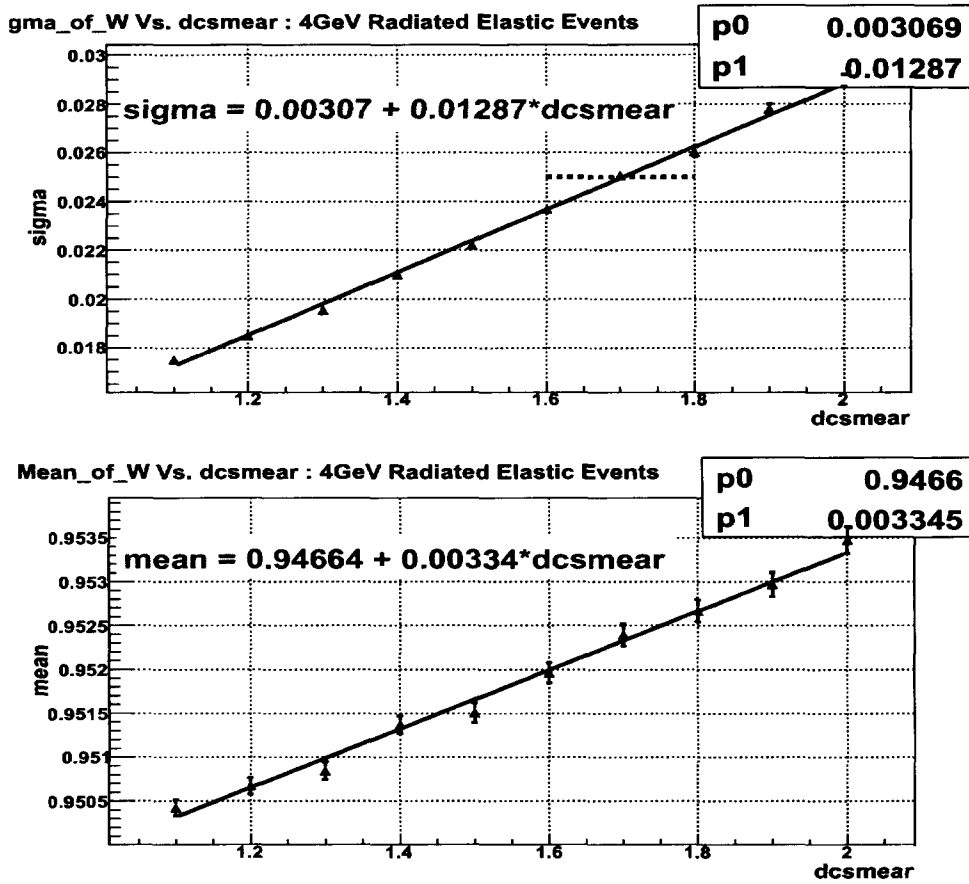


FIG. 42: The  $W$  resolution for the 4 GeV simulation as a function of the DC smearing scale value.

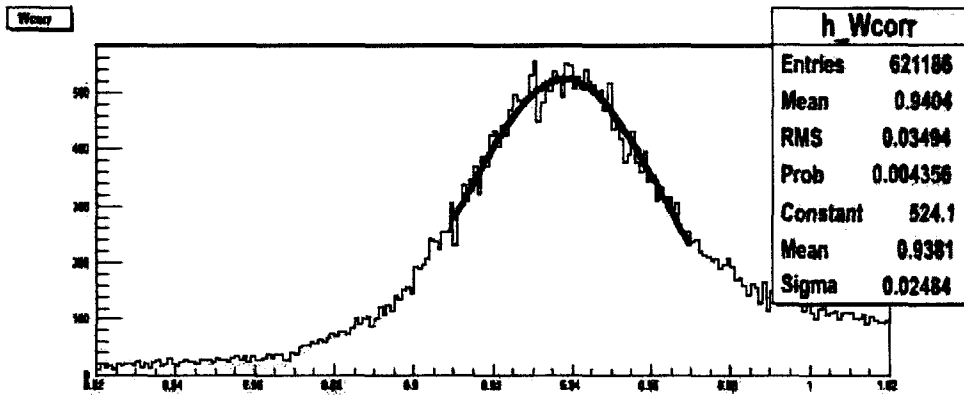


FIG. 43: The  $W$  resolution for the 4 GeV real data after momentum correction.

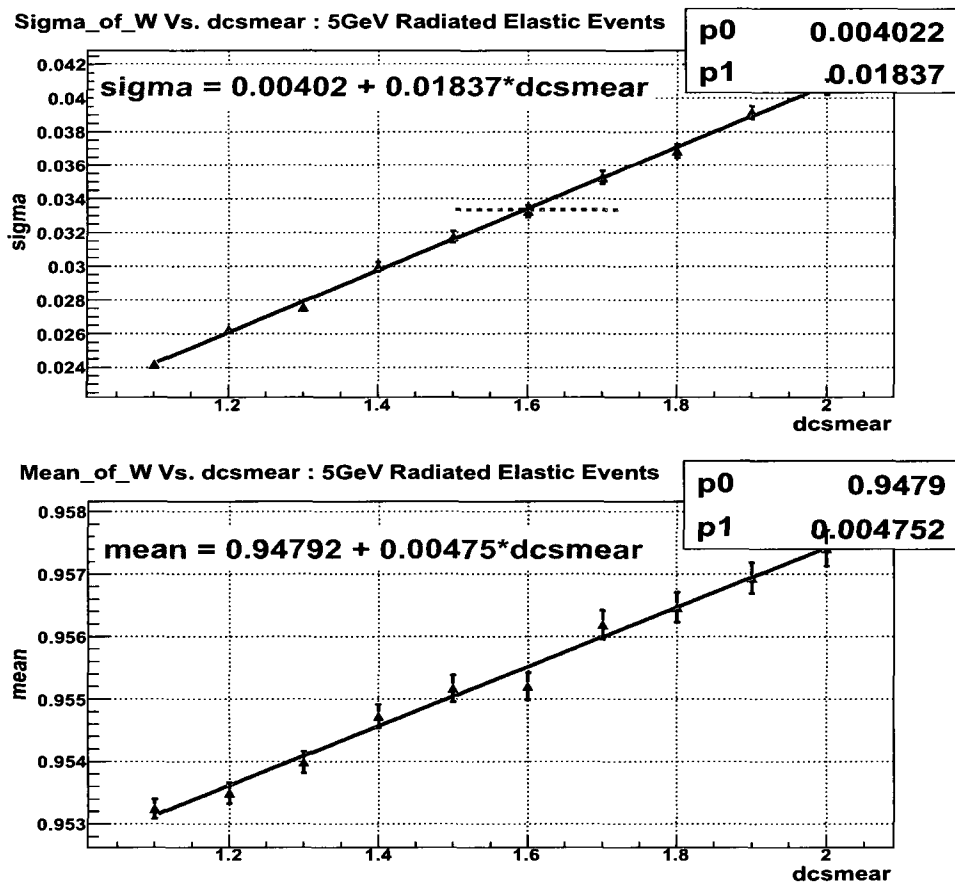


FIG. 44: The  $W$  resolution for the 5 GeV simulation as a function of the DC smearing scale value.

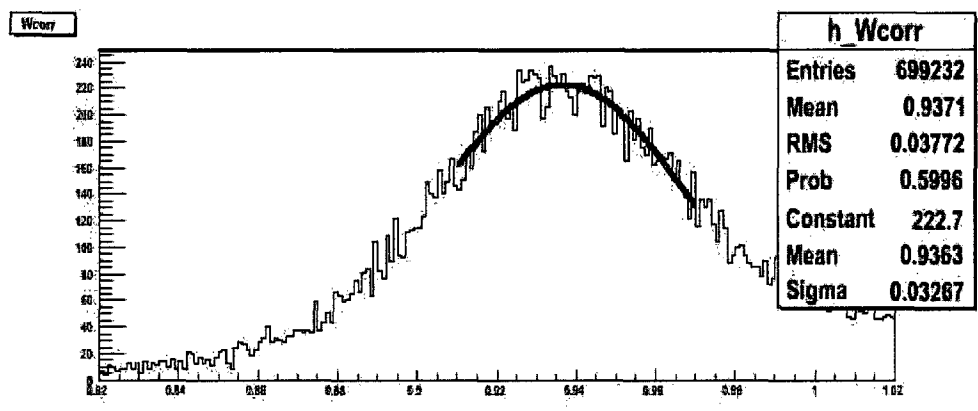


FIG. 45: The  $W$  resolution for the 5 GeV real data after momentum correction.

## IV.5 EVENT GENERATORS

The event generator determines the initial kinematics of the particles in an event according to a specified distribution. It is very important because one can save a lot of CPU time with a good event generator which can generate events that match the real experimental data. This kind of event generator usually contains the cross sections information. However, the cross section for  $D(e, e'\pi^-p)$  is not well known yet due to the lack of data, so we had to generate event according to other criteria. In this analysis, two event generators have been used. One is for inclusive simulation and the other is for exclusive simulation.

### IV.5.1 Inclusive Event Generator

The event generator used in inclusive and semi-inclusive simulation was written and maintained by S. Kuhn. It used the RCSLACPOL code developed at SLAC to do the radiative corrections [59, 60]. In addition to the cross section information, a deuteron wave function obtained from the Paris potential solution [61] was also included to account for the Fermi motion of the neutron. To meet the goal of inclusive analysis, three types of events were generated: 1) electron scattering from the deuteron or proton  $D(e, e')$  and  $H(e, e')$ ; 2) quasi-elastic scattering from the neutron inside the deuteron  $D(e, e'p_s)$ ; 3) inelastic scattering from the neutron  $D(e, e'p_s)X$ .

In order to generate the neutron quasi-elastic and inelastic scattering events with Fermi motion, this event generator first picked the Fermi momentum for the spectator proton,  $\mathbf{p}_s$ , according to the deuteron wave function. Assuming the deuteron was at rest, the kinematics for the neutron were given by:

$$\mathbf{p}_n = -\mathbf{p}_s; \quad (26)$$

$$E_n = M_d - E_p = M_d - \sqrt{M_p^2 + \mathbf{p}_s^2}; \quad (27)$$

$$M'_n = \sqrt{E_n^2 - \mathbf{p}_n^2} = \sqrt{(M_d - \sqrt{M_p^2 + \mathbf{p}_s^2})^2 - \mathbf{p}_s^2}. \quad (28)$$

Note that the off-shell mass of the neutron here is different from the free neutron mass at rest. Then the generator picked a random  $Q^2$  and  $\nu$  within the boundaries defined in the configuration file to generate the kinematics for the scattered electron,  $e'$ .

The full radiative cross section for the generated events was calculated, and the event was written out if the cross section was larger than a random number thrown with uniform distribution. Pre-scattering radiative corrections were taken into account at this step. The  $H(e, e')$  simulation was used to search for the proper parameters for the GPP (see Section IV.4). The  $D(e, e')$ ,  $D(e, e'p_s)$  and  $D(e, e'p_s)X$  simulations were used to extract the trigger efficiency of CLAS and for inclusive analysis purposes.

### IV.5.2 Exclusive Event Generator

The event generator used for exclusive  $D(e, e'\pi^-pp_s)$  simulation is called Final State GENERator (FSGEN)[64], and was provided by S. Stepanyan. This code was written based on the PYTHIA package [65, 66], which generated the  $D(e, e'\pi^-pp_s)$  events uniformly or under a given distribution in the center-of-mass frame. The Fermi motion of the initial neutron was modeled using the deuteron momentum distribution obtained from the Bonn potential. No cross section is yet included in FSGEN. To run this event generator, one needs to provide a configuration file to specify the final state and the kinematic boundaries. One can also limit some kinematic distributions, for example,  $W$ ,  $Q^2$ ,  $t$  (the momentum transfer square between the virtual photon and outgoing hadron  $\pi^-$ :  $t \equiv (q^\mu - \pi^\mu)^2$ ), such that the simulated data can match the experimental data.

FSGEN generates  $D(e, e'\pi^-pp_s)$  events by first selected the momentum for the spectator proton  $\mathbf{p}_s$  according to the Bonn potential. The momentum and the energy for the neutron were then determined using Eqs. (26) and (27). Then  $W$  and  $Q^2$  were chosen within the boundaries of the given distribution, if there was any, or according to the default flat distribution. Note that this  $W$  does not yet include the Fermi motion information. Knowing the beam energy  $E$  and according to the Eqs. (1) and (2), the electron scattering angle  $\theta_e$  and the final energy  $E'$  were then calculated. A value for the azimuthal angle,  $\phi_e$ , under a flat distribution was generated. From here it obtained the four-momentum for the virtual photon,  $q^\mu$ .

To obtain the four-momenta for the outgoing hadrons ( $\pi^-$  and proton) in the

reaction  $\gamma^*n \rightarrow \pi^-p$ , the FSGEN used the following definitions:

$$q_{\text{cm}}^\mu = (0, 0, E_{\text{cm}}, E_{\text{cm}}); \quad (29)$$

$$n_{\text{cm}}^\mu = (0, 0, p_{\text{Tcm}}, E_{\text{Tcm}}); \quad (30)$$

$$\pi_{\text{cm}}^\mu = (\mathbf{p}_{\pi\text{cm}}, E_{\pi\text{cm}}). \quad (31)$$

Since the square of the four-momentum is frame invariant,

$$q_{\text{cm}}^{\mu 2} = -Q^2, \quad (32)$$

$$n_{\text{cm}}^{\mu 2} = M_T^2 = E_p^2 - \mathbf{p}_n^2, \quad (33)$$

the CM beam energy  $E_{\text{cm}}$  and the target neutron's CM momentum  $P_{\text{Tcm}}$  can be determined. Using the constraint from the invariant variable  $t$ ,

$$t = (q_{\text{lab}}^\mu - \pi_{\text{lab}}^\mu)^2 = (q_{\text{cm}}^\mu - \pi_{\text{cm}}^\mu)^2, \quad (34)$$

$$= M_\pi^2 - Q^2 - 2(E_{\text{cm}}E_{\pi\text{cm}} - E_{\text{cm}}|\mathbf{p}_{\pi\text{cm}}|\cos\theta_\pi^*), \quad (35)$$

and using a uniform  $\theta_\pi^*$  and a uniform  $\phi_\pi^*$  distribution, the  $\pi^-$  four-momentum was determined. The four momentum of the outgoing proton was finally determined based on

$$p_{\text{cm}}^\mu = q_{\text{cm}}^\mu + n_{\text{cm}}^\mu - \pi_{\text{cm}}^\mu.$$

Finally  $\pi_{\text{cm}}^\mu$  and  $p_{\text{cm}}^\mu$  were boosted from the CM frame back to the lab frame.

The  $D(e, e'\pi^-pp_s)$  simulation was used for the exclusive analysis to calculate the acceptance and particle detection efficiencies and to model the background. Since there was no cross section information included, the simulated data may not match the experimental data. In order to correct for this, we weighted each generated event by  $r(W', Q^2, \cos\theta_\pi^*, \phi_\pi^*)$ , which came from the ratio of the kinematics distribution of the real data to that of the simulated data. The definition of  $r$  is given as:

$$r \equiv r_1(W')r_2(Q^2)r_3(\cos\theta_\pi^*)r_4(\phi_\pi^*), \quad (36)$$

where  $r_1$ ,  $r_2$ ,  $r_3$  and  $r_4$  are the distribution ratios of the real data to that of the detected simulated data (where the area of the distribution for the simulated data has been normalized to that of the real data) as a function of  $W'$ ,  $Q^2$ ,  $\cos\theta_\pi^*$  and  $\phi_\pi^*$ ,



respectively:

$$r_1(W') = \frac{\text{data}(W')}{\text{simulation}(W')}; \quad (37)$$

$$r_2(Q^2) = \frac{\text{data}(Q^2)}{\text{simulation}(Q^2)}; \quad (38)$$

$$r_3(\cos \theta_\pi^*) = \frac{\text{data}(\cos \theta_\pi^*)}{\text{simulation}(\cos \theta_\pi^*)}; \quad (39)$$

$$r_4(\phi_\pi^*) = \frac{\text{data}(\phi_\pi^*)}{\text{simulation}(\phi_\pi^*)}. \quad (40)$$

We understood that extracting a value for  $r$  in each four-dimensional bin would be better than using the product of the four individual ratios defined above. We would have extracted  $r$  for each four-dimensional bin if there were enough statistics in the experimental data. Figures 46 to 49 show the ratios of the  $D(e, e'\pi^- p_{\text{CLAS}})p$  event distributions for the 5 GeV real data to the simulated data for  $W'$ ,  $Q^2$ ,  $\cos \theta_\pi^*$  and  $\phi_\pi^*$ , respectively. Figures 50 to 53 show the same ratios but for  $D(e, e'\pi^- p_{\text{RTPC}})p$  events.

This weight was used in the calculation of acceptance. In general, the acceptance would be given by

$$A = \frac{\text{number of reconstructed events}}{\text{number of generated events}} = \frac{\sum_{rec} 1}{\sum_{gen} 1}.$$

In this analysis, the acceptance was calculated according to:

$$A = \frac{\sum_{rec} r}{\sum_{gen} r}.$$

Details about the acceptance calculation will be described later in Section V.6.

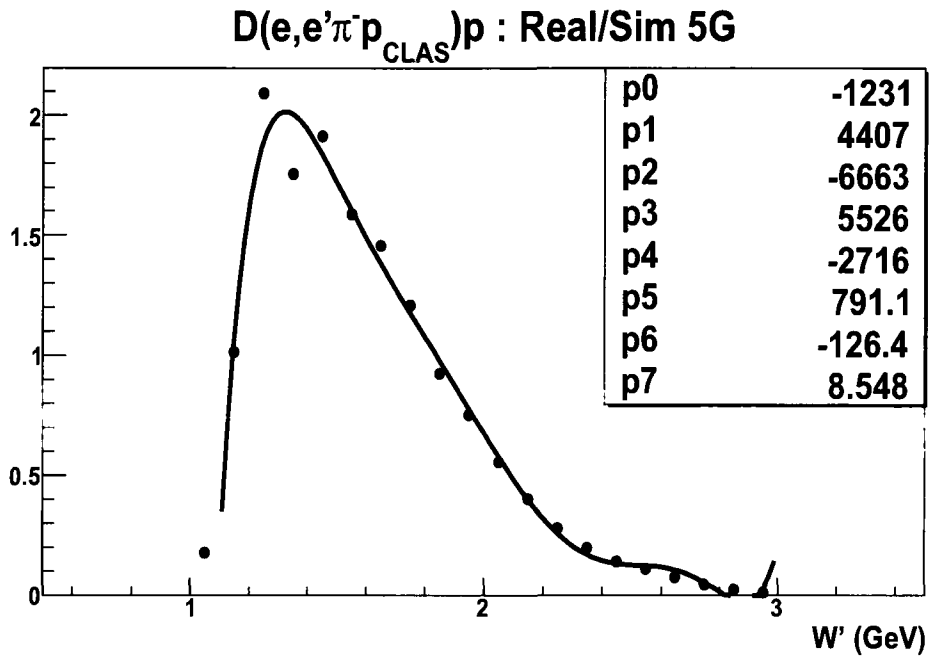


FIG. 46: Ratio of the  $D(e, e' \pi^- p_{\text{CLAS}}) p$  events for the 5 GeV real data to the simulated data as a function of  $W'$ .

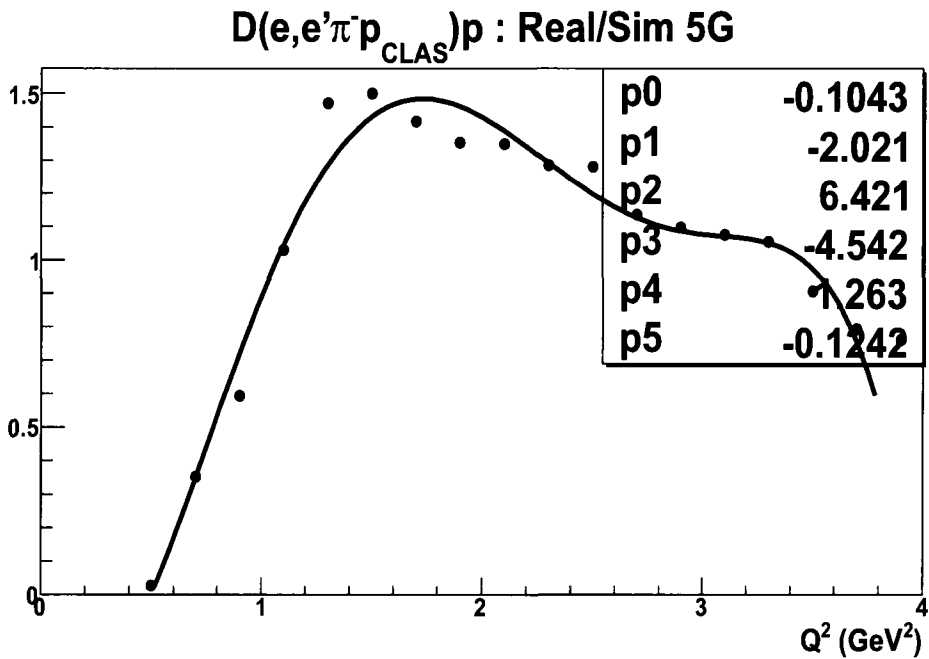


FIG. 47: Ratio of the  $D(e, e' \pi^- p_{\text{CLAS}}) p$  events for the 5 GeV real data to the simulated data as a function of  $Q^2$ .

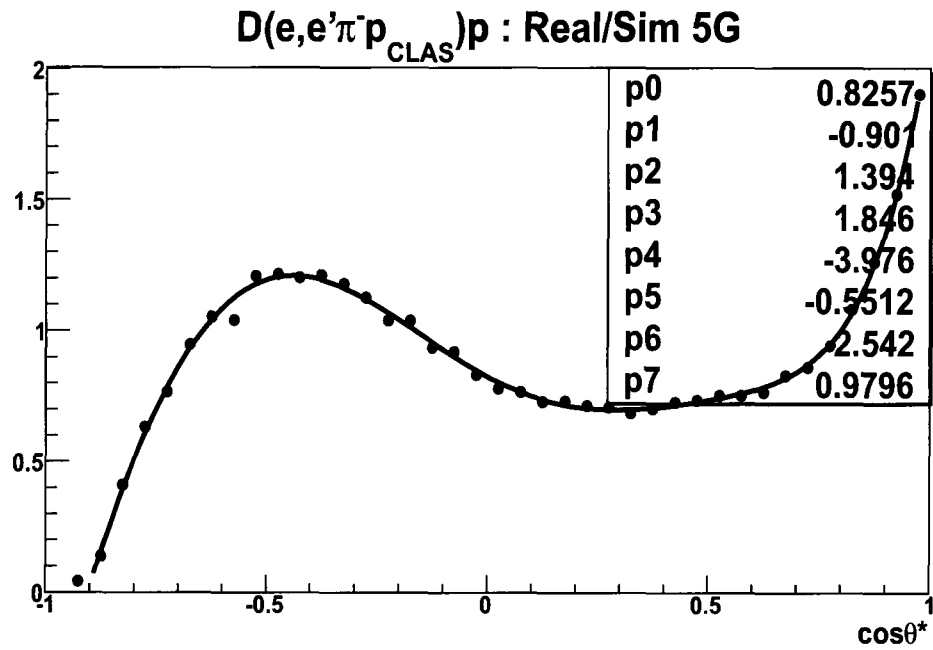


FIG. 48: Ratio of the  $D(e, e' \pi^- p_{\text{CLAS}}) p$  events for the 5 GeV real data to the simulated data as a function of  $\cos \theta_\pi^*$ .

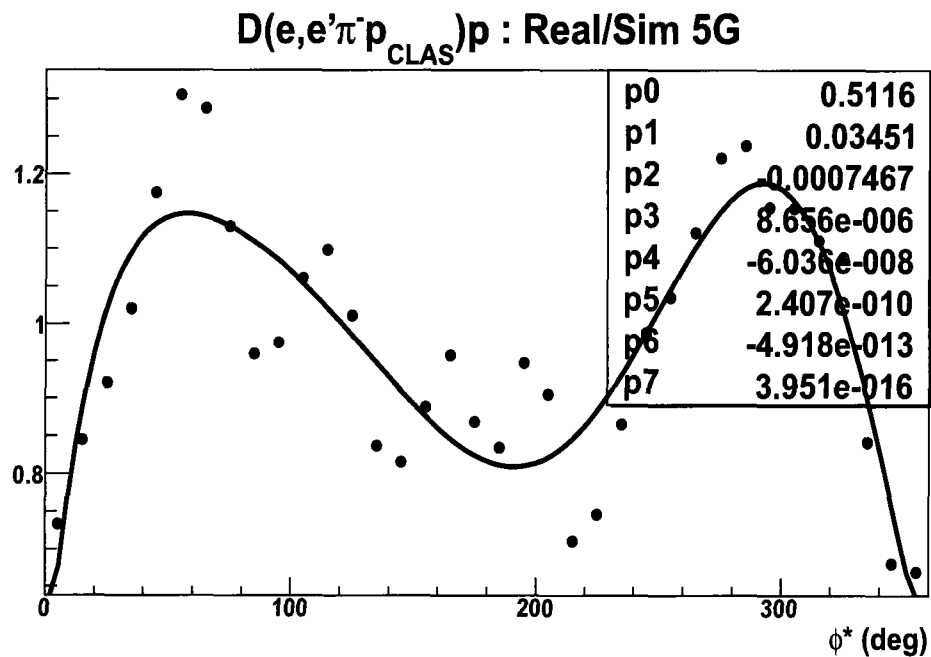


FIG. 49: Ratio of the  $D(e, e' \pi^- p_{\text{CLAS}}) p$  events for the 5 GeV real data to the simulated data as a function of  $\phi_\pi^*$ .

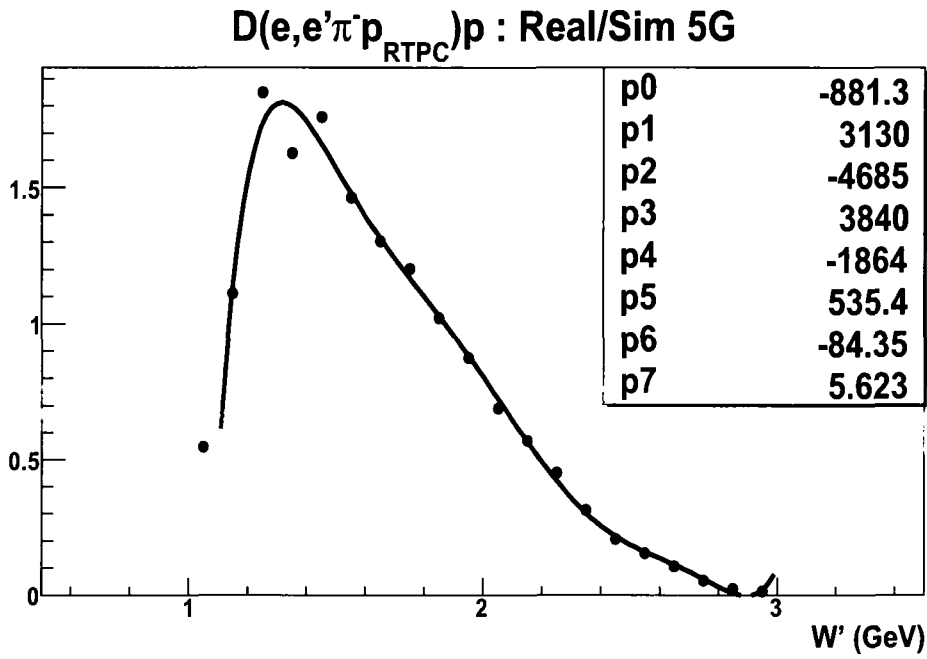


FIG. 50: Ratio of the  $D(e, e' \pi^- p_{\text{RTPC}}) p$  events for the 5 GeV real data to the simulated data as a function of  $W'$ .

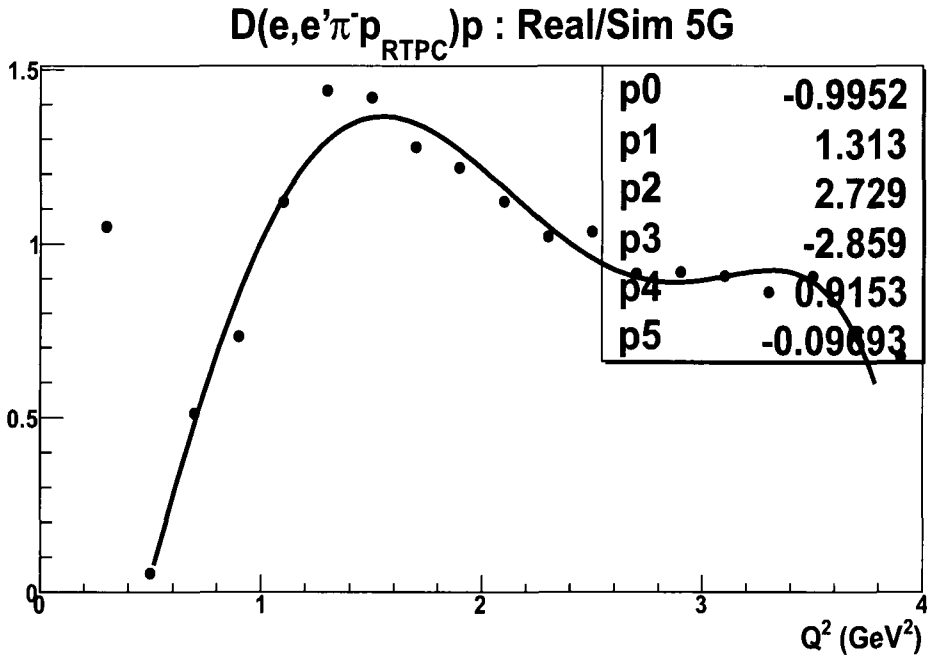


FIG. 51: Ratio of the  $D(e, e' \pi^- p_{\text{RTPC}}) p$  events for the 5 GeV real data to the simulated data as a function of  $Q^2$ .

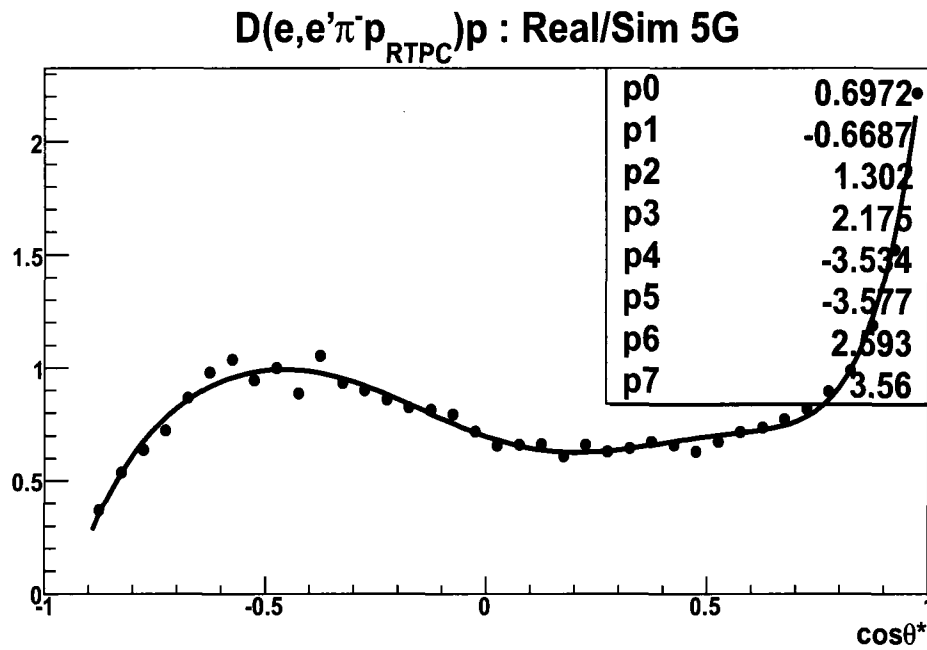


FIG. 52: Ratio of the  $D(e, e' \pi^- p_{\text{RTPC}})p$  events for the 5 GeV real data to the simulated data as a function of  $\cos \theta_\pi^*$ .

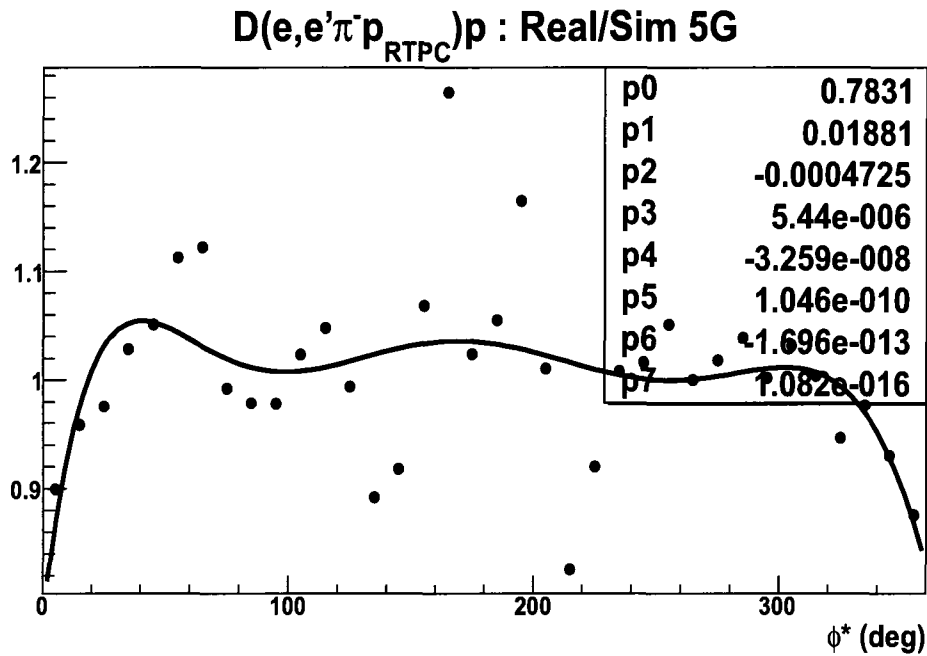


FIG. 53: Ratio of the  $D(e, e' \pi^- p_{\text{RTPC}})p$  events for the 5 GeV real data to the simulated data as a function of  $\phi_\pi^*$ .

## CHAPTER V

### DATA ANALYSIS

The BoNuS experiment was performed from Oct. 12 to Dec. 24 in 2005. Data were collected on a 7 atmosphere gaseous deuterium target with incident electron beam energies of 1.1005, 2.1424, 4.2262 and 5.2681 GeV. The 1 GeV data were used for calibrations. Table 6 lists the whole run period of the BoNuS experiment, which includes calibration and background runs on hydrogen and helium. For some runs we used the beam stopper in front of the Faraday Cup (FC). The status of the beam stopper is also listed in this table. For this analysis we used the deuterium data collected with 2, 4 and 5 GeV beam energy. The trigger was defined by a cluster with deposited energy above threshold in the electromagnetic calorimeter together with a hit above threshold in the Cherenkov counter for the same sector. The data rate was about 0.7 kHz and the dead time less than 25%.

Several calibrations and corrections were applied to obtain accurate data for the final physics analysis. The data processing, calibrations and corrections will be addressed in the following sections.

#### V.1 DATA PROCESSING

The collected data were processed using the CLAS REConstruction and analySIS framework (RECSIS). RECSIS consists of several modules designed to reconstruct hits from the raw detector data. This program converts the raw detector information into momenta, vertices, times and particle information, i.e. charge and mass. During the reconstruction of an event, the raw data from all involved detectors are read in and then processed by their corresponding modules. The result is then passed to the Simple Event Builder module (SEB), which writes all the reconstructed information into the output file. Overall, RECSIS is in charge of the following tasks:

- geometrically match each track in the drift chamber to the corresponding hits in the other detectors, for example CC, SC and EC;
- identify the trigger particle (i.e., the electron) for an event;

run_min	run_max	target	stopper (in out)	beam_energy (GeV)	torus (A)	thresholds (mV)		
						CC	EC <sub>inner</sub>	EC <sub>total</sub>
49471	49499	D <sub>2</sub>	out	4.2262	2250	75	70	200
49500	49522	D <sub>2</sub>	out	4.2262	2250	20	70	150
49523	49640	D <sub>2</sub>	out	4.2262	2250	75	70	200
49642	49663	H <sub>2</sub>	in	4.2262	2250	75	70	200
49664	49691	D <sub>2</sub>	out	4.2262	2250	75	70	200
49692	49798	D <sub>2</sub>	in	4.2262	2250	75	70	200
49799	49807	He	in	4.2262	2250	75	70	200
49808	49821	He	in	5.2681	2250	75	70	200
49822	49927	D <sub>2</sub>	in	5.2681	2250	75	70	200
49928	49938	H <sub>2</sub>	in	5.2681	2250	75	70	200
49939	49943	He	in	5.2681	2250	75	70	200
49944	50013	He	out	5.2681	2250	75	70	200
50014	50050	H <sub>2</sub>	out	5.2681	2250	75	70	260
50051	50061	H <sub>2</sub>	in	5.2681	2250	75	70	260
50062	50105	D <sub>2</sub>	in	5.2681	2250	75	70	260
50108	50236	D <sub>2</sub>	in	5.2681	2250	75	70	260
50237	50251	H <sub>2</sub>	in	5.2681	2250	75	70	260
50252	50268	He	in	5.2681	2250	75	70	260
50269	50283	He	in	2.1424	1500	75	70	260
50284	50290	H <sub>2</sub>	in	2.1424	1500	75	70	260
50291	50296	D <sub>2</sub>	in	2.1424	1500	75	70	260
50297	50308	D <sub>2</sub>	out	2.1424	1500	75	70	260
50309	50331	D <sub>2</sub>	out	2.1424	1500	75	70	150
50333	50340	H <sub>2</sub>	out	1.1005	1500	75	70	150
50341	50349	D <sub>2</sub>	out	1.1005	1500	75	70	150

TABLE 6: All runs of the BoNuS experiment. The target type, beam energy, torus current and trigger thresholds are listed. For some runs we used the beam stopper in front of the Faraday Cup (FC). The status of the beam stopper is also listed.

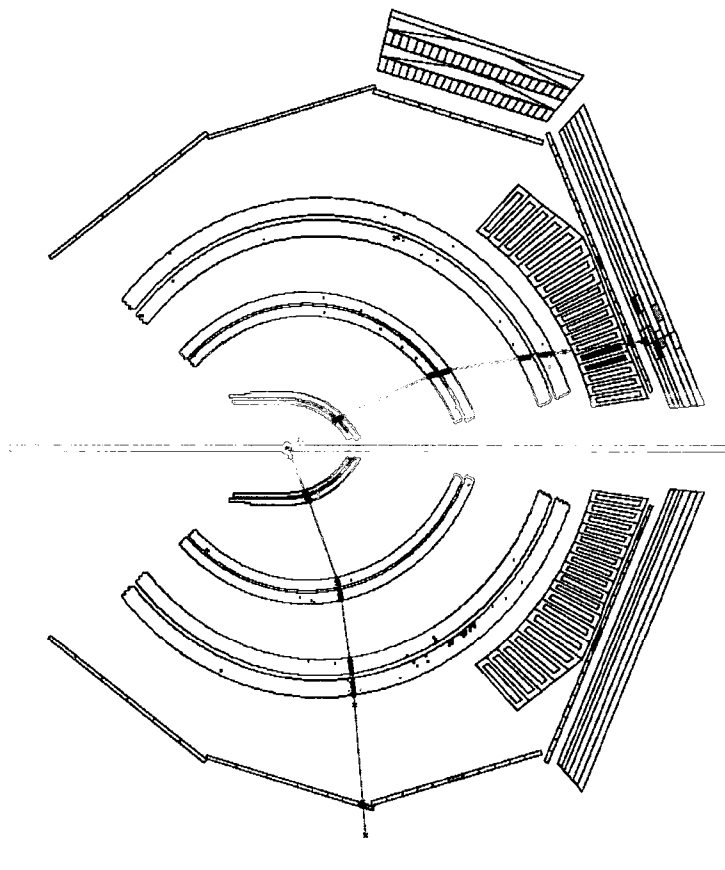


FIG. 54: An example of an event reconstructed by RECSIS. The inbending track on the top half of the detector corresponds to the electron that triggered the event, the outbending track on the lower half corresponds to a positively charged particle.

- calculate the trigger time and event start time;
- identify the particle, i.e. electron,  $\pi^-$ ,  $\pi^+$ , proton, *etc.*, for each reconstructed track;
- build an event and write it to the output file.

Figure 54 shows an example of an event reconstructed by RECSIS. An “inbending” track, in this case the electron, bends toward the beam line. Positive particles bend away from the beam line.



## V.2 DETECTOR CALIBRATIONS

In each CLAS experiment, the detectors are calibrated to ensure that experimental quantities such as time or energy are correctly determined from the raw ADC and TDC information. The calibration changes from experiment to experiment and even from run to run. For example, the TOF calibration might change due to changes in the electronics or wiring; the DC electron drift velocity varies with changes in atmospheric pressure, temperature, humidity and gas mixture, all of which can affect the drift time to drift distance relationship. The tasks of data calibration were performed by several collaborators. The calibrations of the TOF, DC and EC energy done by other collaborators will be summarized briefly. The EC timing calibration performed by J. Zhang will be described more thoroughly.

### V.2.1 Time of Flight Calibration

The calibration of the Scintillator Counters should be carried out first because 1) the SC provides the start time of each event; 2) all the timing information from other detectors in CLAS is relative to the SC time. For these reasons the quality of the SC timing calibration is always required to be very accurate since it strongly affects all the other time related calibrations, *i.e.* the DC and EC timing calibration.

A TOF calibration consists of the pedestal calibration, the TDC calibration, the left-right PMT alignment, the attenuation length calibration and the counter to counter calibration. The SC calibration for BoNuS was done by N. Kalantarians. For details about the calibration procedure please refer to [67, 68, 69].

### V.2.2 Drift Chamber Calibration

The CLAS drift chambers were designed to measure particle momentum with a resolution of 0.5% for 1 GeV particles [36], which requires the hit positions along a track to be measured very precisely and the magnetic field to be known accurately. Before the BoNuS experiment, part of the drift chamber had been pulled out for repair, then reinstalled. It is not possible to ensure that a chamber is installed exactly at the same position as it was previously located. Therefore a calibration of the DC

alignment is very necessary, in addition to the regular drift velocity calibration.

As described in Section III.3.1, the DC consists of six identical sectors. Each sector is divided into three regions. Each region has two superlayers, axial and stereo. The schematic view of the Drift Chambers is shown in Fig. 16. Each superlayer contains six layers of sense wires except superlayer 1, which has only four layers. Each superlayer should be separately calibrated, which yields 34 sets of calibration constants.

The primary purpose of the Drift Chamber calibration is to refine the drift time to drift distance conversion to optimize position measurements. The constants for the time-to-distance conversion have to be systematically calibrated and checked for stability over the course of the experiment. The calibration procedure consists of several iterations of running the reconstruction program followed by refitting the calibration constants.

The DC calibration was done by S. Tkachenko. His calibration was successful in realigning the 34 drift cell layers into a straight line and improving the resolution. The time residual before and after his calibration is shown in Figs. 55 and 56, respectively.

More details about this calibration can be found in [63, 70].

### V.2.3 Electromagnetic Calorimeter Time Calibration

The Electromagnetic Calorimeter (EC) is an important part of the CLAS detector. It is used to detect electrons, and in combination with the CC, is usually part of the trigger requirement. In addition, the EC was designed to detect neutral particles, for example photons,  $\pi^0$ ,  $\eta$ , and neutrons [41].

Since the EC time is relative to the SC time, the calibration of the EC timing should always be performed after the SC calibration is finished. The EC timing is calibrated by comparing the time measured by the EC to the time expected from the TOF for electrons. The expected time of an electron hit in the EC extrapolated from the SC time should be:

$$T_{\text{EC}}^{\text{cal}} = T_{\text{TOF}} + \frac{d_{\text{trk}}}{c}, \quad (41)$$

where  $T_{\text{TOF}}$  is the time measured by the TOF, and  $d_{\text{trk}}$  is the path-length between TOF and EC strips. The time measured by the EC ( $T_{\text{EC}}$ ) is then compared with this expected time for each PMT. The EC time calibration constants were adjusted to

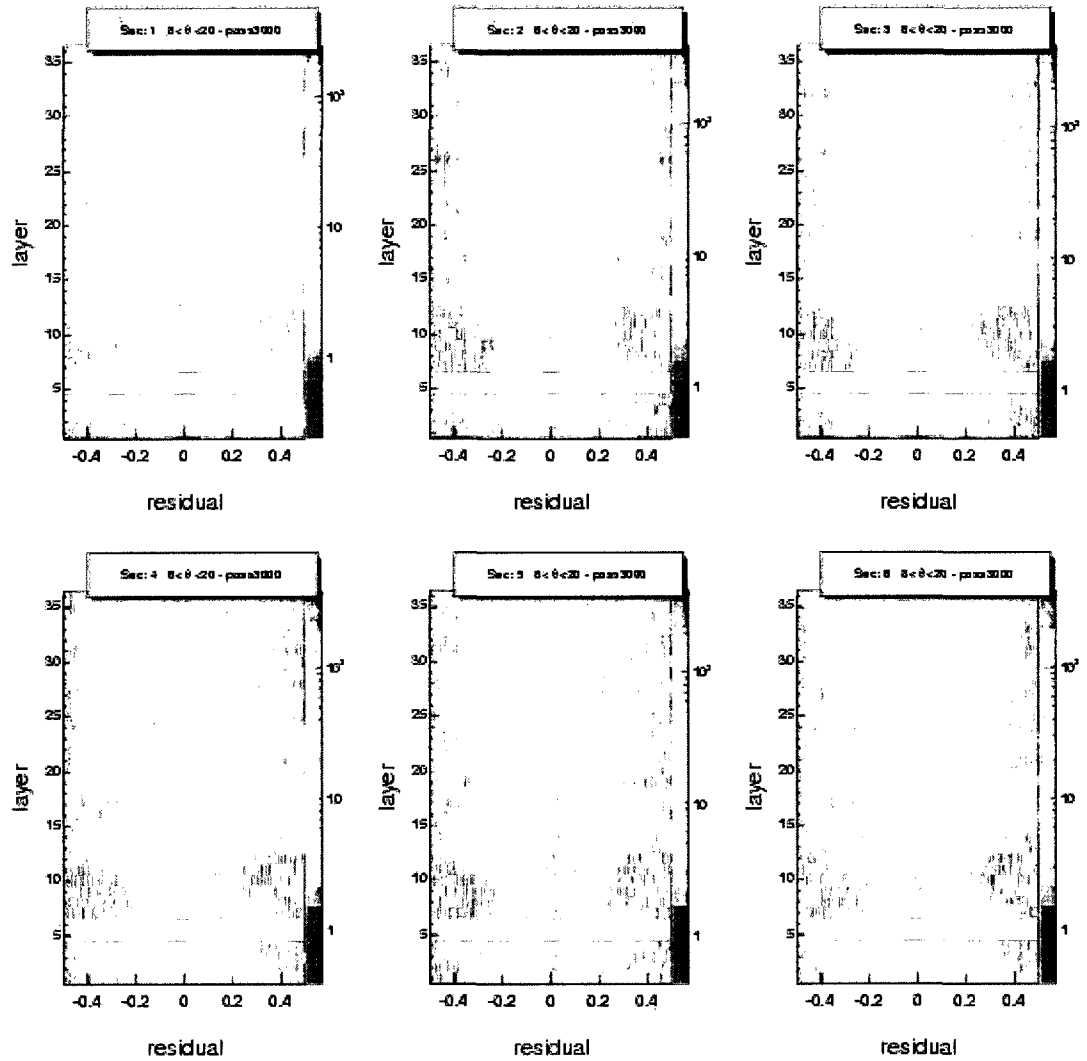


FIG. 55: DC residuals before calibration for each layer in sectors 1 to 6.

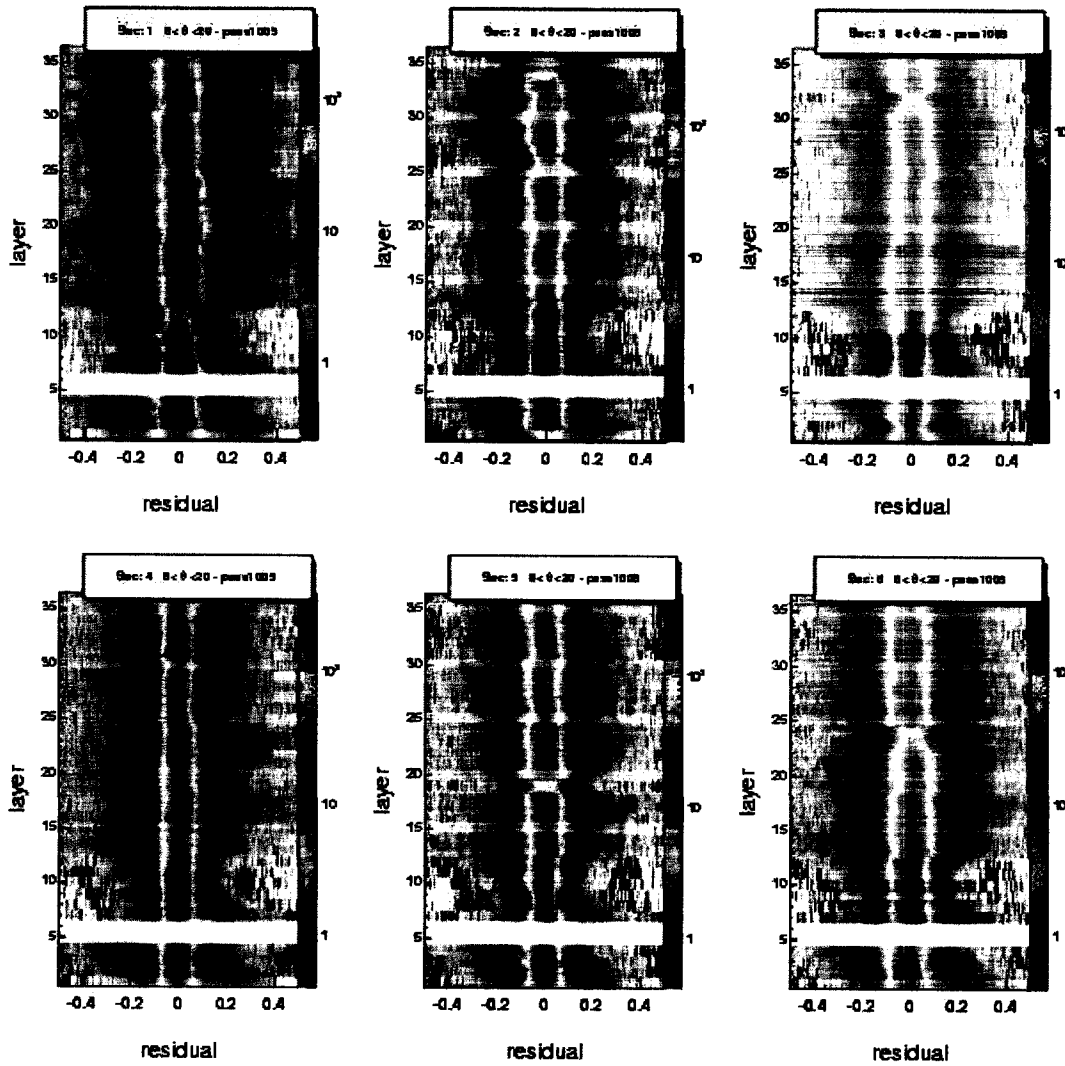


FIG. 56: DC residuals after calibration for each layer in sectors 1 through 6.

keep the difference between expected time and measured time in the EC, defined as

$$\Delta t_{\text{ECSC}} = T_{\text{EC}} - T_{\text{EC}}^{\text{cal}}, \quad (42)$$

as close to zero as possible. This can be checked by fitting the  $\Delta t_{\text{ECSC}}$  for electrons with a gaussian function. Figs. 57 and 58 show the  $\Delta t_{\text{ECSC}}$  before and after this calibration. One can see that after the calibration, the average values of  $\Delta t_{\text{ECSC}}$  for each sector are close to zero.

#### V.2.4 Electromagnetic Calorimeter Energy Calibration

The calibration of the electromagnetic calorimeter energy was done by EC expert C. Smith [72]. Cosmic ray runs were taken with a special trigger which used a threshold of 10% minimum ionizing energy and forced a hit in both the inner and outer layers of the EC module. This excludes triggers that would never satisfy the pixel cut. The pixel cut simply demands that a single overlapping pixel fires in both the inner and outer layers. Since cosmic muons are minimum ionizing, the energy deposited depends only on the track length for that pixel, which is fixed by geometry. By confining the muon track to a single pixel, the mean energy deposited in the scintillator, corrected for attenuation, can be related to the response of a single PMT. The gain factor for each PMT is then adjusted so that the overall gain of all PMTs are matched and signals are properly converted into deposited energy (GeV).

#### V.2.5 Cherenkov Counter Calibration

Normally the Cherenkov counter calibration is done by CC experts. In the case of BoNuS experiment, the ADC calibration for the CC detector is not yet done. As a result the average number of reconstructed photoelectrons for electrons in each sector of the CC detector in the BoNuS experiment is lower than other experiments. The number of photoelectrons was used to identify the trigger electrons. In order to avoid losing triggers a very loose cut at the hardware threshold was applied.

The TDC calibration for the CC detector is also problematic. During the data analysis, I was able to identify some bugs in the TDC reconstruction for the CC detector in the RECSIS code. These bugs have since been fixed and a new TDC calibration has been performed by me. This calibration was done by adjusting the

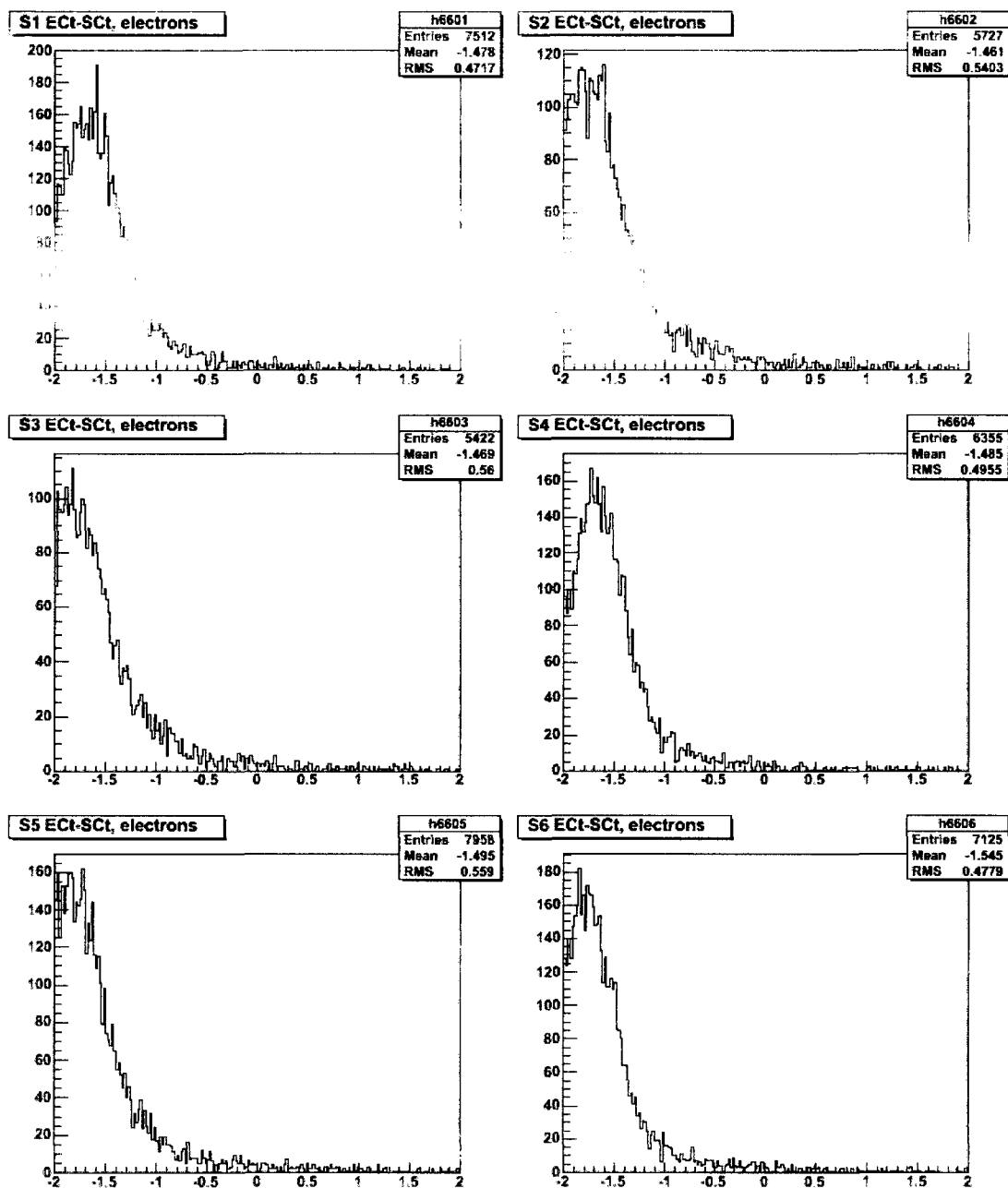


FIG. 57:  $\Delta t_{\text{ECSC}}$  before the EC time calibration.

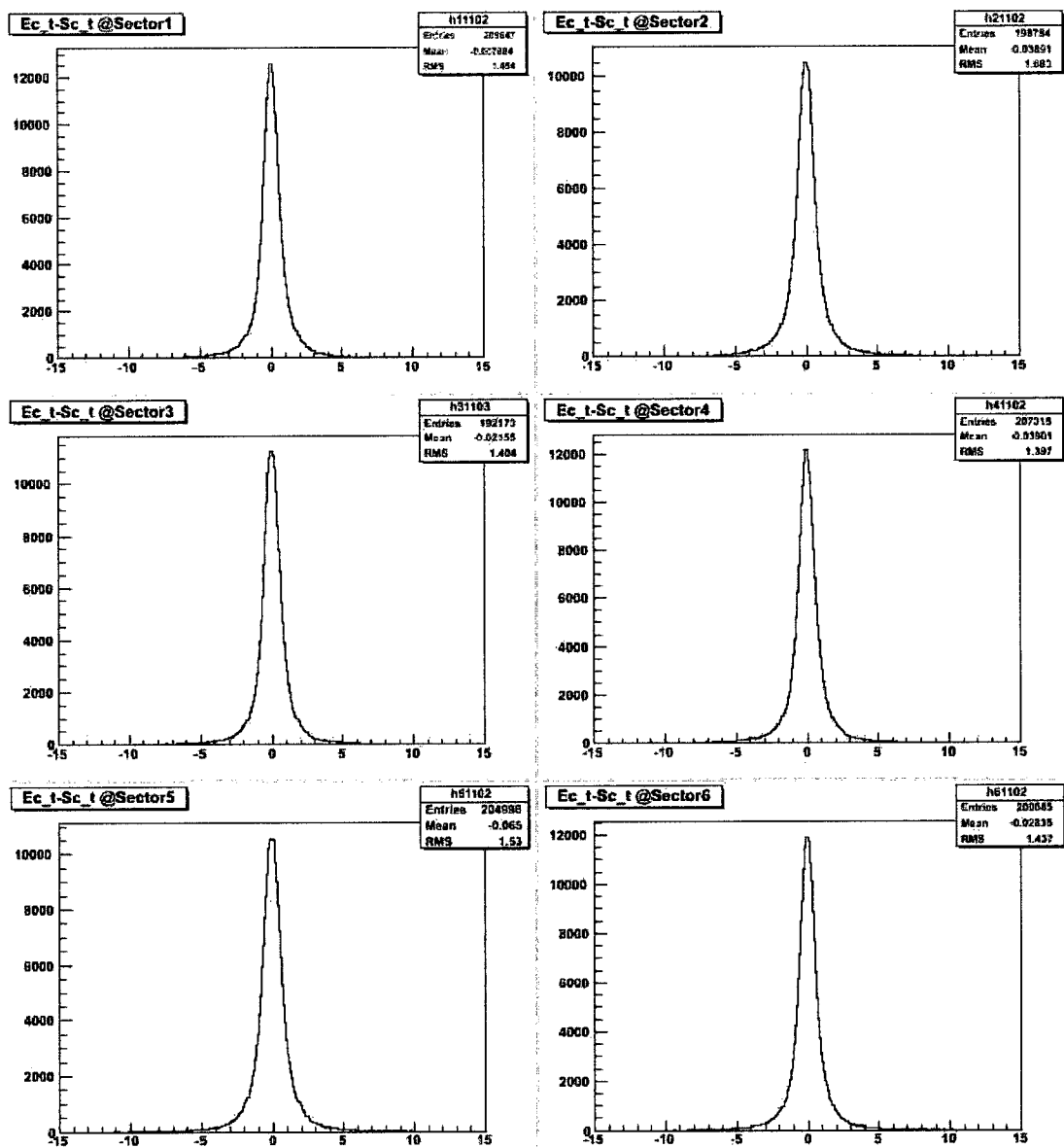


FIG. 58:  $\Delta t_{ECSC}$  after the EC time calibration.

calibration constants such that the timing information measured by CC matches that of the SC, similar to the method used for EC timing calibration. Because the CC TDC information was not used in this analysis, we did not reanalyze the experimental data to pick up the correct CC calibration information. However, other members may need to reanalyze the data if they plan to use CC TDC related measurements.

### V.2.6 RTPC Calibration

The calibration of the RTPC detector was done by N. Baillie. In Section IV.2.5 we described the drift path package that was used in the reconstruction of RTPC raw data. This drift path package includes several analytical functions. A lot of parameters are used in these functions, eight of which require calibration: the helium gas percentage in the He/DME drift gas mixture, the voltage of the cathodes in both left and right halves, the Lorentz angle offsets for both left and right halves, RTPC readout electronic time offset and the beam positions  $x_B$  and  $y_B$ . Calibration data were taken for which the RTPC high voltages were turned up high to detect the scattered electrons in the RTPC. In these data, the scattered electrons were measured in both the RTPC and the CLAS detectors. The 8 parameters were then adjusted such that the RTPC reconstruction of the scattered electrons matches that of the CLAS. For details about this calibration please refer to [57].

## V.3 QUALITY CHECKS

There may exist some runs with problems in the data we collected. In order to achieve a high quality analysis result, all such data should be removed as part of the data analysis. Therefore quality checks become very important. Based on the fact that the probability of scattering an electron from a target depends only on the target, beam energy and torus current, we use the ratio of the scattered electrons to the total incident electrons to determine the quality of a run.

Before starting, all known bad runs should be removed from the data. This could save a lot of time and energy during the checking procedure. Since we care about the fraction of scattered electrons to the total incident electrons, we need to group our data based on the following characteristics:



- beam energy;
- target type;
- the existence of the beam stopper in front of the Faraday Cup (FC);
- detector configuration, i.e. trigger thresholds and torus current.

Due to the fact that the beam tune changes each time the target is changed or refilled, we usually include only continuous runs in a group to ensure that the beam tune is remained unchanged. The beam tune should not make a huge difference unless it was really bad. In practice one can check the experiment running logs, and plot the fraction mentioned above as a function of time (or run number) and look for times when the value changes. Fig. 59 shows the ratio of the good scattered electrons to the total charge for various targets: hydrogen (black squares), deuterium (red circles) and helium (blue triangles). The ratio varies due to the beam energy,

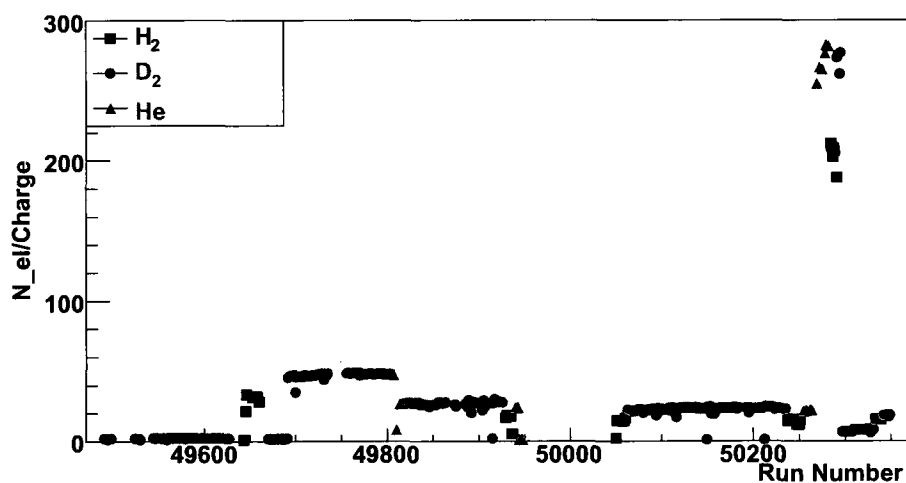


FIG. 59: Ratio of the good trigger electrons to the accumulated charge (in arbitrary units) in the FC (without stopper correction) as a function of the run number for various targets: the black square points are for hydrogen, the red circle points are for deuterium and the blue triangle points are for helium.

target, the existence of the stopper, beam tune and also the trigger configuration. Sometimes one finds some mistakes in the database by looking at these kinds of plots. Using this procedure it became clear that some runs were mislabeled in the database.

For instance, runs from 50108 to 50132 and run 50340 were marked with the wrong target in the database.

The detailed procedure for checking the quality of the data is the following. For each group (data set) mentioned above, we plot the ratio of the good trigger electrons to the accumulated charge in the FC (without stopper correction) for that run, “N\_el/Charge”, into a one dimensional histogram, and then fit it with a gaussian function for the mean and sigma values. It is important to check the fit by eye and adjust the fitted region to make sure the fit is good. If the gaussian fit doesn’t work we use the arithmetic mean and root mean square (RMS) from the histogram. Figure 60 shows an example of the 1-D histogram of “N\_el/Charge” for runs from 49692 to 49798. We would like to use a cut at about  $3\text{-}\sigma$  (or RMS) to select good

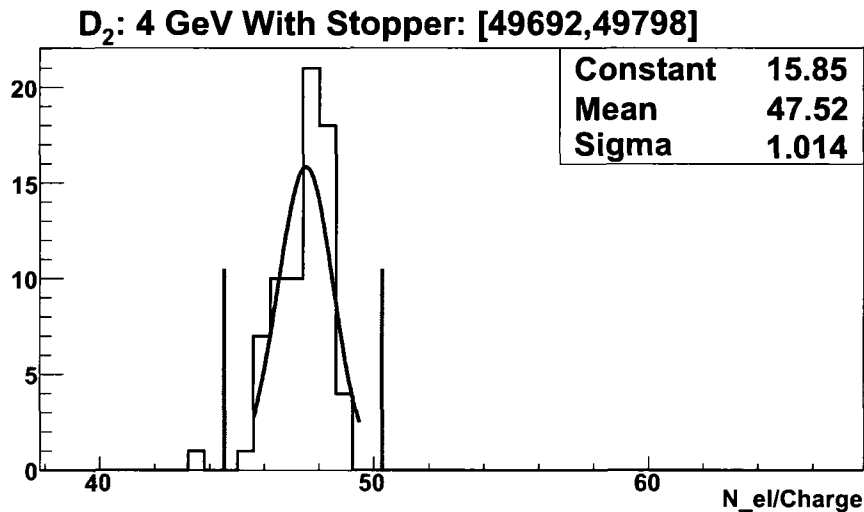


FIG. 60: Ratio of the good trigger electrons to the accumulated charge in the FC (without stopper correction) for runs from 49692 to 49798. The red lines indicate the cut selecting good runs.

data, but in most cases the final cut value was slightly different from  $3\text{-}\sigma$ . To find the best cut value, we marked those runs whose ratio was close to  $3\text{-}\sigma$  (or RMS) limit, and then we tried to understand why this ratio was not at the center of the distribution. In practice the CLAS\_ONLINE running log books were checked together with the database to search for any messages related to those runs. Based on all the available information we determined whether the run was bad or not. Finally a flag identifying good or bad runs was added to the database.

## V.4 CORRECTIONS AND CUTS

### V.4.1 Trigger Particle Identification

Readout of the CLAS detector is triggered by a coincidence between a signal in the Cherenkov counter (CC), and the electromagnetic calorimeter (EC). However, not all triggers are caused by good electrons, and we have to apply several cuts to select good electrons. In this analysis, a good trigger electron must be the first particle found in the event with negative charge. The trigger electron is likely to have more momentum than other final state particles. If there are several electrons identified by RECSIS in an event, the highest momentum one will always be chosen as the trigger electron. We also must impose several cuts on the CC and the EC detectors, as described in the next several subsections.

#### CC cuts

In CLAS, the Cherenkov counters are used to separate negative pions from electrons. The energy threshold for a pion to generate Cherenkov light is about 2.5 GeV, see Section III.3.2. The CC hardware threshold in the BoNuS experiment was set high at 75 mV, (*cf.* Table 6), which corresponds to 1.5 photoelectrons. Looking at the distribution of the number of photoelectrons ( $nphe$ ), one can see that the data has a very sharp drop below  $nphe = 1.5$  (*cf.* Fig. 61). There was no evidence that any other cut was needed. Therefore we applied a very loose cut,  $nphe > 1.5$ . Clearly for momentum above 2.5 GeV/c, the CC  $nphe$  can no longer be used to reject pions. In order to minimize the edge effects and also keep all possible electron candidates, we lower the  $nphe$  cut to 1.0 for momenta above 3.0 GeV/c (instead of 2.5 GeV/c).

If one looks at the momentum distribution for electrons and negative pions, especially for the 4 and 5 GeV data set (*cf.* Fig. 62), one can see that there are still some small fraction of pions with momenta above 3.0 GeV/c. For these electron candidates, the geometry matching quantity  $cc\_c2$  can be used to remove bad electrons. The variable  $cc\_c2$  is the quality of the geometrical matching in the Cherenkov counters and the scintillation counters, i.e. the angle between the CC hit and the nearest hit in the SC. We required a cut of  $0 < cc\_c2 < 0.8$  (*cf.* Fig. 63) to ensure good electrons.

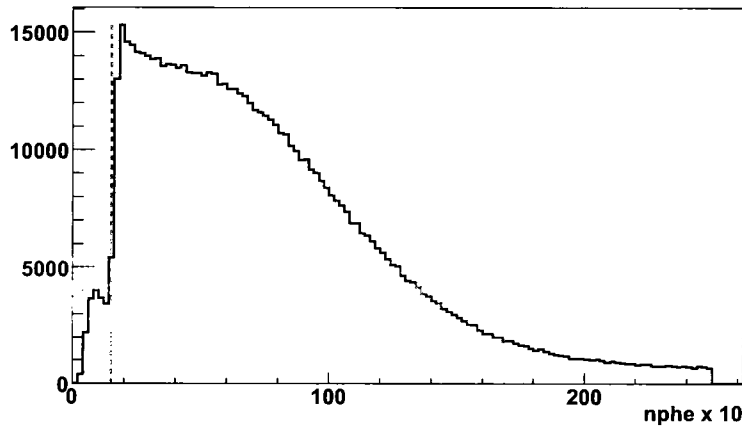


FIG. 61: Distribution of photoelectrons  $\times 10$  in the Cherenkov counter for the trigger electrons identified by RECSIS. The red vertical line indicates the cut for electron candidates with momentum below 3.0 GeV/c

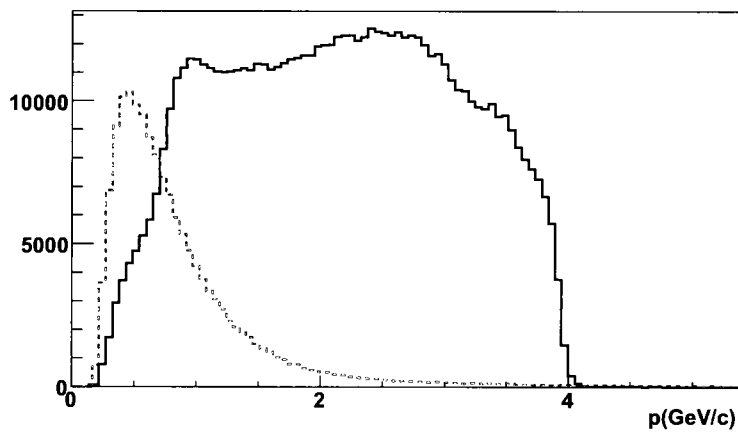


FIG. 62: Momentum distribution for trigger electrons (black) and negative pions (red, with peak value around 0.5 GeV/c) identified by RECSIS.

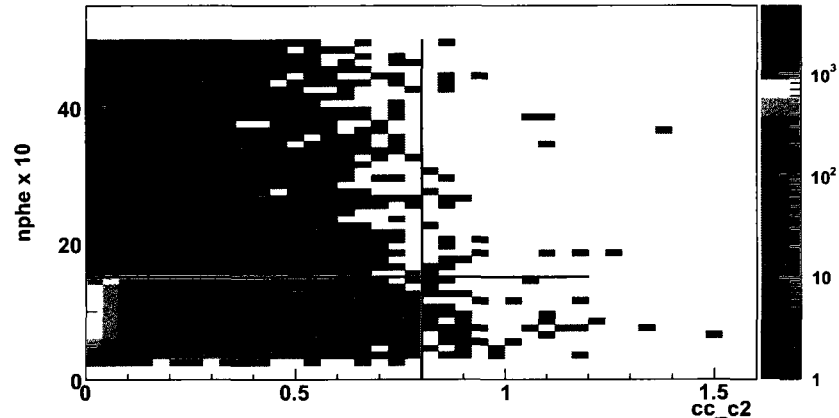


FIG. 63: Number of photoelectrons  $\times 10$  as a function of  $cc\_c2$  for trigger electrons identified by RECSIS. The black lines indicate the cuts.

### EC cuts

In addition to the CC  $nphe$  cut and geometry matching cut, cuts based on EC information can also be used to improve the separation between electrons and negative pions. It is well known that an electron creates a shower when traveling in the EC, whereas a pion just loses energy by ionization. Typically a pion will deposit around 2 MeV per centimeter when it passes through the scintillator, so the total energy deposited in the detector should be independent of momentum. When an electron creates a shower in the EC it usually deposits all of its energy, so the energy deposited will be proportional to its momentum. In Fig. 64, the left panel shows the energy deposited in the EC inner layers for all negative particles as a function of the momentum; the right panel shows the ratio of the energy deposited in all the EC layers to the particle momentum for all negative particles as a function of the momentum. The contribution from minimum ionizing particles, *i.e.* pions, is located in the lower band of the left plot and in the lower left corner of the right plot. To eliminate the pion contribution, we required

$$E_{in} > 0.06$$

and

$$0.15 + 0.016p < E_{tot}/p < 0.34.$$

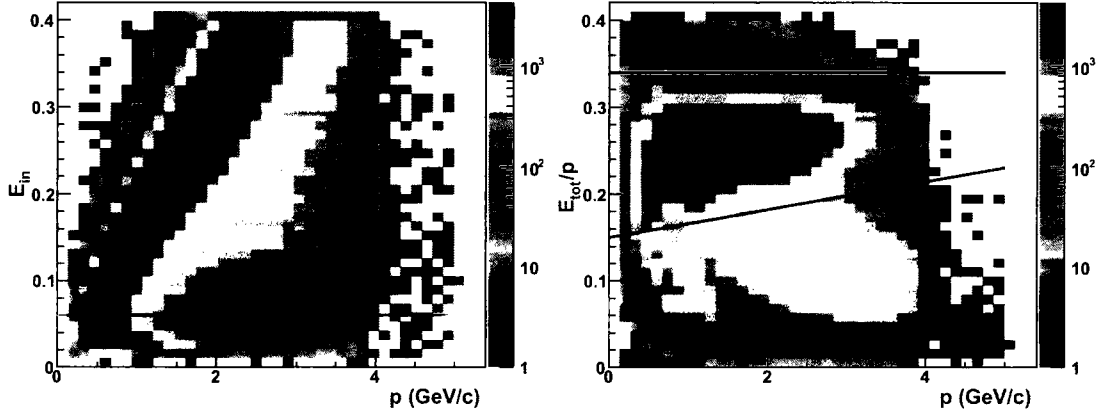


FIG. 64: The energy deposited in the EC inner layer (left) and the ratio of the energy deposited in all layers of the EC to the momentum (right) as a function of the momentum for all electrons identified by RECSIS under the CC cuts. The lines indicate the cuts that were applied to select good electrons.

We also apply a cut on the energy of the trigger electrons [44] due to the fact that we used very high EC hardware thresholds in the BoNuS experiment (*cf.* Table 6). We used three different  $EC_{\text{total}}$  thresholds, 150, 200 and 260 mV, during data collection. The electron energy cuts corresponding to these thresholds are 575, 700 and 875 MeV/c, respectively.

In summary, the electron identification includes the following requirements:

- First particle in an event;
- Negative charge;
- CC  $nphe$  cut:  $nphe > 1.5$  for  $P < 3.0$  or  $nphe > 1.0$  for  $P \geq 3.0$ ;
- CC geometry matching cut:  $0 < cc\_c2 < 0.8$  ;
- EC inner energy cut:  $E_{\text{in}} > 0.06$  ;
- EC total energy cut:  $0.15 + 0.016p < E_{\text{tot}}/p < 0.34$  ;
- Energy cut due to the EC threshold: 575, 700 and 875 MeV/c corresponding to the EC thresholds of 150, 200 and 260 mV, respectively.

### V.4.2 Electron Identification for Exclusive Analysis

The electron identification described above can select “golden” electrons. As a result it also removes some electrons which might not be bad. The EC total energy cut especially removes about 26.6% of electron candidates after the CC cuts and EC inner energy cuts have been applied (*cf.* Fig. 65).

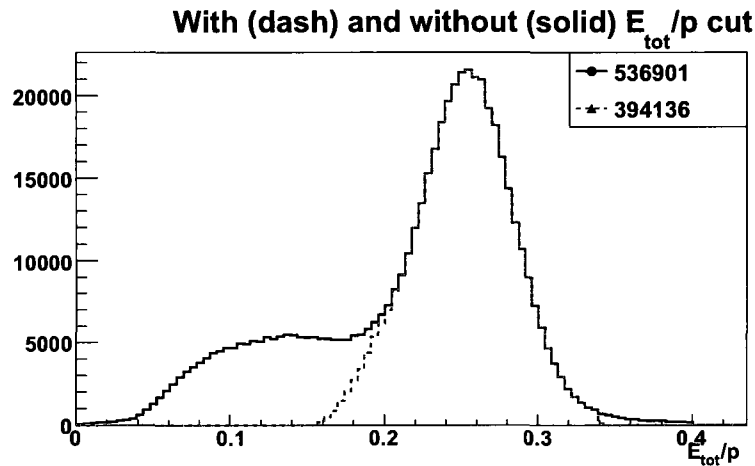


FIG. 65:  $E_{tot}/p$  distribution for the trigger electrons identified by RECSIS. The red dash curve is with EC and CC cuts and the black solid curve is under the same cuts except without the  $E_{tot}/p$  cut. The entries of both distributions are also shown in the up-right corner. The red dash curve is just 73.4% of the black.

In my analysis, the statistics are so limited that we do not want to lose any possible good exclusive events. In order to select the exclusive  $\pi^-$  reaction, a missing mass cut (described in Section V.4.8) will be applied. It is very unlikely for an event to satisfy the missing mass cut if one of the final state particles has been misidentified. Therefore it does not matter if the EC total energy cut is included or not for this exclusive analysis. A close study of this showed that by removing the EC total energy cut from electron identification, about 5% of  $D(e, e'\pi^-p)p$  events were gained. Fig. 66 shows the missing mass distribution for the 5 GeV  $D(e, e'\pi^-p_{CLAS})X$  events in which the electron candidates pass (top left and top right) and do not pass (bottom left and bottom right) the EC total energy cut. The plots on the right show only events under the exclusive peaks. By comparing the shapes between top left and bottom left one can see that the EC total energy cut can be released in this exclusive analysis because the missing mass still has a dominant peak at the mass of a proton. By

comparing the exclusive events in top right and bottom right one can see that about 5% of the events were regained by removing the EC total energy cut.

Note that the EC total energy cut can be removed only for the exclusive analysis. In order to gain statistics, we finally decided not to use the EC total energy cut in this analysis. To avoid confusion, I refer to the electron identification with the EC total energy cut as the STANDARD electron identification, which was used for inclusive analysis. If not specifically indicated, the electron identification for the remaining of this text refer to the exclusive electron identification.

### V.4.3 Fiducial Cut for Electrons

In order to measure the cross section precisely we must know the efficiency of all the subsystems of the CLAS detector. The Cherenkov counter in particular has regions of inefficiency and events in those regions must be removed. The fiducial cut is developed especially for this purpose. Details about the procedure to find the fiducial cut can be found in [74] and [75]. To obtain the fiducial cut, we have run through the following steps.

For each sector, we binned the momentum into 12 bins starting from 200 MeV/c and with a bin width of 300 MeV/c. Then we selected good electrons using the standard electron identification to fill the “ $\phi_{\text{dc1}}^s$  vs.  $\theta_{\text{dc1}}$ ” histogram for each momentum bin. Both  $\phi_{\text{dc1}}^s$  and  $\theta_{\text{dc1}}$  were measured at DC Region 1 and  $\phi_{\text{dc1}}^s$  was converted into the sector coordinates ( $-30^\circ \leq \phi_s < 30^\circ$ ), by

$$\phi_{\text{dc1}}^s = (\phi_{\text{dc1}}) - 60 \times (\text{sector} - 1) ,$$

where *sector* was the DC sector number for this particle from 1 through 6. An example of these histograms is shown in Fig. 67. For each histogram, we fitted a trapezoid to the distribution of  $\phi_{\text{dc1}}^s$  in each  $\theta_{\text{dc1}}$  bin to determine the boundary values of the fiducial region. Figure 68 shows an example of this trapezoid fitting. Then we parameterized the boundary values on the positive side with the function

$$\phi_{\text{dc1}}^s(\theta_{\text{dc1}}) = a[1.0 - (1.0 + \lambda(\theta_{\text{dc1}} - c)^b)^{-1}] , \quad (43)$$

where *a*, *b*, and *c* are parameters to be fit and  $\lambda$  is a constant that was introduced to make this function useful for all particles, such as pions and protons. For electrons,  $\lambda$  is empirically optimized to 0.35. The same procedure was repeated to the negative



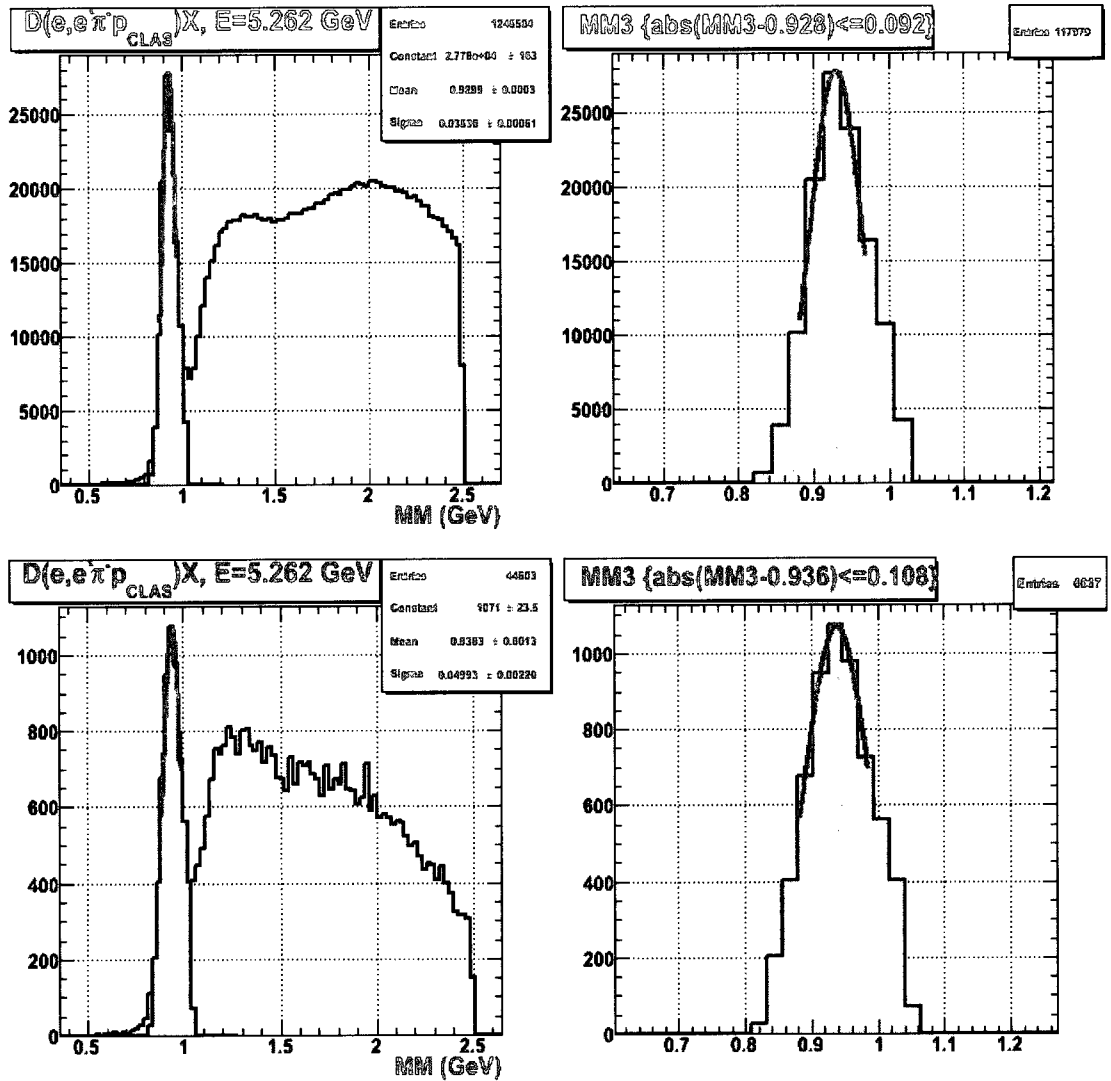


FIG. 66: Missing mass distribution for the 5 GeV  $D(e, e' \pi^- p_{\text{CLAS}})X$  events for which the electron candidates pass (top left and top right) and do not pass (bottom left and bottom right) the EC total energy cut. The plots on the right show only events under the exclusive peaks.

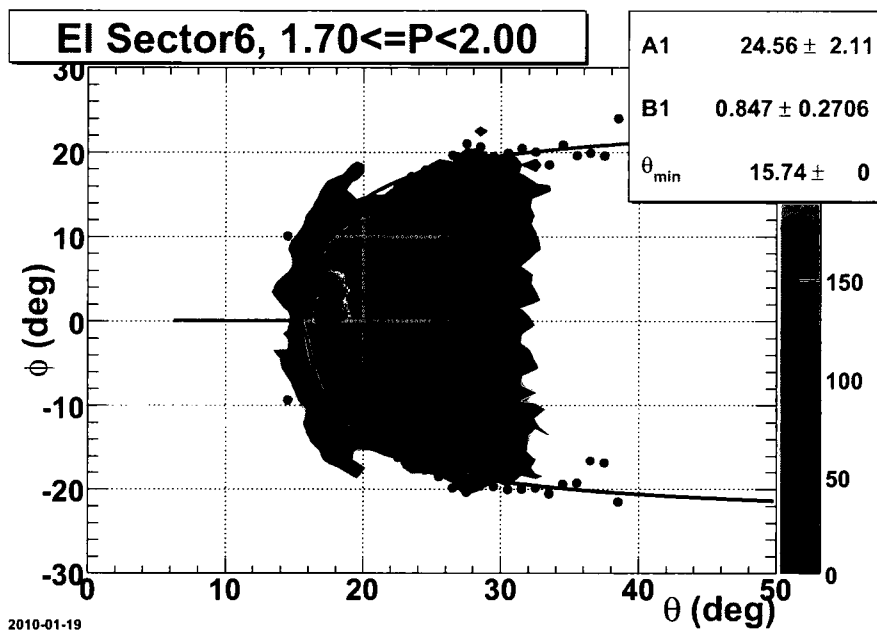


FIG. 67:  $\phi_{\text{dc1}}^s$  vs.  $\theta_{\text{dc1}}$  for electrons with momenta  $1.7 \leq p < 2.0$  GeV/c in sector 6. The red and black curves makes the boundary for the fiducial region.

boundary values of  $\phi_{\text{dc1}}^s$  as well. The red and black curves in Fig. 67 indicate the fiducial boundary for that particular histogram. The complete fitting results for electrons in sector 6 are shown in Figs. 69 and 70. In the end, a fiducial cut look up table is created with the values  $a$ ,  $b$  and  $c$  for each sector and each momentum bin. Since the momentum was binned only up to 3.8 GeV/c, electrons with momenta above 3.8 GeV/c would be treated as if the momenta at 3.8 GeV/c.

#### V.4.4 Fiducial Cut for Hadrons

The fiducial cut for electrons is used to remove the low efficiency regions of the CC, whereas the fiducial cuts for hadrons are used to define good regions of the DC. By repeating the same procedure described above, with  $\lambda = 1.0$  for  $\pi^-$  and  $\lambda = 3.0$  for protons, similar fiducial cut look up tables were created for  $\pi^-$  and protons. Figures 71 and 72 show the fiducial boundary for  $\pi^-$  detected in sector 6 in momenta range below and above 2.0 GeV/c, respectively. Figures 73 and 74 show the same,

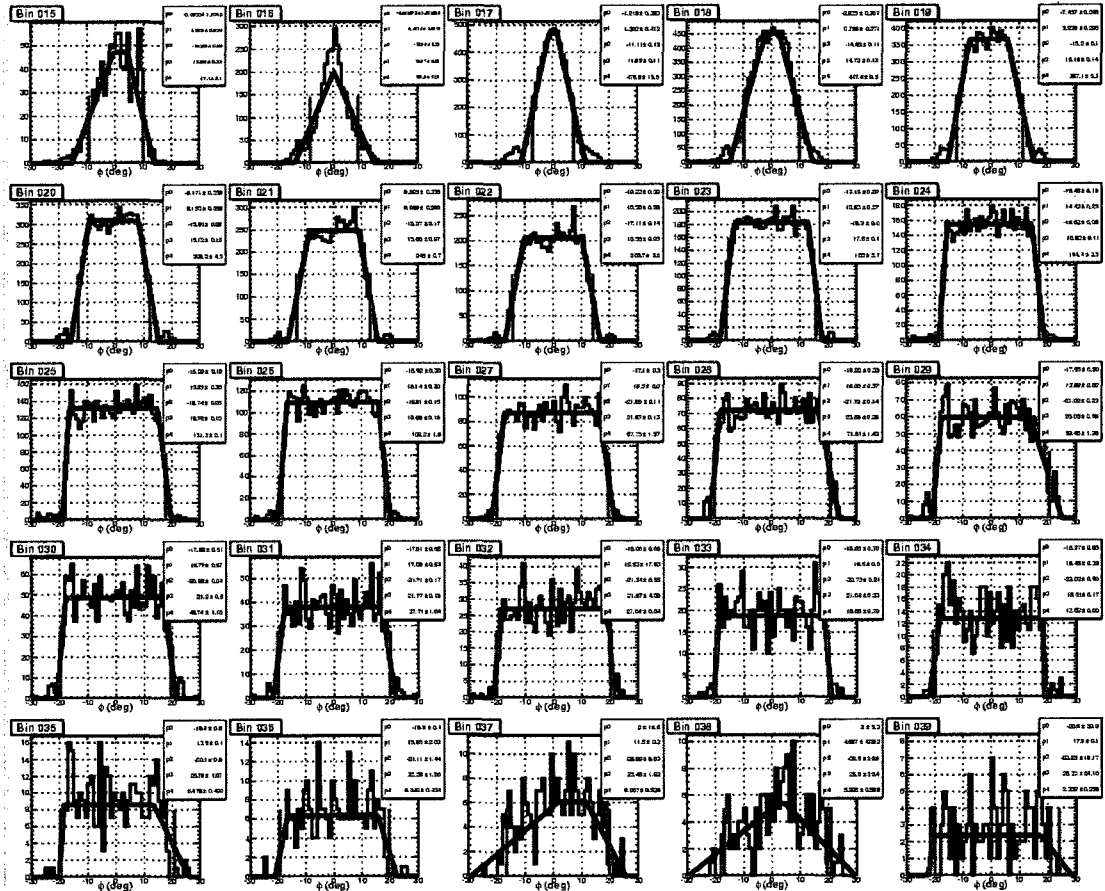


FIG. 68: Trapezoidal fit to  $\phi_{\text{dc1}}^s$  distribution for electrons in narrow  $\theta_{\text{dc1}}$  bin in the histogram shown in Fig. 67. The red vertical lines indicate the fiducial boundary values.

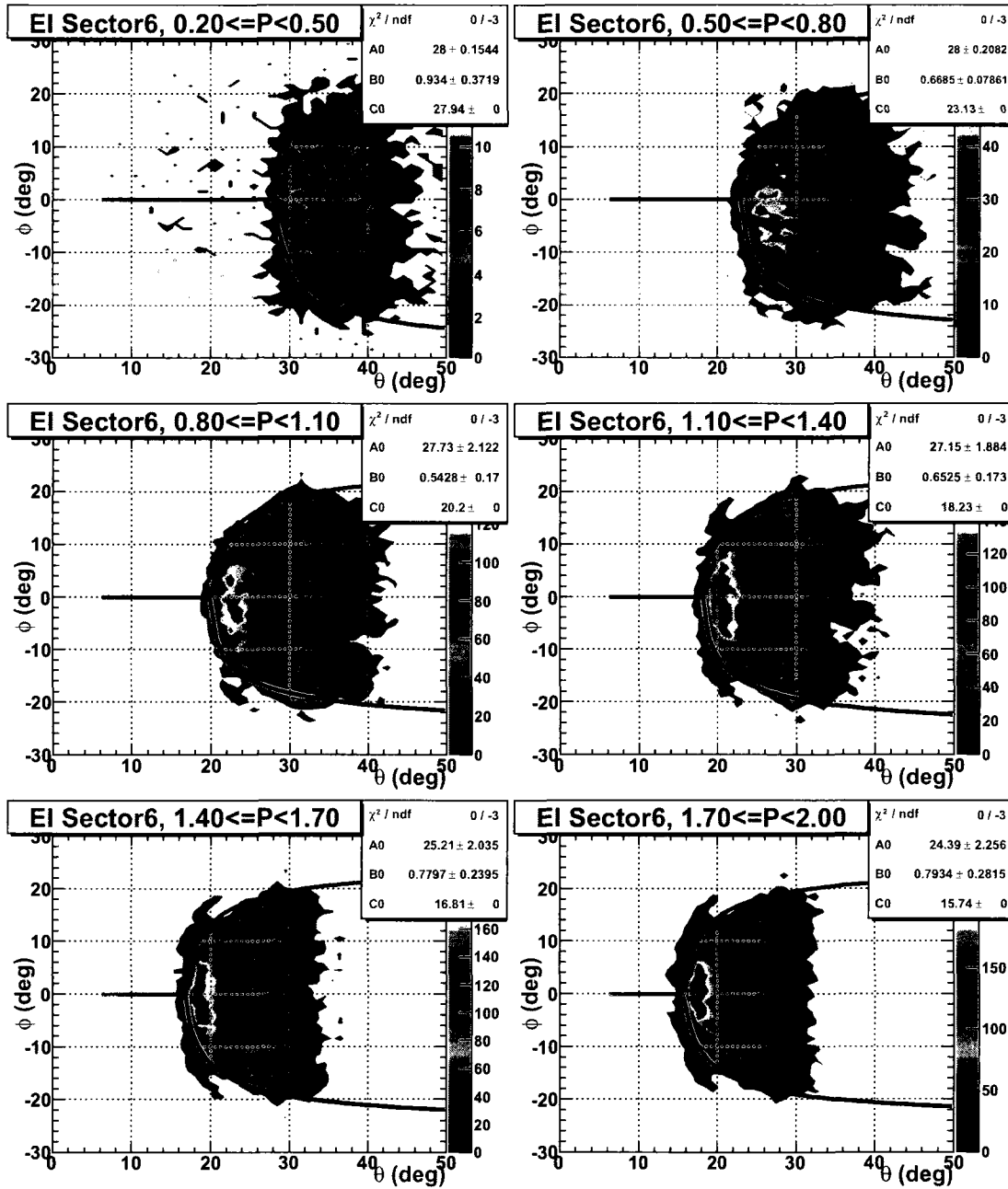


FIG. 69:  $\phi_{\text{dcl}}^s$  vs.  $\theta_{\text{dcl}}$  for electrons with momenta  $p \leq 2.0$  GeV/c in sector 6. The curves are the fiducial boundary.

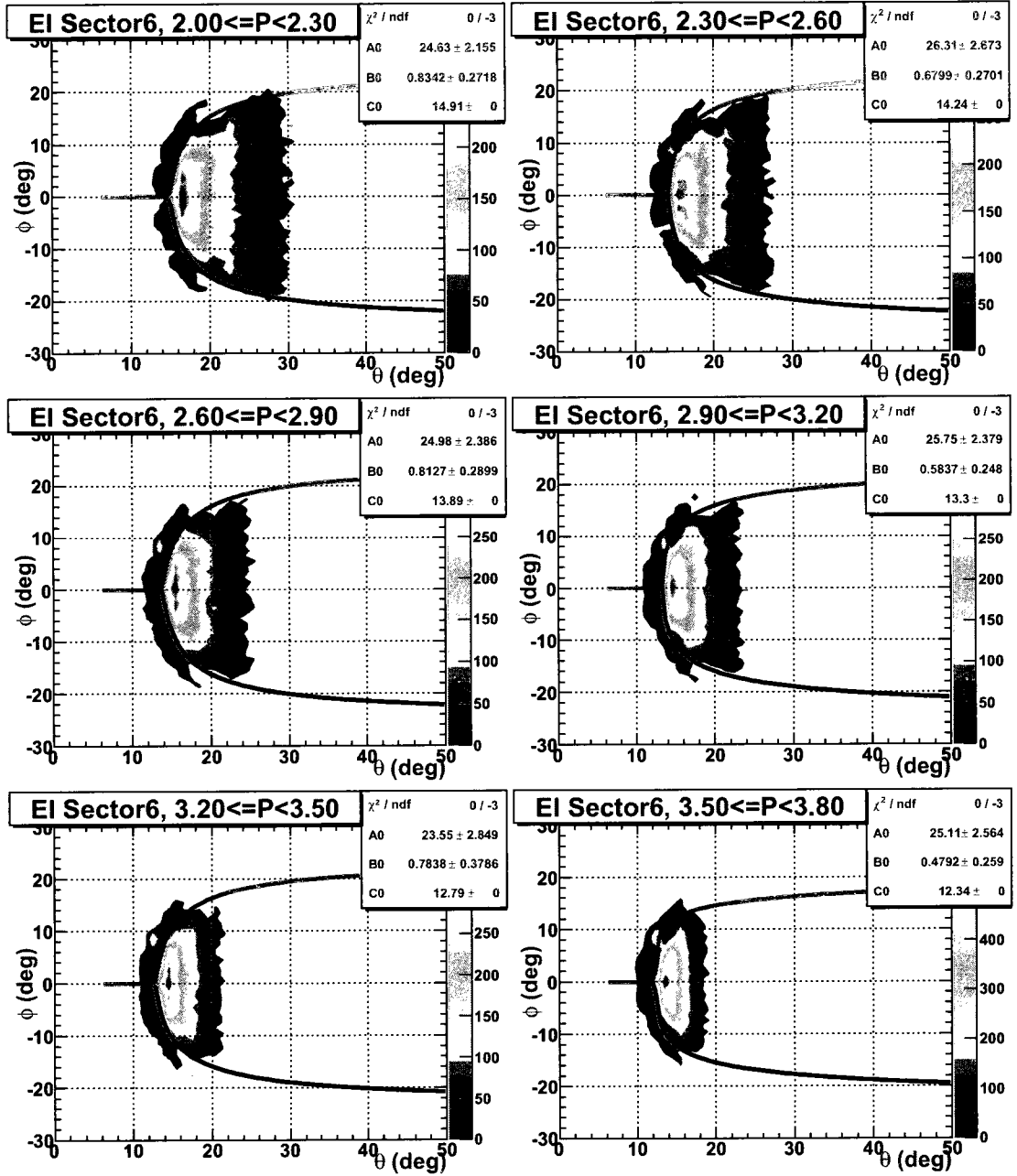


FIG. 70:  $\phi_{dc1}^s$  vs.  $\theta_{dc1}$  for electrons with momenta  $p > 2.0$  GeV/c in sector 6. The curves indicate the fiducial boundary.

except for protons.

#### V.4.5 Solenoid geometry $\theta$ - $z$ cut

In the BoNuS experiment, The RTPC detector was placed in the center of a solenoid, which providing the magnetic field for the RTPC. A side view of the geometry of this solenoid is shown in Fig 75. In order to remove particles hitting the solenoid, we applied the  $\theta$ - $z$  correlation cut to all particles seen by CLAS.

#### V.4.6 Beam Line and Vertex Correction

It is necessary to apply cuts on the interaction vertex in order to avoid events from reactions in the walls or the inefficient part of the target. Although the designed length of the RTPC detector is 20.0 cm, the useful part of the target length is only about 16.0 cm, because of an aluminum cover surrounding the entrance part of the RTPC for 4.0 cm, as shown clearly in Fig. 76. The vertex distribution of the trigger electrons is shown in Fig. 77. There are two peaks which come from the aluminum entrance window and the aluminum end cap. The segment from  $-64.0$  to  $-48.0$  cm is the valid length used in our analysis.

During the reconstruction, RECSIS extrapolates the track to the  $z$  axis, assuming that the beam goes along the  $z$  axis. However, the beam might have a small offset from the  $z$  axis and/or have a very small polar angle with respect to the  $z$  axis. The effect of this offset can be seen in Fig. 78 (top) where the  $\phi$  dependence of the reconstructed vertex is shown. The  $z$  position of the down stream cap of the target straw, which is located 14.5 cm downstream from the target center (see Section III.3.6), appears shifted depending on the sector, which can not be true.

The deuterium target of BoNuS is relatively long compared to other CLAS experiments. Therefore we need to determine not only the distance of the beam from the  $z$  axis, but also the direction of the beam. To define a straight line in space, we define a point  $O(x_0, y_0, z_0 = -59.0 \text{ cm})$  which this line goes through. Then the three dimensional line function is given as

$$\begin{aligned} x &= x_0 + K_{xz}(z - z_0); \\ y &= y_0 + K_{yz}(z - z_0), \end{aligned}$$

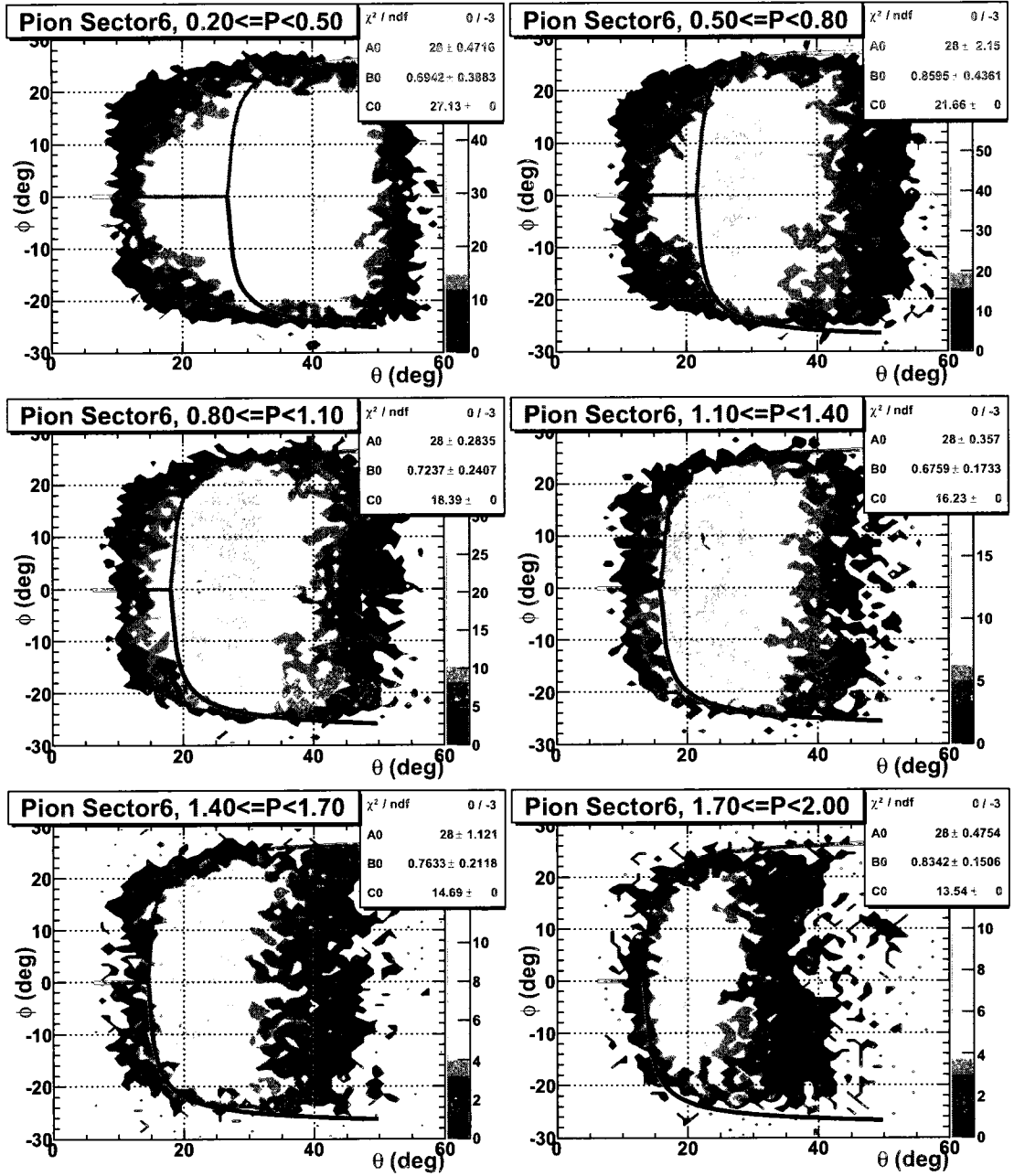


FIG. 71:  $\phi_{\text{dcl}}^s$  vs.  $\theta_{\text{dcl}}$  for  $\pi^-$  with momenta  $p \leq 2.0$  GeV/c in sector 6. The curves indicate the fiducial boundary.

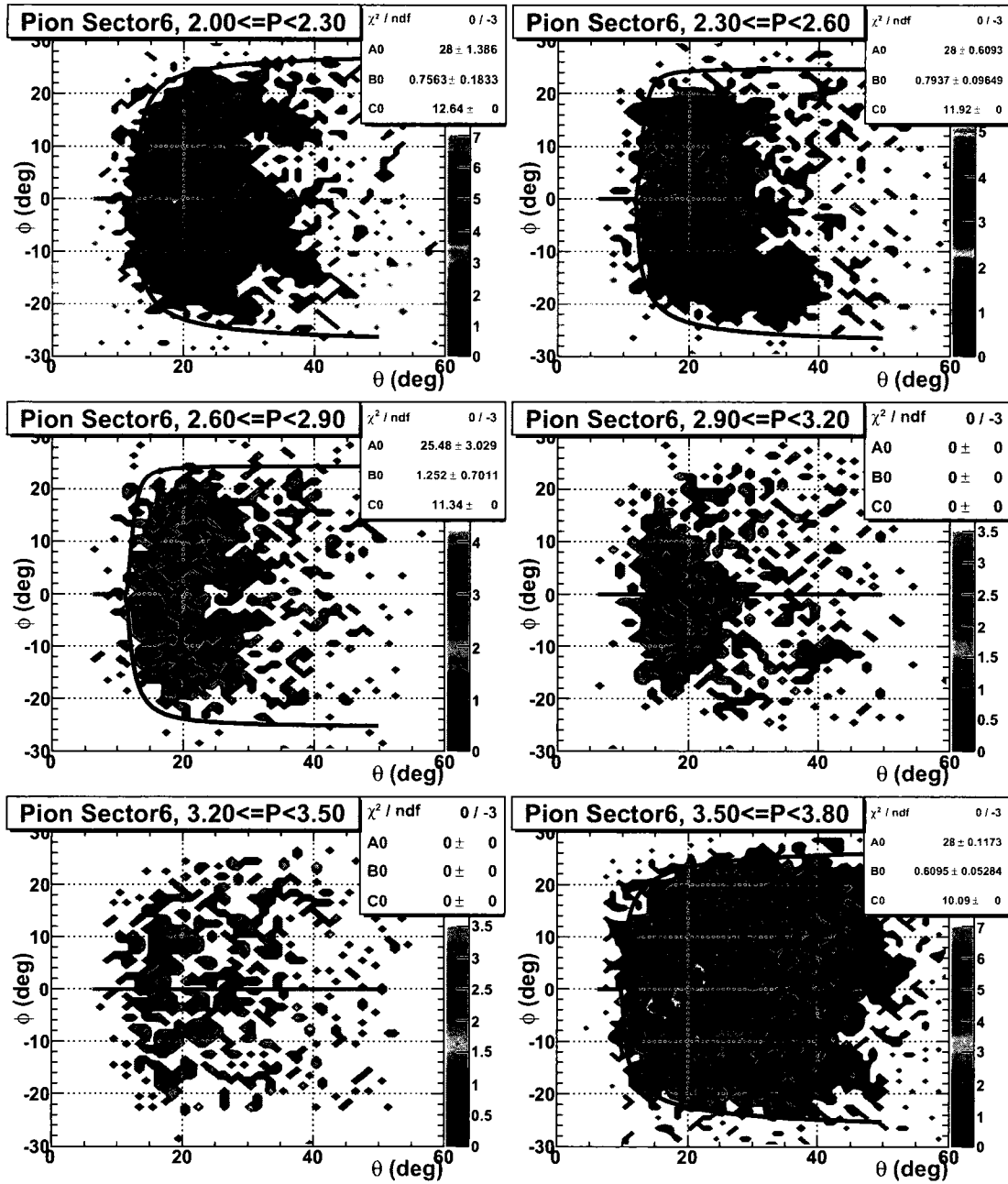


FIG. 72:  $\phi_{\text{dc1}}^s$  vs.  $\theta_{\text{dc1}}$  for  $\pi^-$  with momenta  $p > 2.0$  GeV/c in sector 6. The curves indicate the fiducial boundary.



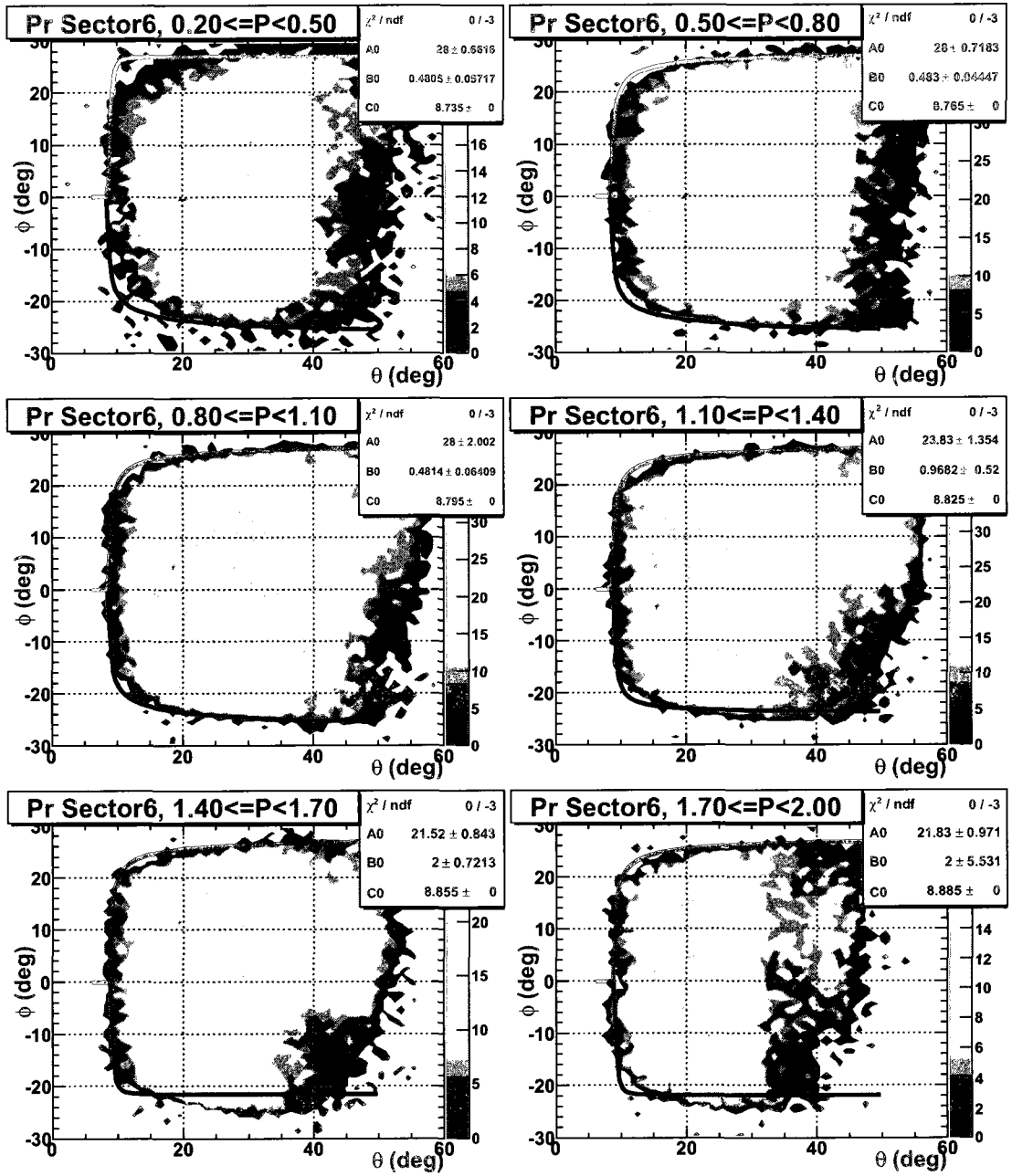


FIG. 73:  $\phi_{dc1}^s$  vs.  $\theta_{dc1}$  for protons with momenta  $p \leq 2.0$  GeV/c in sector 6. The curves indicate the fiducial boundary.

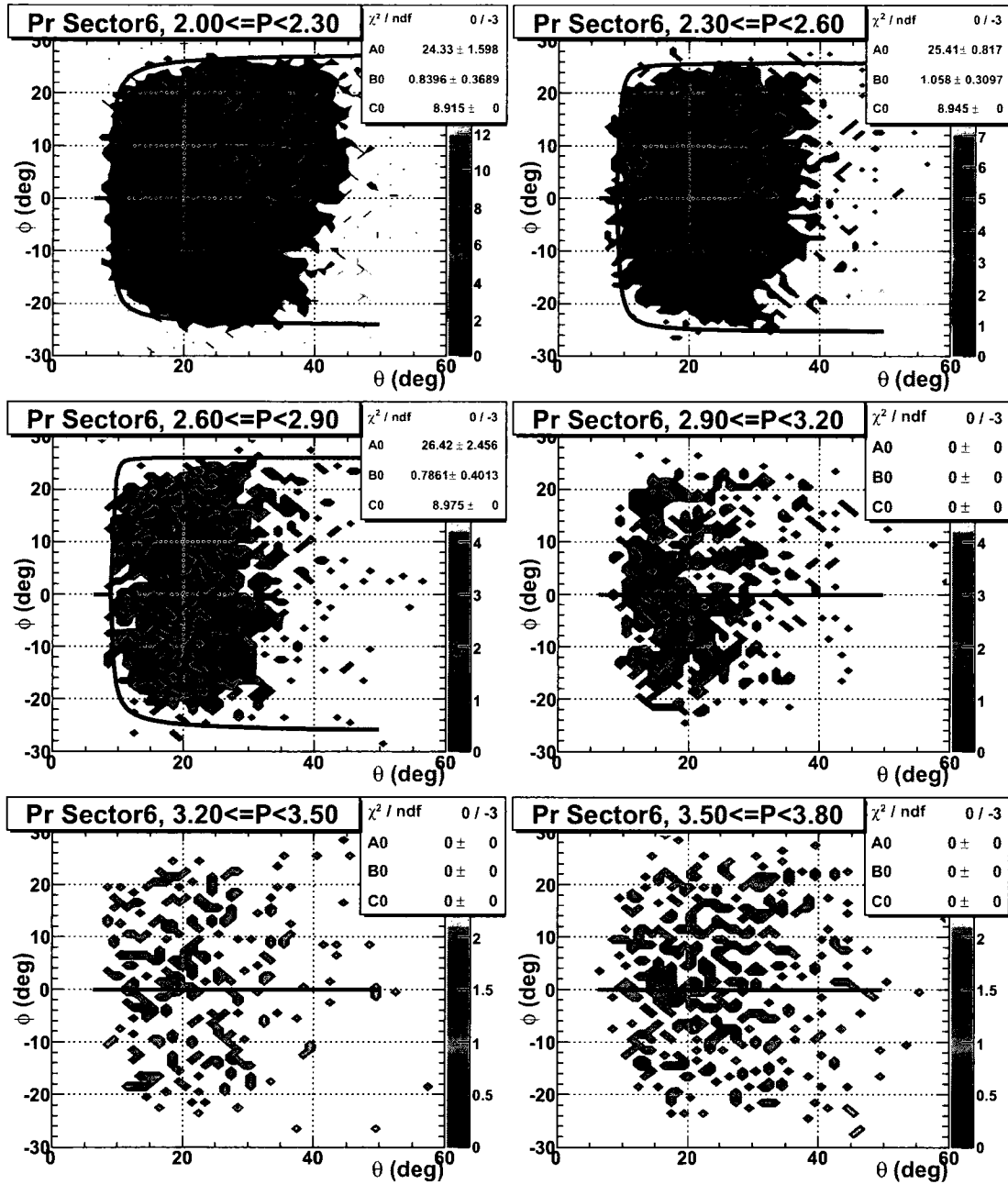


FIG. 74:  $\phi_{\text{dcl}}^s$  vs.  $\theta_{\text{dcl}}$  for protons with momenta  $p > 2.0$  GeV/c in sector 6. The curves indicate the fiducial boundary.

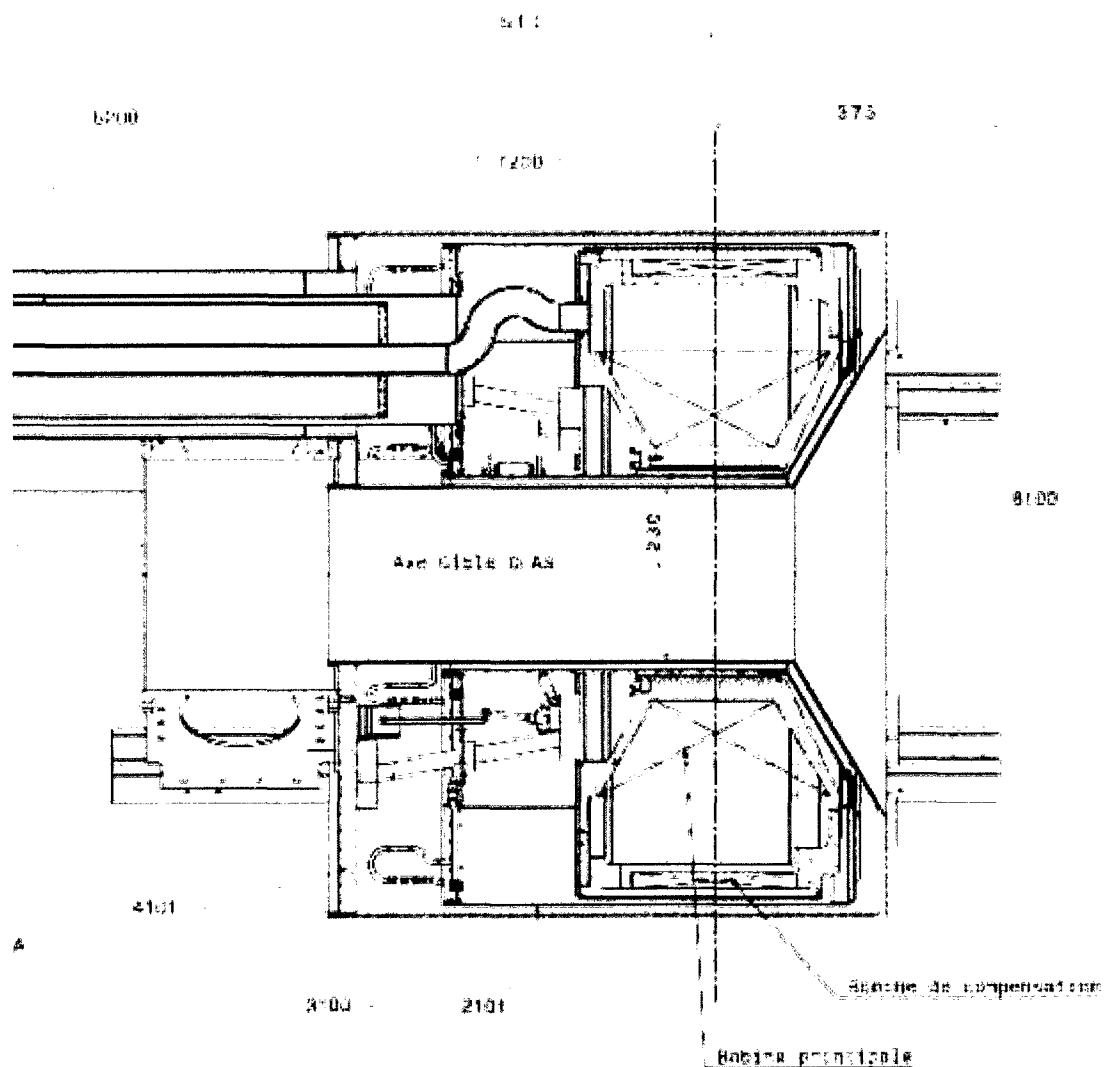


FIG. 75: Side view of the solenoid used in the BoNuS experiment. This solenoid can provide up to 4 T magnetic field. The light green color area indicates the RTPC position. Some particles may hit this solenoid before they are detected by CLAS. A vertex  $z$  dependent  $\theta$  cut was applied in order to eliminate particles hitting this solenoid.

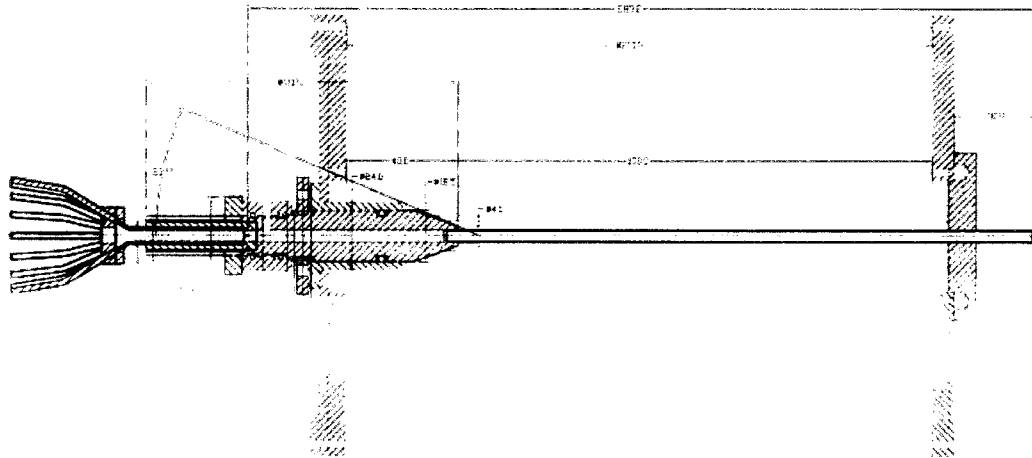


FIG. 76: RTPC target system. There is an aluminum cover surrounding the first 4 cm of the entrance part, which distorts particles originating from this region.

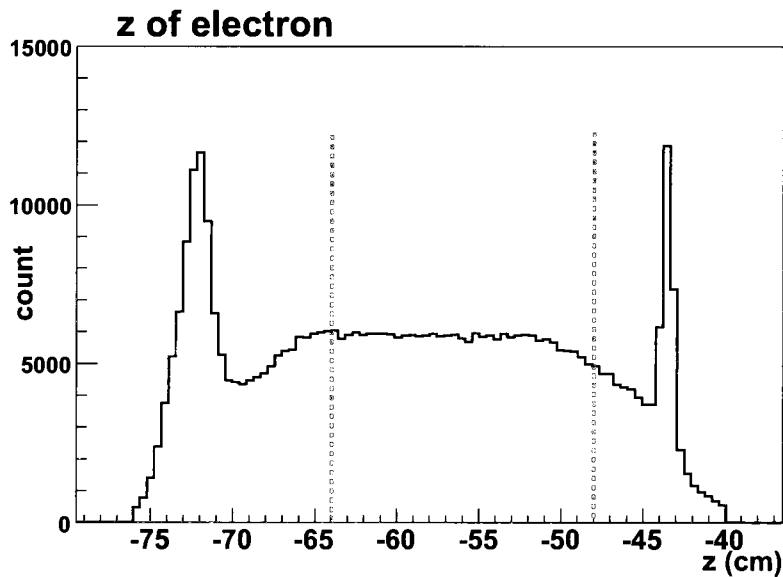


FIG. 77: Vertex  $z$  distribution for electrons. There are two peaks which come from the aluminum entrance window and the aluminum end cap. The blue dash lines located at  $-64.0$  cm and  $-48.0$  cm indicate the cut position.

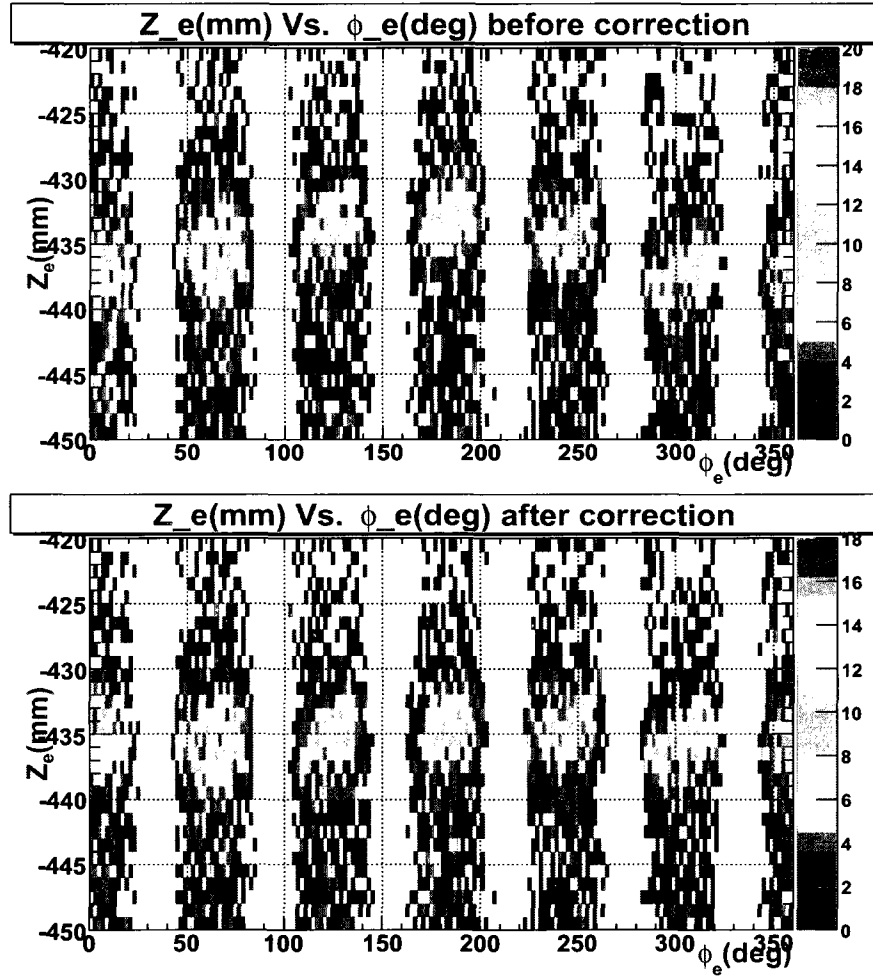


FIG. 78: Vertex  $z$  distribution for the end cap before (top) and after (bottom) the beam line correction as a function of  $\phi$ . The vertex range shown here is for the aluminum end cap which is located at  $z \approx 435$  mm.

where  $K_{xz}$  and  $K_{yz}$  are the slopes of the line's projections onto the X-Z and Y-Z planes, respectively, and  $x_0$  and  $y_0$  are the beam positions corresponding to  $z = 59.0$  cm. With these four parameters, the beam offset  $(x, y)$  corresponding to any arbitrary  $z$  can be easily determined.

The reconstructed vertex  $z_{\text{rec}}$  in RECSIS for each track is determined under the wrong assumption that the beam goes along the  $z$  axis. To correct this effect, we chose events with multiple particles in the final state and fitted them to determined the best  $z$  position ( $z_{\text{cor}}$ ) which minimizes  $\chi^2$ :

$$\chi^2 = \sum_1^N (z_{\text{cor}} - z_{\text{rec}})^2, \quad (44)$$

where  $z_{\text{cor}}$  is the fit parameter (corrected vertex  $z$ ). To do this we defined:

$$x_{\text{cor}} = x_0 + K_{xz}(z_{\text{rec}} - z_0); \quad (45)$$

$$y_{\text{cor}} = y_0 + K_{yz}(z_{\text{rec}} - z_0); \quad (46)$$

$$x' = \frac{x_{\text{cor}} \cos \phi_s + y_{\text{cor}} \sin \phi_s}{\cos(\phi - \phi_s)}; \quad (47)$$

$$z_{\text{cor}} = z_{\text{rec}} + x' / \tan \theta, \quad (48)$$

where  $x'$  is a measure of the distance along the track length which was not taken into account in the tracking,  $\phi$  is the azimuthal angle and  $\theta$  is the polar angle of the particle, and  $\phi_s$  is the central azimuthal angle of the sector which the track fired, given in degrees by  $\phi_s = (S - 1) \times 60.0$ , where  $S$  is the sector number, from 1 to 6. Minimizing  $\chi^2$  determines these four parameters:  $x_0$ ,  $y_0$ ,  $K_{xz}$  and  $K_{yz}$ . This procedure was repeated for each run to generate a vertex correction table. An example of the result of this beam line and vertex correction is shown in Fig. 78 (bottom). The  $z$  position of the end cap is aligned to about  $-435$  mm in all 6 sectors.

#### V.4.7 Energy Loss corrections

When a charged particle travels through matter, it interacts electromagnetically with the electrons of atoms in the material and loses energy as a result of this interaction. The energy losses are more significant for lower momentum and heavier particles. The Bethe-Bloch formula describes the energy loss per unit distance traveled

very well for heavy particles like kaons, protons, alpha particles and atoms, but not for electrons [78]. For electrons, the energy loss is slightly different than the hadrons because of the fact that the electrons lose their energy mostly by Bremsstrahlung. In order to get a reliable analysis result, we had to make an energy loss correction for the particles detected in the event. One way to study energy loss of each detected particle is by using simulations. Many particles were generated and run through the detector simulation train (BONUS+GSIM+RECSIS, see Chapter IV). Using the simulation, we compared the particle's original energy and the reconstructed energy and studied its dependence on the reconstructed momentum,  $\theta$ ,  $\phi$  and vertex  $z$ . Finally, the kinematic dependence of the correction was parameterized for electrons, positive and negative pions, positive and negative kaons, and protons.

Obtaining a correction table for each particle requires a few steps. The following is a detailed procedure for developing the energy loss correction for protons. First of all, protons with a flat distribution of vertex  $z$  (cm)  $\in [-64, 48.0)$ , flat  $\phi$  (degree)  $\in [0, 360.0)$ , flat  $\theta$  (degree)  $\in [10, 80.0)$  and flat momentum (GeV/c)  $\in [0.2, 6.0)$  were generated and run through the simulation train (BONUS+GSIM+RECSIS) to get reconstructed momenta. Bad events needed to be removed from the reconstructed output. The following criteria were used to define bad events:

- Events that cannot pass the solenoid geometry cut (the  $\theta - z$  correlation cut, see Section V.4.5);
- Events with a difference between true and reconstructed momenta larger than 0.08 GeV/c:  $|p_{true} - p| > 0.08$  ;
- Events with a difference between true and reconstructed  $\theta$  angles larger than 5.0 degrees:  $|\theta_{true} - \theta| > 5.0$  ;
- Events with a difference between true and reconstructed vertex  $z$  larger than 3.2 cm:  $|z_{true} - z| > 3.2$  ;
- For electrons only, the reconstructed electrons cannot pass the CC fiducial cut.

All the good particles (using the reconstructed variables) then were binned as follows:

- momentum: 27 bins, covering from 0.2 to 6.0 GeV/c, with variable bin width to ensure that each bin has reasonable statistics;
- $\theta$ : 21 bins, 3 degrees each, from 8.0 to 75.0 degrees;

- vertex  $z$ : 8 bins, 2 cm each, from  $-64.0$  to  $-48.0$  cm;
- $\phi$ : currently only 1 bin, from 0 to 360.0 degrees.

For each four dimensional bin of  $p$ ,  $\theta$ ,  $\phi$  and  $z$ , we fitted a gaussian function to the difference between the true and the reconstructed momentum,  $\delta p = p_{true} - p$ , to find the peak value. This value is the most likely amount of momentum loss for protons in that four dimensional bin. Repeat the same fitting for each bin to find out all peak values to create a look up table, which contains the enregy losses for every bin. Because using this look up table was CPU inefficiency due to the fact that variable bin width in momentum was used, we parameterized the momentum dependence of the energy loss. For each three dimensional bin of  $\theta$ ,  $\phi$  and  $z$ , we plotted peak values as a function of momentum and fit it with a kinematic correction function:

$$\begin{aligned}
 p_i &= \sqrt{E_i^2 - m^2}; \\
 E_i &= m + K_i; \\
 K_i &= (K_f^b + am^{b-1})^{1/b} + c + d \ln \gamma; \\
 K_f &= E_f - m = \sqrt{p_f^2 + m^2} - m; \\
 \gamma &= \frac{1}{\sqrt{1 - \beta^2}} = \frac{\sqrt{m^2 + p_f^2}}{m}; \\
 \delta p &\equiv p_i - p_f = f(a, b, c, d, m, p_f),
 \end{aligned} \tag{49}$$

where  $p_f$  is the final (reconstructed) momentum,  $K_f$  is the final (reconstructed) kinematic energy,  $E_f$  is the final (reconstructed) total energy,  $p_i$  is the initial momentum,  $K_i$  is the initial kinematic energy,  $E_i$  is the initial total energy and  $m$  is the mass of the particle. This function is an approximation of the integrated Bethe-Bloch function and returns four parameters:  $a$ ,  $b$ ,  $c$ , and  $d$  (mass  $m$  is a constant). Sometimes there are some special cases need to be dealt with. For instance, some of the above three dimensional bin do not have enough momentum values (less than 4) to fit Eq. (49), which is a four-parameter-function. For this situation, we set parameter  $a = 0$ ,  $b = 1$  and  $d = 0$  to make the fitting function a constant. In this way, a table for  $a$ ,  $b$ ,  $c$ , and  $d$  for each three dimensional bin was generated.

Repeating the same procedure for  $\pi^-$ ,  $\pi^+$  and kaons, one can obtain similar energy loss correction tables. Since the energy loss behavior for electrons is different from other particles, we changed the fit function by setting  $a = 0$  and  $b = 1$ , which reduces



the fitting function to  $K_i = c + d \ln \gamma$ , and matches the physics of electrons' energy loss very well.

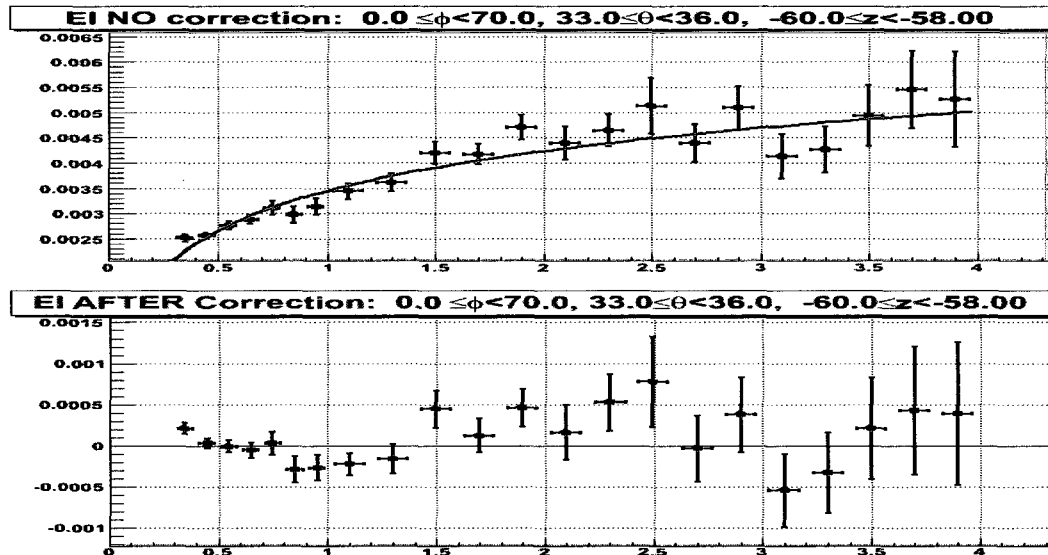


FIG. 79: The peak values of the difference between the original and the reconstructed momentum for electrons versus the reconstructed momentum at  $0 \leq \phi < 70$ ,  $33 \leq \theta < 36$ , and  $-60 \leq z < -58$ , before (top) and after (bottom) the energy loss correction. The red curve in the top plot is the fitted correction function.

A few examples of the energy loss results are shown in Figs. 79 to 82. Figure 79 shows  $\delta p$  before (top) and after (bottom) the energy loss correction as a function of momentum for electrons at one bin of  $\theta$ ,  $\phi$  and  $z$ . Figs. 80, 81 and 82 are the same as Fig. 79 but is for pions, kaons and proton, respectively. Figure 83 shows the overall result of the energy loss correction for all electrons. One can see that before the correction (top)  $\delta p$  is centered at around 3 to 5 MeV/c with a clear momentum dependence. After the correction (bottom)  $\delta p$  is centered close to zero and has no dependence on momentum.

Due to the fact that the torus magnetic field will affect the trajectory of particles, the energy loss table must be generated for each torus current. In the BoNuS experiment the 4 and 5 GeV data were taken with torus current of 2250 A while the 2 and 1 GeV data were taken with 1500 A. Two sets of tables, one for torus current 2250 A and another for torus current 1500 A, had been generated.

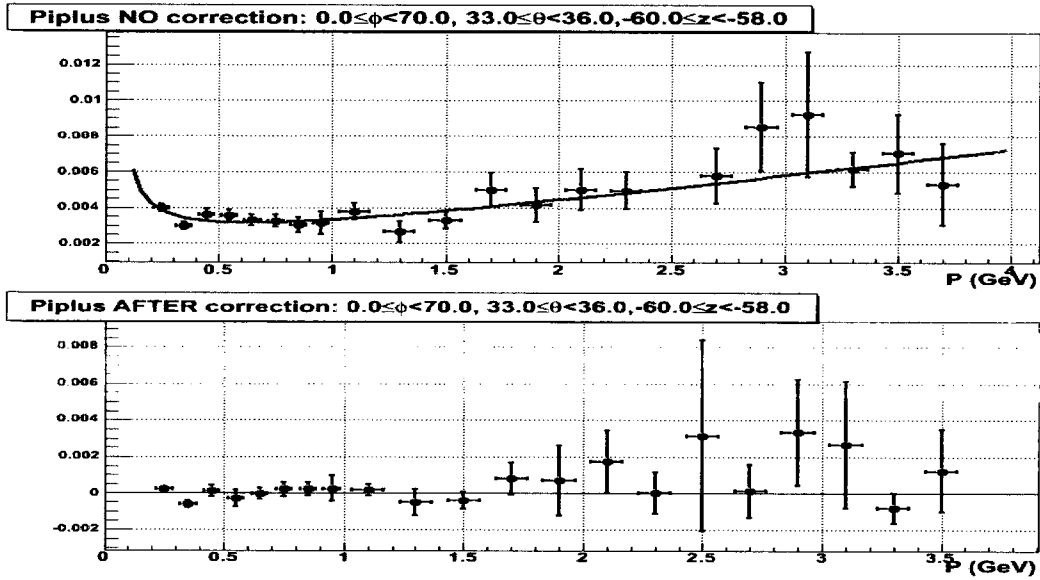


FIG. 80: Same as Fig. 79 but for positive pions.

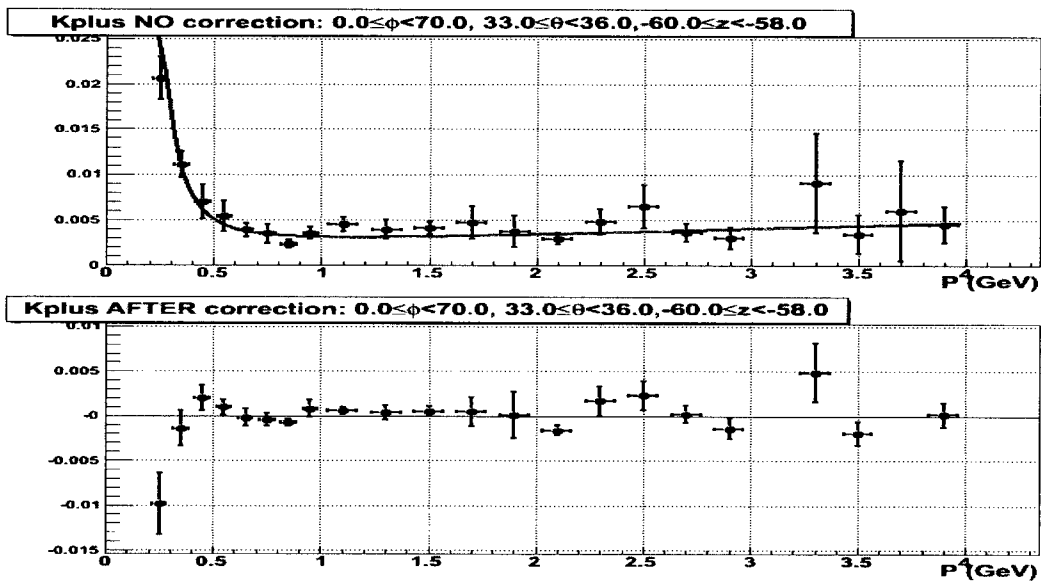


FIG. 81: Same as Fig. 79 but for positive kaons.

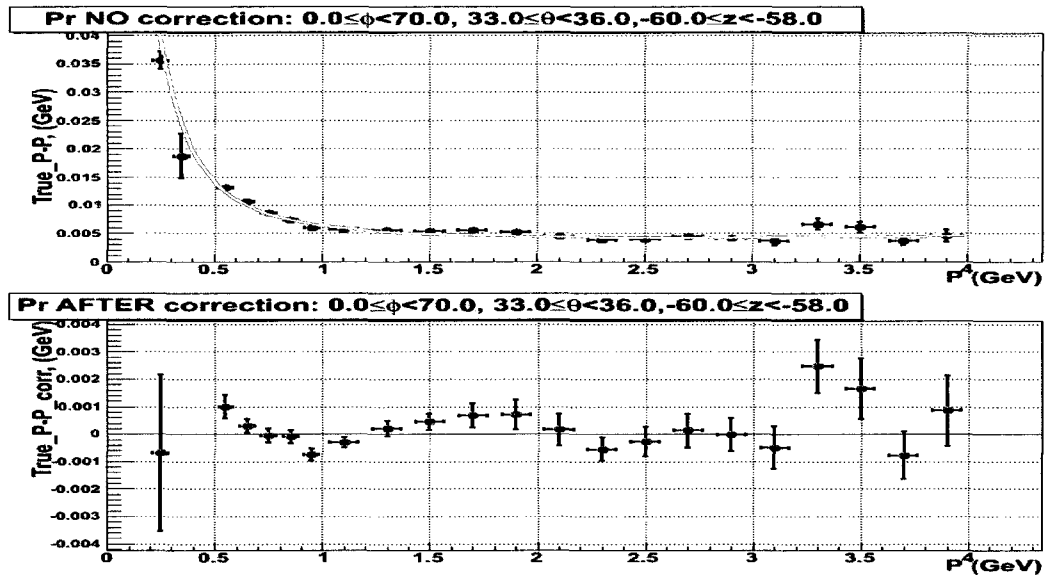


FIG. 82: Same as Fig. 79 but for protons.

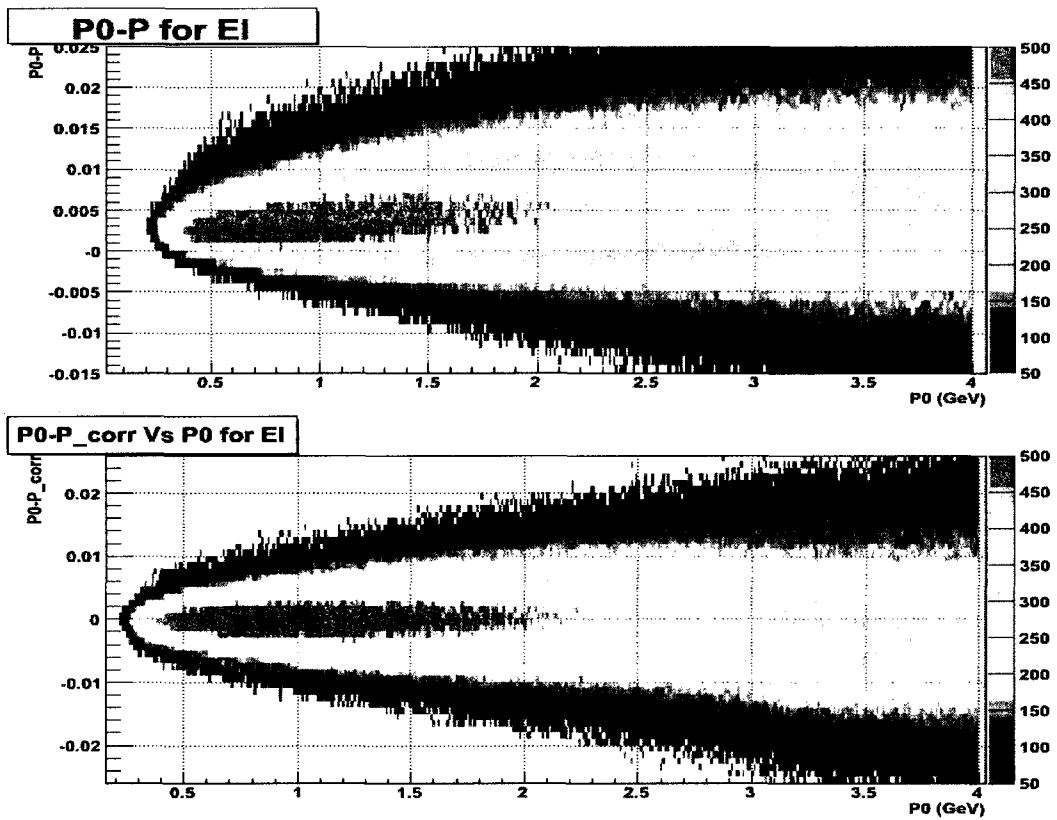


FIG. 83: The difference between the original and the reconstructed momentum for electrons as a function of momentum before (top) and after (bottom) the energy loss correction.

#### V.4.8 $D(e, e'\pi^-p)$ Event Selection

To select a good exclusive  $\pi^-$  event, first we selected events that satisfied 1) a good trigger electron (using the electron identification without the EC total energy cut, described in Section V.4.1) detected within the CC fiducial region; 2) one additional negative particle passing the  $\pi^-$  fiducial cut; 3) one positive particle passing the proton fiducial cut; 4) each of these particles has vertex  $z$  position within 2.71 cm from the trigger electron. Then we calculated the missing mass for these events, which should have a peak at the mass of a proton. In order to determine the peak value, width and the background contribution, the missing mass peak is fitted with a combined function of gaussian signal and exponential background. The fitted gaussian indicated the missing mass peak and width. We selected exclusive  $\pi^-$  events by putting a  $2\text{-}\sigma$  missing mass cut on the gaussian peak. Figure 84 shows the missing mass distribution with the fitted functions for the 5 GeV  $D(e, e'\pi^-p_{\text{CLAS}})X$  (top) and  $D(e, e'\pi^-p_{\text{RTPC}})X$  (bottom) events. The fit is also used for background subtraction, which will be described in detail later.

Note that the strict missing mass requirement for final events does not require more strict identification of the  $\pi^-$  and proton. In summary, the following cuts must be applied to select exclusive  $\pi^-$  events:

- Exclusive electron cut;
- Electron must pass CC fiducial cut;
- Fiducial cut for  $\pi^-$ ;
- Fiducial cut for protons;
- Solenoid geometry cut ( $\theta - z$  correlation cut) for electrons,  $\pi^-$  and protons;
- RTPC vertex window cut ( $-64.0 < z < -48.0(\text{cm})$ );
- Vertex  $z$  correlation cut: ( $|z_i - z_{el}| < 2.71(\text{cm})$ , where  $i = \pi^-, p$  or  $p_s$ );
- $2\text{-}\sigma$  missing mass cut.

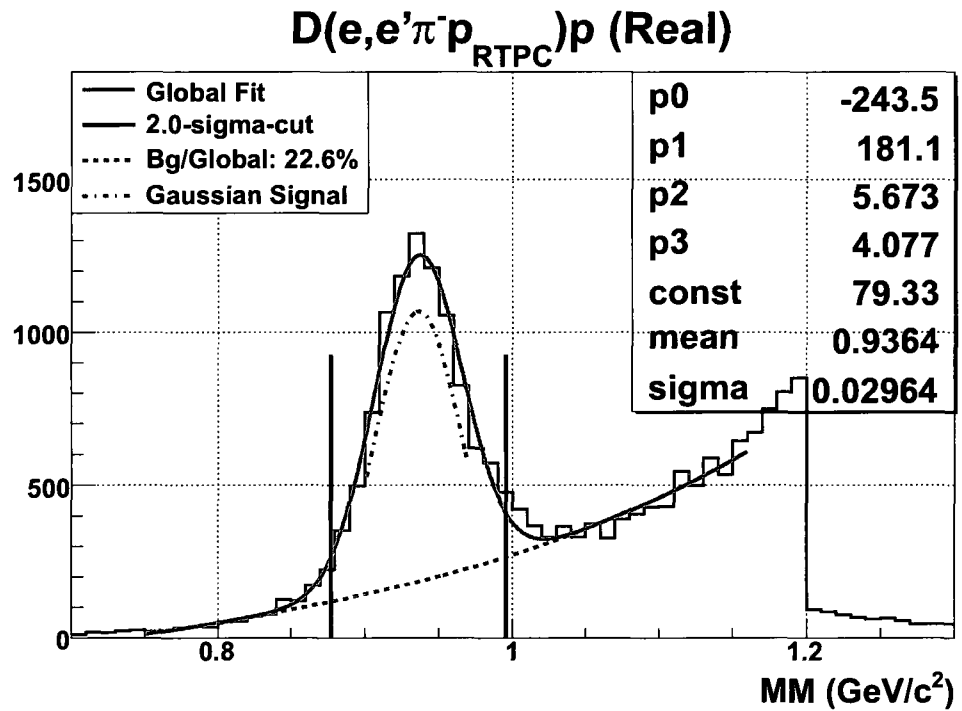
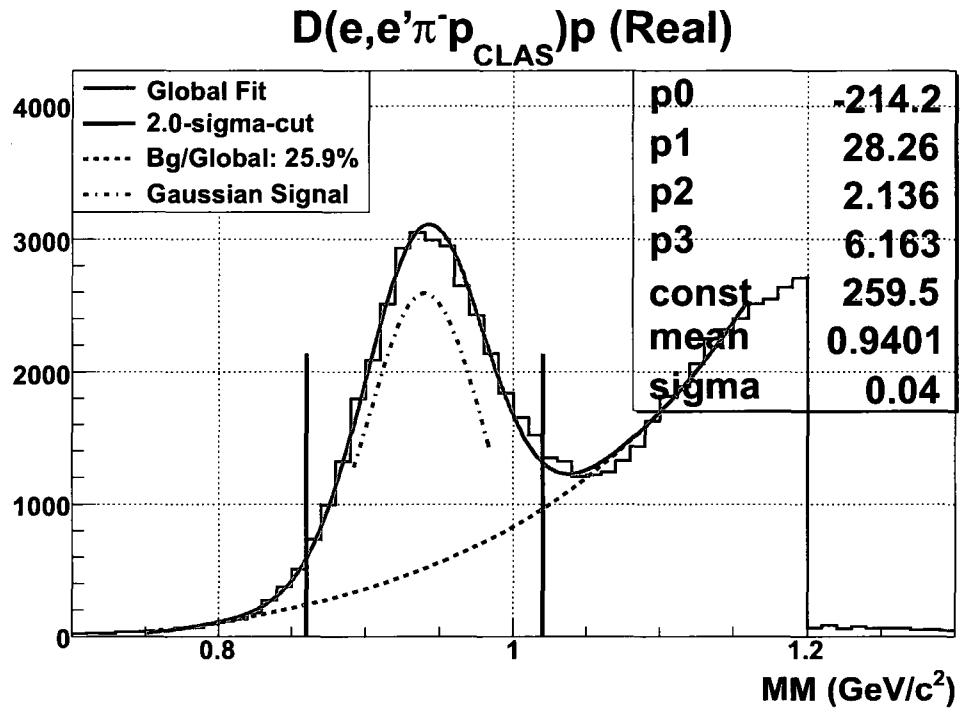


FIG. 84: The missing mass distribution for the 5 GeV  $D(e, e' \pi^- p_{CLAS})p$  (top) and  $D(e, e' \pi^- p_{RTPC})p$  (bottom) events. Both are fitted with a combined function of gaussian (blue dash-dot-dash curve) plus exponential (red dash line). The black vertical lines indicate the  $2\text{-}\sigma$  selection cuts for exclusive events.

## V.5 KINEMATIC COVERAGE AND DATA BINNING

We binned the data in the following four kinematic variables:  $W'$ ,  $Q^2$ ,  $\cos\theta_\pi^*$  and  $\phi_\pi^*$ . Because there are very few neutron cross section results published, we wanted to bin the data in the same way as other CLAS experiments. However, our limited statistics restricted us from doing that. After looking into the acceptance of  $D(e, e'\pi^- p_{\text{CLAS}})p$  and  $D(e, e'\pi^- p_{\text{RTPC}})p$  as a function of  $W'$ ,  $Q^2$ ,  $\cos\theta_\pi^*$  and  $\phi_\pi^*$ , respectively, we finally binned these four kinematic variables as shown in Table 7.

TABLE 7: Binning information for  $D(e, e'\pi^- p)$  analysis

variable	number	lower limit	higher limit	description
$W'$	12	1.15 GeV	2.95 GeV	0.15 GeV each bin
$Q^2$	6	0.131 GeV <sup>2</sup>	4.524 GeV <sup>2</sup>	boundaries at 0.131, 0.379, 0.770, 1.100, 1.563, 2.660, 4.524
$\cos\theta_\pi^*$	8	-1.0	1.0	boundaries at -1.0, -0.5, -0.1, 0.3, 0.55, 0.7, 0.8, 0.9, 1.0
$\phi_\pi^*$	15	0.0 deg	360.0 deg	24 degrees each bin

BoNuS has a wide kinematic coverage in  $W'$  and  $Q^2$ . For the 5 GeV data set,  $W'$  covers up to 3 GeV and  $Q^2$  covers up to 5 GeV<sup>2</sup>. Figure 85 shows the kinematic bins and the coverage of  $W'$  and  $Q^2$  for the 5 GeV data. Figures 86 and 87 show the same as Fig. 85 but for the 4 and 2 GeV data sets, respectively. Because CLAS has a nearly  $4\pi$  detection capability, the coverage of  $\theta_\pi^*$  and  $\phi_\pi^*$  in the center of mass frame is almost  $4\pi$ , although most data were at  $\cos\theta_\pi^*$  close to 1. Figures 88, 89 and 90 show the coverages and bins of  $\cos\theta_\pi^*$  and  $\phi_\pi^*$  for the 5, 4 and 2 GeV data sets, respectively.

## V.6 ACCEPTANCE CORRECTION

The acceptance for a four dimensional kinematic bin,  $W'$ ,  $Q^2$ ,  $\cos\theta_\pi^*$  and  $\phi_\pi^*$ , is the fraction of events in that bin that are detected. In general, the acceptance was

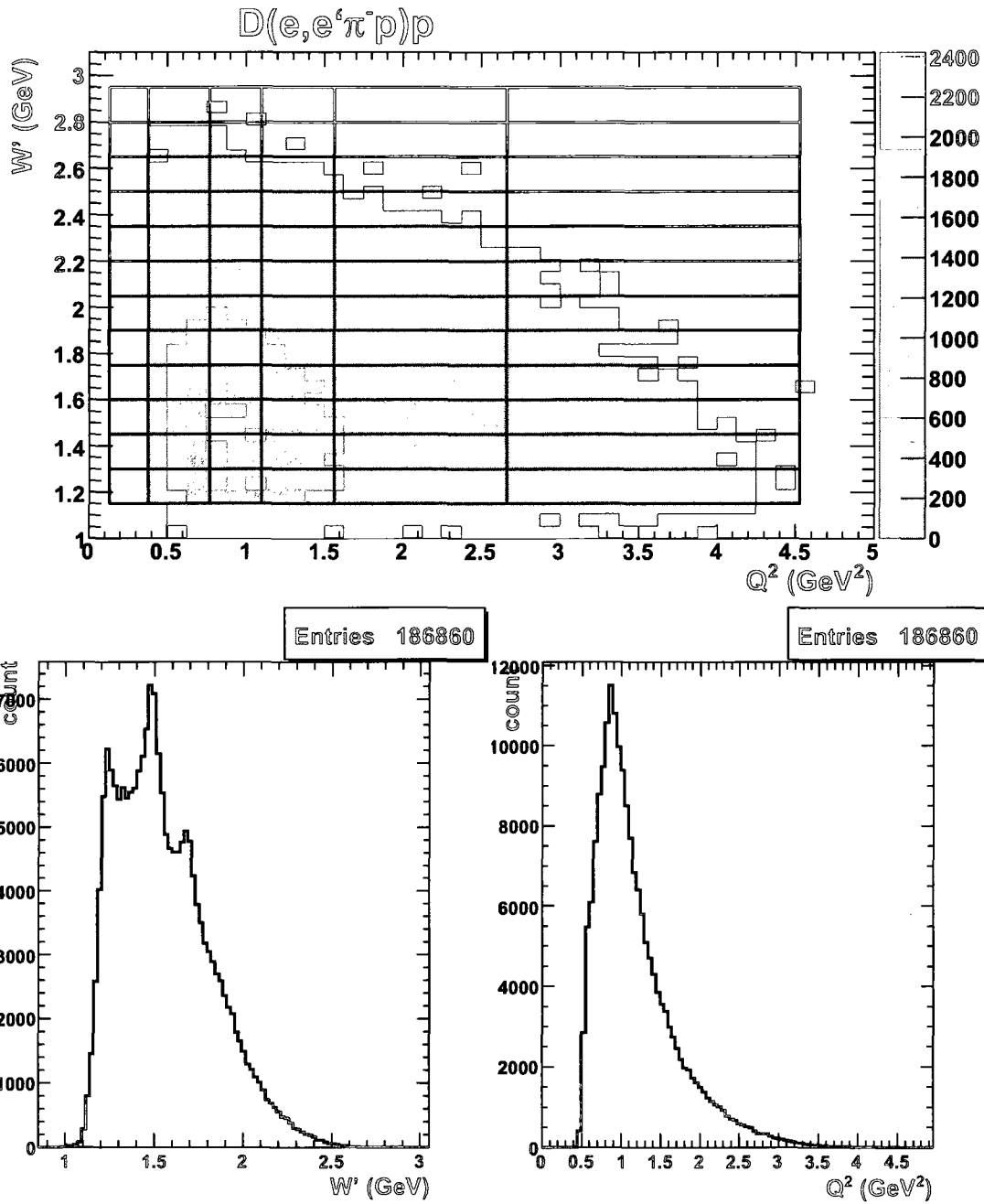


FIG. 86:  $W'$  vs.  $Q^2$  (top) for the 4 GeV data. The black lines indicate the bins. The  $W'$  (bottom left) and  $Q^2$  (bottom right) distributions are also plotted.

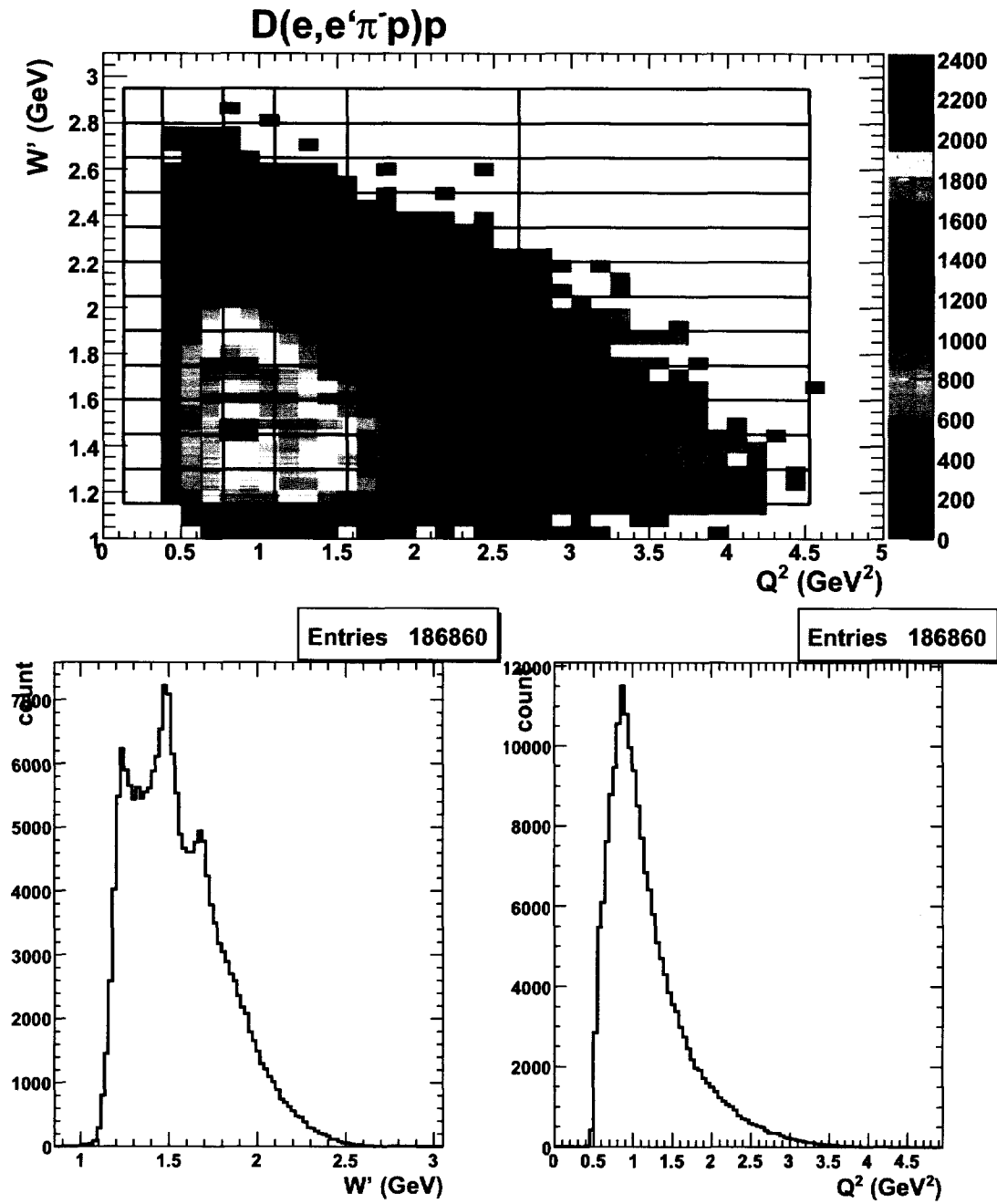


FIG. 86:  $W'$  vs.  $Q^2$  (top) for the 4 GeV data. The black lines indicate the bins. The  $W'$  (bottom left) and  $Q^2$  (bottom right) distributions are also plotted.



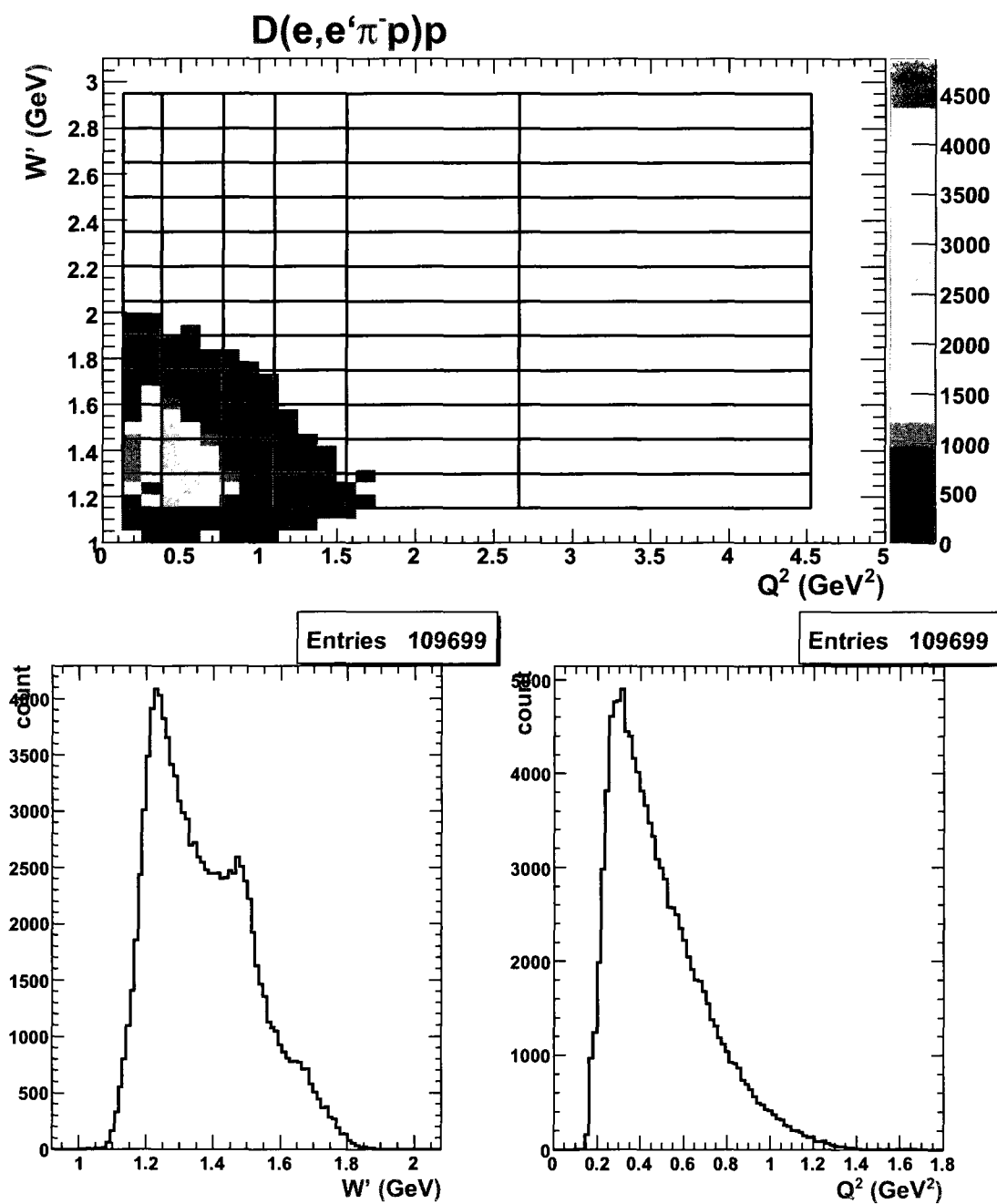


FIG. 87:  $W'$  vs.  $Q^2$  (top) for the 2 GeV data. The black lines indicate the bins. The  $W'$  (bottom left) and  $Q^2$  (bottom right) distributions are also plotted.

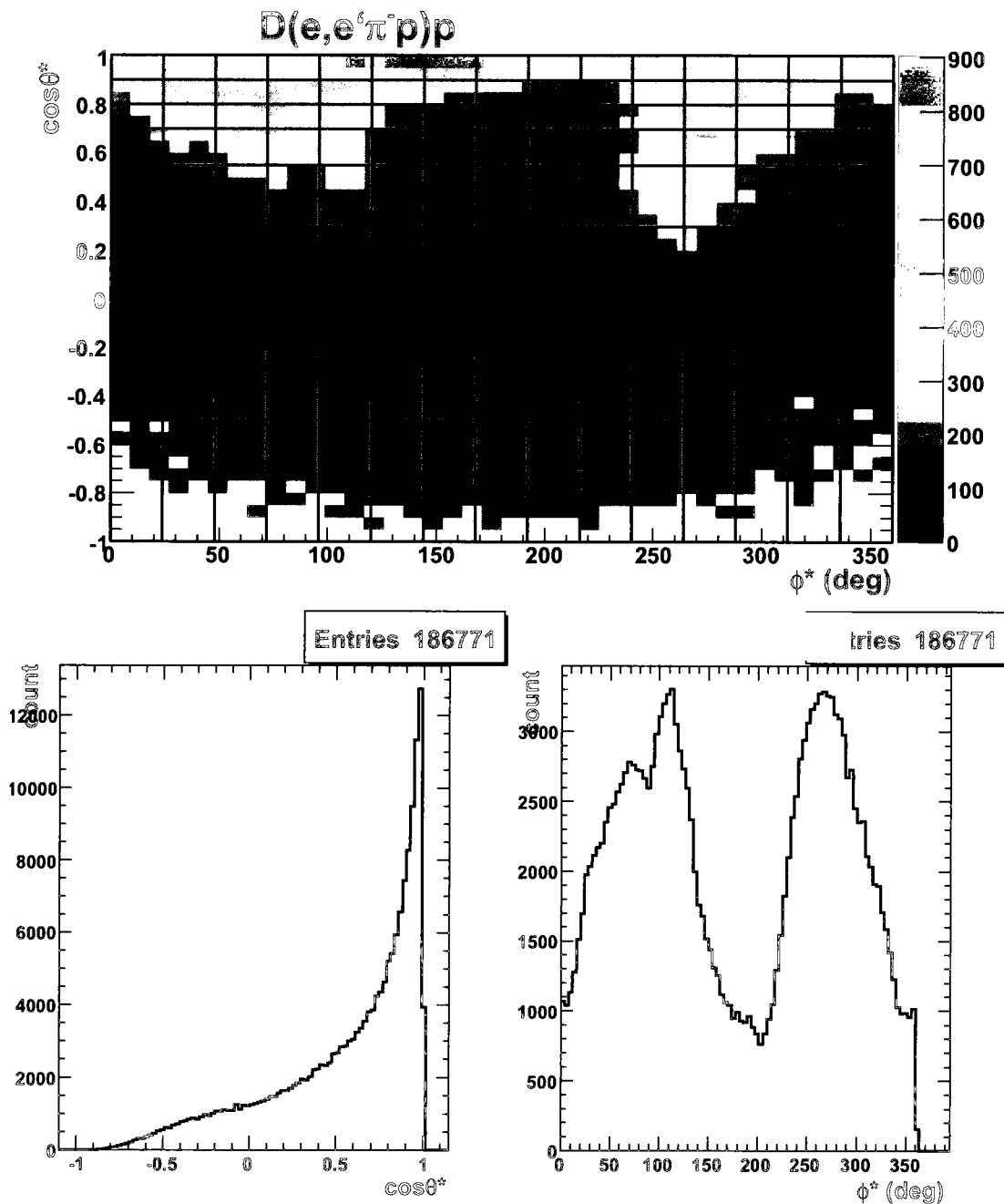


FIG. 88:  $\cos \theta_\pi^*$  vs.  $\phi_\pi^*$  (top) for the 5 GeV data. The black lines indicate the bins. The  $\cos \theta_\pi^*$  (bottom left) and  $\phi_\pi^*$  (bottom right) distributions are also plotted.

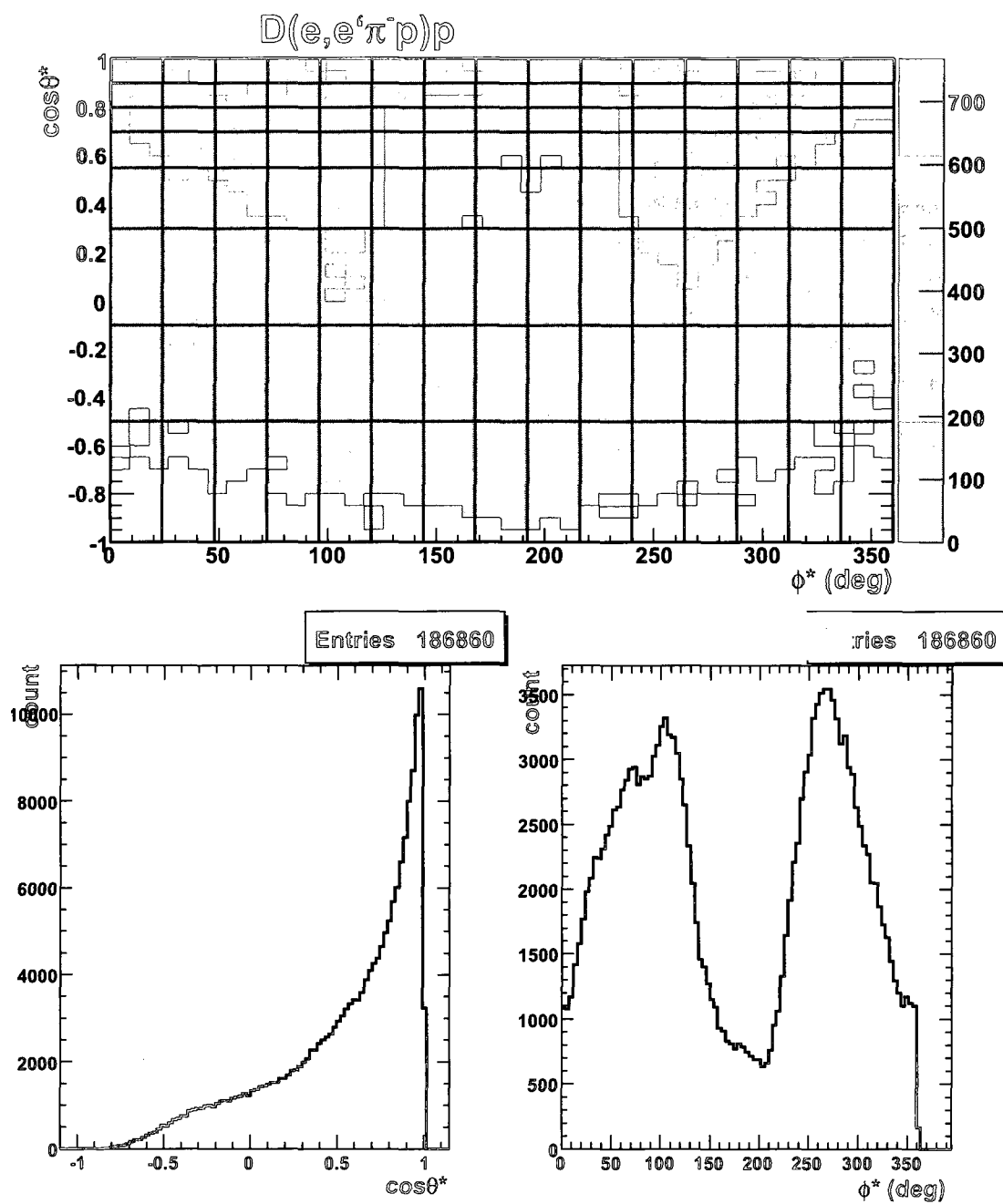


FIG. 89:  $\cos\theta_\pi^*$  vs.  $\phi_\pi^*$  (top) for the 4 GeV data. The black lines indicate the bins. The  $\cos\theta_\pi^*$  (bottom left) and  $\phi_\pi^*$  (bottom right) distributions are also plotted.

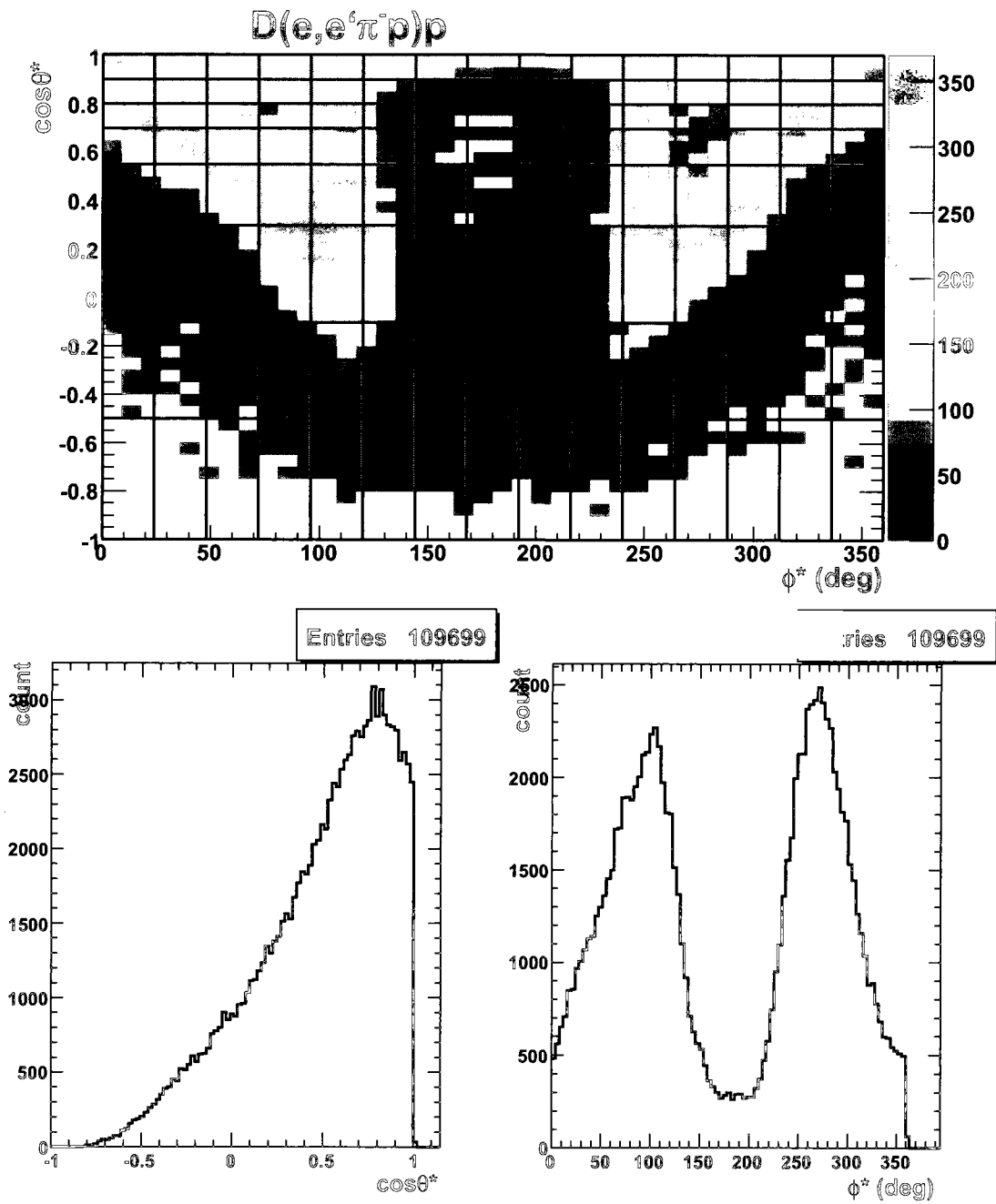


FIG. 90:  $\cos \theta_\pi^*$  vs.  $\phi_\pi^*$  (top) for the 2 GeV data. The black lines indicate the bins. The  $\cos \theta_\pi^*$  (bottom left) and  $\phi_\pi^*$  (bottom right) distributions are also plotted.

calculated by

$$A = \frac{\text{number of reconstructed events}}{\text{number of generated events}} = \frac{\sum_{rec} 1}{\sum_{gen} 1}.$$

After generating a large amount of simulated events (more than 200 millions events) for each beam energy data set, the acceptance  $A$  was calculated as the ratio of the weighted number of detected events to the weighted number of generated events in the same bin:

$$A(W', Q^2, \theta_\pi^*, \phi_\pi^*) = \frac{N_{\text{detected}}^{\text{weighted}}(W', Q^2, \theta_\pi^*, \phi_\pi^*)}{N_{\text{generated}}^{\text{weighted}}(W', Q^2, \theta_\pi^*, \phi_\pi^*)} = \frac{\sum_{\text{detected}} r}{\sum_{\text{generated}} r}, \quad (50)$$

where  $r$  is the distribution weight of the generated events (described in Section IV.5.2). It is also very interesting to plot the integrated acceptance as a function of any one of these four variables  $W'$ ,  $Q^2$ ,  $\theta_\pi^*$  and  $\phi_\pi^*$ , which is known as the one dimensional acceptance  $A_1$ . In this case, both the  $N_{\text{detected}}$  and  $N_{\text{generated}}$  are integrated over the other three variables, and then the ratio is calculated as before. For example,

$$A_1(W') = \frac{N_{\text{detected}}^{\text{weighted}}(W')}{N_{\text{generated}}^{\text{weighted}}(W')} = \frac{\sum_{Q^2, \theta_\pi^*, \phi_\pi^*} N_{\text{detected}}^{\text{weighted}}(W', Q^2, \theta_\pi^*, \phi_\pi^*)}{\sum_{Q^2, \theta_\pi^*, \phi_\pi^*} N_{\text{generated}}^{\text{weighted}}(W', Q^2, \theta_\pi^*, \phi_\pi^*)}. \quad (51)$$

Figs. 91 to 94 show the four one dimensional acceptance distributions. However, it is the four-dimension acceptance that is used to calculate the cross section in this analysis.

## V.7 PARTICLE DETECTION EFFICIENCY

In this section, the particle detection efficiency for the trigger electron, the fast proton detected by CLAS and the spectator proton detected by the RTPC will be described.

### V.7.1 Trigger Efficiency

The trigger efficiency is the fraction of the scattered electrons detected by the CLAS. In order to find the trigger efficiency, inclusive events of  $D(e, e')$ ,  $D(e, e'p_s)$

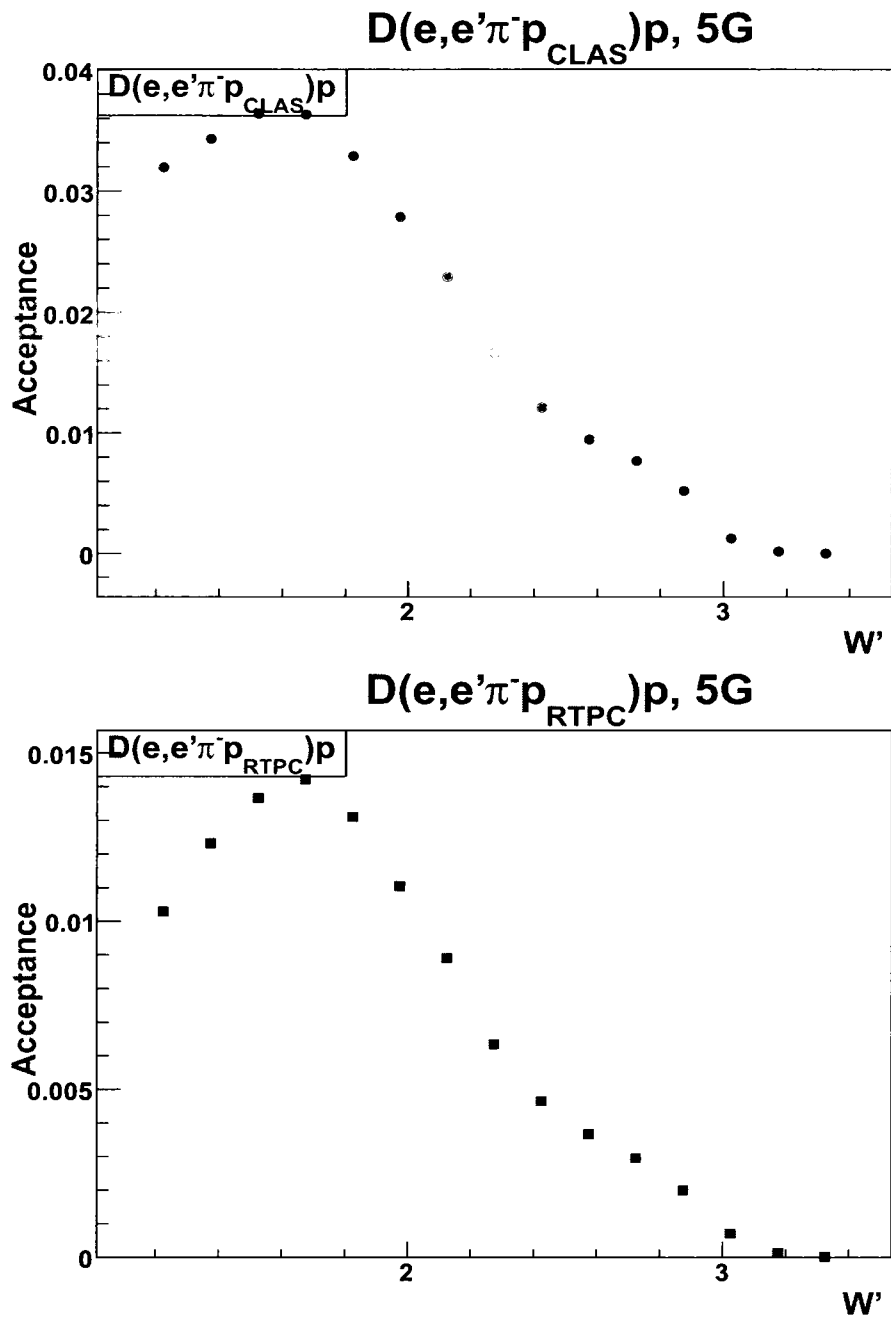


FIG. 91: Acceptance for the 5 GeV data as a function of  $W'$ . The top panel is for  $D(e, e' \pi^- p_{\text{CLAS}}) p$  and the bottom is for  $D(e, e' \pi^- p_{\text{RTPC}}) p$  events.

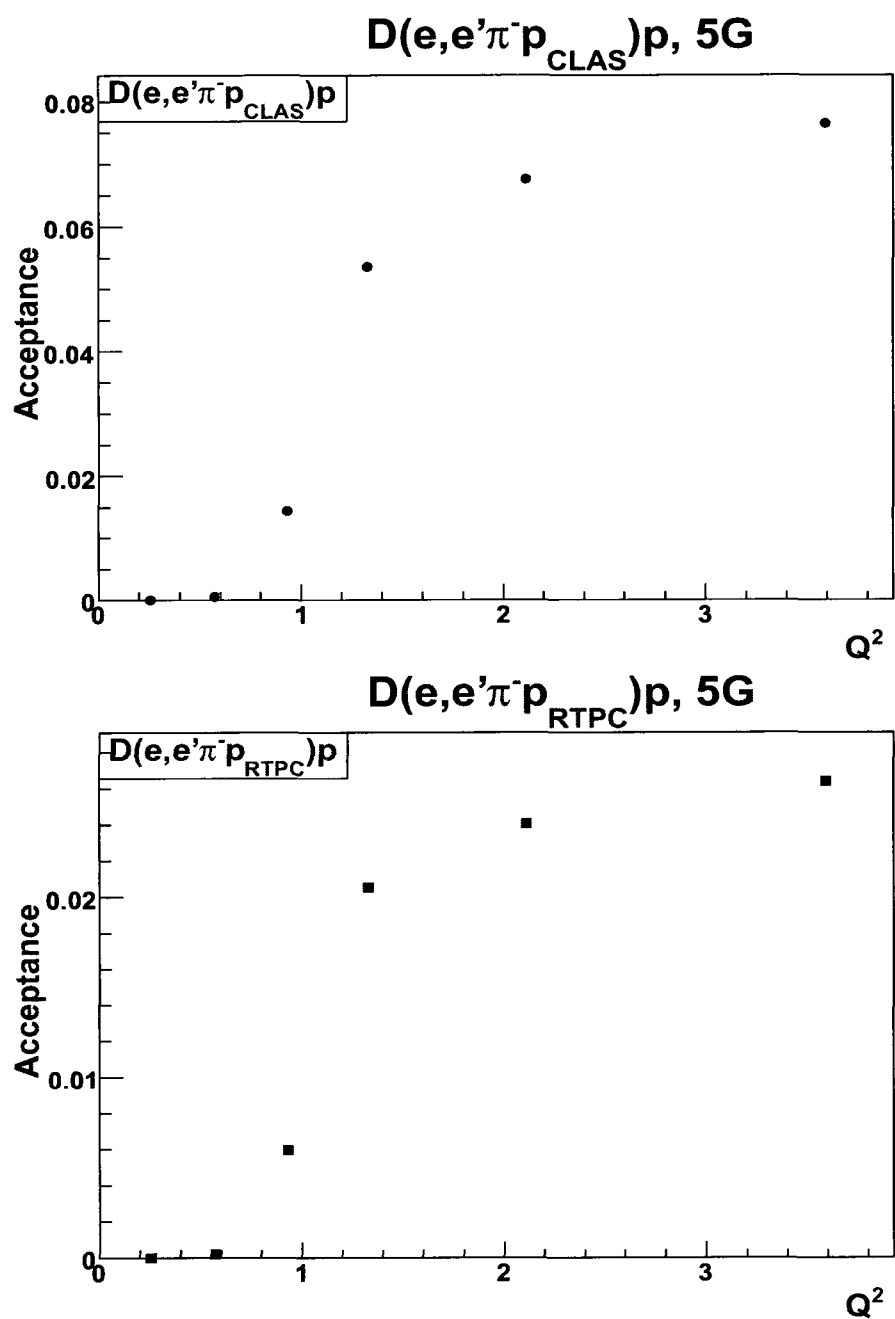


FIG. 92: Acceptance for the 5 GeV data as a function of  $Q^2$ . The top panel is for  $D(e, e' \pi^- p_{\text{CLAS}}) p$  and the bottom is for  $D(e, e' \pi^- p_{\text{RTPC}}) p$  events.

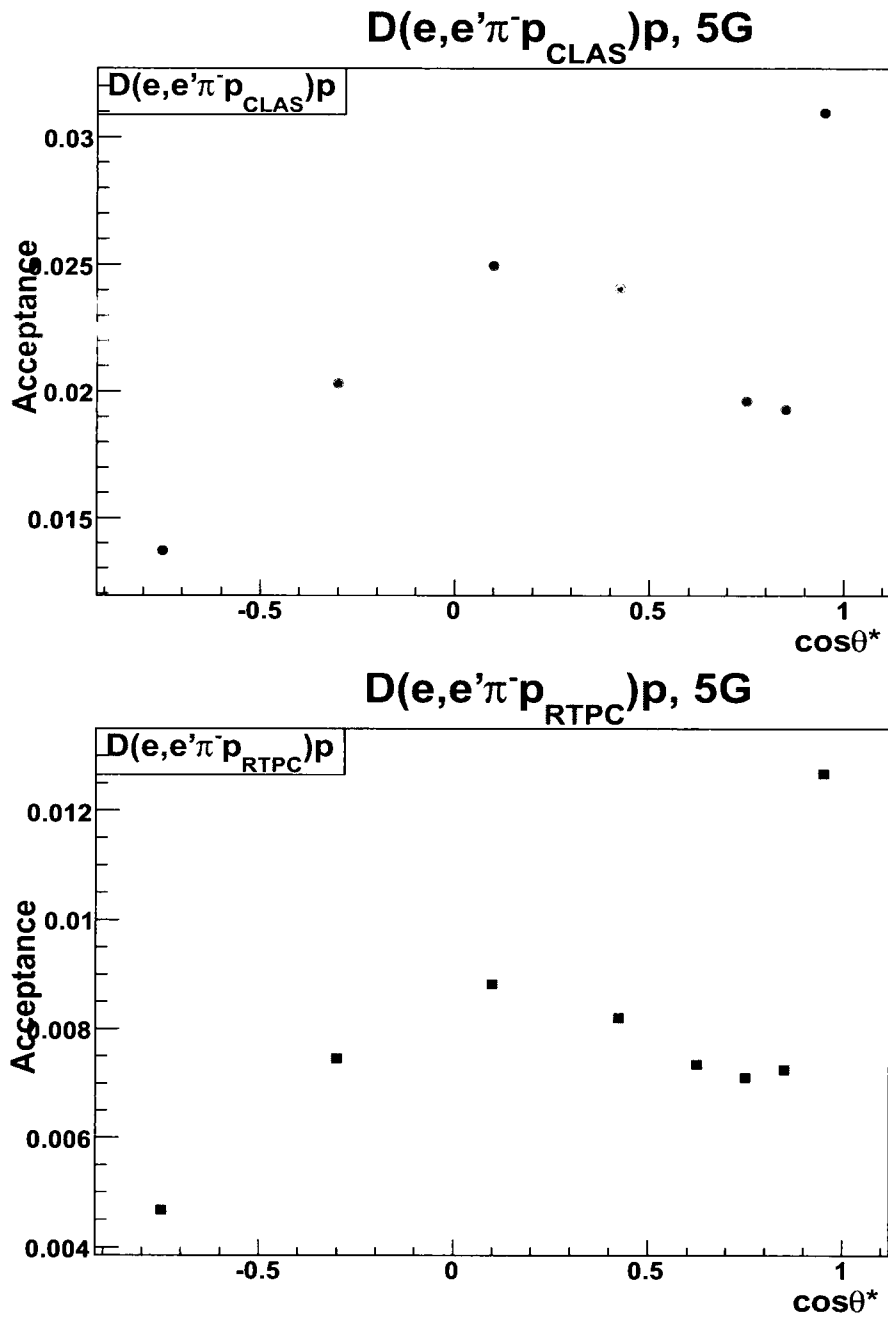


FIG. 93: Acceptance for the 5 GeV data as a function of  $\cos \theta_{\pi}^*$ . The top panel is for  $D(e, e' \pi^- p_{\text{CLAS}})p$  and the bottom is for  $D(e, e' \pi^- p_{\text{RTPC}})p$  events.



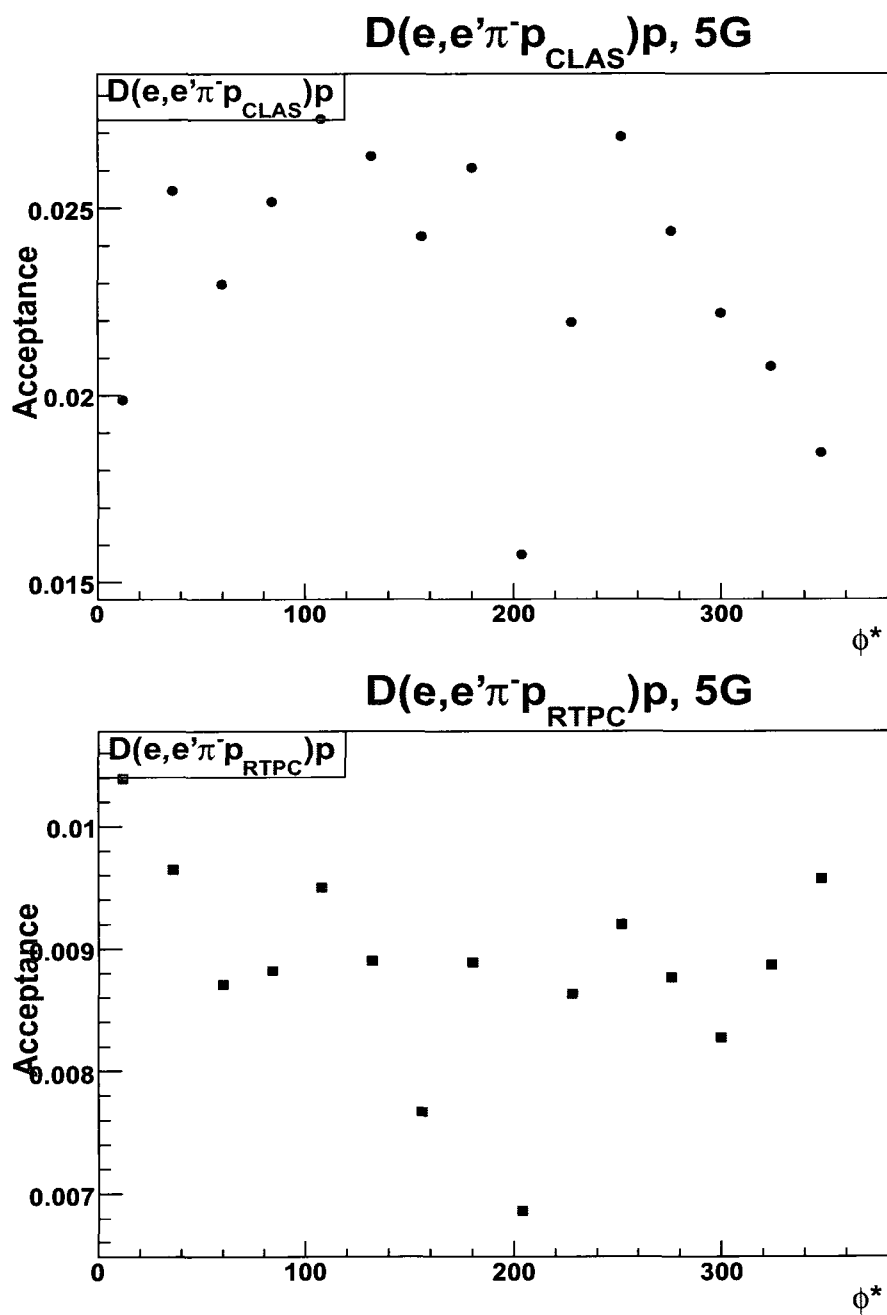


FIG. 94: Acceptance for the 5 GeV data as a function of  $\phi_\pi^*$ . The top panel is for  $D(e, e' \pi^- p_{\text{CLAS}}) p$  and the bottom is for  $D(e, e' \pi^- p_{\text{RTPC}}) p$  events.

and  $D(e, e'p_s)X$  were generated using S. Kuhn's event generator according to a model of the inclusive cross section. These events were then run through the simulation train. Both the experimental data and the simulated data were analyzed. Due to the fact that the simulated data had a different integrated luminosity from the real data, a scale value,  $L_{r2s}$ , was introduced to scale the simulated data to match the real data. The scale value is given by

$$L_{r2s} \equiv \frac{L_{\text{real}}}{L_{\text{sim}}},$$

where  $L_{\text{real}}$  and  $L_{\text{sim}}$  are the time integrated luminosity for the real data and the simulated data, respectively. The trigger efficiency currently used in this analysis is implemented in a look up table in bins of electron's momentum and scattered angle. The detection efficiency of the trigger electrons,  $\eta_e$ , was obtained by taking the ratio of the number of events found in the real data to that of the scaled simulation in the same bin:

$$\eta_e = \frac{\sum_{\text{real}} 1}{L_{r2s} \sum_{\text{sim}} 1}.$$

Figure 95 shows the trigger efficiency (in percentage) in each  $p$ - $\theta$  bin.

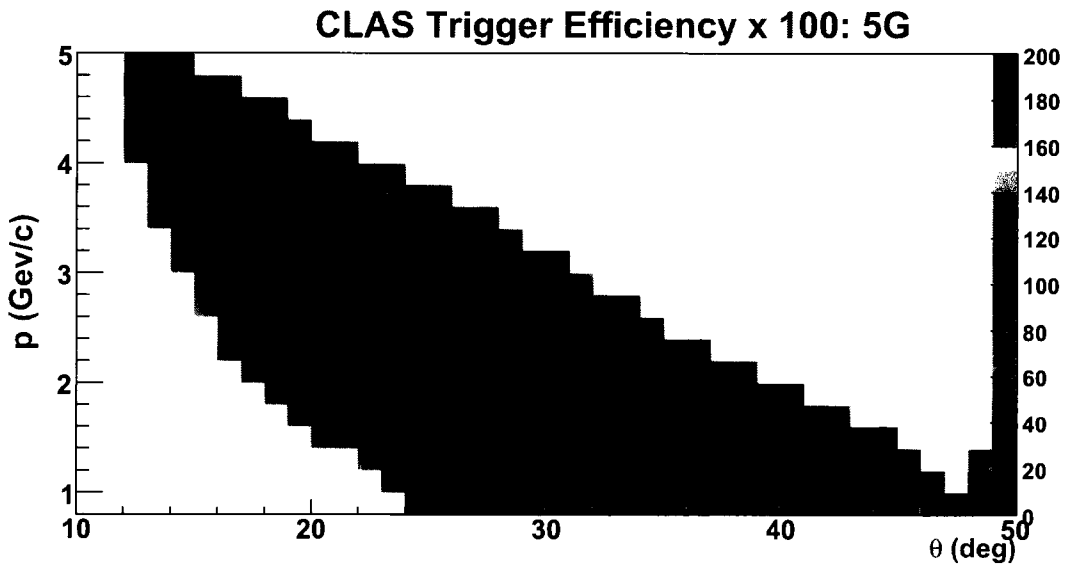


FIG. 95: CLAS trigger efficiency for the 5 GeV data is plotted as text in percentage for each momentum-theta bin.

### V.7.2 Proton Detection Efficiency in CLAS

The CLAS proton efficiency can be obtained through the exclusive analysis by using  $D(e, e'\pi^- p_{\text{CLAS}} p_{\text{RTPC}})$  events in which all four particles in the final state were detected. By taking the ratio of  $D(e, e'\pi^- p_{\text{CLAS}} p_{\text{RTPC}})$  to  $D(e, e'\pi^- p_{\text{RTPC}})p$  one can obtain the detection efficiency of the CLAS proton,

$$\eta_p = \frac{D(e, e'\pi^- p_{\text{CLAS}} p_{\text{RTPC}})}{D(e, e'\pi^- p_{\text{RTPC}})p}.$$

In this analysis, the CLAS proton detection efficiency was determined in  $p$ - $\theta$  bins. Figure 96 shows the proton detection efficiency for the real data (top) and the simulated data (bottom). One can see that the simulated efficiency is a little bit higher than that of the real data. Note that we will correct for the acceptance to calculate the cross section, which means that the proton detection efficiency from the simulation will be applied as part of the acceptance. In order to correct for an additional inefficiency in CLAS for detecting protons, a ratio of the real data efficiency to the simulated data efficiency is required:

$$\eta_p^{r2s} = \frac{\eta_p^{\text{real}}}{\eta_p^{\text{sim}}}. \quad (52)$$

Fig. 97 shows this ratio. Note that this ratio must be used together with the acceptance correction.

### V.7.3 Proton Detection Efficiency in the RTPC

The RTPC proton detection efficiency can be determined in the same way as the proton detection efficiency of CLAS. It can be obtained from:

$$\eta_{\text{RTPC}} = \frac{D(e, e'\pi^- p_{\text{CLAS}} p_{\text{RTPC}})}{D(e, e'\pi^- p_{\text{CLAS}})p}.$$

The super ratio of the real data efficiency to the simulated data efficiency is defined as

$$\eta_{\text{RTPC}}^{r2s} = \frac{\eta_{\text{RTPC}}^{\text{real}}}{\eta_{\text{RTPC}}^{\text{sim}}}. \quad (53)$$

In this analysis, the RTPC proton detection efficiency was found in  $p$ - $\cos\theta_{pq}$  bins. Figure 98 shows the RTPC proton detection efficiency for the real data (top) and

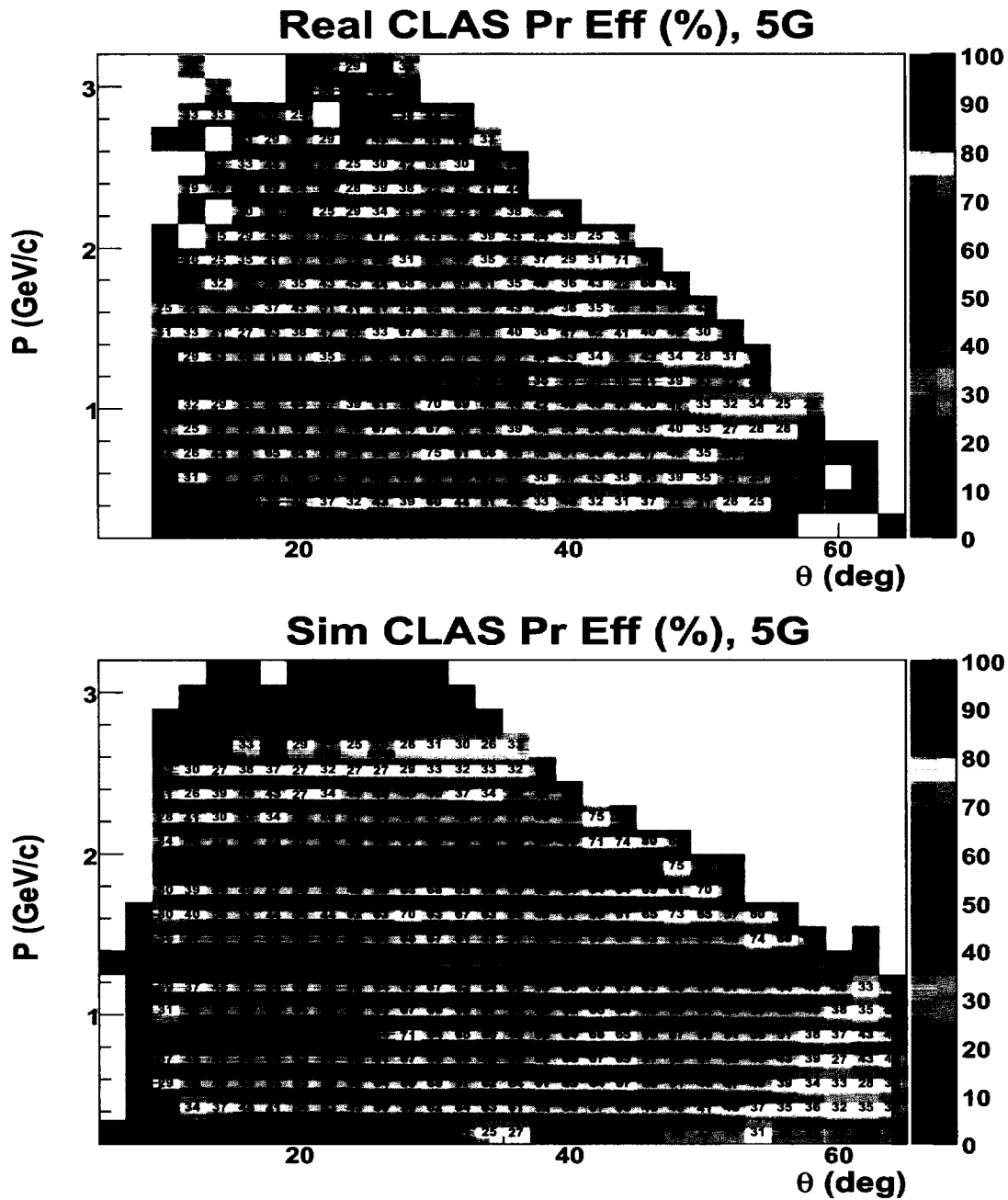


FIG. 96: The proton detection efficiency in CLAS for the 5 GeV data in each momentum-theta bin for the real data (top) and the simulated data (bottom).

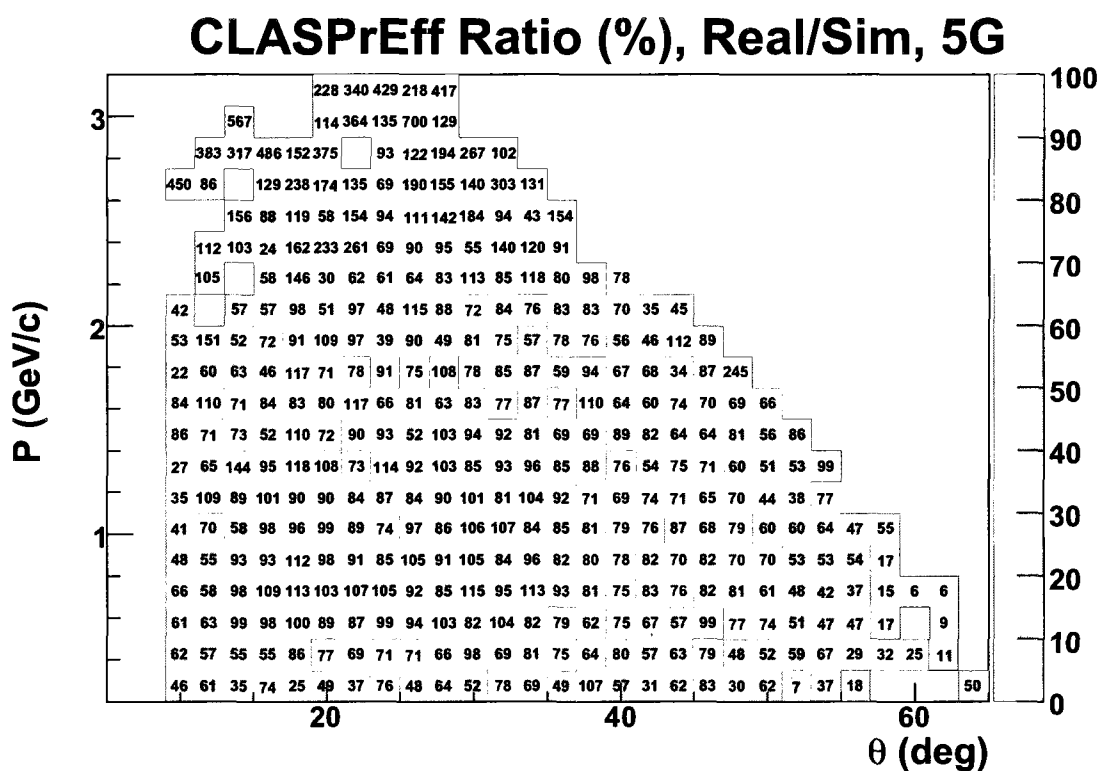


FIG. 97: Super ratio (in percentage) of the CLAS proton detection efficiency for the 5 GeV real data to that in simulation in  $p$ - $\theta$  bins.

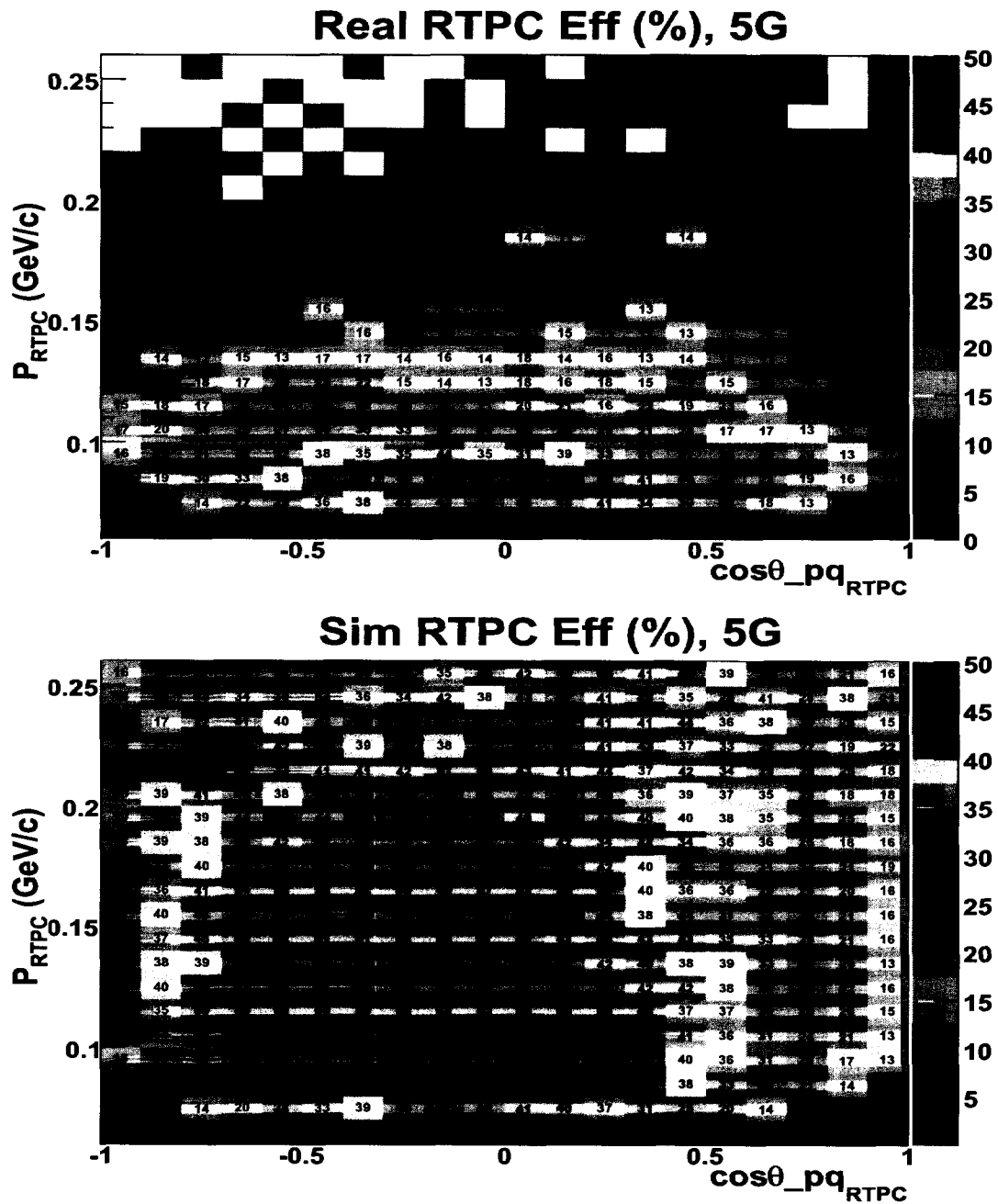


FIG. 98: The RTPC proton detection efficiency in each momentum- $\cos\theta_{pq}$  bin for the 5 GeV real data (top) and for the 5 GeV simulated data (bottom).

the simulated data (bottom). Figure 99 shows the super ratio of the real efficiency to that of the simulation. For the same reason mentioned above, this super ratio was used together with the acceptance correction.

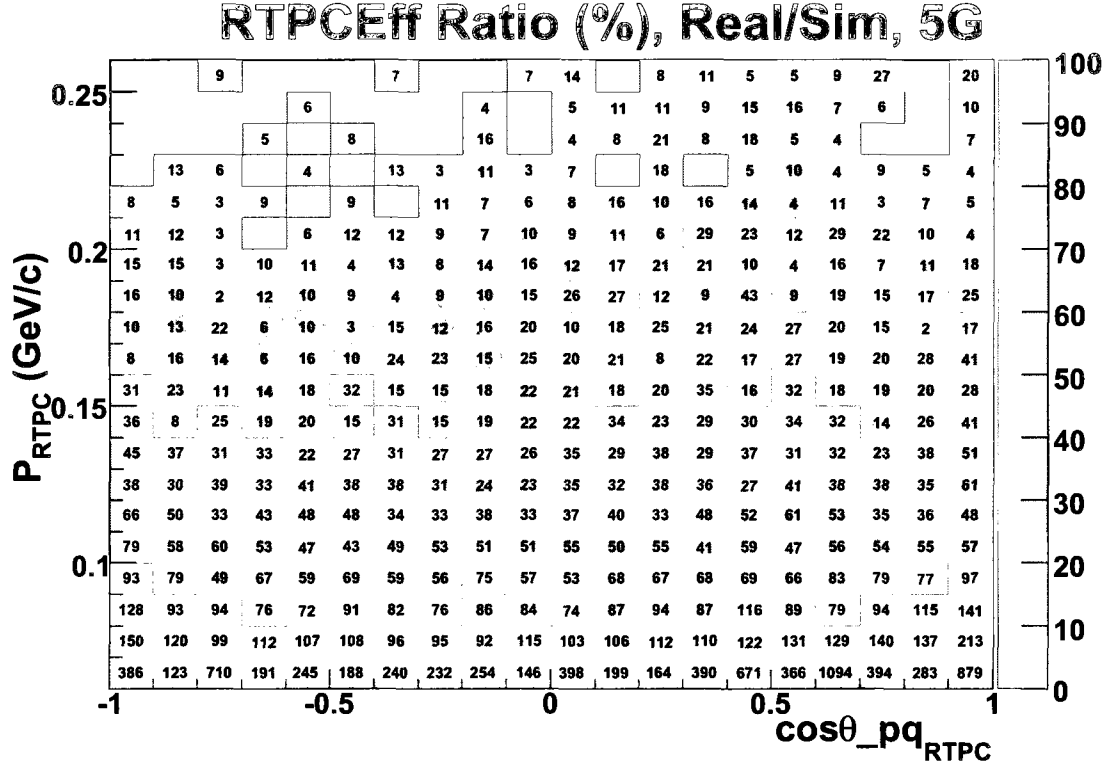


FIG. 99: Super ratio (in percentage) of the RTPC proton detection efficiency for the 5 GeV real data to that in simulation in  $p\text{-}\cos\theta_{pq}$  bins.

#### V.7.4 $\pi^-$ Detection Efficiency

The  $\pi^-$  detection efficiency can be given by

$$\eta_{\pi} = \frac{D(e, e' \pi^- p_{\text{CLAS}} p_{\text{RTPC}})}{D(e, e' p_{\text{CLAS}} p_{\text{RTPC}}) \pi^-}$$

Currently this efficiency has not yet been implemented, so  $\eta_{\pi} = 1$  was used.

## V.8 BACKGROUND SUBTRACTION

In order to select the valid exclusive events, we need to correct for the background under the missing mass peak. As mentioned earlier we fit the missing mass distribution of  $D(e, e'\pi^- p_{\text{CLAS}})X$  and  $D(e, e'\pi^- p_{\text{RTPC}})X$  events with a combined function of a gaussian signal plus an exponential background. The portion covered by the exponential function was treated as background from non-exclusive events. Due to the limited statistics we can not determine the fraction of background events for each  $W'$ ,  $Q^2$ ,  $\cos\theta_\pi^*$  and  $\phi_\pi^*$  bin. To achieve a reliable result we first look for the background dependence on each of these four variables  $f_1^{\text{real}}(W')$ ,  $f_2^{\text{real}}(Q^2)$ ,  $f_3^{\text{real}}(\theta_\pi^*)$  and  $f_4^{\text{real}}(\phi_\pi^*)$ . The four-dimensional background fraction for real data,  $f^{\text{real}}$ , is then found according to

$$f^{\text{real}}(W', Q^2, \theta_\pi^*, \phi_\pi^*) = f_3^{\text{real}}(\theta_\pi^*) \frac{f_1^{\text{real}}(W')}{\langle f_1^{\text{real}}(W') \rangle} \frac{f_2^{\text{real}}(Q^2)}{\langle f_2^{\text{real}}(Q^2) \rangle} \frac{f_4^{\text{real}}(\phi_\pi^*)}{\langle f_4^{\text{real}}(\phi_\pi^*) \rangle}, \quad (54)$$

where  $\langle f(x) \rangle$  means the event weighted average of  $f(x)$  over the whole  $x$  range.

The background defined by the exponential function includes some good events. This can be seen by plotting the missing mass distribution for simulated data, which contains no background (*cf.* Fig. 108-115). Clearly the exclusive events fall in a wide non-gaussian tail. The background defined by Eq. (54) assumes that the exponential is entirely background, while obviously over estimates the real background events. In order to find out how many good events were treated as background we went through the same procedure with the simulated data.

Repeating the previous procedure we found the functions  $f_1^{\text{sim}}(W')$ ,  $f_2^{\text{sim}}(Q^2)$ ,  $f_3^{\text{sim}}(\theta_\pi^*)$  and  $f_4^{\text{sim}}(\phi_\pi^*)$ . We then determined what fraction of the simulated data would be wrongly labeled as background  $f^{\text{sim}}$ :

$$f^{\text{sim}}(W', Q^2, \theta_\pi^*, \phi_\pi^*) = f_3^{\text{sim}}(\theta_\pi^*) \frac{f_1^{\text{sim}}(W')}{\langle f_1^{\text{sim}}(W') \rangle} \frac{f_2^{\text{sim}}(Q^2)}{\langle f_2^{\text{sim}}(Q^2) \rangle} \frac{f_4^{\text{sim}}(\phi_\pi^*)}{\langle f_4^{\text{sim}}(\phi_\pi^*) \rangle}. \quad (55)$$

Taking into account the fact that a  $2\text{-}\sigma$  cut on a gaussian just finds 95.45% of the whole exclusive peak, we arrive at the final expression for the background correction:

$$B \equiv \frac{\text{GoodData}}{\text{Total}} = (1.0 - f^{\text{real}}(W', Q^2, \theta_\pi^*, \phi_\pi^*) + f^{\text{sim}}(W', Q^2, \theta_\pi^*, \phi_\pi^*))/0.9545, \quad (56)$$

where B is defined as the fraction of good exclusive events to all events under the missing mass peak. Figures 100 to 107 show the background fits and the resulting functions  $f_1^{\text{real}}$ ,  $f_2^{\text{real}}$ ,  $f_3^{\text{real}}$  and  $f_4^{\text{real}}$  for  $D(e, e'\pi^- p_{\text{CLAS}})X$  events for the real data. Figures 108 to 115 show the same background fits except for for the simulated data.



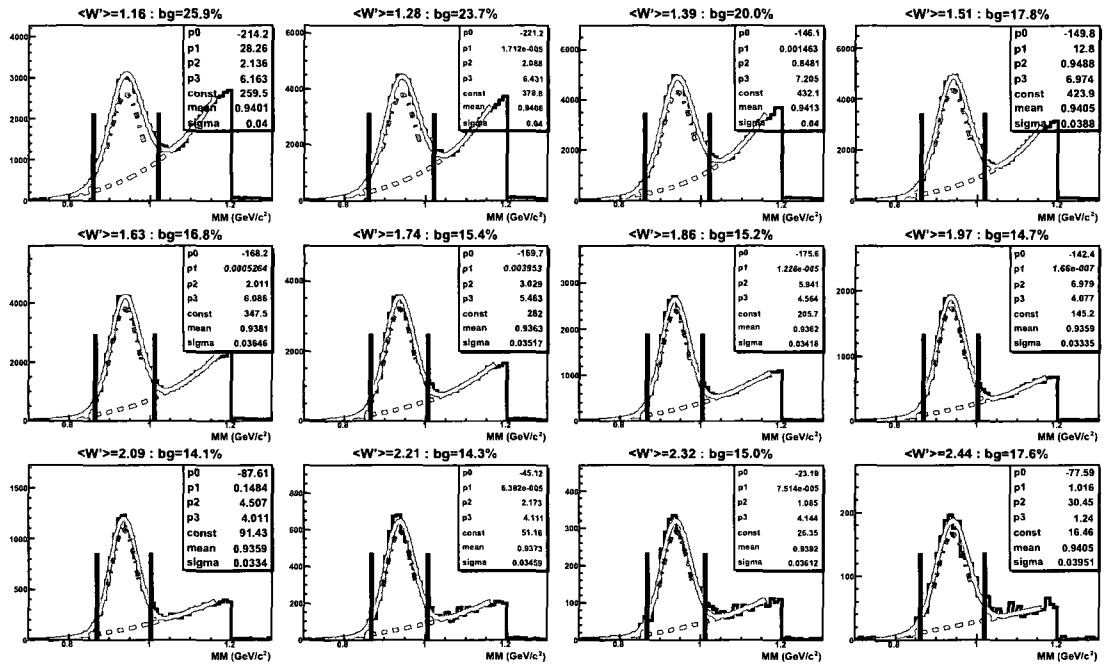


FIG. 100: Missing mass for  $D(e, e' \pi^- p_{\text{CLAS}})X$  events in each  $W'$  bin. The blue line indicates the gaussian peak and the red line indicates the total and background fits. The black vertical lines indicate the  $2\text{-}\sigma$  cut to select exclusive events. Events shown here are from the 5 GeV data.

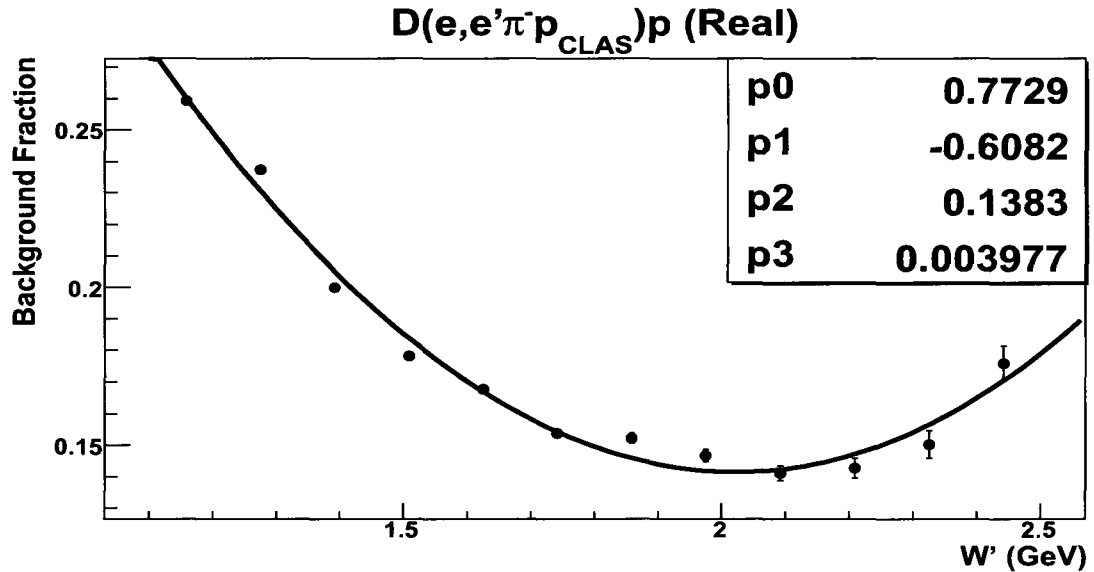


FIG. 101: Background fraction for the 5 GeV  $D(e, e' \pi^- p_{\text{CLAS}})p$  events as a function of  $W'$  using 5 GeV data. The black curve is the fitted function  $f_1^{\text{real}}$ .

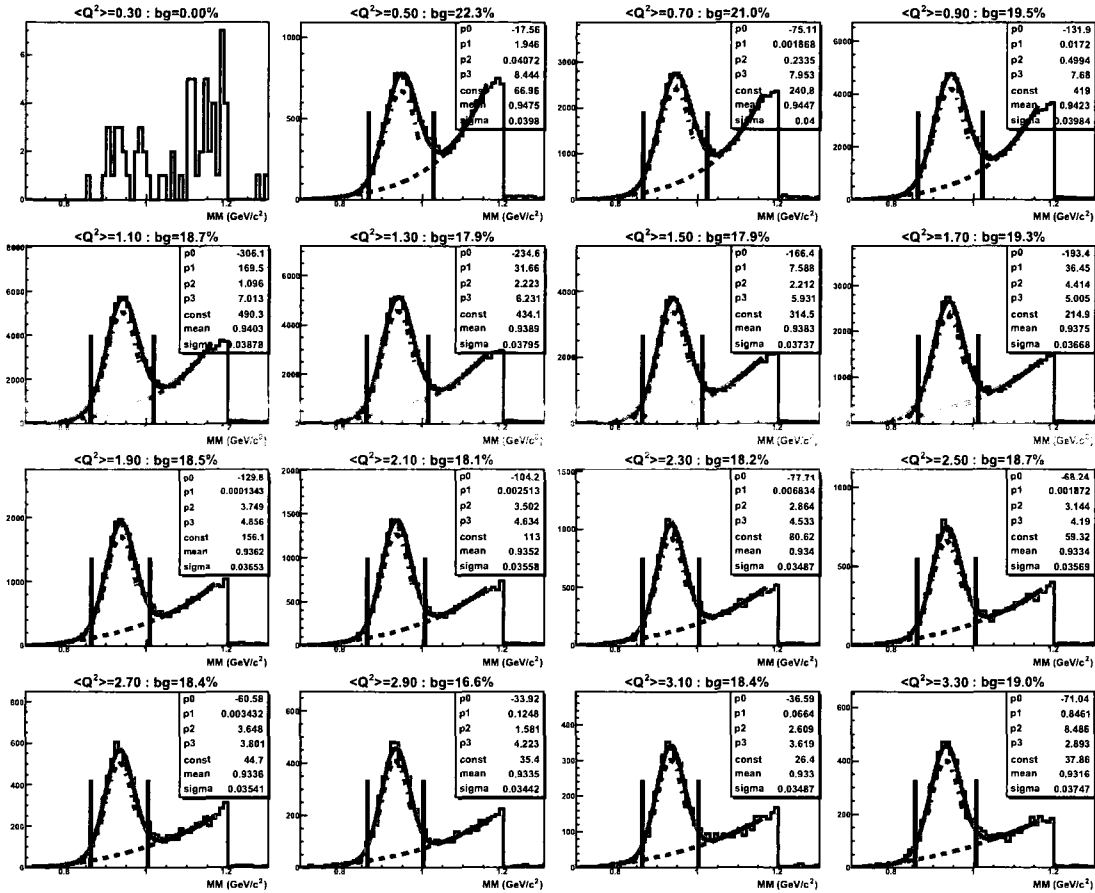


FIG. 102: Same as Fig. 100 except for bins in  $Q^2$ .

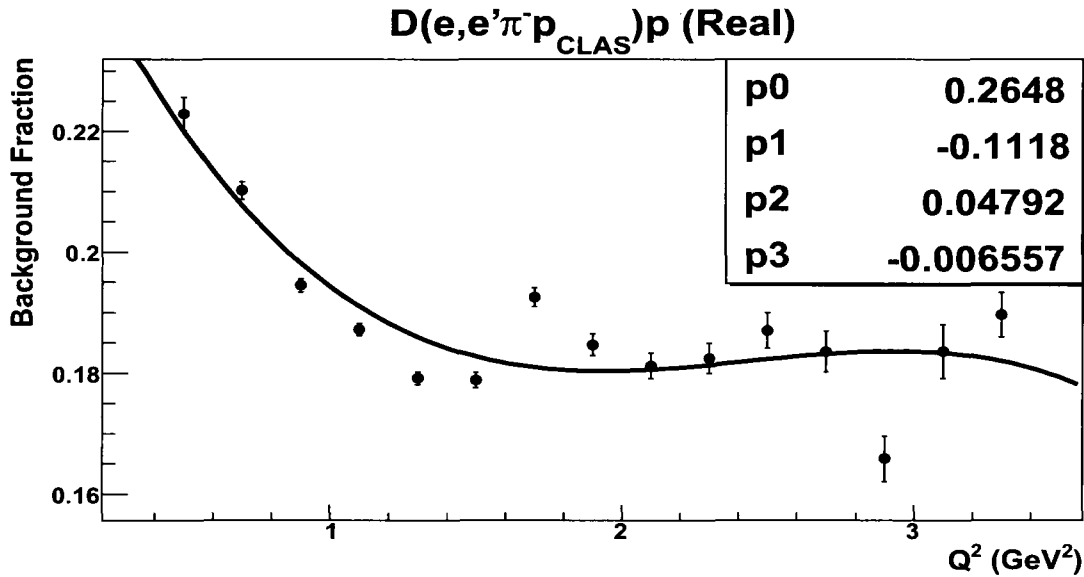


FIG. 103: Same as Fig. 101 except as a function of  $Q^2$ .

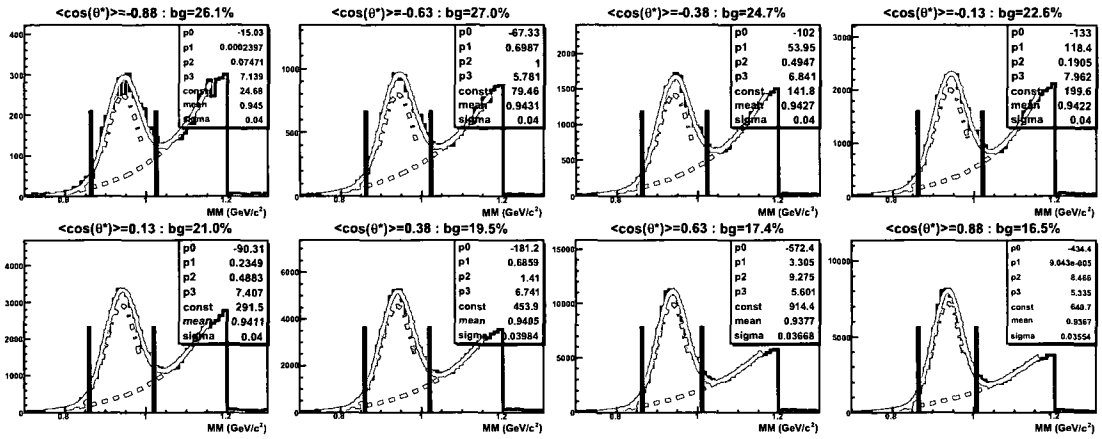


FIG. 104: Same as Fig. 100 except for bins in  $\cos\theta^*$ .

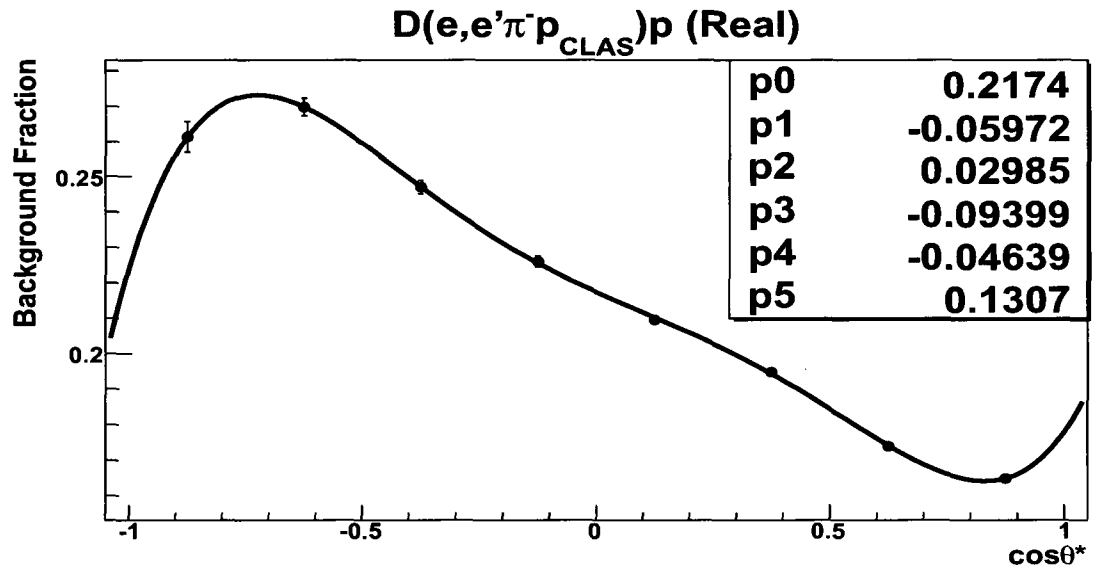


FIG. 105: Same as Fig. 101 except as a function of  $\cos\theta^*$ .

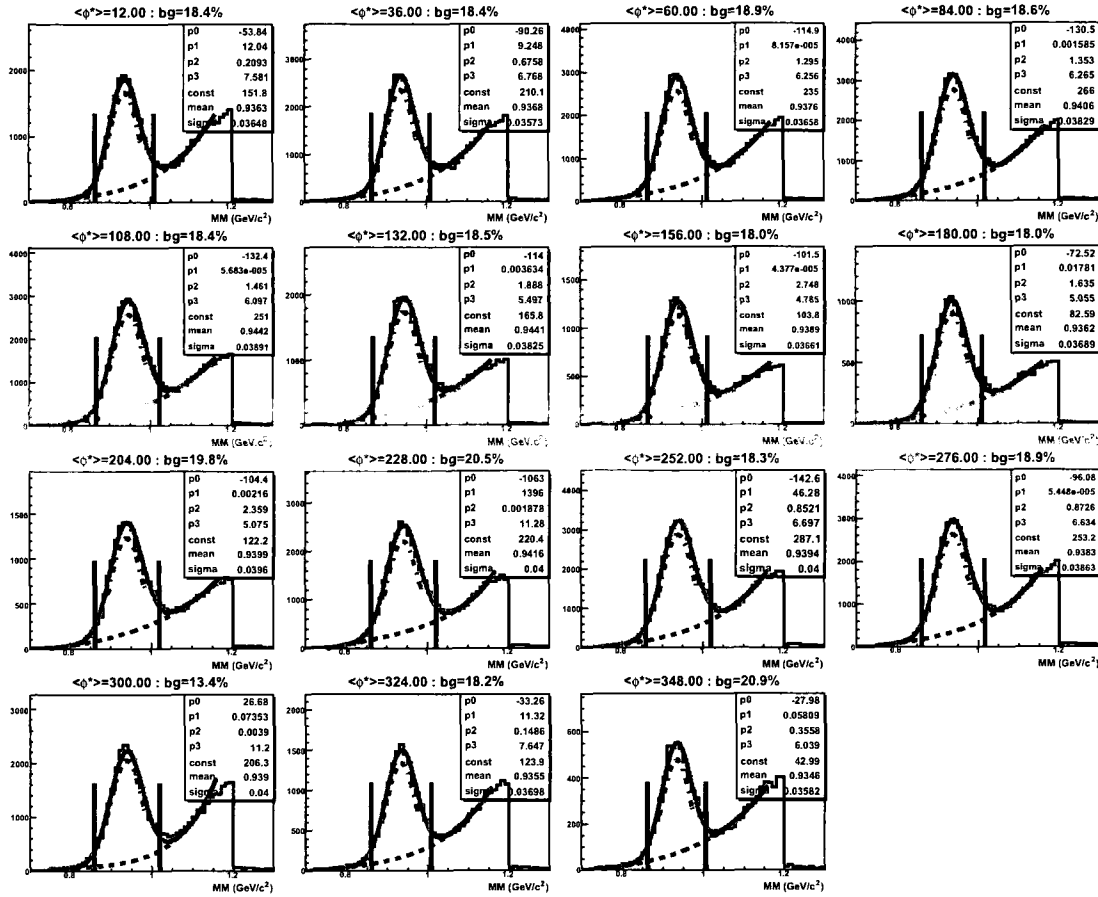


FIG. 106: Same as Fig. 100 except for bins in  $\phi^*$ .

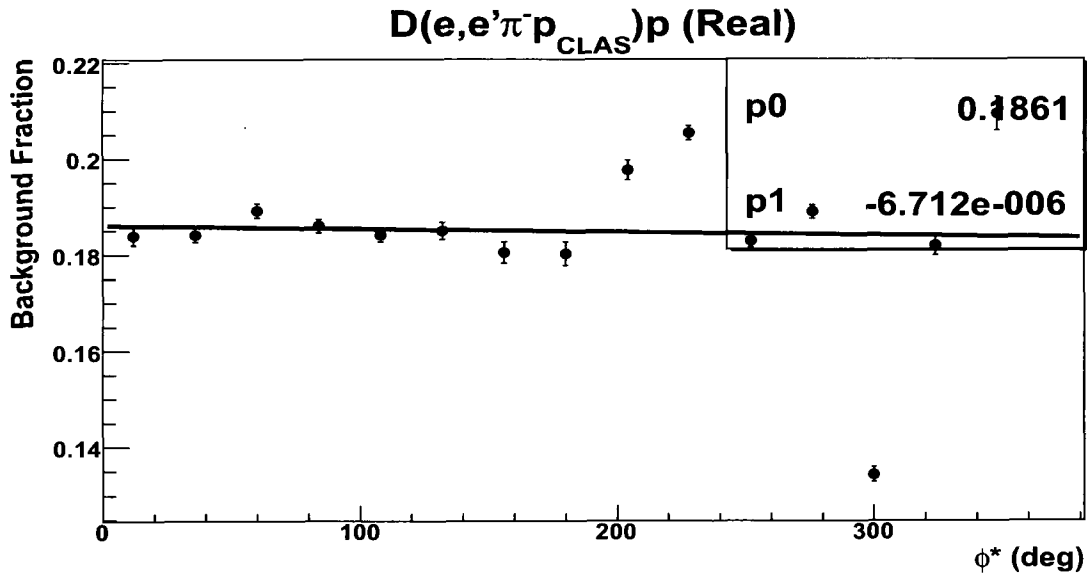


FIG. 107: Same as Fig. 101 except as a function of  $\phi^*$ .

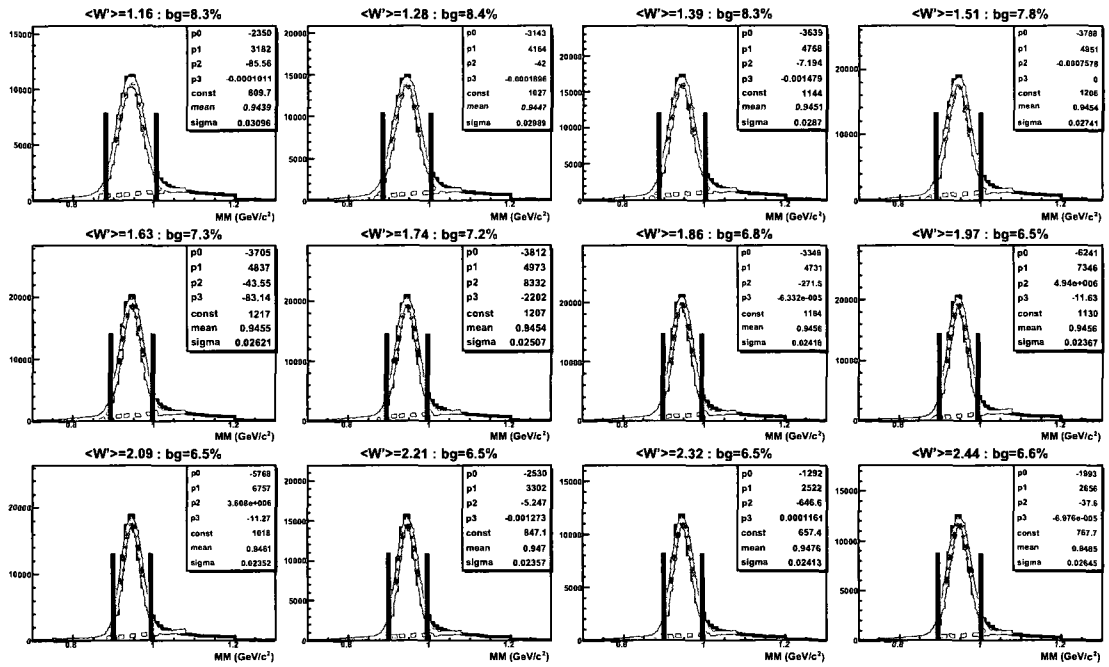


FIG. 108: Missing mass for  $D(e, e'\pi^- p_{\text{CLAS}})X$  events in each  $W'$  bin. The pink solid line indicates the global fit, the blue dash-dot-dash line indicates the gaussian peak and the red dash lines indicate background fit.. The black vertical lines indicate the 2- $\sigma$  cut to select exclusive events. Events shown here are from the 5 GeV simulated data.

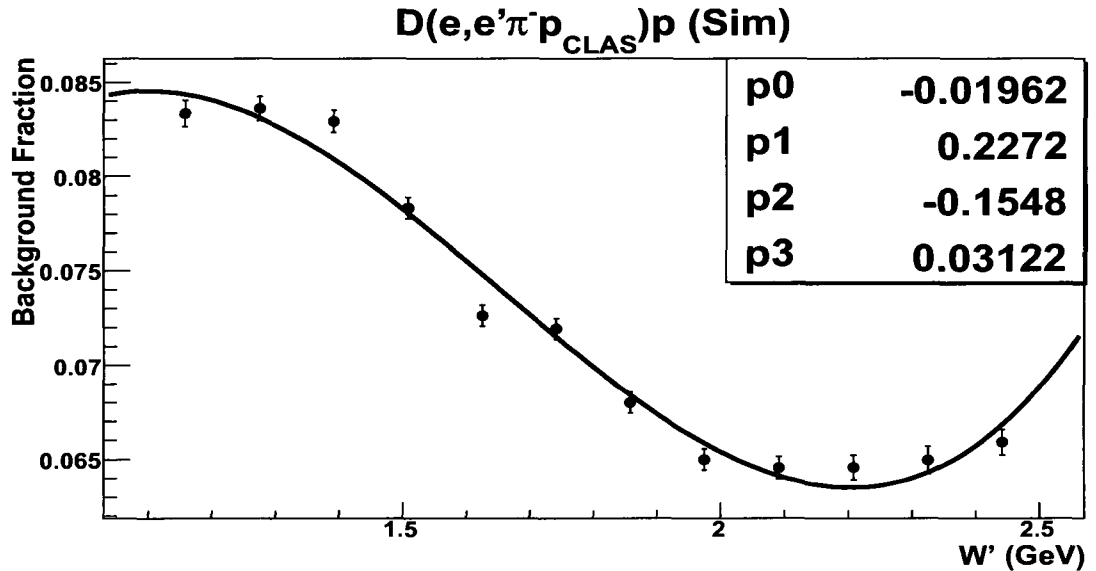


FIG. 109: Background fraction for the 5 GeV  $D(e, e'\pi^- p_{\text{CLAS}})p$  events as a function of  $W'$  using 5 GeV simulated data. The black curve is the fitted function  $f_1^{\text{sim}}$ .

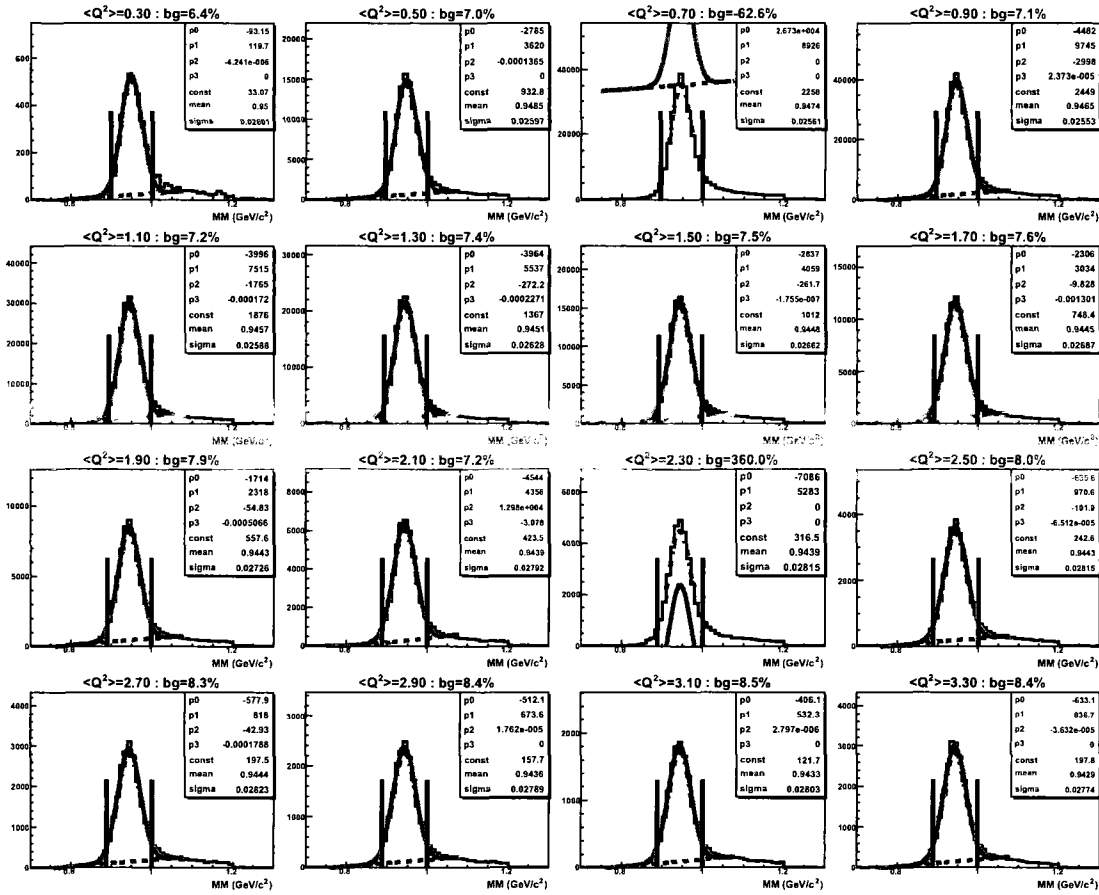


FIG. 110: Same as Fig. 108 except for bins in  $Q^2$ .

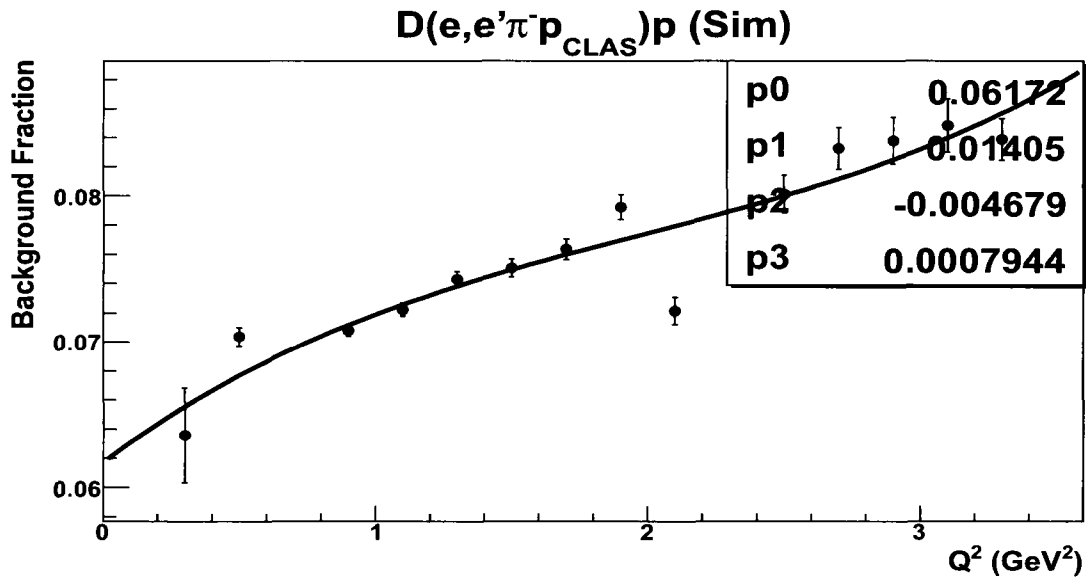


FIG. 111: Same as Fig. 109 except as a function of  $Q^2$ .

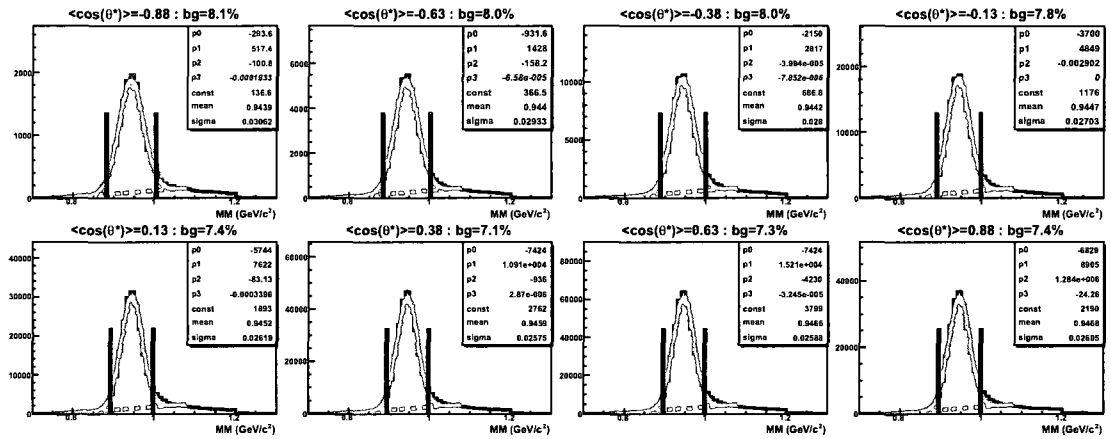


FIG. 112: Same as Fig. 108 except for bins in  $\cos \theta_{\pi}^*$ .

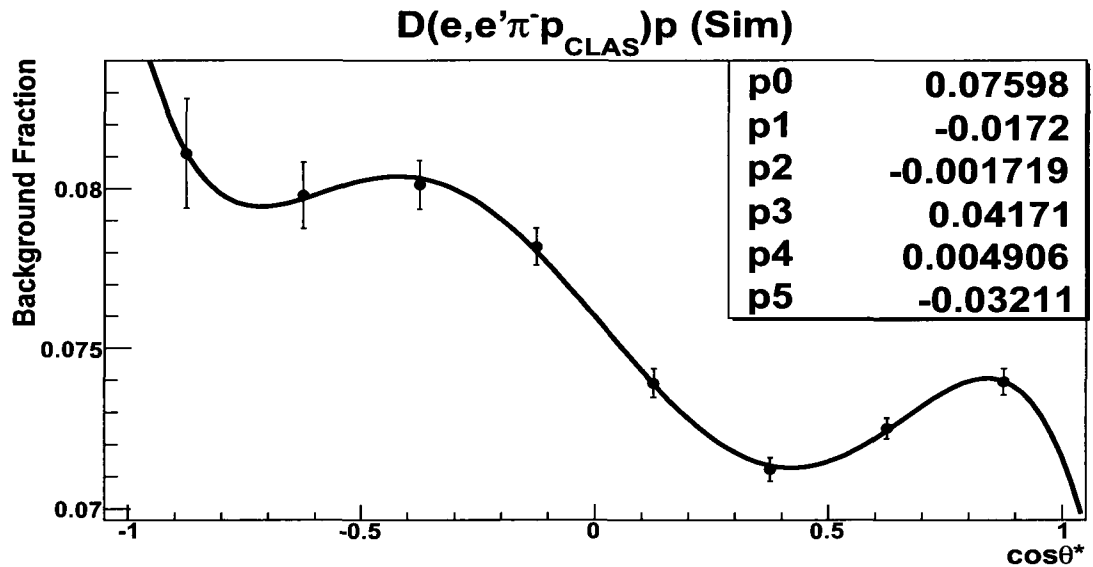


FIG. 113: Same as Fig. 109 except as a function of  $\cos \theta_{\pi}^*$ .

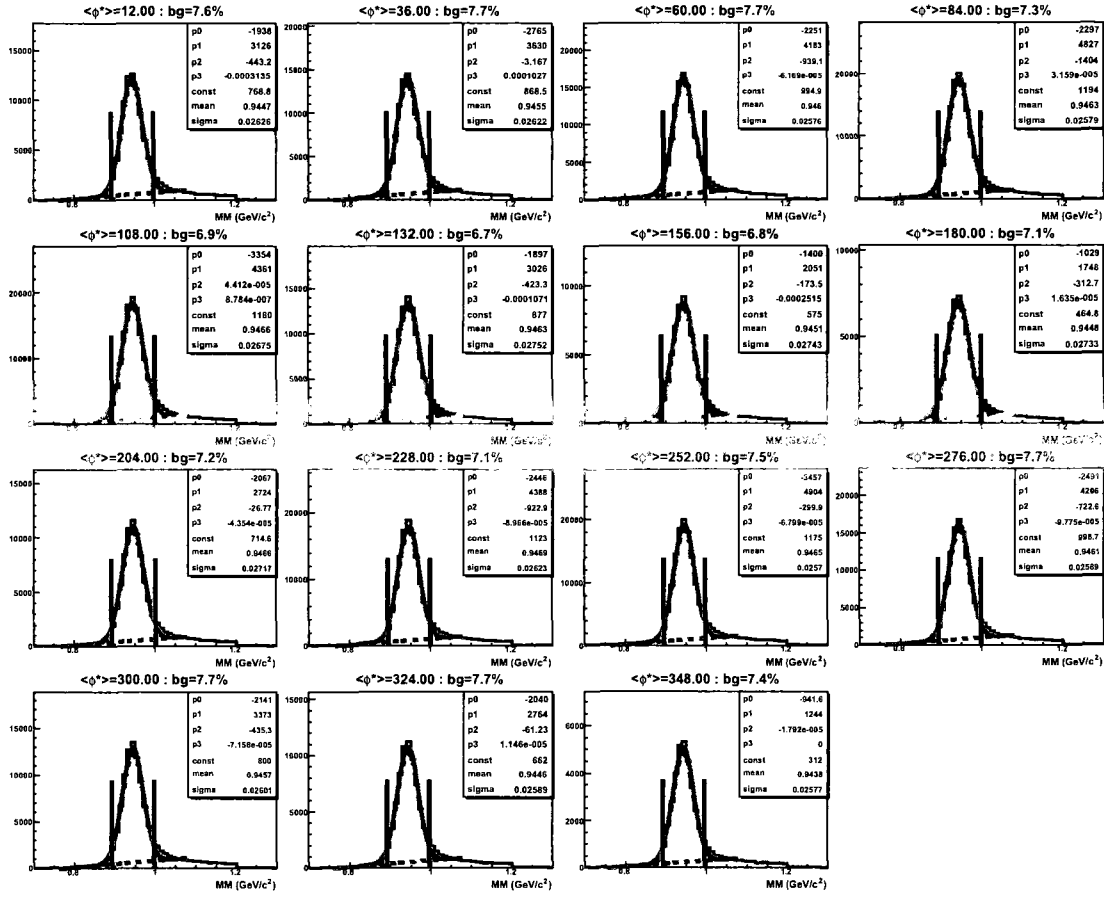


FIG. 114: Same as Fig. 108 except for bins in  $\phi_\pi^*$ .

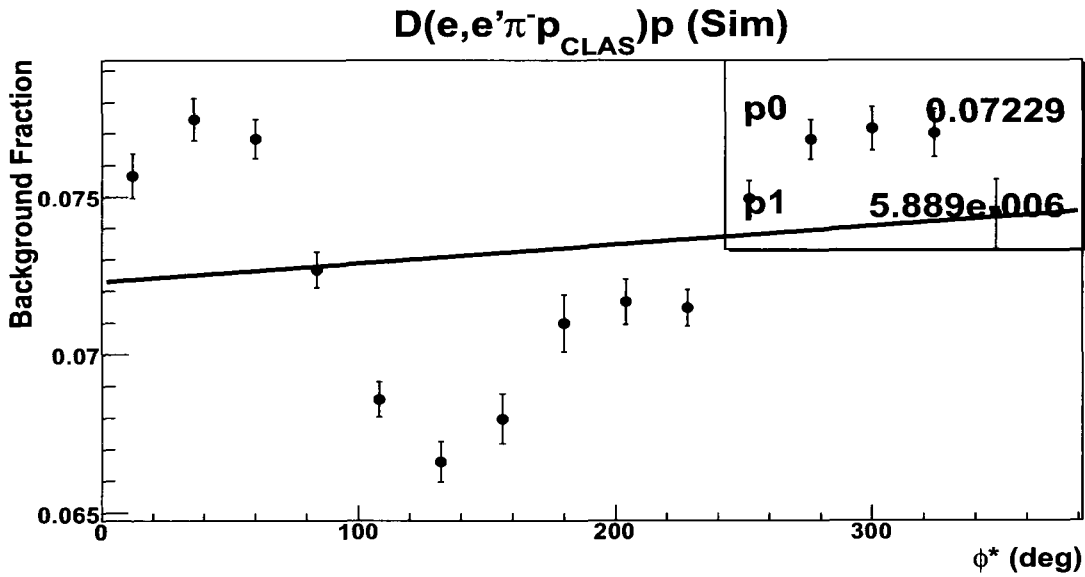


FIG. 115: Same as Fig. 109 except as a function of  $\phi_\pi^*$ .



## V.9 LUMINOSITY

In electron scattering physics, the luminosity is defined as the number of beam particles per unit time times the number of target nuclei per unit area, usually expressed in either CGS units,  $\text{cm}^{-2}\text{s}^{-1}$ , or  $\text{b}^{-1}\text{s}^{-1}$ . The integrated luminosity is the integral of the luminosity with respect to time, and is a very important value in cross section calculations:

$$L_{\text{inte}} = \int L dt = \frac{N_B \times N_{\text{target}}}{A}, \quad (57)$$

where  $N_B$  is the total number of incident electrons,  $N_{\text{target}}$  is the number of target nuclei and  $A$  is the intersection area of the beam and the target. The details of how to calculate the luminosity for the BoNuS experiment will be described in this section.

### V.9.1 Charge Calculation

$N_B$  will be easily known if we have the total incident charge in hand. In Hall B, the total charge is usually measured using the Faraday Cup (FC) at the end of the beam line (see Section III.2). The total charge for one run can be achieved by accumulating all the FC readings. Note that the gain factor of the FC was set to only one-tenth of the typical values in order to utilize high beam current in the BoNuS experiment, the FC readings need to multiply 10.

We only need the charge accumulated when the experiment is “live” and this quantity is available because the FC scaler is always gated on the “experiment live” condition. Sometimes the FC can become too hot while running with high beam current. In order to protect this device a stopper (mass shielding) was placed in front of it for some BoNuS runs. This stopper blocked most of the incident electrons from reaching the FC. To calculate the total charge for the runs with the stopper, one needs to know its penetration efficiency, which is the fraction of the number of incident electrons that reach the Faraday cup. In CLAS, the Beam Position Monitor (BPM), which is placed in front of the target, is another device which can provide the beam current information. If there was no stopper in the beam line, the ratio of the beam current measured by FC to that measured by the BPM should be very close to 1 because very few of the beam electrons are scattered away by the target nuclei.

When the stopper is in the beam line, this ratio,  $\beta$  is the penetration efficiency of the stopper (*cf.* Fig. 116),

$$\beta = \frac{FC_i}{BPM_i}, \quad (58)$$

where  $i$  is an index for the epics event,  $FC_i$  is the live gated Faraday Cup signal and  $BPM_i$  is the gated beam current measured by the BPM at the 2H01 position. We

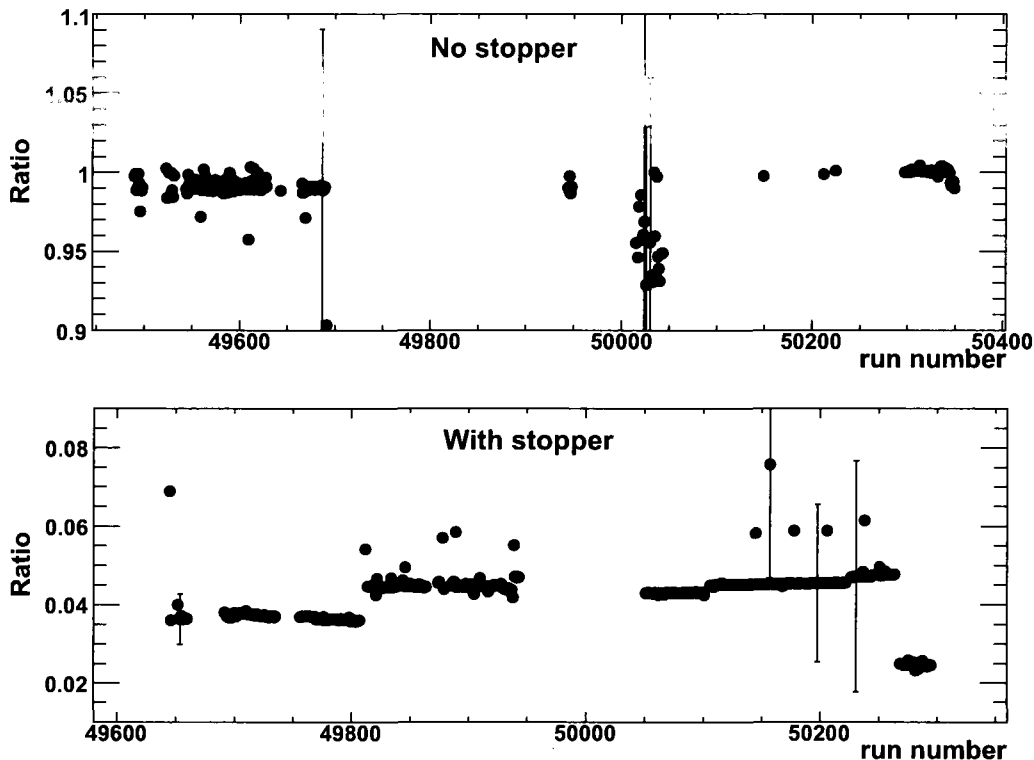


FIG. 116: Ratio of Faraday cup to BPM current for runs without stopper (top) and with stopper (bottom).

expect that the penetration efficiency may depend on beam energy, beam position and the target thickness only. Therefore we grouped our data into various data sets depending on the those quantities and whether or not the stopper was inserted.

We would like to have only one value of the penetration efficiency for each data set. In the experiment the FC and the BPM gave a reading for each scaler event. In each run there are hundreds of epics events. To get a valid effective penetration efficiency for one run, the histogram of FC vs. BPM was fit with a straight line. The slope of the fitted line is  $\beta$ . If this fit was not good, the histogram of the ratio of FC

current to BPM current was fit with a gaussian function, and the mean value of the gaussian was taken as  $\beta$ . Figures 117 and 118 show examples of these fits for runs without and with the stopper, respectively.

The  $\beta$  values for various runs in a data set may fluctuate slightly. These values were fitted to determine a constant  $\bar{\beta}$ , which was used as the penetration efficiency for the whole data set. Figure 119 shows the fitted  $\bar{\beta}$  for 4 GeV runs from 49664 to 49691, without the stopper. Figure 120 shows the corresponding plot for 4 GeV runs from 49692 to 49796, with the stopper inserted.

Usually we calculate the total charge for one run without the stopper using

$$Q_{\text{run}} = \sum FC = q_l, \quad (59)$$

where  $q_l$  is the accumulated “live” gated charge for that run, which is given by RECSIS. The total charge for a run with the stopper needs to be corrected for the penetration efficiency:

$$Q_{\text{run}}^{r\text{stopper}} = \frac{q_l}{\bar{\beta}}. \quad (60)$$

Accumulating the charge for each run in the same data set allowed us to determine the total charge for the whole data set. Figure 121 shows the charge for each run after the penetration efficiency correction.

To check if the total charge calculated above is correct or not, we plot the ratio of the number of good trigger electrons to the total charge with penetration efficiency correction for each run as a function of run number. With the same beam condition and the same type of target, these ratios should not vary. Our result is shown in Fig. 122.

### V.9.2 Target Pressure Calculation

The number of target nuclei can be calculated through the ideal gas law, namely the Clapeyron equation:

$$PV = nRT \quad (61)$$

where  $P$  is the absolute pressure of the gas,  $V$  is the volume,  $n$  is the amount of substance of the gas measured in moles,  $R$  is the gas constant which is equal to  $8.314472 \text{ JK}^{-1}\text{mol}^{-1}$  and  $T$  is the absolute temperature measured in Kelvins. For a

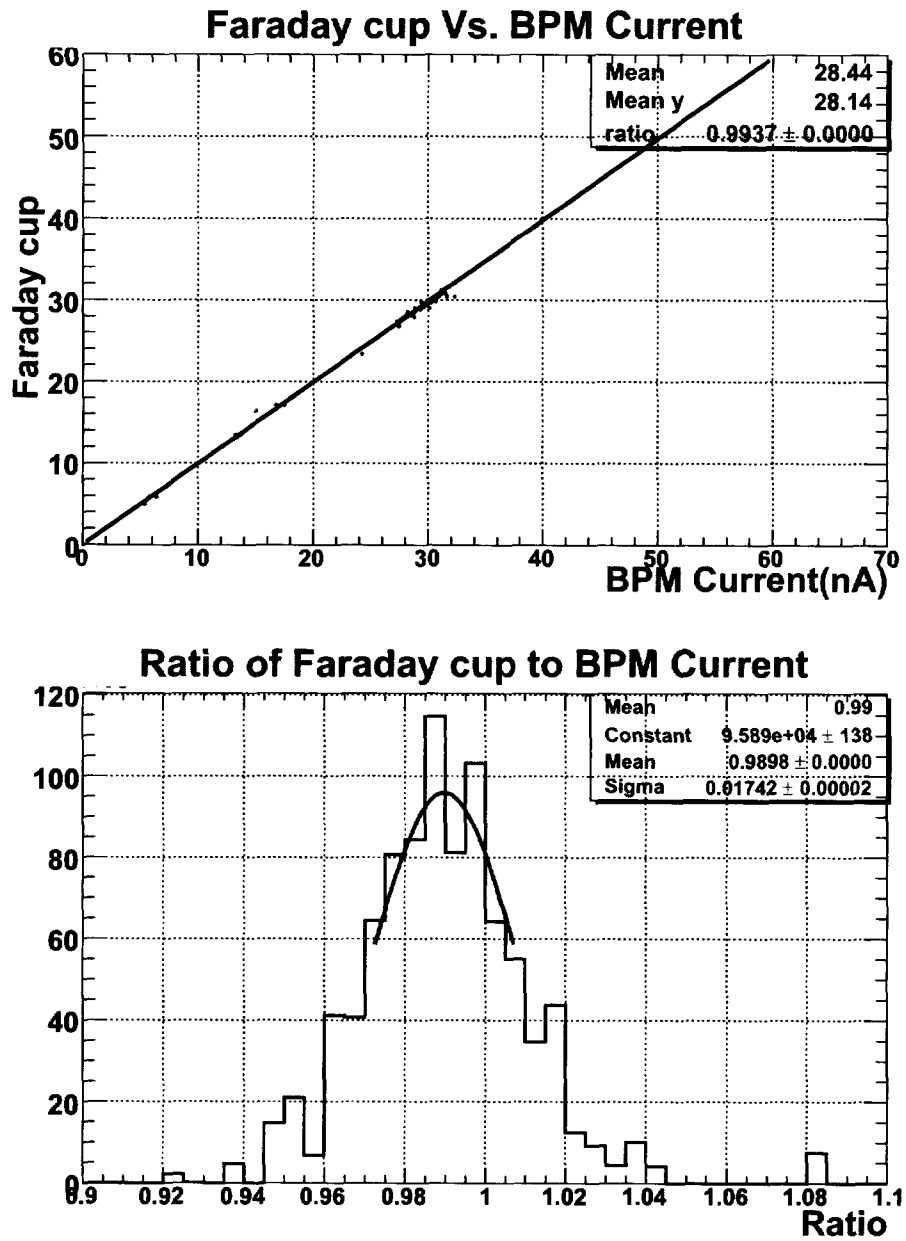


FIG. 117: Distribution of the ratio of FC to BPM for run 49566, without stopper.

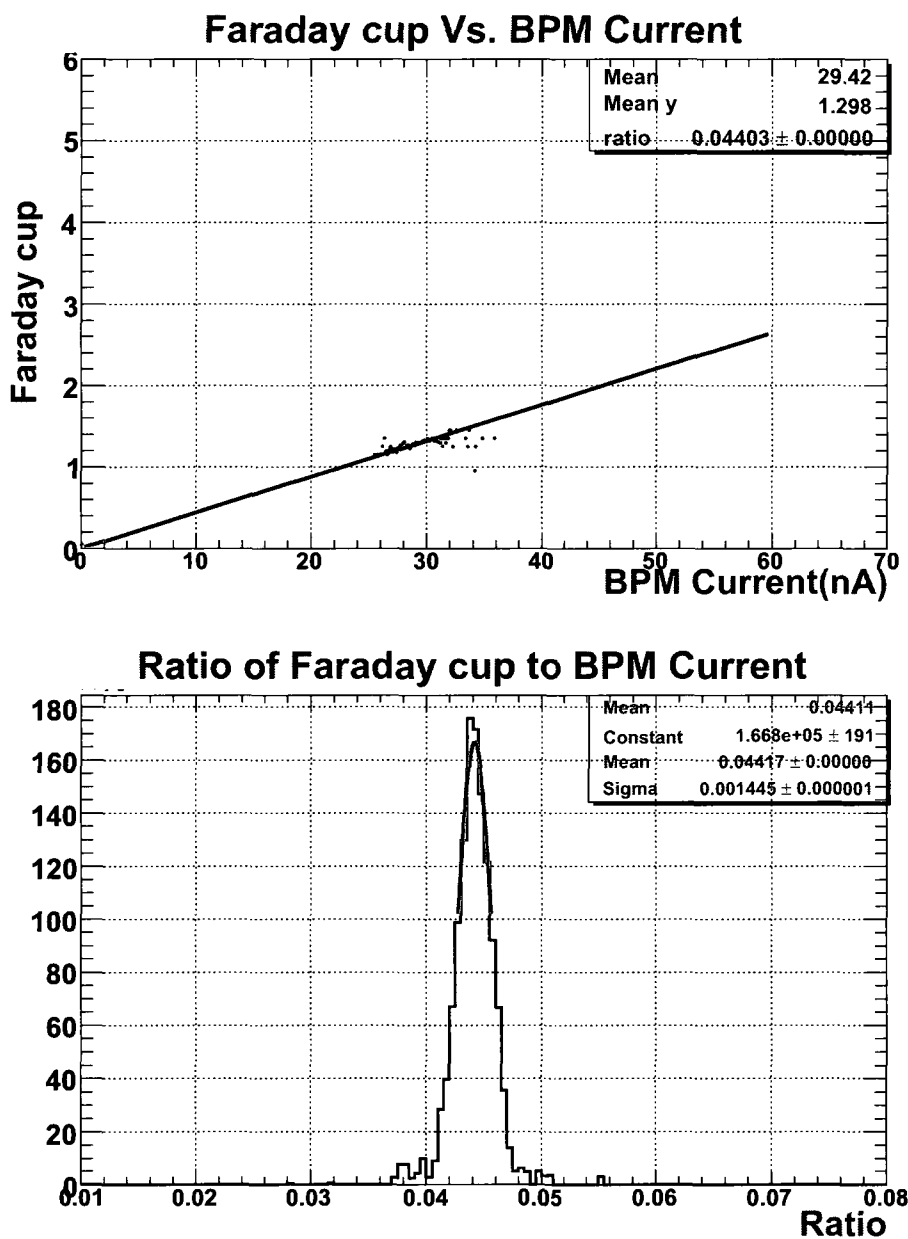


FIG. 118: Distribution of the ratio of FC to BPM for run 49935, with stopper.

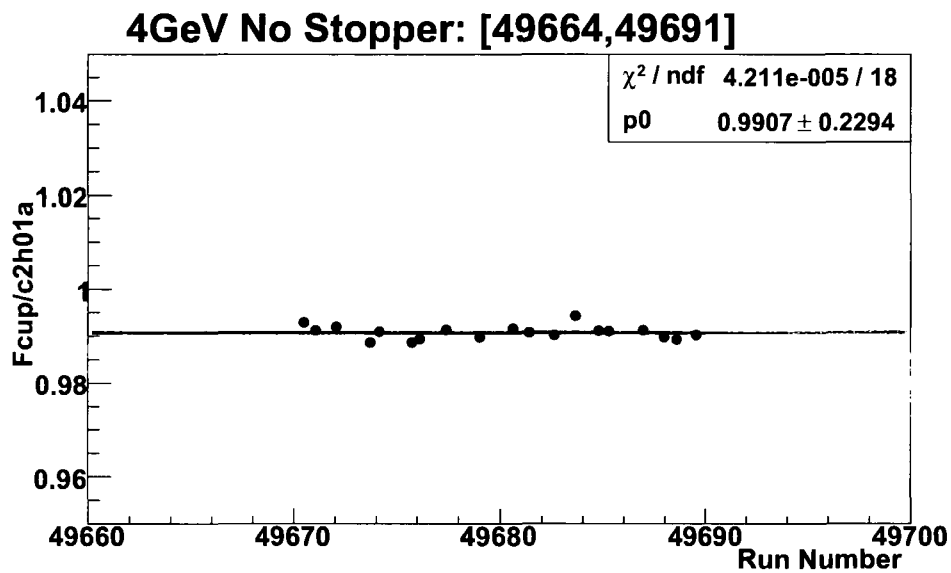


FIG. 119: The fitted penetration efficiency for 4 GeV runs from 49664 to 49691, without stopper.

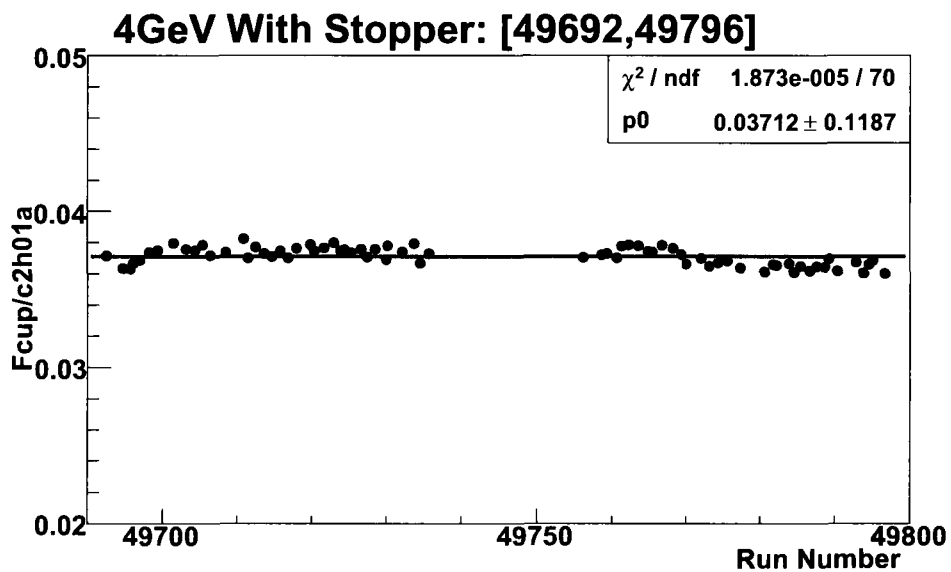


FIG. 120: The fitted penetration efficiency for 4 GeV runs from 49692 to 49796, with stopper.

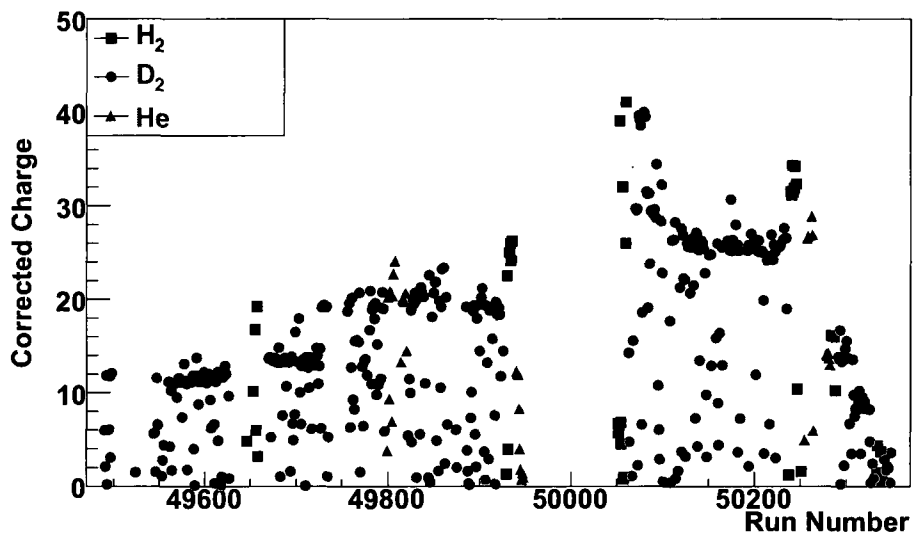


FIG. 121: Charge for each run after the penetration efficiency correction for various targets: the black square points are for hydrogen, the red circle points are for deuterium and the blue triangle points are for helium.

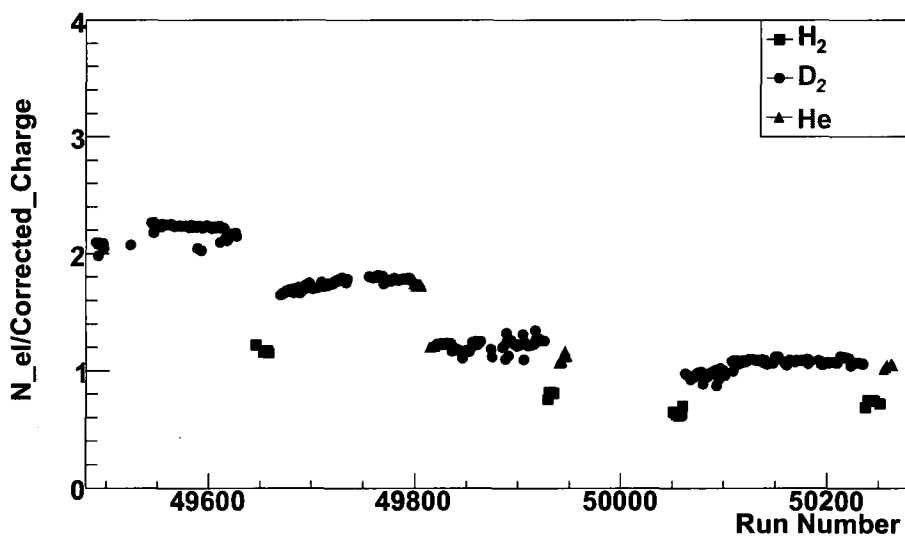


FIG. 122: Ratio of the number of electrons to the total charge after the penetration efficiency correction has been applied for each run.

deuterium target, the number of nuclei is given by

$$N_{\text{target}} = 2nN_A = \frac{2PVN_A}{RT}, \quad (62)$$

where the factor 2 comes from the fact that a deuterium molecule contains two atoms, and  $N_A = 6.02205 \times 10^{23}/\text{mol}$  is Avogadro's Constant. Ignoring the temperature fluctuation of the target system, and choosing the normal room temperature  $293 \pm 5$  Kelvins, it is very straight forward to calculate  $N_{\text{target}}$  if one knows the pressure of the target gas.

As mentioned earlier, we proposed to use a gaseous deuterium target at 7.0 atmosphere and we tried our best to keep this pressure during data taking. Unfortunately, the target system was not perfect and there was a slow leak. The target pressure dropped down from 98 to about 85 psi in about 72 hours so we had to refill the target from time to time. The target pressure was measured in various intervals of 30, 60 or 120 seconds, and these values were averaged to determine the pressure for each run (*cf.* Fig. 123). There are multiple runs in each data set. In order to determine

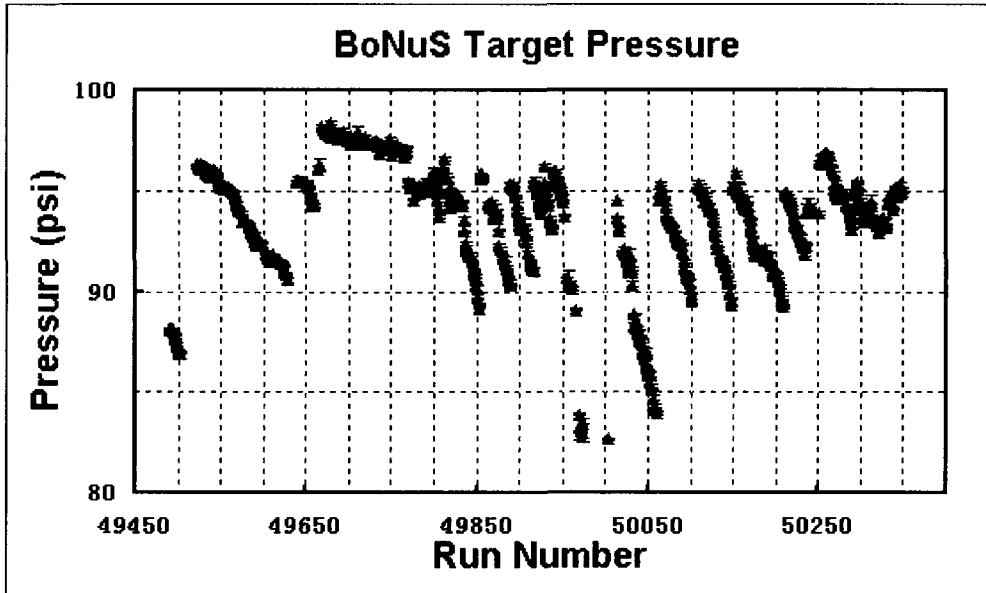


FIG. 123: The target pressure for all runs.

the effective target pressure for the whole data set, the pressure for each run was



weighted by the trigger count for the same run,  $N_{\text{run}}^{\text{el}}$ :

$$P_{\text{eff}} = \frac{\sum_{\text{run}=\text{begin}}^{\text{end}} P_{\text{run}} N_{\text{run}}^{\text{el}}}{\sum_{\text{run}=\text{begin}}^{\text{end}} N_{\text{run}}^{\text{el}}}. \quad (63)$$

The effective pressures calculated with Eq. (63) for each data set are shown in Table 8.

TABLE 8: Effective target pressure

Target	Beam (GeV)	$P_{\text{eff}}$ (psi)
H <sub>2</sub>	1.1	95.350
D <sub>2</sub>	1.1	96.041
H <sub>2</sub>	2.1	95.156
D <sub>2</sub>	2.1	95.104
He	2.1	95.721
H <sub>2</sub>	4.2	95.542
D <sub>2</sub>	4.2	95.874
He	4.2	95.596
H <sub>2</sub>	5.3	92.531
D <sub>2</sub>	5.3	93.635
He	5.3	96.693

### V.9.3 Time Integrated Luminosity

Using the information of beam charge and target pressure calculated above, the time integrated luminosity is given by

$$L = \frac{N_B \times N_{\text{target}}}{A} = \frac{N_B \times 2PVN_A}{ART} = \frac{2N_B PlN_A}{RT}, \quad (64)$$

where  $l$  is the valid target length, which is 16.0 cm. Considering the temperature will have a fluctuation of  $\pm 5$  Kelvins, the uncertainty of this integrated luminosity is about 2%. Table 9 shows the integrated luminosity for various BoNuS data sets with the deuterium target only.

## V.10 CROSS SECTION CALCULATIONS

TABLE 9: Time integrated luminosity for the BoNuS experiment

Beam (GeV)	Luminosity ( $10^{34}/\text{cm}^2$ )
2.1	10158.4
4.2	59060.0
5.3	11303.1

For an unpolarized electron beam and unpolarized deuteron target, the cross section for the exclusive channel  $D(e, e'\pi^-p)p$  is given by

$$\frac{\partial^5 \sigma}{\partial E' \partial \Omega_e \partial \Omega_\pi^*} = \Gamma_v \cdot \frac{\partial^2 \sigma}{\partial \Omega_\pi^*}, \quad (65)$$

with

$$\Gamma_v = \frac{\alpha}{2\pi^2} \frac{E'}{E} \frac{K_\gamma}{Q^2} \frac{1}{1-\varepsilon}, \quad (66)$$

$$\frac{\partial^2 \sigma}{\partial \Omega_\pi^*} = \sigma_T + \varepsilon \sigma_L + \sqrt{2\varepsilon(1+\varepsilon)} \sigma_{LT} \cos \phi_\pi^* + \varepsilon \sigma_{TT} \cos 2\phi_\pi^*, \quad (67)$$

where  $\Gamma_v$  is the virtual photon flux and  $\frac{\partial^2 \sigma}{\partial \Omega_\pi^*}$  is the differential pion photo-absorption cross section. In the above equations,  $\alpha = 1/137$  is the electromagnetic coupling constant. We have introduced the ‘‘photon equivalent energy’’,  $K_\gamma = (W^2 - M_n^2)/2M_n$ , the laboratory energy necessary for a real photon to excite a hadronic system with center of mass energy  $W$ . The degree of longitudinal polarization of the virtual photon is represented by

$$\varepsilon = \left(1 + \frac{2\mathbf{q}^2}{Q^2} \tan^2 \frac{\theta_e}{2}\right)^{-1},$$

which is frame independent.

As described earlier, the data were binned in  $W'$ ,  $Q^2$ ,  $\cos \theta_\pi^*$  and  $\phi_\pi^*$ . The cross section was determined as

$$\sigma(W', Q^2, \theta_\pi^*, \phi_\pi^*) = \frac{N(W', Q^2, \theta_\pi^*, \phi_\pi^*)}{LA(W', Q^2, \theta_\pi^*, \phi_\pi^*)}, \quad (68)$$

where  $N(W', Q^2, \theta_\pi^*, \phi_\pi^*)$  is the number of  $D(e, e'\pi^-p)p$  events in the given bin,  $A(W', Q^2, \theta_\pi^*, \phi_\pi^*)$  is the acceptance of the same bin and  $L$  is the time integrated luminosity, as given in 64. The statistical uncertainty of the differential cross section is given by

$$\delta\sigma(W', Q^2, \theta_\pi^*, \phi_\pi^*) = \frac{\sigma(W', Q^2, \theta_\pi^*, \phi_\pi^*)}{\sqrt{N(W', Q^2, \theta_\pi^*, \phi_\pi^*)}}. \quad (69)$$

The cross section for the exclusive reaction  $D(e, e' \pi^- p)$  in each bin is the main result of this work. However, we have also studied the  $\phi_\pi^*$  dependence of the cross section as described in Chapter VI.

## V.11 RADIATIVE CORRECTIONS

After the cross section is extracted from the data, one more correction, the radiative correction, needs to be applied. The electron can radiate a photon in the presence of the nuclear electromagnetic field which changes the cross section. Electrons can radiate real or virtual photons either in the electromagnetic (Coulomb) field of the nucleus involved in the reaction (internal bremsstrahlung) or in the electromagnetic field of the other nuclei (external bremsstrahlung). Also the electron-target interaction followed by the ionization of the target atoms results in electron energy losses (Landau straggling).

The radiative correction calculation was done by Andrei Afanasev [79]. He estimated of the radiative correction to the cross section for pion electro-production to be  $0.81 \pm 0.04$ , which means we had to divide the experimental cross section by 0.81 to recover a leading-order one-photon-exchange cross section. This correction includes radiation in a soft-photon approximation, which makes the prediction model-independent. There may be about 5% additional correction due to hard photon emission that would depend on the form of the cross section that enters the integral.

## V.12 SYSTEMATIC ERROR EVALUATION

This section describes the systematic errors in determining the cross section. The systematic errors may come from different cuts, corrections, algorithms and calibrations. The systematic errors due to the missing mass cut, background subtraction, acceptance cut, radiative corrections and particle (electron,  $\pi^-$  and proton) identifications are presented below.

- The electron identification and detection efficiency has uncertainty of about 8%, as estimated by S. Tkachenko [63].

- The missing mass cut was varied to determine the effect of that cut. In general a 5% uncertainty was observed, but it varies from bin to bin.
- The background subtraction was changed by using a 3rd order polynomial fitting function instead of the standard exponential function to fit the background. The effect on the cross section varies for each bin. In a few bins the effect is as large as 60% but for most bins it is about 5%.
- The acceptance had a big effect on the measured cross section in each bin. To estimate the systematic uncertainty from the acceptance, we recalculated the acceptance without the weighting factor described in Sections IV.5.2 and V.6. This change should be most critical in regions where the acceptance is varying. In general we observed a 10% effect from this change but the systematic uncertainty varies from bin to bin.
- Since the temperature in the hall fluctuated by about  $\pm 5$  Kelvins, we estimated a 2% uncertainty in the luminosity, which eventually would contribute about 2% uncertainty in the final cross section.
- The radiative correction calculated by A. Afanasev was estimated to have a 5% uncertainty in the cross section.

TABLE 10: Summary of the systematic errors for the 5GeV data set

Uncertainty source	Uncertainty
Electron identification and detection efficiency	8%
Acceptance	10%
Missing mass cut	5%
Background subtractions	5%
Luminosity	2%
Radiative corrections	5%
Total	15%

Table 10 summarizes the systematic errors. In the next chapter we present our result for the differential cross section and describe a fitting procedure which we used to extract the structure functions  $\sigma_T + \varepsilon\sigma_L$ ,  $\sigma_{LT}$  and  $\sigma_{TT}$ .

## CHAPTER VI

### PHYSICS RESULTS

#### VI.1 DIFFERENTIAL CROSS SECTION

The formalism for the differential cross section for  $\pi^-$  unpolarized electro-production has been described in Section V.10. In a given four dimensional (4-D) bin of  $W'$ ,  $Q^2$ ,  $\cos\theta_\pi^*$  and  $\phi_\pi^*$ , the differential cross section in this analysis is calculated as

$$d^5\sigma \Delta E' \Delta \Omega_e \Delta \Omega_\pi^* = \int \Gamma_\nu dE' d\Omega_e \int \frac{\partial^2 \sigma}{\partial \Omega_\pi^*} d\Omega_\pi^*. \quad (70)$$

Lets define a correction factor for each event in the  $D(e, e'\pi^- p_{\text{CLAS}})p$  or  $D(e, e'\pi^- p_{\text{RTPC}})p$  reactions as

$$\lambda_{\text{CLAS}} = \frac{B}{R \cdot \eta_e \cdot \eta_\pi \cdot \eta_p^{r2s} \cdot A}; \quad (71)$$

$$\lambda_{\text{RTPC}} = \frac{B}{R \cdot \eta_e \cdot \eta_\pi \cdot \eta_{\text{RTPC}}^{r2s} \cdot A}, \quad (72)$$

where  $R = 0.81$  is the average radiative correction (see Section V.11),  $\eta_e(p_e, \theta_e)$  and  $\eta_\pi(p_\pi, \theta_\pi)$  are the detection efficiencies for the trigger electrons and  $\pi^-$ , respectively, and  $\eta_p(p_p, \theta_p)$  and  $\eta_{\text{RTPC}}(p_{ps}, \theta_{pq})$  are the detection efficiency super ratios of experimental to simulated data for the CLAS protons and RTPC protons, respectively. Each of these detection efficiencies has its own kinematic dependence.  $B(W', Q^2, \cos\theta_\pi^*, \phi_\pi^*)$  is the background correction factor, which is the fraction of good data (no background) to the total (good + background), as described in V.8.  $A(W', Q^2, \cos\theta_\pi^*, \phi_\pi^*)$  is the acceptance of the reaction to which the event belongs. With these definitions, the effective number of events detected in the given 4-D bin is given as

$$N_{eff} = \sum_{events} (1 \cdot \lambda),$$

where  $\lambda$  is either  $\lambda_{\text{CLAS}}$  or  $\lambda_{\text{RTPC}}$  depending on the reaction. Then we have

$$N_{eff} = L \int \Gamma_v dE' d\Omega_e \int \frac{\partial^2 \sigma}{\partial \Omega_\pi^*} d\Omega_\pi^*, \quad (73)$$

$$= L \int \Gamma_v \left| \frac{\partial E'}{\partial W'} \quad \frac{\partial E'}{\partial Q^2} \right| dW' dQ^2 \int \frac{\partial^2 \sigma}{\partial \Omega_\pi^*} d\cos \theta_\pi^* d\phi_\pi^*, \quad (74)$$

$$= L \int \Gamma_v \frac{\pi W'}{EE' M_n} dW' dQ^2 \int \frac{\partial^2 \sigma}{\partial \Omega_\pi^*} d\cos \theta_\pi^* d\phi_\pi^*, \quad (75)$$

$$= L\tau \int \frac{\partial^2 \sigma}{\partial \Omega_\pi^*} d\cos \theta_\pi^* d\phi_\pi^*, \quad (76)$$

where  $L$  is the time integrated luminosity and  $\tau$  is the virtual photon flux integrated over a given  $W'$  and  $Q^2$  range:

$$\tau = \int \Gamma_v \frac{\pi W'}{EE' M_n} dW' dQ^2 \quad (77)$$

$$= \int \frac{\alpha}{2\pi^2} \frac{E'}{E} \frac{W'^2 - M_n^2}{2M_n Q^2} \frac{1}{1 - \varepsilon} \frac{\pi W'}{EE' M_n} dW' dQ^2 \quad (78)$$

$$= \frac{\alpha}{4\pi E^2 M_n^2} \int \frac{(W'^2 - M_n^2) W'}{Q^2 (1 - \varepsilon)} dW' dQ^2 \quad (79)$$

$$= \frac{\alpha}{8\pi E^2 M_n^2} \int \frac{W'^2 - M_n^2}{Q^2 (1 - \varepsilon)} dW'^2 dQ^2. \quad (80)$$

In this analysis, the cross section is considered to be a single value in the given bin by which Eq. (76) can be simplified as

$$\sum_{events} (1 \cdot \lambda) = L\tau \Delta(\cos \theta_\pi^*) \Delta\phi_\pi^* \frac{\partial^2 \sigma}{\partial \Omega_\pi^*} \quad (81)$$

or

$$\frac{\partial^2 \sigma}{\partial \Omega_\pi^*} = \frac{\sum_{events} (1 \cdot \lambda)}{L\tau \Delta(\cos \theta_\pi^*) \Delta\phi_\pi^*}. \quad (82)$$

The differential cross sections are calculated according to Eq. (82) for the 2, 4 and 5 GeV data sets. They are shown as a function of  $\phi_\pi^*$  from Figs. 124 to 132 for three bins in  $W'$  corresponding to interesting areas of the resonance region. Cross sections for other  $W'$  bins were also extracted but not all of them are shown here. Predictions from the MAID07 (black curve) and SAID08 (purple curve) models are also shown. Note that the blue triangles corresponding to the  $D(e, e'\pi^- p_{\text{RTPC}})p$  reaction and that the red squares corresponding to the  $D(e, e'\pi^- p_{\text{CLAS}})p$  reaction. In general the two channels are consistent with each other, given the statistical and systematic uncertainties. The differential cross sections for the 2 GeV data set show

much less strength than predicted by the models, which may indicate a normalization or acceptance problem in the data. The results for the 4 and 5 GeV data sets seem to qualitatively agree with both models. The acceptance near  $\phi_\pi^* = 180^\circ$  is too small to pass the acceptance cut in most bins, which causes the differential cross section measurements to have a hole in these bins. This may affect the attempts to fit for the structure functions  $\sigma_T + \varepsilon\sigma_L$ ,  $\sigma_{LT}$  and  $\sigma_{TT}$ , which will be described later.

One can see that the cross section decreases with increasing  $Q^2$  in all three resonance regions, as expected. The bin centered at  $W' = 1.230$  corresponds to the  $\Delta(1232)$  resonance and should be well described by the models, which is what we see for the 4 GeV data. The 5 GeV data in the  $\Delta(1232)$  resonance region show more strength than predicted by the models, especially at the forward  $\theta_\pi^*$ . The  $W' = 1.525$  bin covers part of the 2nd resonance region where the  $S_{11}(1535)$  and  $D_{13}(1520)$  are particularly strong. Here we see that again the models underestimate the data, especially for the 5 GeV at the forward  $\theta_\pi^*$  angle. This trend is also seen in the  $W' = 1.675$  bin, which corresponds to the third resonance region (*cf.* Figs. 129 and 132).

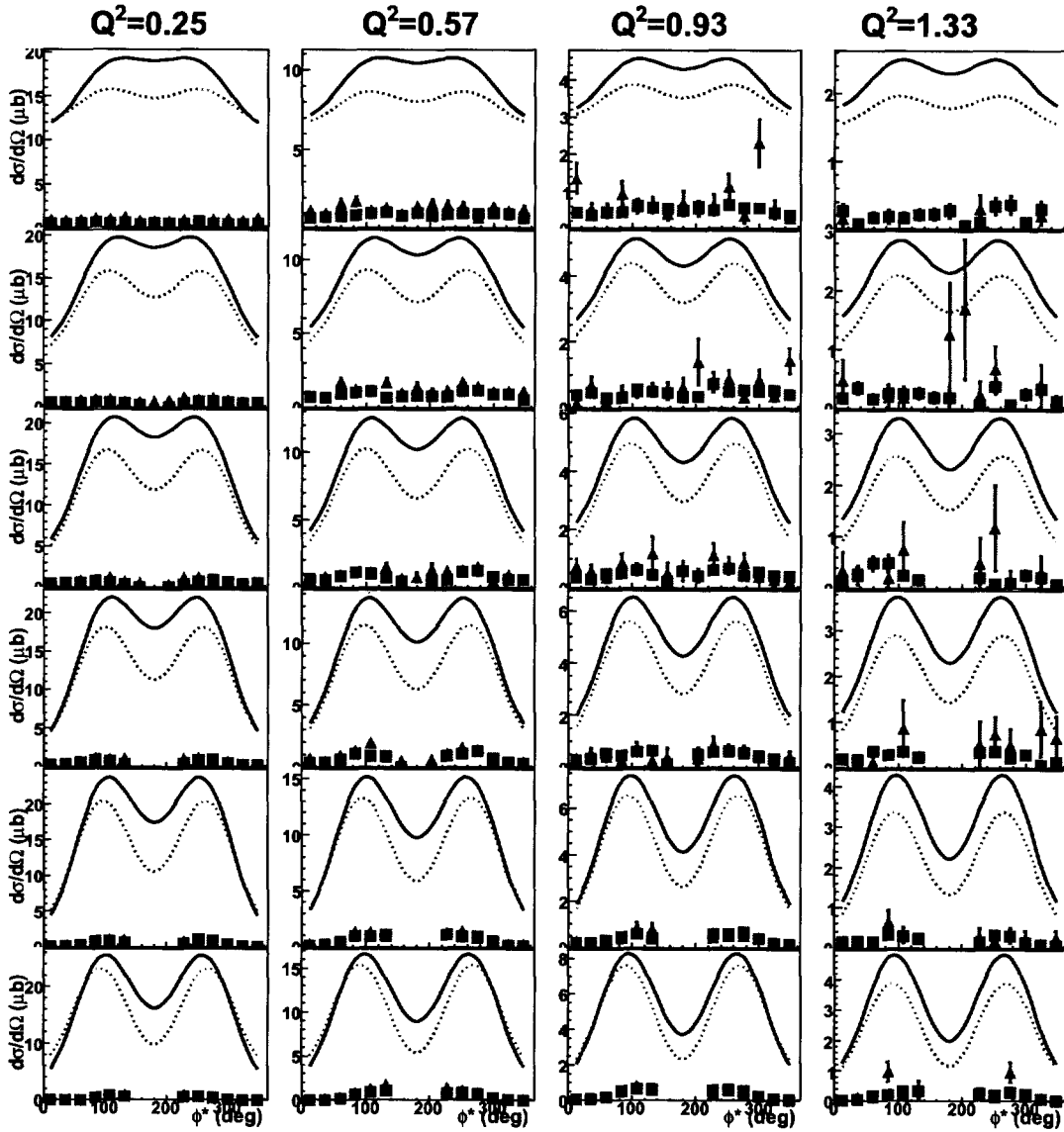


FIG. 124: Differential cross section vs.  $\phi_\pi^*$  at  $W' = 1.230$  and various  $\cos\theta_\pi^*$  and  $Q^2$  bins for the 2 GeV data set. The  $\cos\theta_\pi^*$  values are 0.100, 0.425, 0.625, 0.750, 0.850 and 0.950, increasing from the bottom to the top panel. The black solid curve is the MAID07 prediction and the pink dash line is the SAID08 prediction. The red squares and blue triangles represent  $D(e, e'\pi^- p_{CLAS})p$  and  $D(e, e'\pi^- p_{RTPC})p$  measurements, respectively.



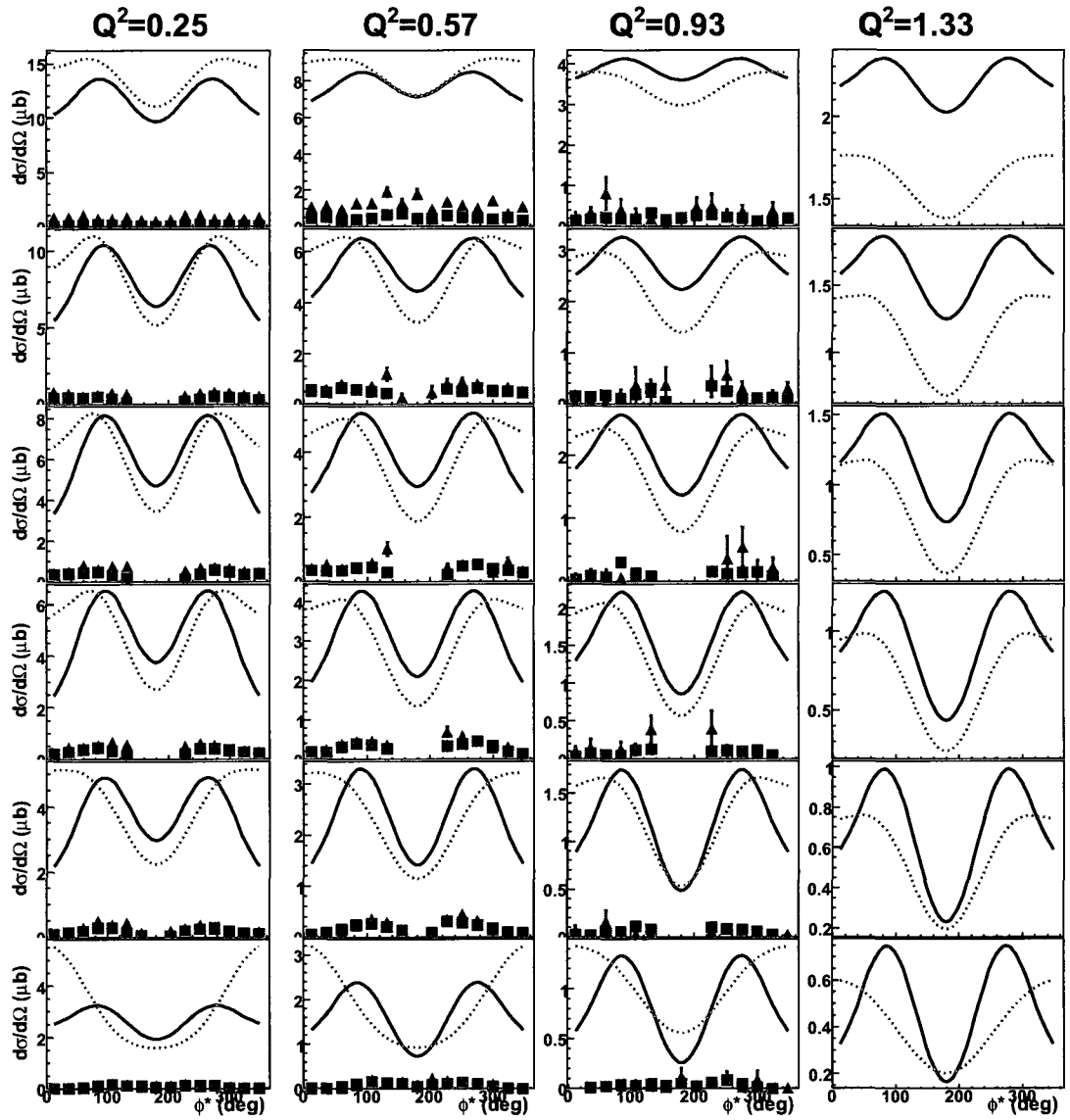


FIG. 125: Differential cross section vs.  $\phi_\pi^*$  at  $W' = 1.525$  and various  $\cos\theta_\pi^*$  and  $Q^2$  bins for the 2 GeV data set. The  $\cos\theta_\pi^*$  values are 0.100, 0.425, 0.625, 0.750, 0.850 and 0.950, increasing from the bottom to the top panel. The black solid curve is the MAID07 prediction and the pink dash line is the SAID08 prediction. The red squares and blue triangles represent  $D(e, e'\pi^- p_{\text{CLAS}})p$  and  $D(e, e'\pi^- p_{\text{RTPC}})p$  measurements, respectively.

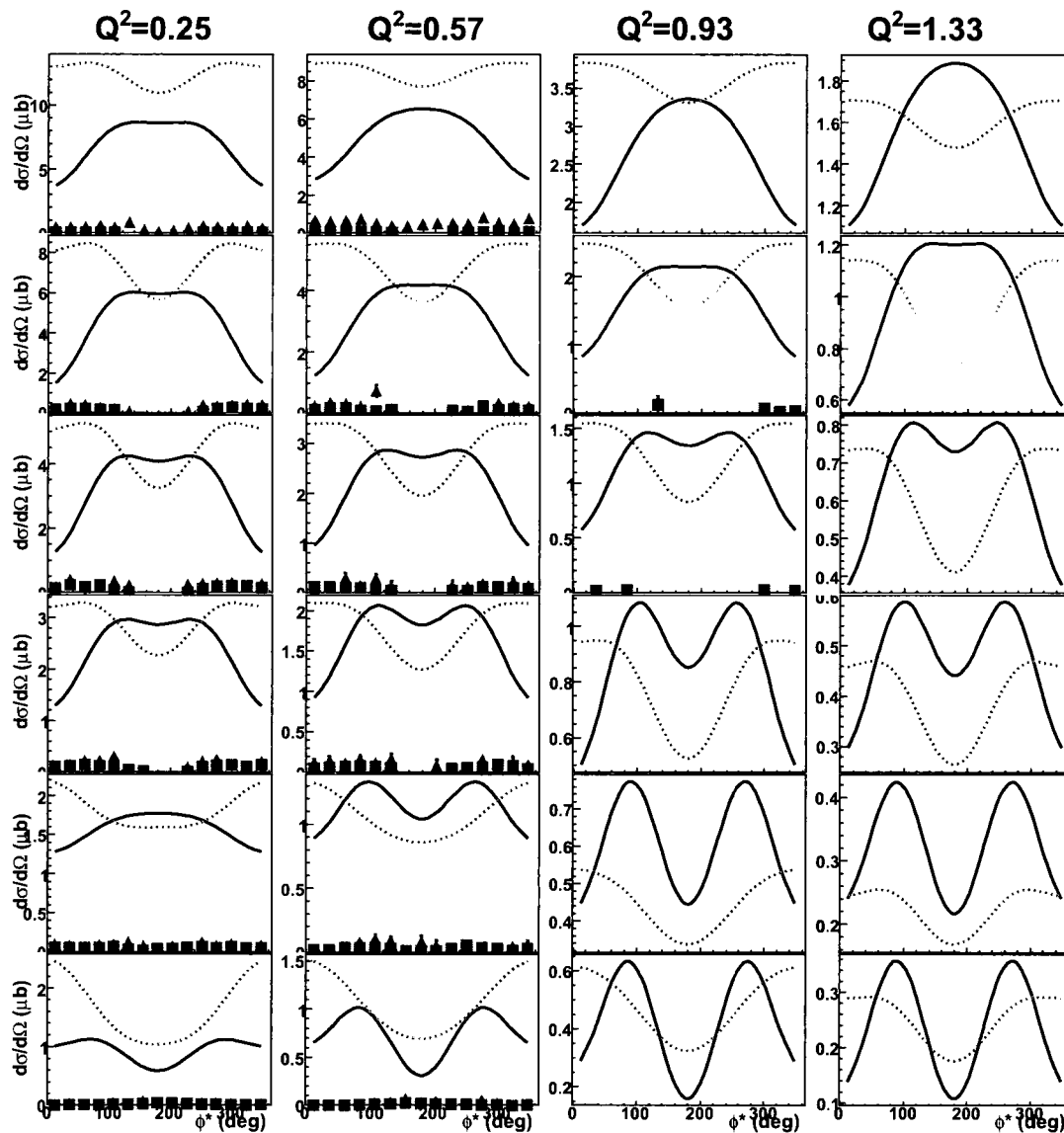


FIG. 126: Differential cross section vs.  $\phi_\pi^*$  at  $W' = 1.675$  and various  $\cos\theta_\pi^*$  and  $Q^2$  bins for the 2 GeV data set. The  $\cos\theta_\pi^*$  values are 0.100, 0.425, 0.625, 0.750, 0.850 and 0.950, increasing from the bottom to the top panel. The black solid curve is the MAID07 prediction and the pink dash line is the SAID08 prediction. The red squares and blue triangles represent  $D(e, e'\pi^- p_{\text{CLAS}})p$  and  $D(e, e'\pi^- p_{\text{RTPC}})p$  measurements, respectively.

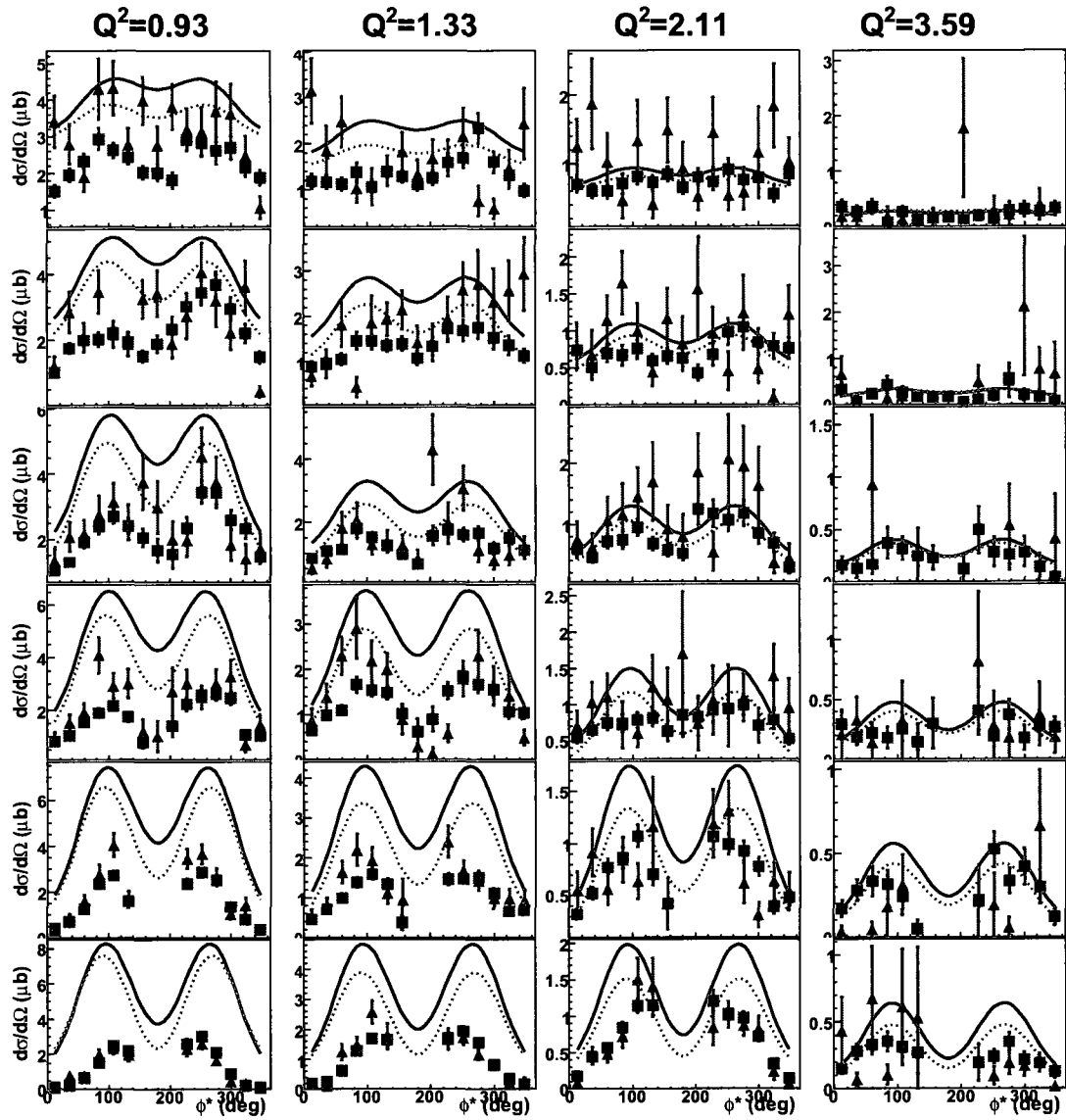


FIG. 127: Differential cross section vs.  $\phi_\pi^*$  at  $W' = 1.230$  and various  $\cos\theta_\pi^*$  and  $Q^2$  bins for the 4 GeV data set. The  $\cos\theta_\pi^*$  values are 0.100, 0.425, 0.625, 0.750, 0.850 and 0.950, increasing from the bottom to the top panel. The black solid curve is the MAID07 prediction and the pink dash line is the SAID08 prediction. The red squares and blue triangles represent  $D(e, e'\pi^- p_{\text{CLAS}})p$  and  $D(e, e'\pi^- p_{\text{RTPC}})p$  measurements, respectively.

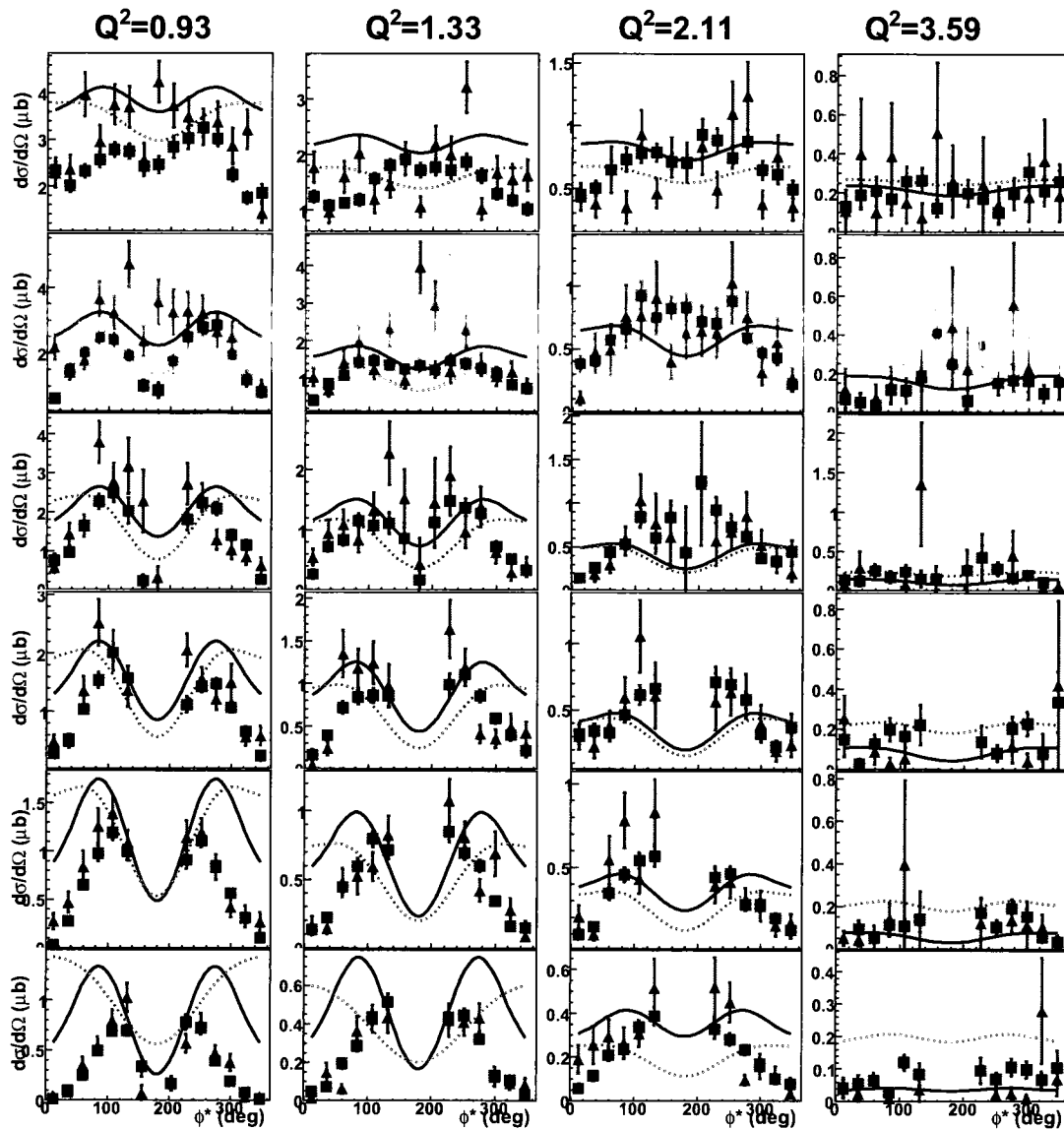


FIG. 128: Differential cross section vs.  $\phi_\pi^*$  at  $W' = 1.525$  and various  $\cos\theta_\pi^*$  and  $Q^2$  bins for the 4 GeV data set. The  $\cos\theta_\pi^*$  values are 0.100, 0.425, 0.625, 0.750, 0.850 and 0.950, increasing from the bottom to the top panel. The black solid curve is the MAID07 prediction and the pink dash line is the SAID08 prediction. The red squares and blue triangles represent  $D(e, e'\pi^- p_{\text{CLAS}})p$  and  $D(e, e'\pi^- p_{\text{RTPC}})p$  measurements, respectively.

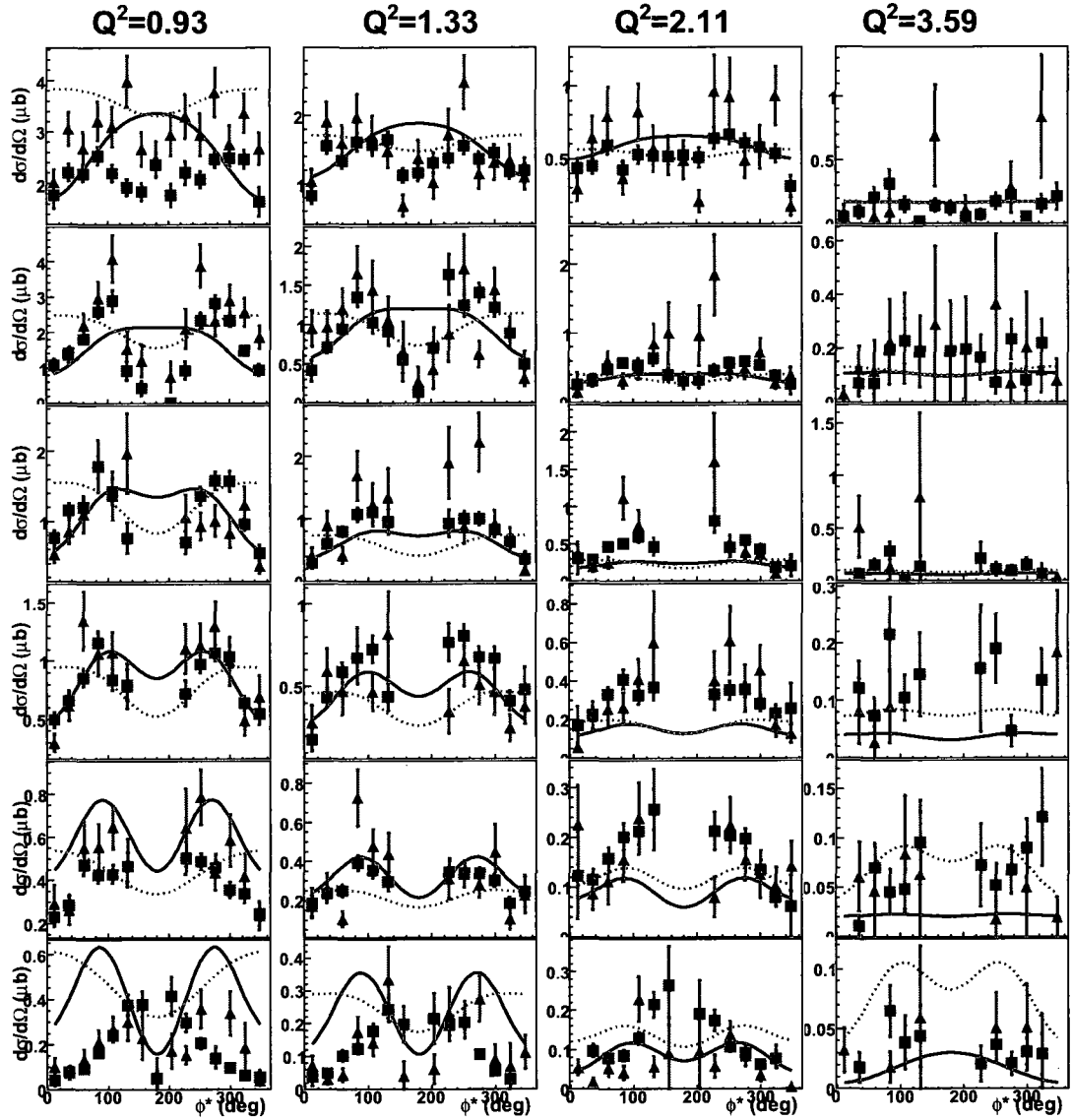


FIG. 129: Differential cross section vs.  $\phi_\pi^*$  at  $W' = 1.675$  and various  $\cos\theta_\pi^*$  and  $Q^2$  bins for the 4 GeV data set. The  $\cos\theta_\pi^*$  values are 0.100, 0.425, 0.625, 0.750, 0.850 and 0.950, increasing from the bottom to the top panel. The black solid curve is the MAID07 prediction and the pink dash line is the SAID08 prediction. The red squares and blue triangles represent  $D(e, e'\pi^- p_{\text{CLAS}})p$  and  $D(e, e'\pi^- p_{\text{RTPC}})p$  measurements, respectively.

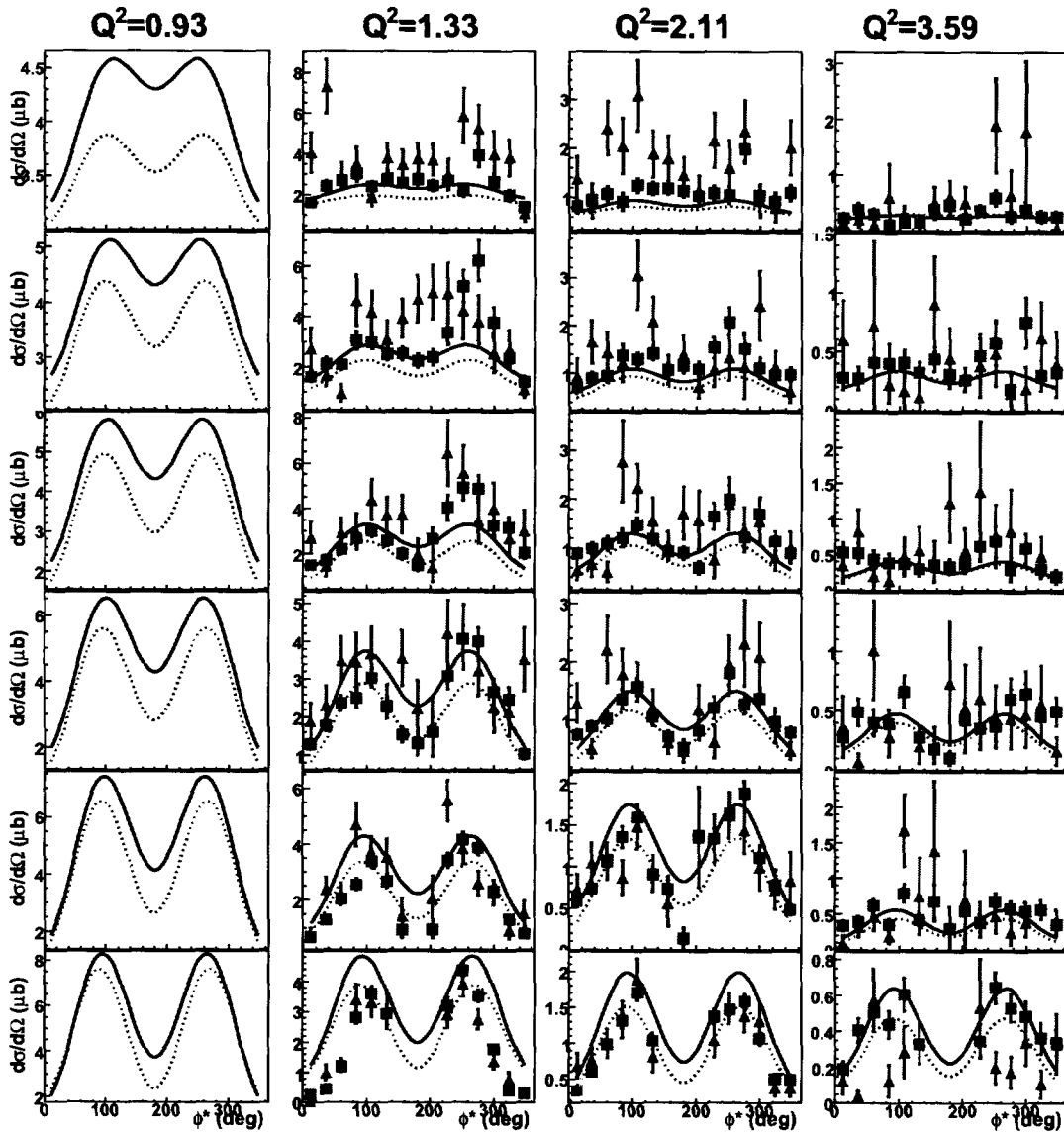


FIG. 130: Differential cross section vs.  $\phi_\pi^*$  at  $W' = 1.230$  and various  $\cos\theta_\pi^*$  and  $Q^2$  bins for the 5 GeV data set. The  $\cos\theta_\pi^*$  values are 0.100, 0.425, 0.625, 0.750, 0.850 and 0.950, increasing from the bottom to the top panel. The black solid curve is the MAID07 prediction and the pink dash line is the SAID08 prediction. The red squares and blue triangles represent  $D(e, e'\pi^- p_{CLAS})p$  and  $D(e, e'\pi^- p_{RTPC})p$  measurements, respectively.

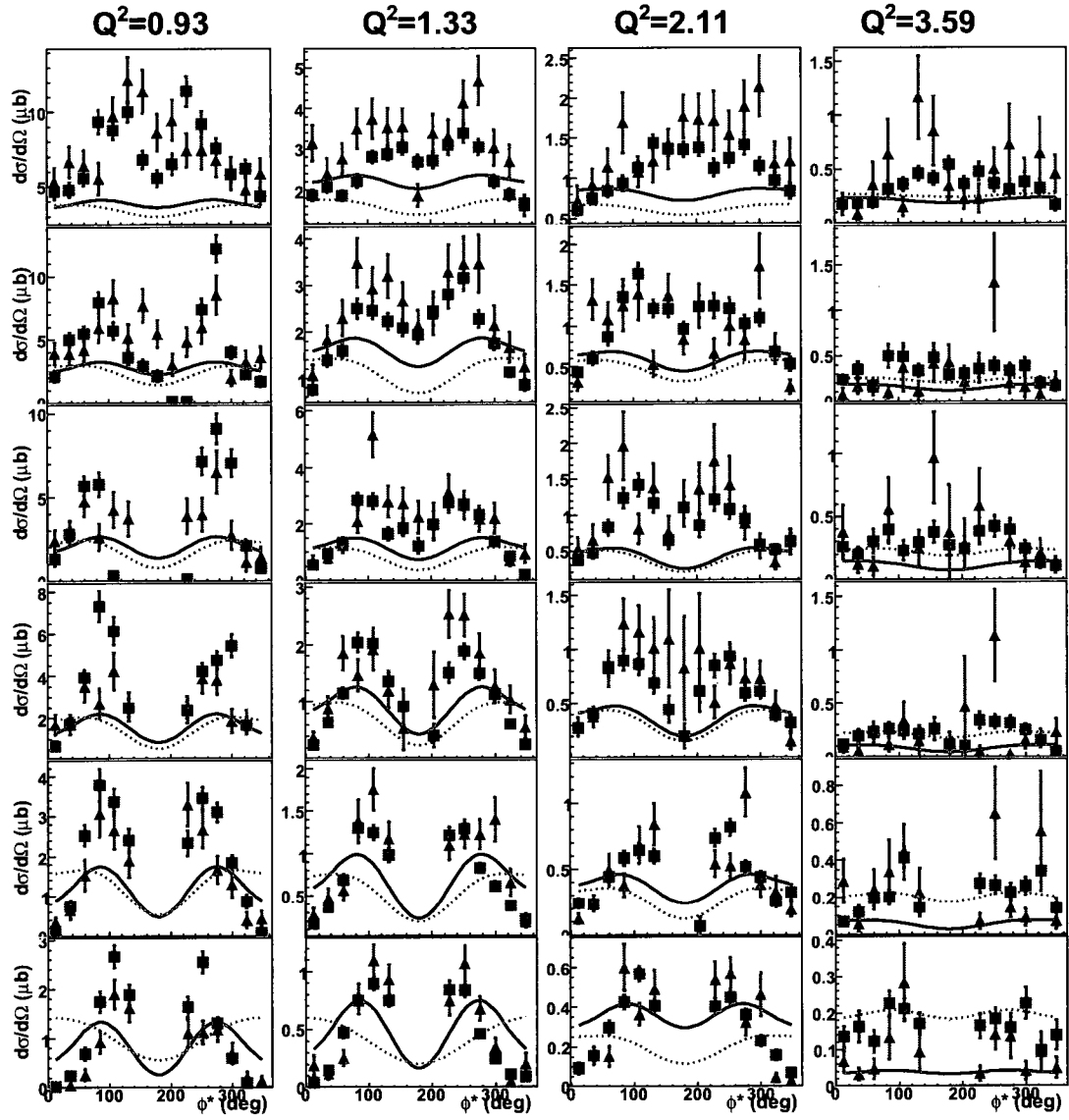


FIG. 131: Differential cross section vs.  $\phi_\pi^*$  at  $W' = 1.525$  and various  $\cos \theta_\pi^*$  and  $Q^2$  bins for the 5 GeV data set. The  $\cos \theta_\pi^*$  values are 0.100, 0.425, 0.625, 0.750, 0.850 and 0.950, increasing from the bottom to the top panel. The black solid curve is the MAID07 prediction and the pink dash line is the SAID08 prediction. The red squares and blue triangles represent  $D(e, e'\pi^- p_{\text{CLAS}})p$  and  $D(e, e'\pi^- p_{\text{RTPC}})p$  measurements, respectively.

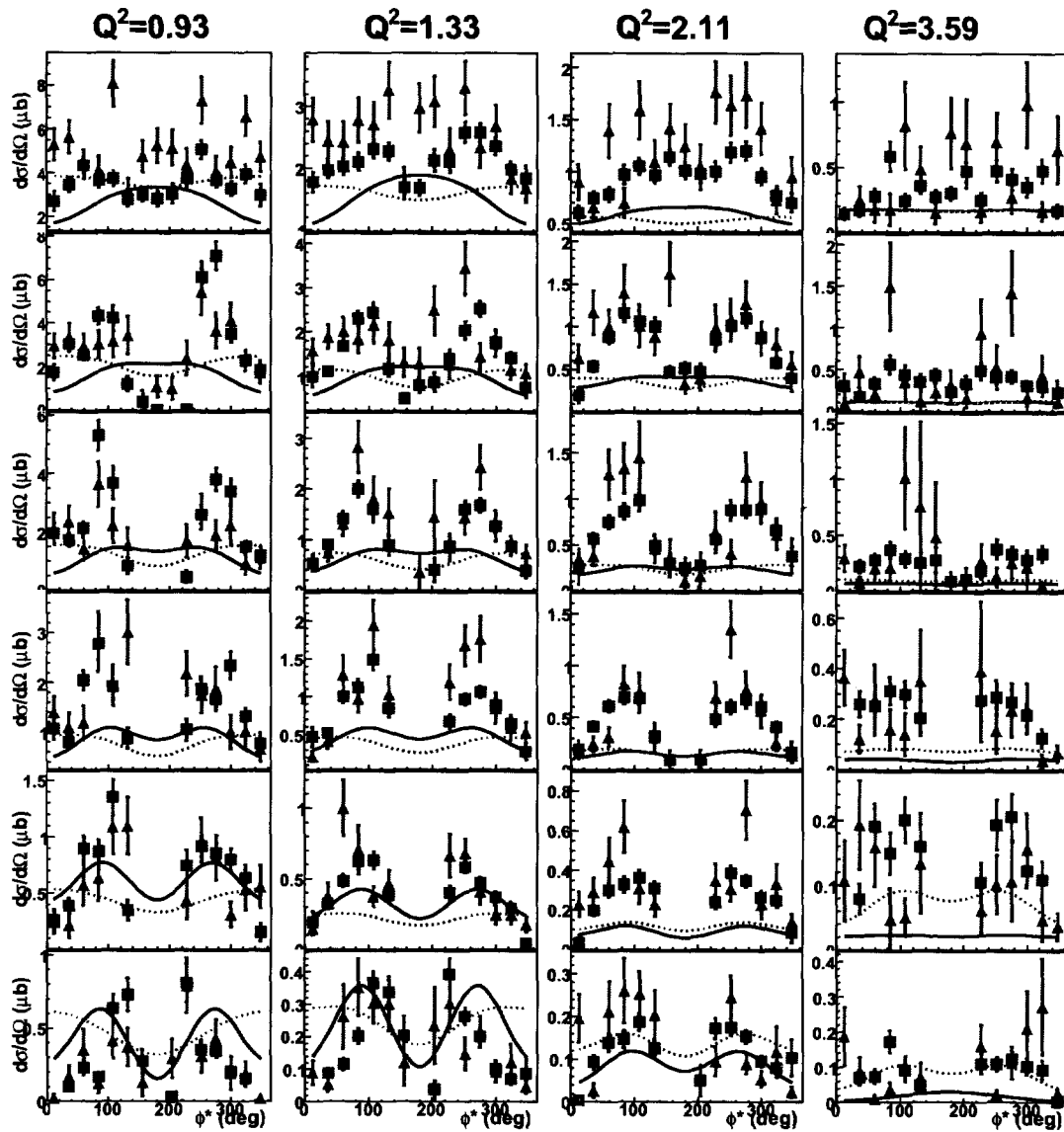


FIG. 132: Differential cross section vs.  $\phi_\pi^*$  at  $W' = 1.675$  and various  $\cos\theta_\pi^*$  and  $Q^2$  bins for the 5 GeV data set. The  $\cos\theta_\pi^*$  values are 0.100, 0.425, 0.625, 0.750, 0.850 and 0.950, increasing from the bottom to the top panel. The black solid curve is the MAID07 prediction and the pink dash line is the SAID08 prediction. The red squares and blue triangles represent  $D(e, e'\pi^- p_{CLAS})p$  and  $D(e, e'\pi^- p_{RTPC})p$  measurements, respectively.



## VI.2 STRUCTURE FUNCTIONS

The differential cross section for  $\pi^-$  electro-production was presented in Chapter II:

$$\frac{\partial^2 \sigma}{\partial \Omega_\pi^*} = (\sigma_T + \varepsilon \sigma_L) + \sqrt{2\varepsilon(1 + \varepsilon)} \sigma_{LT} \cos \phi_\pi^* + \varepsilon \sigma_{TT} \cos 2\phi_\pi^* .$$

We can use the  $\phi_\pi^*$  dependence of the cross section to extract the structure functions  $\sigma_T + \varepsilon \sigma_L$ ,  $\sigma_{LT}$  and  $\sigma_{TT}$  by fitting the cross section with a function

$$\frac{\partial^2 \sigma}{\partial \Omega_\pi^*} = A_0 + A_1 \cos \phi_\pi^* + A_2 \cos 2\phi_\pi^* , \quad (83)$$

where the fit parameters can be easily identified in terms of relevant structure functions:

$$\begin{aligned} A_0 &= \sigma_T + \varepsilon \sigma_L; \\ A_1 &= \sqrt{2\varepsilon(1 + \varepsilon)} \sigma_{LT}; \\ A_2 &= \varepsilon \sigma_{TT}. \end{aligned}$$

By using this procedure the structure functions  $\sigma_T + \varepsilon \sigma_L$ ,  $\sigma_{LT}$  and  $\sigma_{TT}$  can be determined for each three dimensional (3-D) bin in  $W'$ ,  $Q^2$  and  $\cos \theta_\pi^*$ . In this analysis, only those 3-D bins in which there are at least 6  $\phi_\pi^*$  bins that contain no less than 3 detected events after the exclusive cut, as described in Section V.4.8, were fitted to determine the structure functions. A sample of this fitting can be found in Fig. 133. In this figure, the pink data points represent the cross section for one particular bin in the 5 GeV data set. The RTPC and CLAS channels are shown separately.

These fit results are shown in comparison to MAID07 and SAID08 models in Figs. 134 to 149. The  $\cos \theta_\pi^*$  dependence for various  $Q^2$  and  $W'$  bins for all three beam energy data sets are shown. Note that MAID and SAID indicate very different dependence on  $\cos \theta_\pi^*$  in some bins. For many bins the  $D(e, e' \pi^- p_{\text{CLAS}})p$  and  $D(e, e' \pi^- p_{\text{RTPC}})p$  data are consistent with one another. There are significant differences in some bins that may be due to the accuracy of the fit for that bin. Furthermore, in some of the bins with the biggest discrepancy between the model predictions and the data, one sees that one structure function is under predicted by the models and another is over predicted. This pattern again suggests a possible problem with the fit in those bins. It is interesting to note that the models are reasonably close to the data at backward angles, but that at forward angles the discrepancy is quite

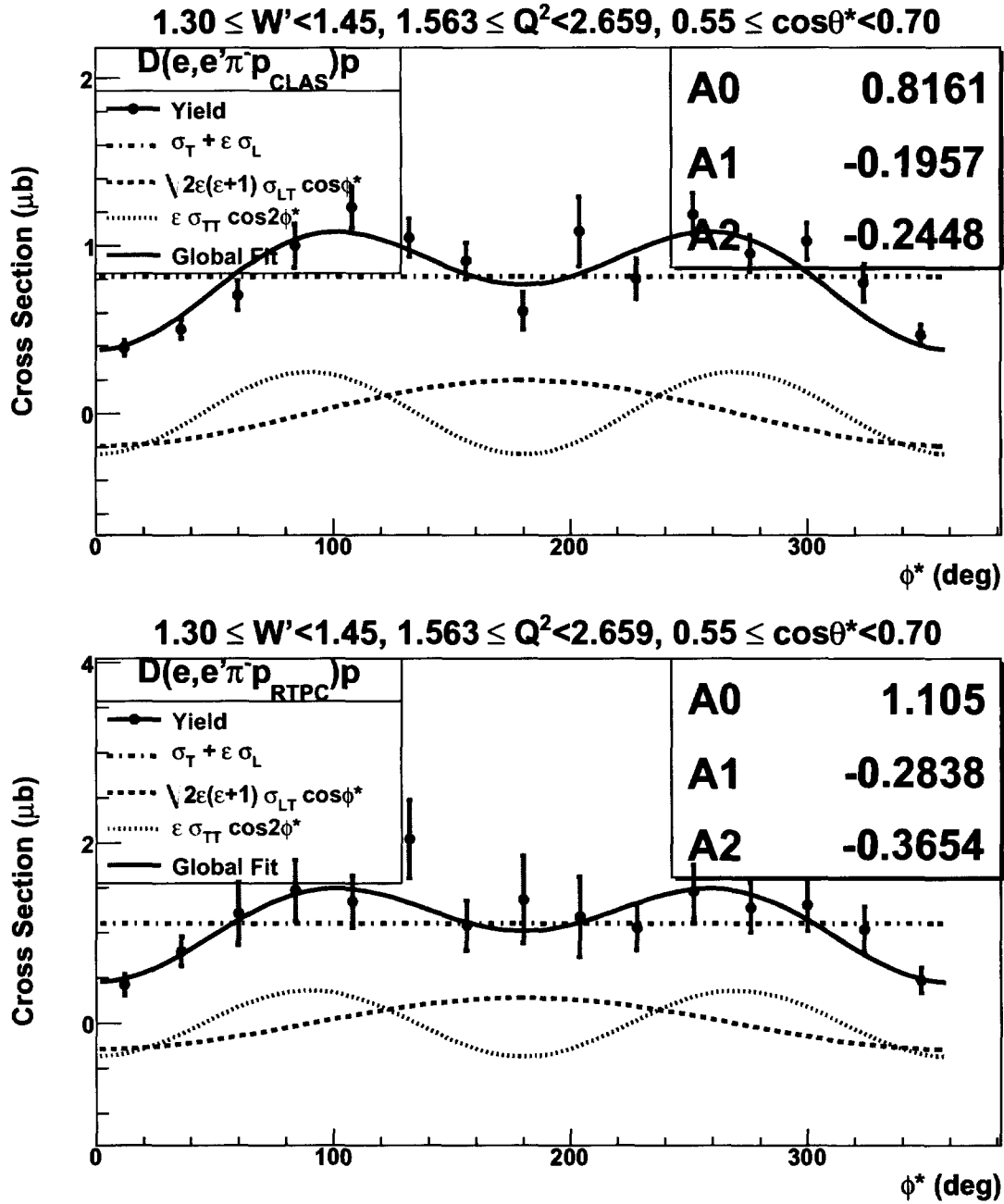


FIG. 133: The differential cross section vs.  $\phi_\pi^*$  for  $1.30 \leq W' < 1.45, 1.563 \leq Q^2 < 2.659, 0.55 \leq \cos\theta_\pi^* < 0.70$  for the 5 GeV data set. The top panel is for  $D(e, e' \pi^- p_{\text{CLAS}}) p$  and the bottom is for  $D(e, e' \pi^- p_{\text{RTPC}}) p$  events. The pink points are the measured cross sections with statistical errors only. The blue solid curve is the global fit function. The black dash-dot-dash line, the red dash line and the green dot line are the individual terms of  $A_0$ ,  $A_1 \cos \phi_\pi^*$  and  $A_2 \cos 2\phi_\pi^*$ , respectively.

pronounced, especially for  $W'$  above the  $\Delta(1232)$  region. Figures 150 to 158 show the structure functions' dependence on  $W'$  at various  $\cos\theta_\pi^*$  and  $Q^2$  bins for all three beam energy data sets. Again one sees that the biggest discrepancy between the data and models occurs at forward angles and lower  $W'$ . Our results do not show a strong peak in the  $\Delta(1232)$  resonance region, which may indicate problem with the acceptance calculation.

In general, however, the data and the models show quantitative agreement in most bins. The hope is that the addition of these data for the neutron will improve the MAID and SAID fits. However, since there are so many more proton data, it is not clear how those models will be affected.

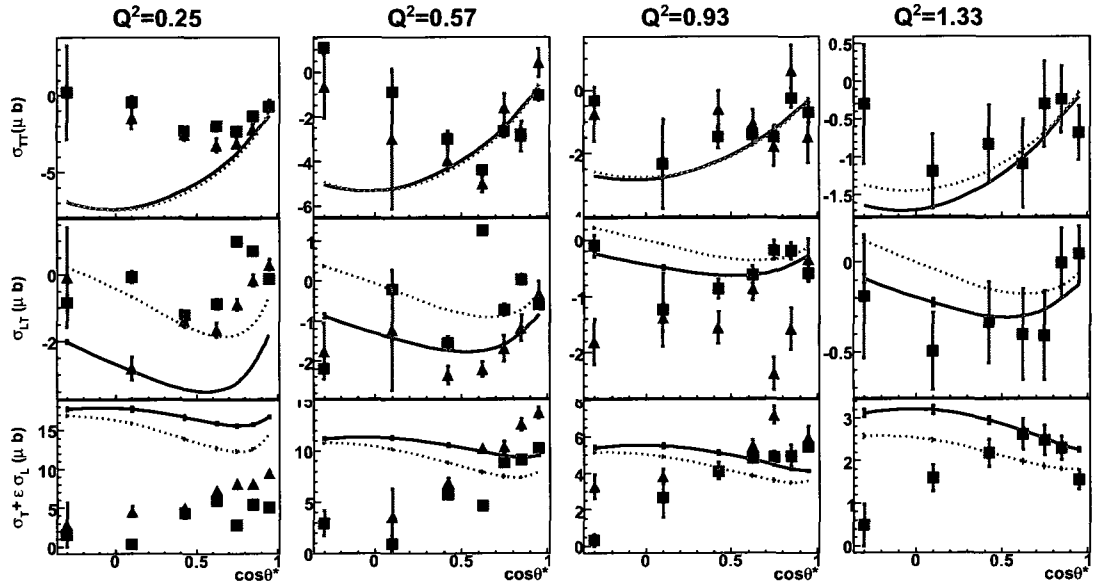


FIG. 134: Structure functions  $\sigma_T + \epsilon\sigma_L$  (bottom),  $\sigma_{LT}$  (middle) and  $\sigma_{TT}$  (top) vs.  $\cos\theta_\pi^*$  at  $W' = 1.230$  and various  $Q^2$  bins for the 2 GeV data set. The black solid curve is the MAID07 prediction and the pink dash line is the SAID08 prediction. The red squares and blue triangles represent  $D(e, e'\pi^- p_{\text{CLAS}})p$  and  $D(e, e'\pi^- p_{\text{RTPC}})p$  measurements,  $D(e, e'\pi^- p_{\text{CLAS}})p$  and  $D(e, e'\pi^- p_{\text{RTPC}})p$  measurements, respectively.

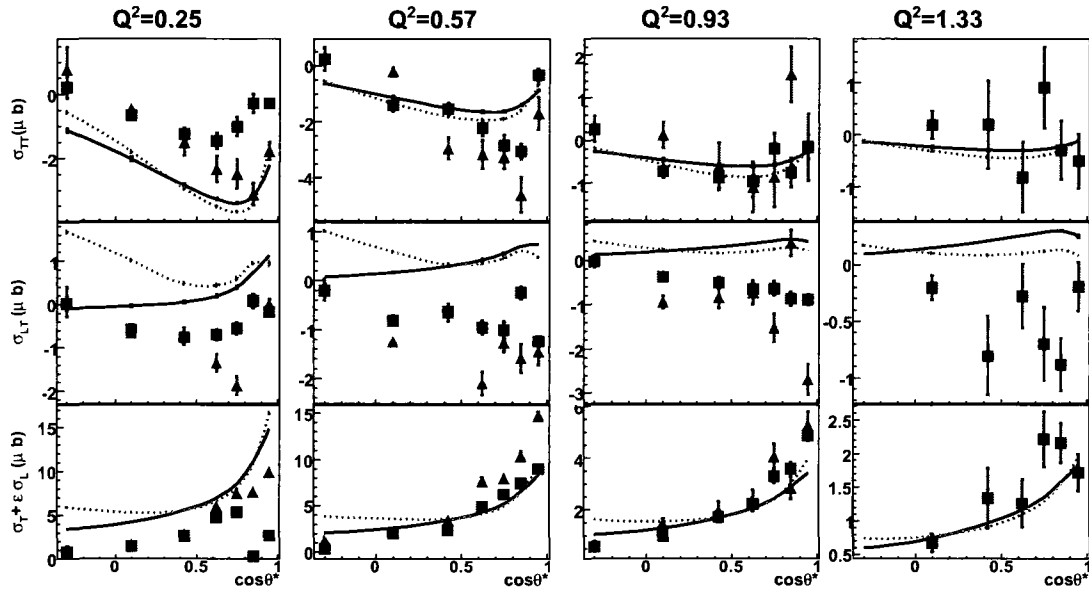


FIG. 135: Same as Fig. 134 except for  $W' = 1.375$  GeV/c.

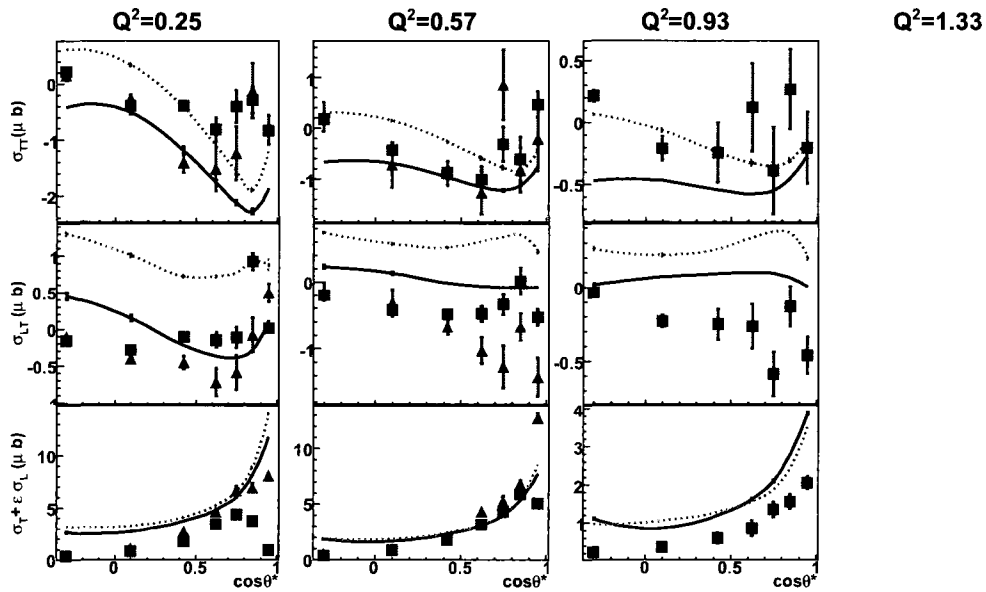


FIG. 136: Same as Fig. 134 except for  $W' = 1.525$  GeV/c.

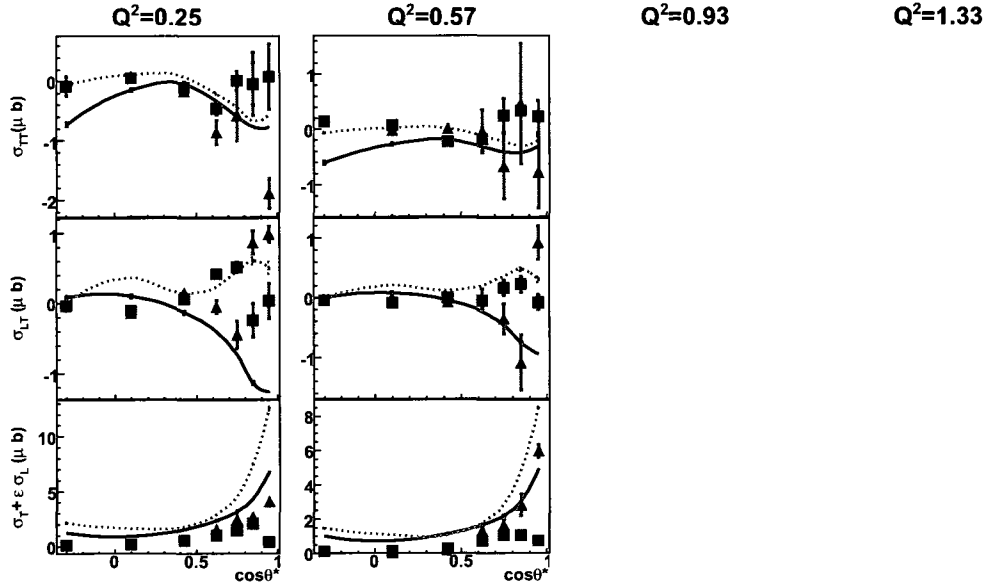


FIG. 137: Same as Fig. 134 except for  $W' = 1.675$  GeV/c.

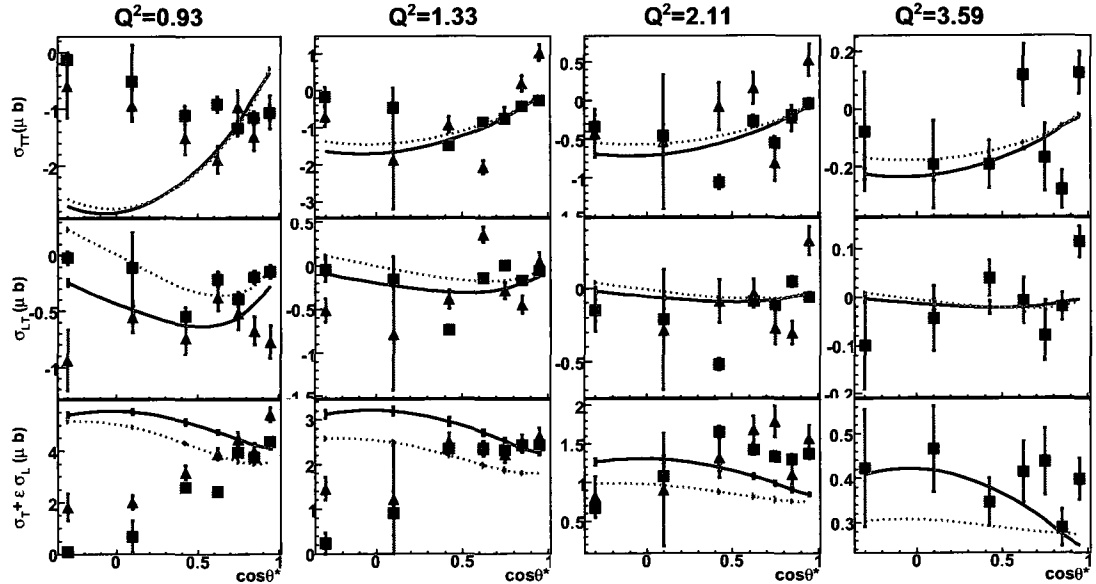


FIG. 138: Structure functions  $\sigma_T + \epsilon\sigma_L$  (bottom),  $\sigma_{LT}$  (middle) and  $\sigma_{TT}$  (top) vs.  $\cos\theta_\pi^*$  at  $W' = 1.230$  GeV/c and various  $Q^2$  bins for the 4 GeV data set. The black solid curve is the MAID07 prediction and the pink dash line is the SAID08 prediction. The red squares and blue triangles represent  $D(e, e'\pi^- p_{\text{CLAS}})p$  and  $D(e, e'\pi^- p_{\text{RTFC}})p$  measurements, respectively.

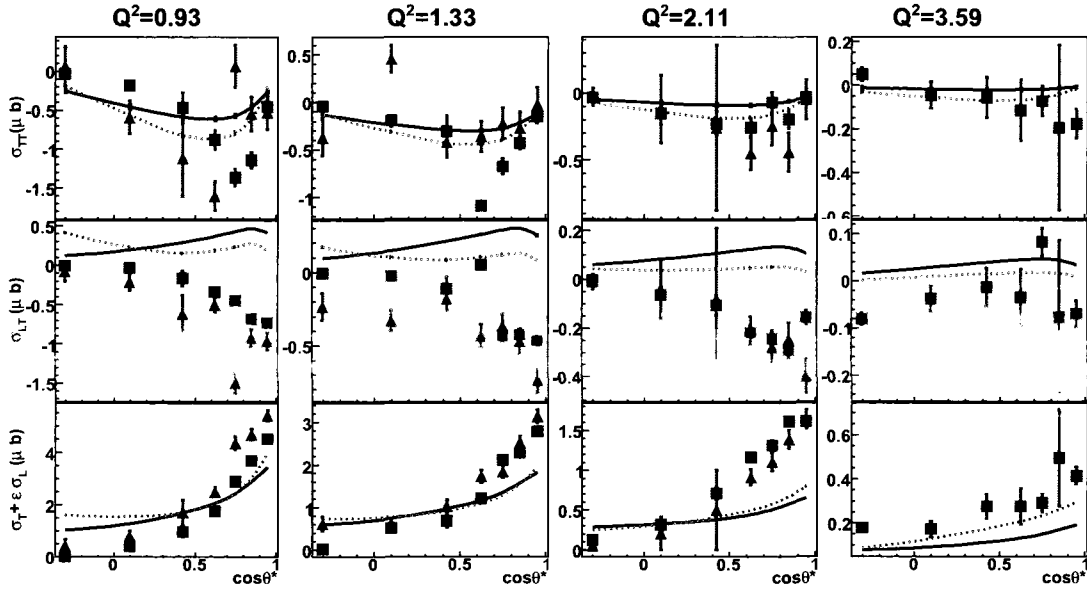


FIG. 139: Same as Fig. 138 except for  $W' = 1.375$  GeV/c.

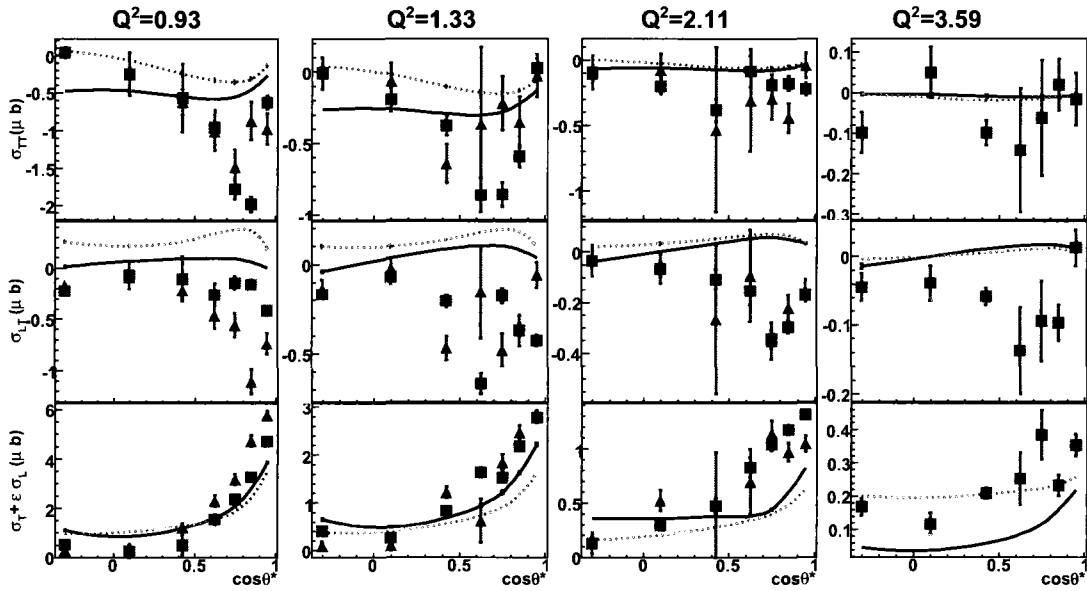


FIG. 140: Same as Fig. 138 except for  $W' = 1.525$  GeV/c.

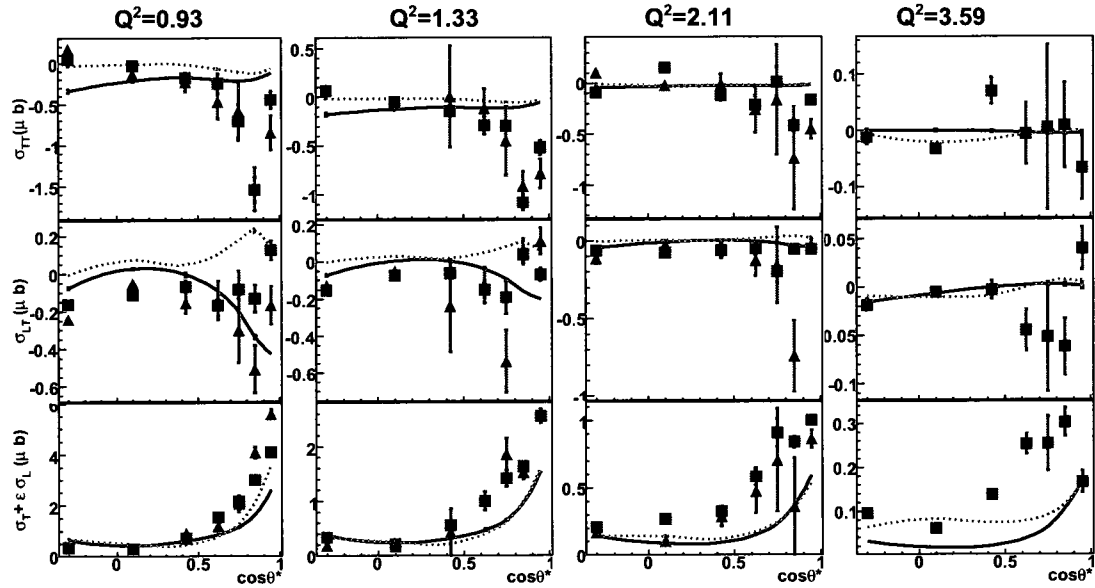


FIG. 141: Same as Fig. 138 except for  $W' = 1.675 \text{ GeV}/c$ .

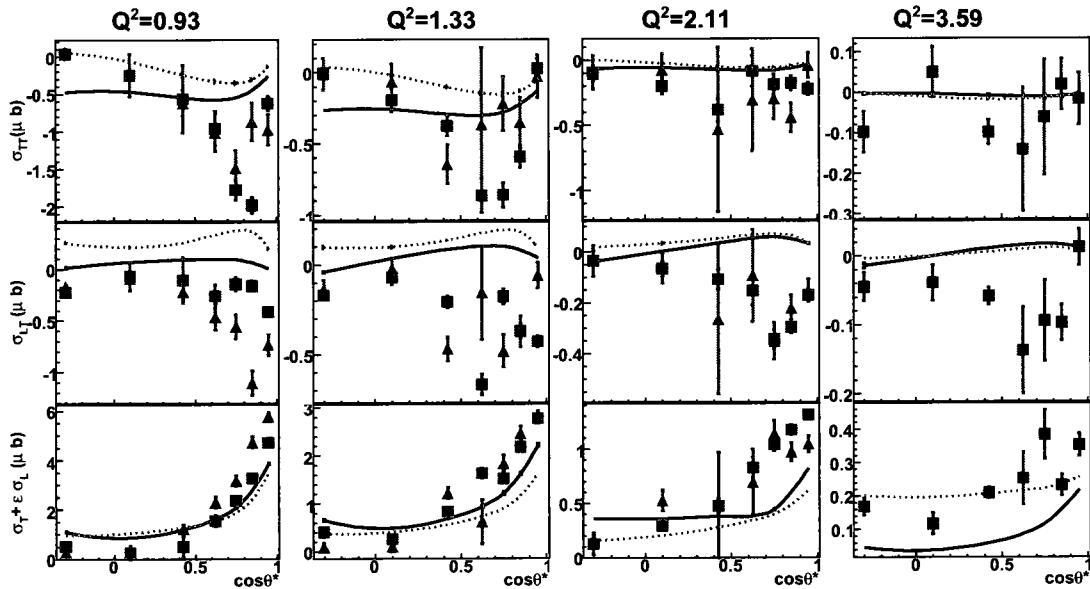


FIG. 142: Same as Fig. 138 except for  $W' = 1.825 \text{ GeV}/c$ .

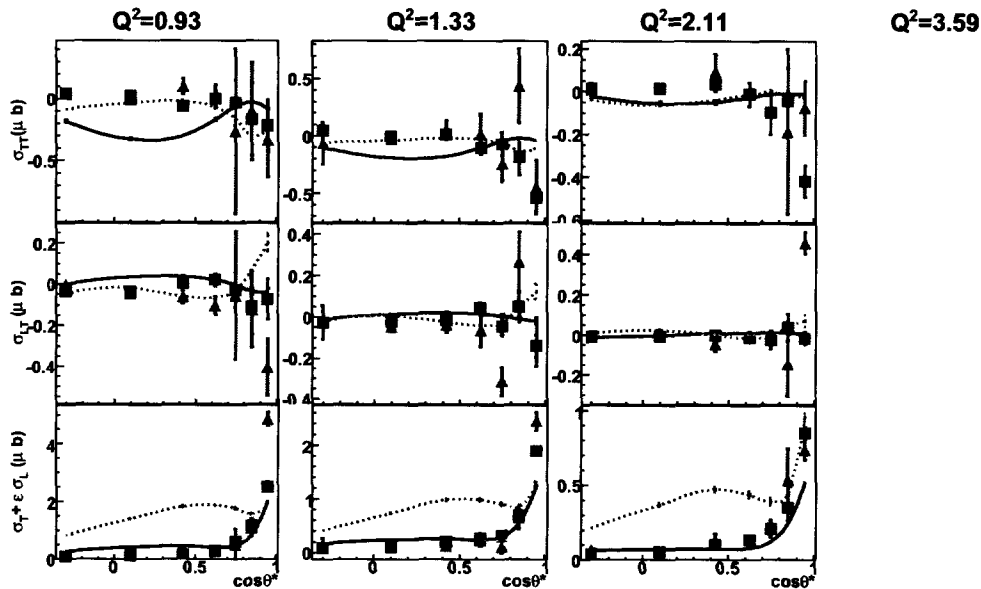


FIG. 143: Same as Fig. 138 except for  $W' = 1.975$  GeV/c.

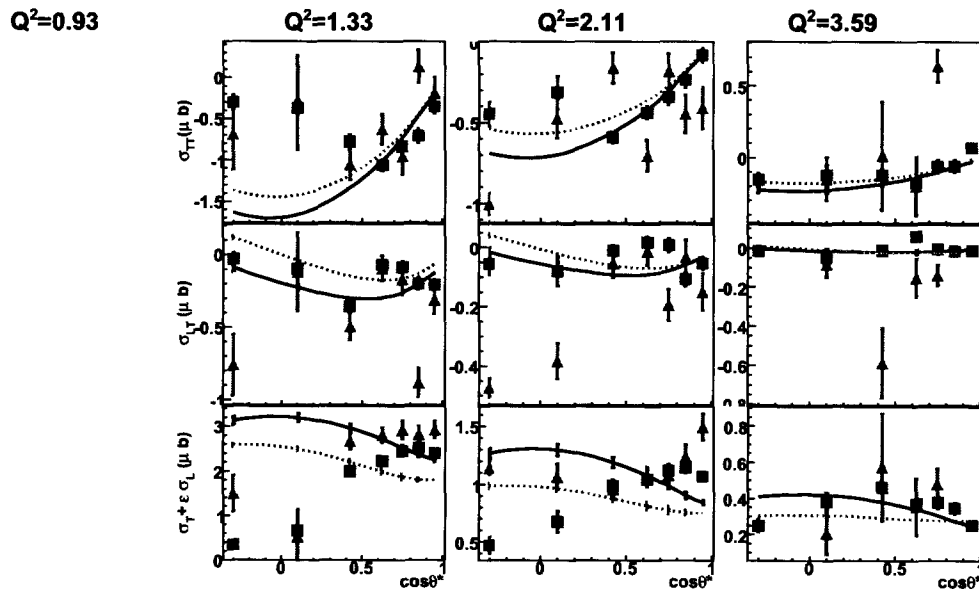


FIG. 144: Structure functions  $\sigma_T + \epsilon\sigma_L$  (bottom),  $\sigma_{LT}$  (middle) and  $\sigma_{TT}$  (top) vs.  $\cos\theta_\pi^*$  at  $W' = 1.230$  and various  $Q^2$  bins for the 5 GeV data set. The black solid curve is the MAID07 prediction and the pink dash line is the SAID08 prediction. The red squares and blue triangles represent  $D(e, e'\pi^- p_{CLAS})p$  and  $D(e, e'\pi^- p_{RTPC})p$  measurements, respectively.



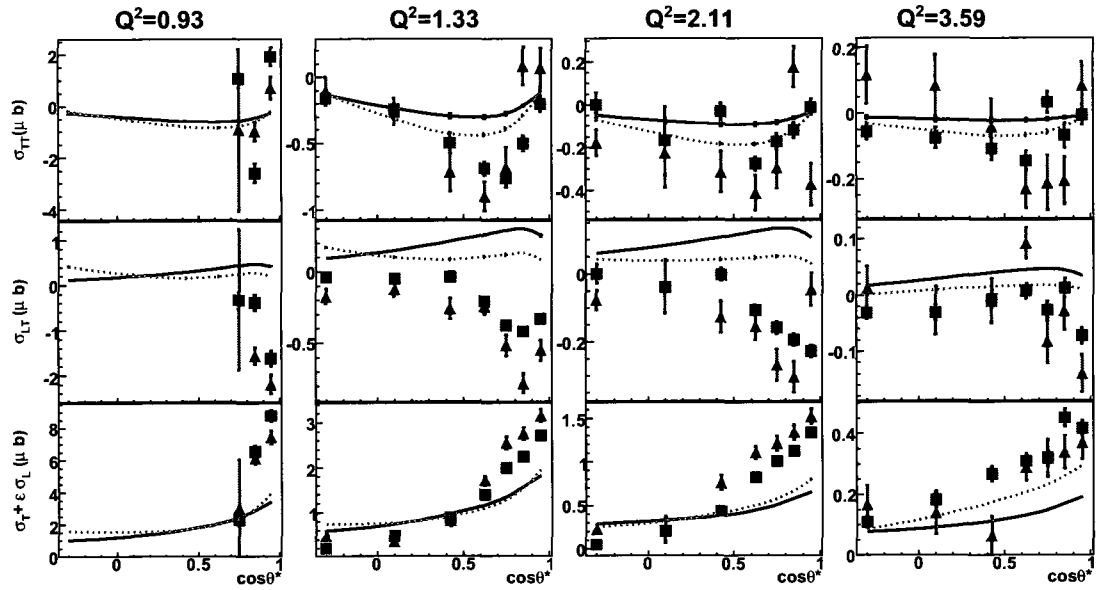


FIG. 145: Same as Fig. 144 except for  $W' = 1.375$  GeV/c.

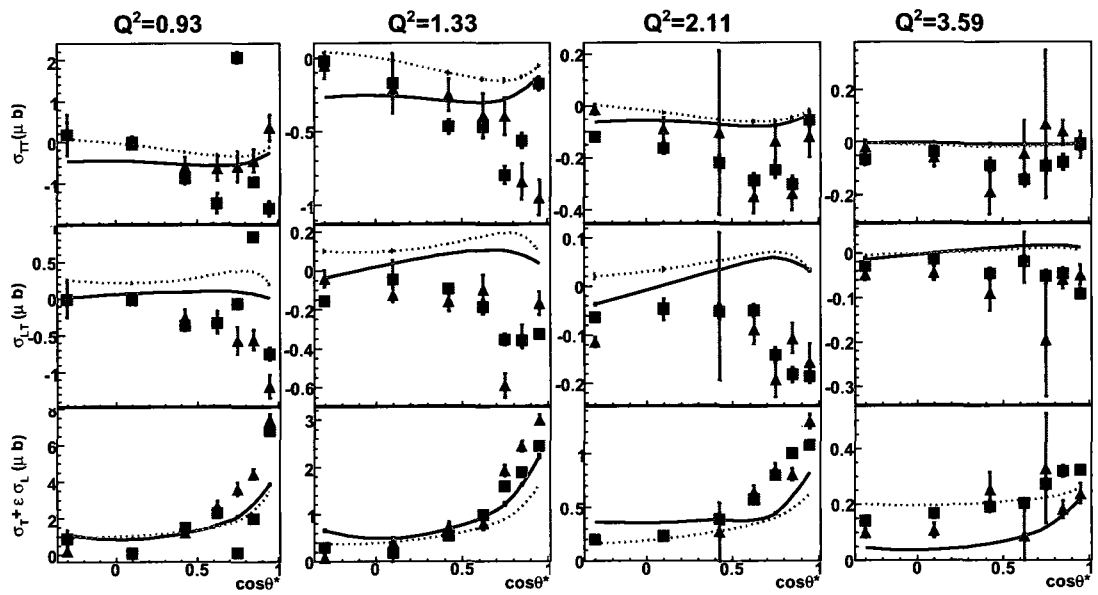


FIG. 146: Same as Fig. 144 except for  $W' = 1.525$  GeV/c.

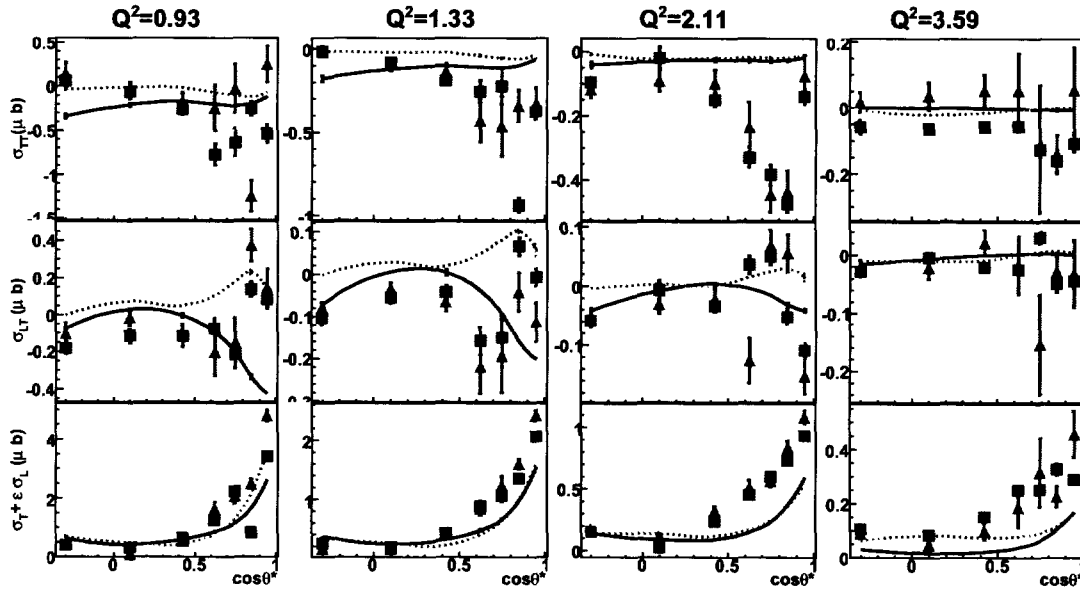


FIG. 147: Same as Fig. 144 except for  $W' = 1.675$  GeV/c.

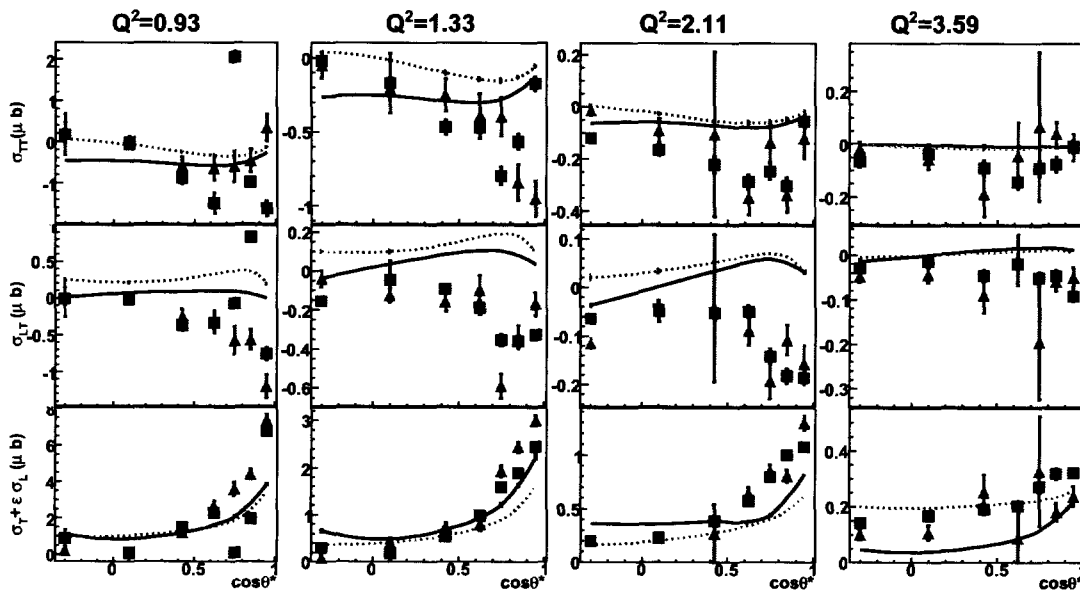


FIG. 148: Same as Fig. 144 except for  $W' = 1.825$  GeV/c.

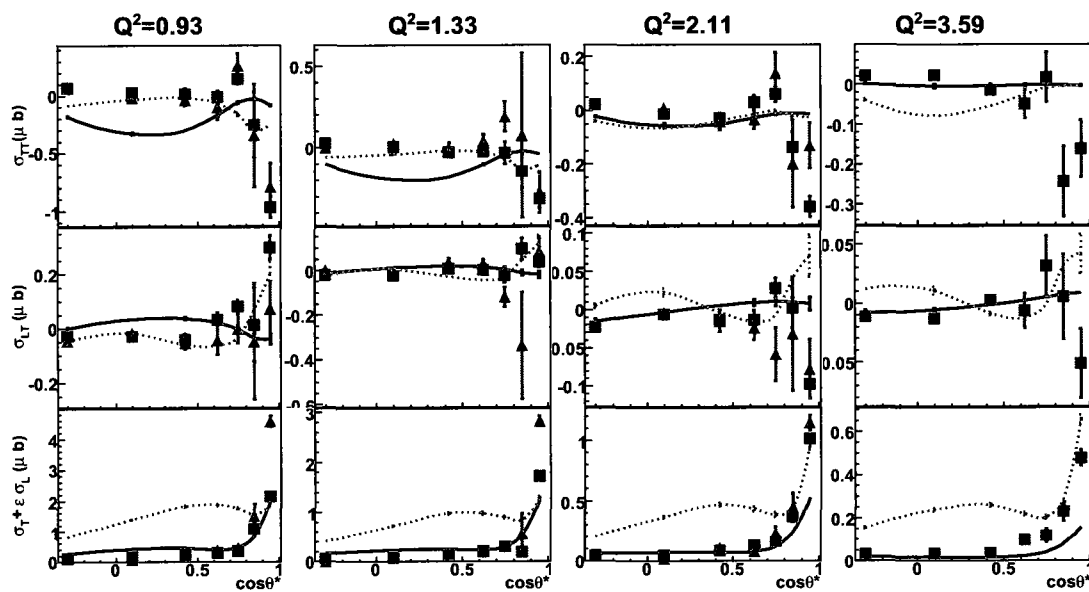


FIG. 149: Same as Fig. 144 except for  $W' = 1.975 \text{ GeV}/c$ .

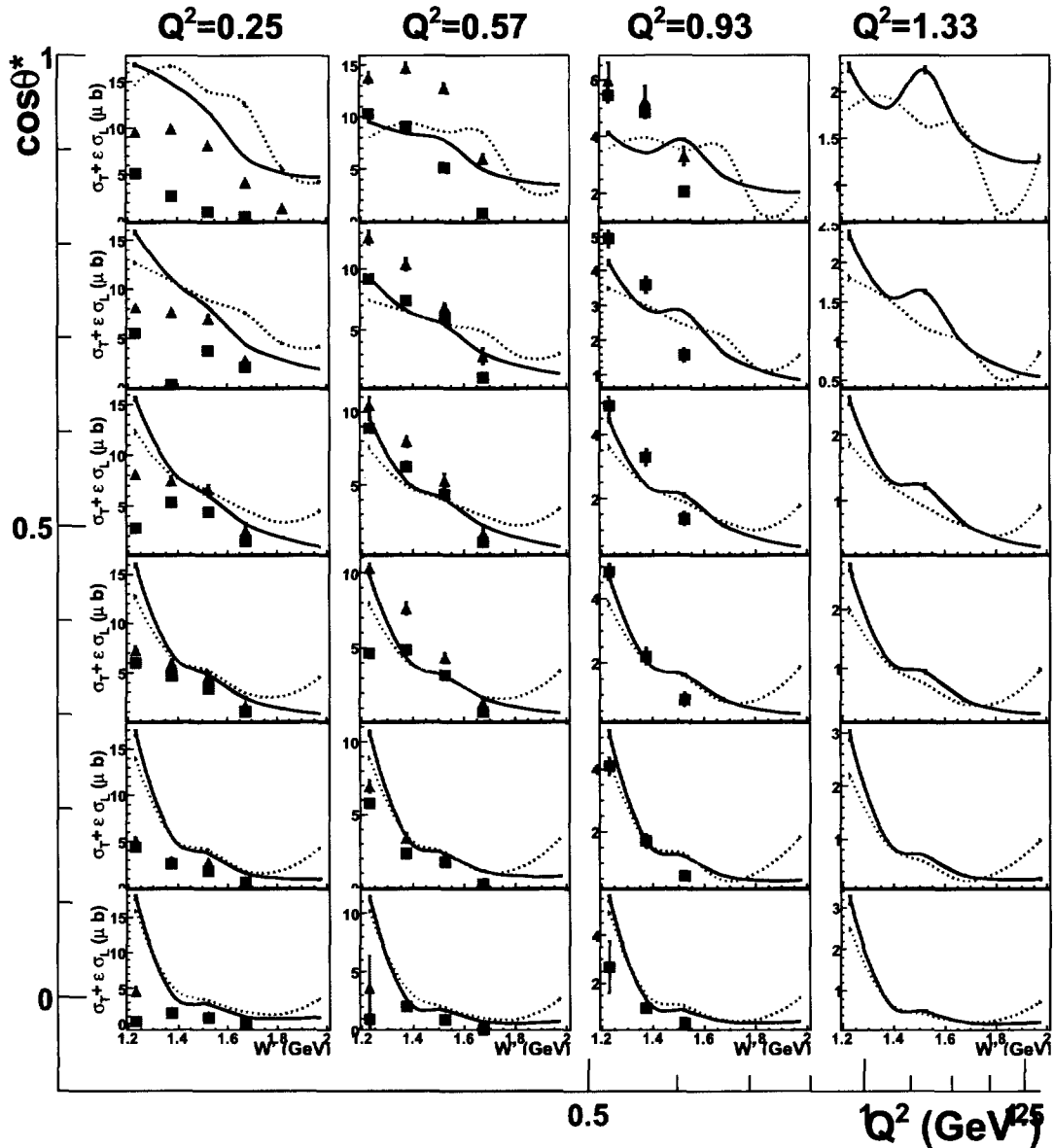


FIG. 150:  $\sigma_T + \epsilon\sigma_L$  vs.  $W'$  at various  $\cos\theta_\pi^*$  and  $Q^2$  bins for the 2 GeV data set. The black solid curve is the MAID07 prediction and the pink dash line is the SAID08 prediction. The red squares and blue triangles represent  $D(e, e'\pi^- p_{\text{CLAS}})p$  and  $D(e, e'\pi^- p_{\text{RTPC}})p$  measurements, respectively.

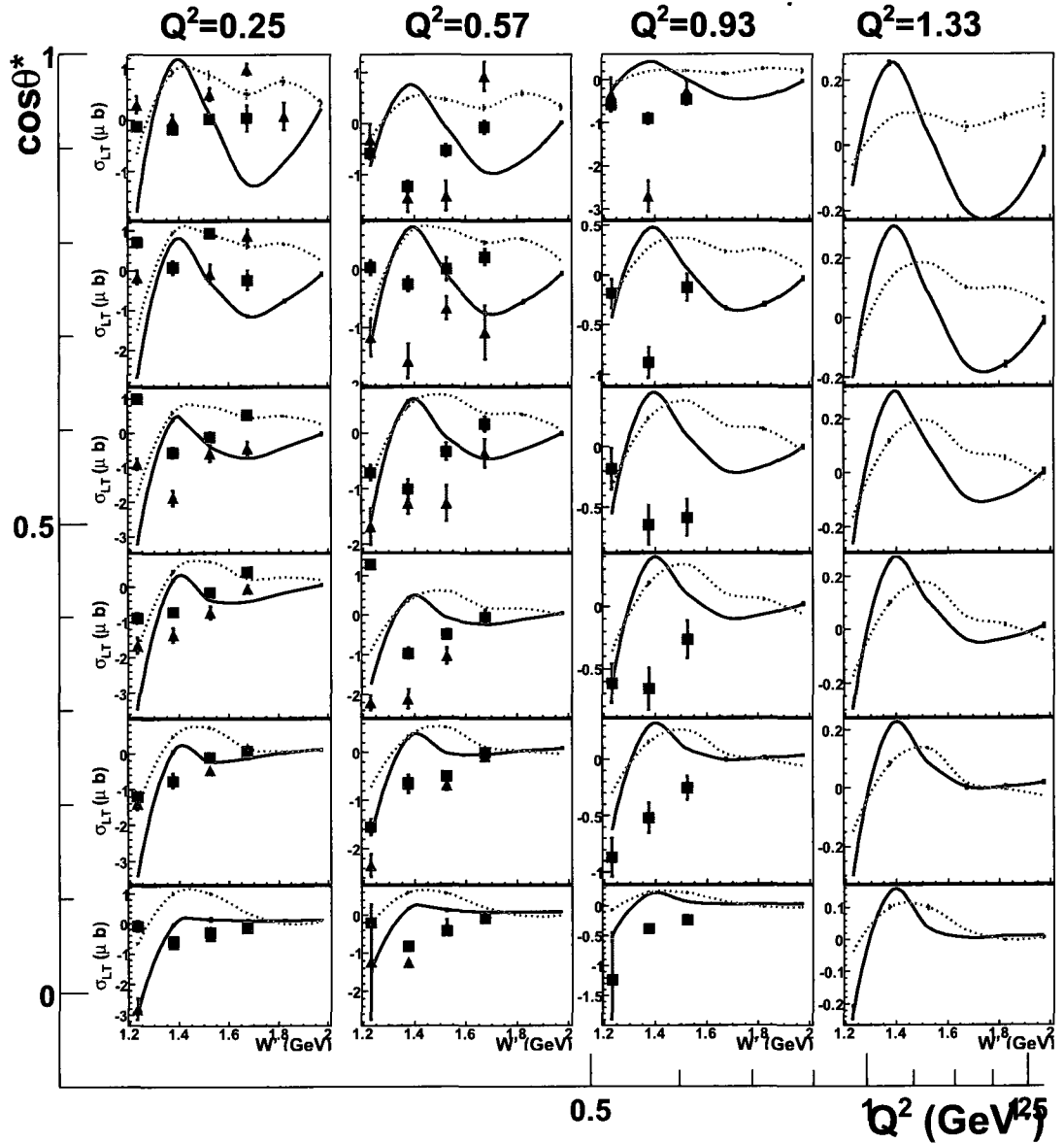


FIG. 151:  $\sigma_{LT}$  vs.  $W'$  at various  $\cos\theta_\pi^*$  and  $Q^2$  bins for the 2 GeV data set. The black solid curve is the MAID07 prediction and the pink dash line is the SAID08 prediction. The red squares and blue triangles represent  $D(e, e'\pi^- p_{\text{CLAS}})p$  and  $D(e, e'\pi^- p_{\text{RTPC}})p$  measurements, respectively.

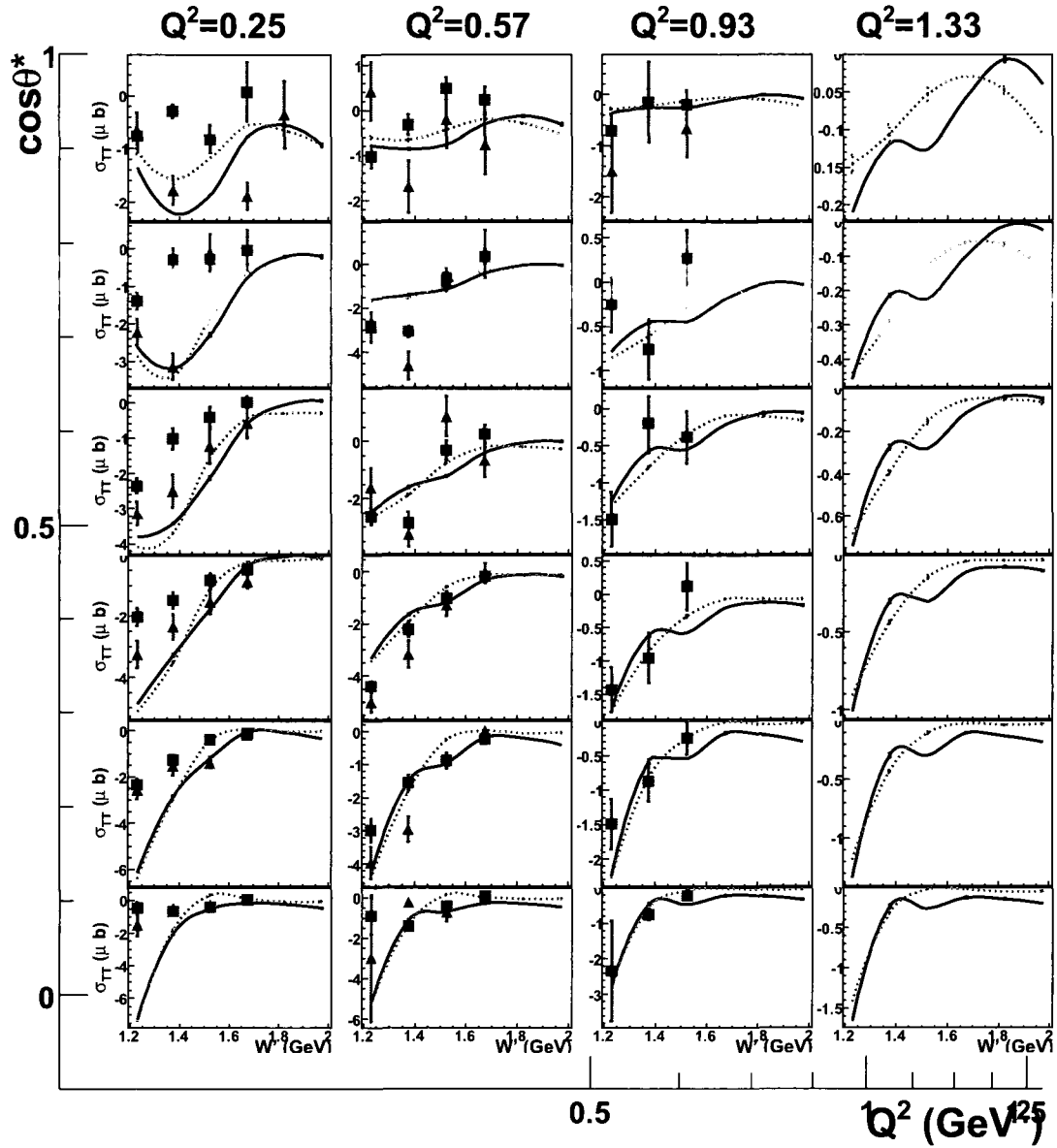


FIG. 152:  $\sigma_{\text{TT}}$  vs.  $W'$  at various  $\cos\theta_\pi^*$  and  $Q^2$  bins for the 2 GeV data set. The black solid curve is the MAID07 prediction and the pink dash line is the SAID08 prediction. The red squares and blue triangles represent  $D(e, e'\pi^- p_{\text{CLAS}})p$  and  $D(e, e'\pi^- p_{\text{RTPC}})p$  measurements, respectively.

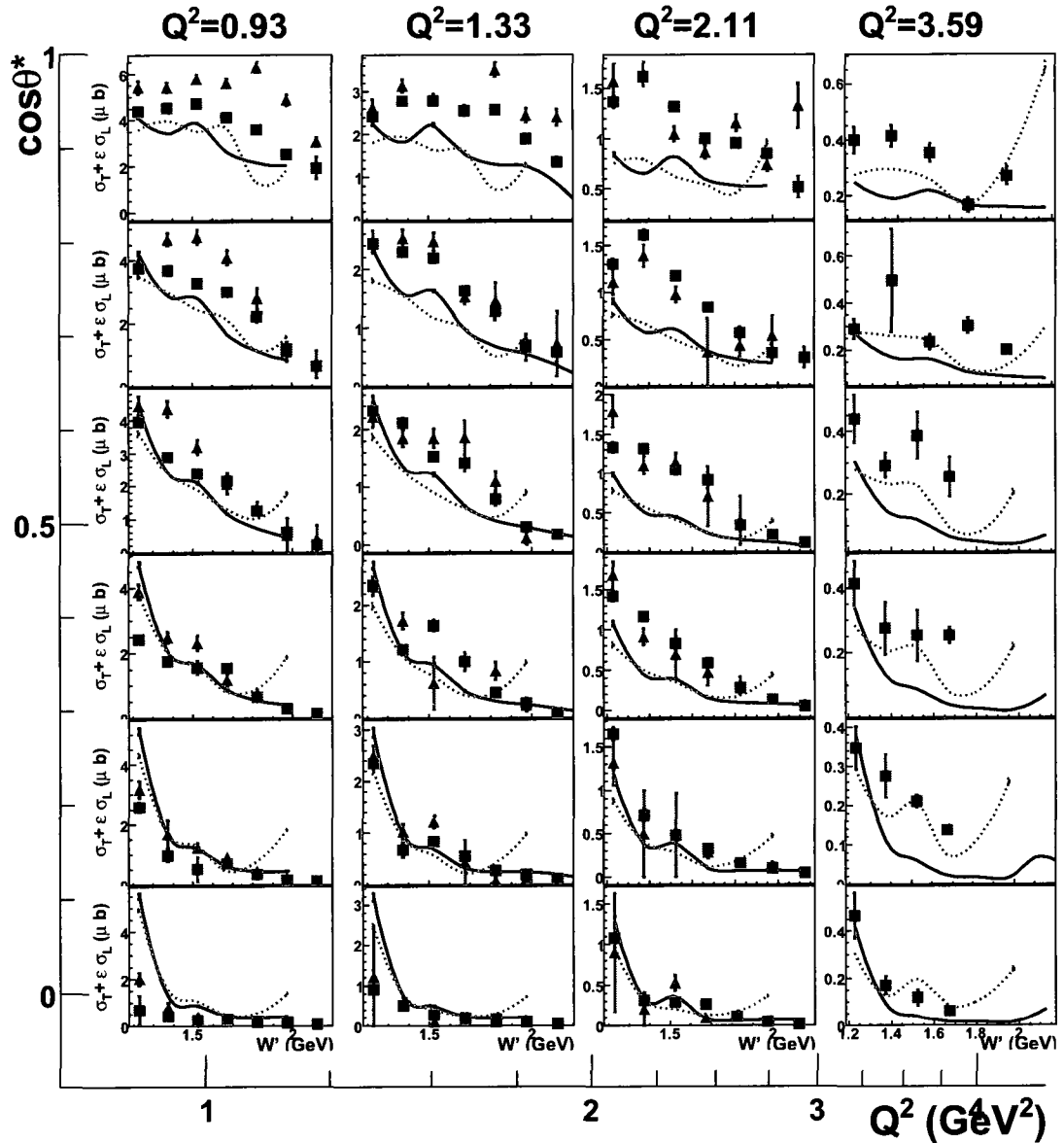


FIG. 153:  $\sigma_T + \epsilon\sigma_L$  vs.  $W'$  at various  $\cos\theta_\pi^*$  and  $Q^2$  bins for the 4 GeV data set. The black solid curve is the MAID07 prediction and the pink dash line is the SAID08 prediction. The red squares and blue triangles represent  $D(e, e'\pi^- p_{\text{CLAS}})p$  and  $D(e, e'\pi^- p_{\text{RTPC}})p$  measurements, respectively.

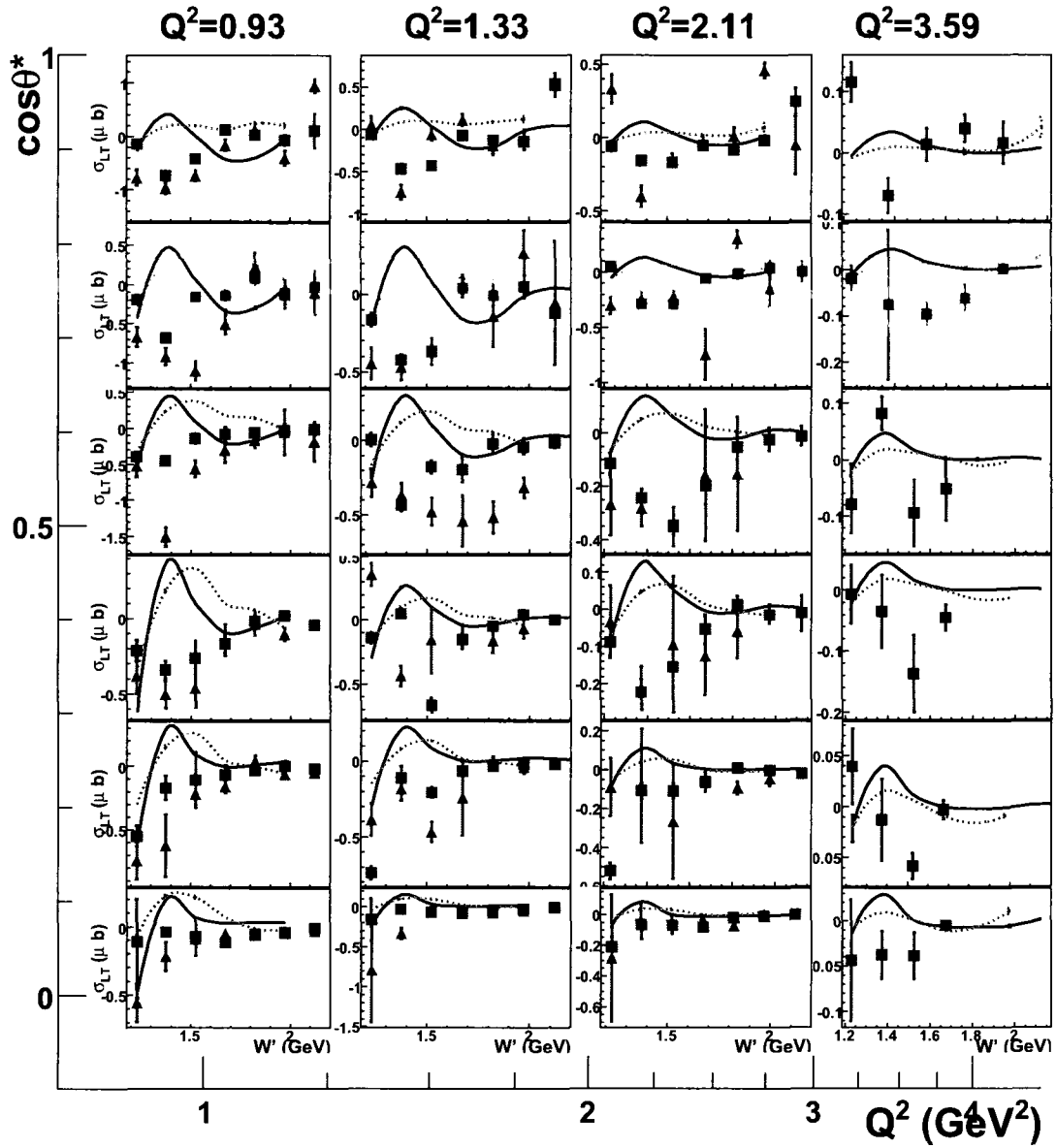


FIG. 154:  $\sigma_{LT}$  vs.  $W'$  at various  $\cos\theta_\pi^*$  and  $Q^2$  bins for the 4 GeV data set. The black solid curve is the MAID07 prediction and the pink dash line is the SAID08 prediction. The red squares and blue triangles represent  $D(e, e'\pi^- p_{CLAS})p$  and  $D(e, e'\pi^- p_{RTPC})p$  measurements, respectively.



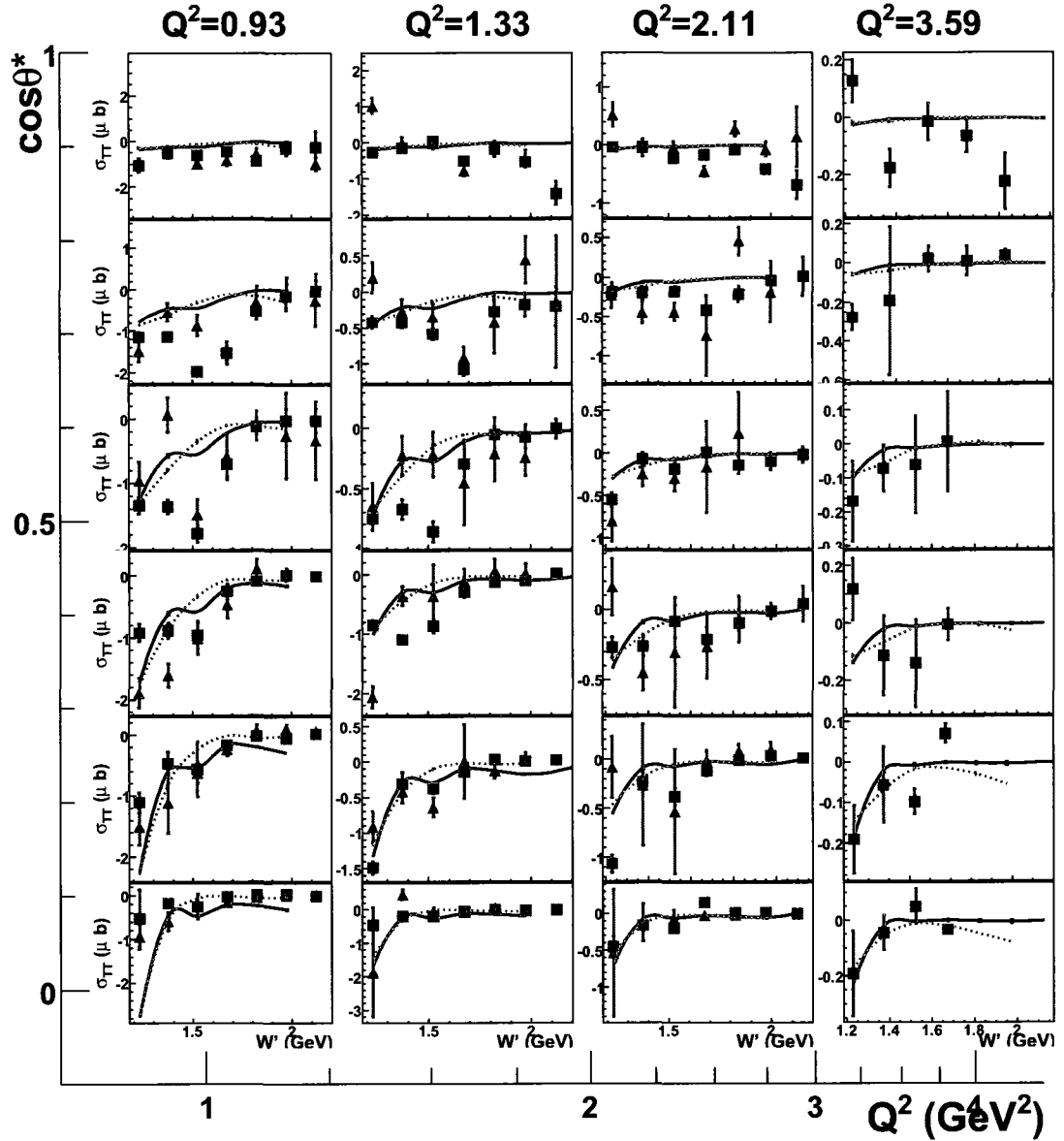


FIG. 155:  $\sigma_{\text{TT}}$  vs.  $W'$  at various  $\cos \theta_{\pi}^*$  and  $Q^2$  bins for the 4 GeV data set. The black solid curve is the MAID07 prediction and the pink dash line is the SAID08 prediction. The red squares and blue triangles represent  $D(e, e'\pi^- p_{\text{CLAS}})p$  and  $D(e, e'\pi^- p_{\text{RTPC}})p$  measurements, respectively.

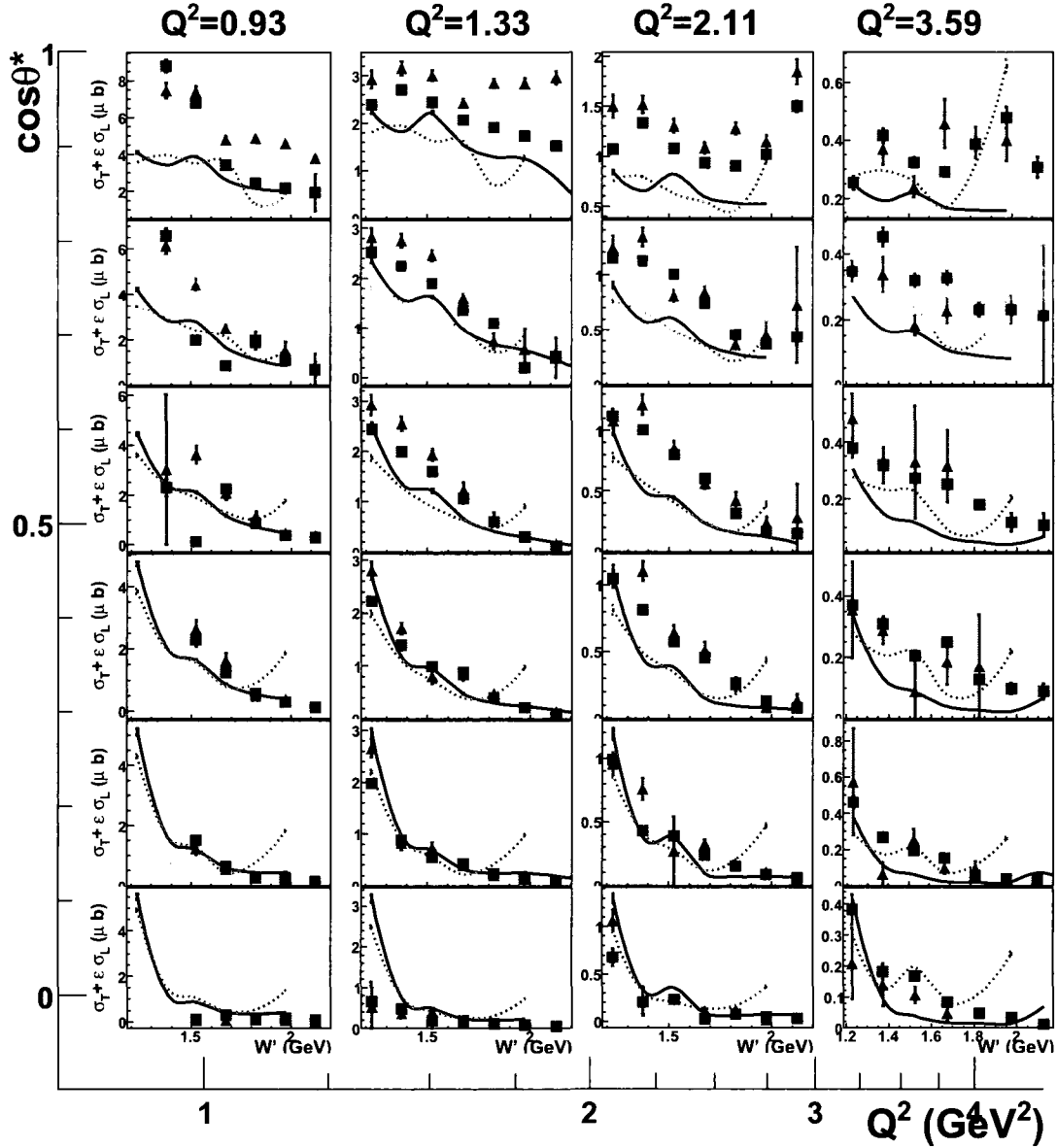


FIG. 156:  $\sigma_T + \epsilon\sigma_L$  vs.  $W'$  at various  $\cos\theta_\pi^*$  and  $Q^2$  bins for the 5 GeV data set. The black solid curve is the MAID07 prediction and the pink dash line is the SAID08 prediction. The red squares and blue triangles represent  $D(e, e'\pi^- p_{\text{CLAS}})p$  and  $D(e, e'\pi^- p_{\text{RTFC}})p$  measurements, respectively.

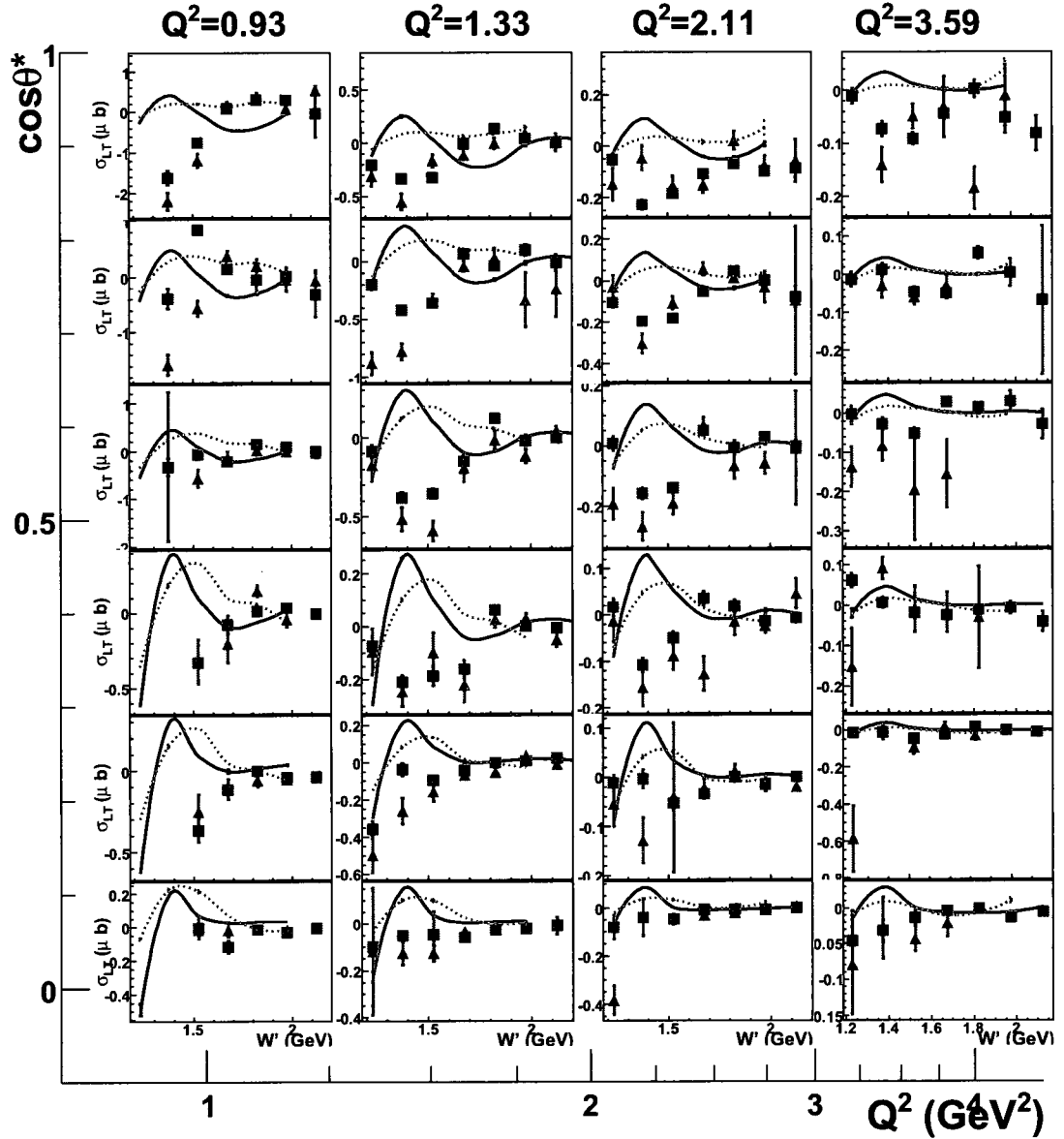


FIG. 157:  $\sigma_{LT}$  vs.  $W'$  at various  $\cos\theta_{\pi^*}$  and  $Q^2$  bins for the 5 GeV data set. The black solid curve is the MAID07 prediction and the pink dash line is the SAID08 prediction. The red squares and blue triangles represent  $D(e, e'\pi^- p_{CLAS})p$  and  $D(e, e'\pi^- p_{RTPC})p$  measurements, respectively.

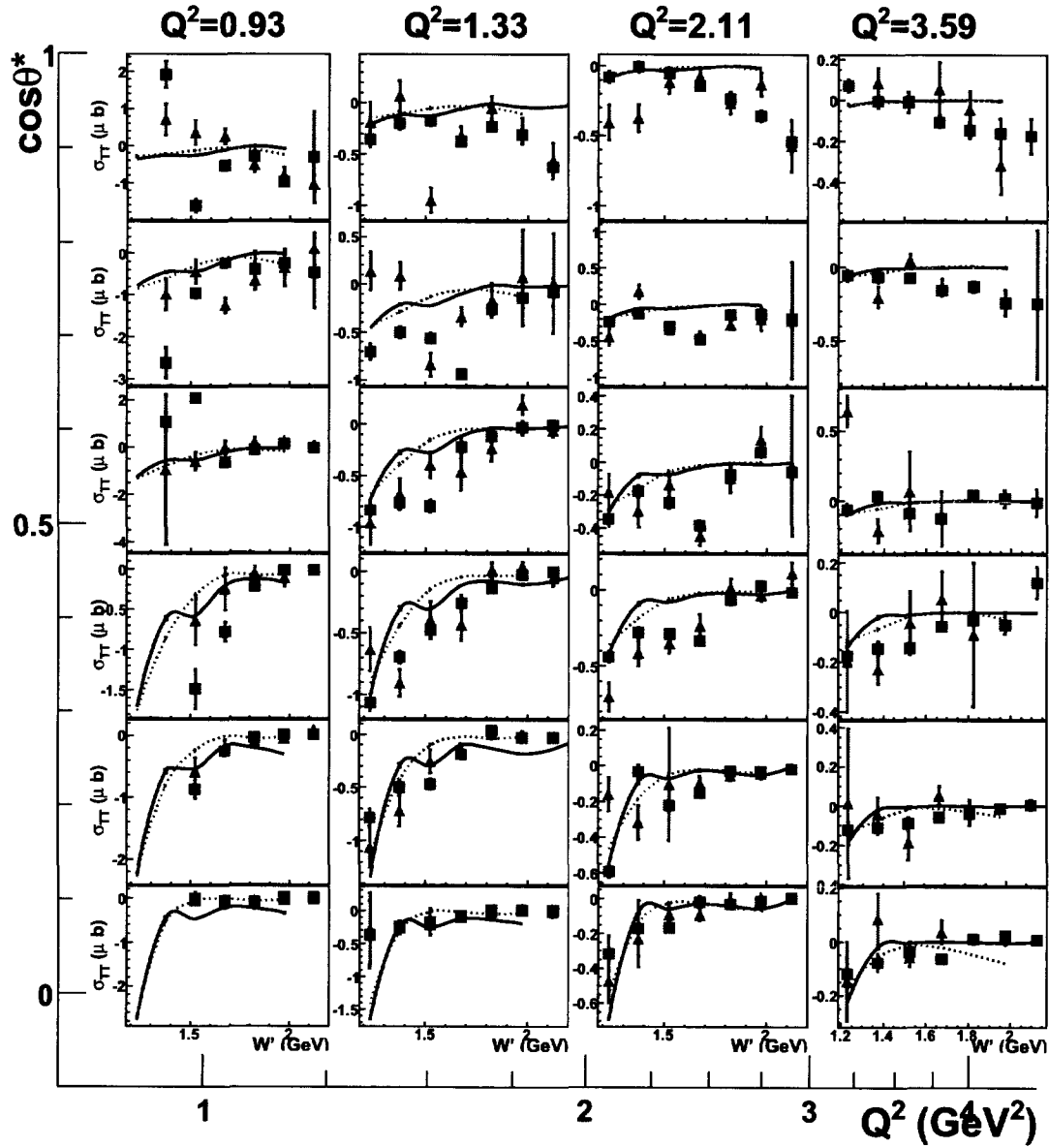


FIG. 158:  $\sigma_{TT}$  vs.  $W'$  at various  $\cos \theta_\pi^*$  and  $Q^2$  bins for the 5 GeV data set. The black solid curve is the MAID07 prediction and the pink dash line is the SAID08 prediction. The red squares and blue triangles represent  $D(e, e' \pi^- p_{CLAS})p$  and  $D(e, e' \pi^- p_{RTPC})p$  measurements, respectively.

### VI.3 RESULT WITH LOW-MOMENTUM SPECTATOR PROTONS

As mentioned in Section II.6.1 and Section II.6.2, off-shell effects and final state interactions were predicted to be as small as 20% when requiring the spectator proton's momentum to be less than 120 MeV/c and  $\theta_{pq}$  (the angle between spectator proton and the virtual photon) to be larger than  $100^\circ$ . Therefore we define a Very Importance spectator Proton (VIP) cut as the following. For the  $D(e, e'\pi^- p_{\text{RTPC}})p$  events in which the spectator proton is detected by the RTPC, we require  $70.0 \leq p_s < 120.0$  (MeV/c) and  $\theta_{pq} > 100.0^\circ$ . In the  $D(e, e'\pi^- p_{\text{CLAS}})p$  reaction in which the fast proton is detected by CLAS, we require the inferred spectator proton to satisfy  $70.0 \leq p_s^{\text{infer}} < 120.0$  (MeV/c) and  $\theta_{pq}^{\text{infer}} > 100.0^\circ$ , where the inferred quantities are calculated based on momentum and energy conservation. The lower limit of the spectator momentum cut here was chosen to be 70 MeV/c for comparison between the  $D(e, e'\pi^- p_{\text{CLAS}})p$  and the  $D(e, e'\pi^- p_{\text{RTPC}})p$  reactions.

The subset of events that satisfy the VIP cut are expected to contain less than 20% contamination from off-shell and FSI effects. To calculate the differential cross section and structure functions, a new acceptance with VIP cut was calculated. By comparing the measurements of  $D(e, e'\pi^- p_{\text{RTPC}})p$  and  $D(e, e'\pi^- p_{\text{CLAS}})p$  with and without the VIP cut, one can estimate the reliability of these measurements. Figures 159 to 167 show the structure functions' dependence on  $\cos\theta_\pi^*$  at various  $W'$  and  $Q^2$  bins for all three beam energy data sets. Figures 168 to 176 are the same except that they show dependence on  $W'$  for various  $\cos\theta_\pi^*$  and  $Q^2$  bins. In these figures, the black curve is the MAID07 prediction. The measurements with and without the VIP cut are consistent in most bins, except at regions of low  $W'$  ( $W' < 1.3$  GeV) or high  $\cos\theta_\pi^*$  ( $\cos\theta_\pi^* > 0.8$ ). Again, these may indicate a problem with the acceptance calculation at the edge of the kinematics.

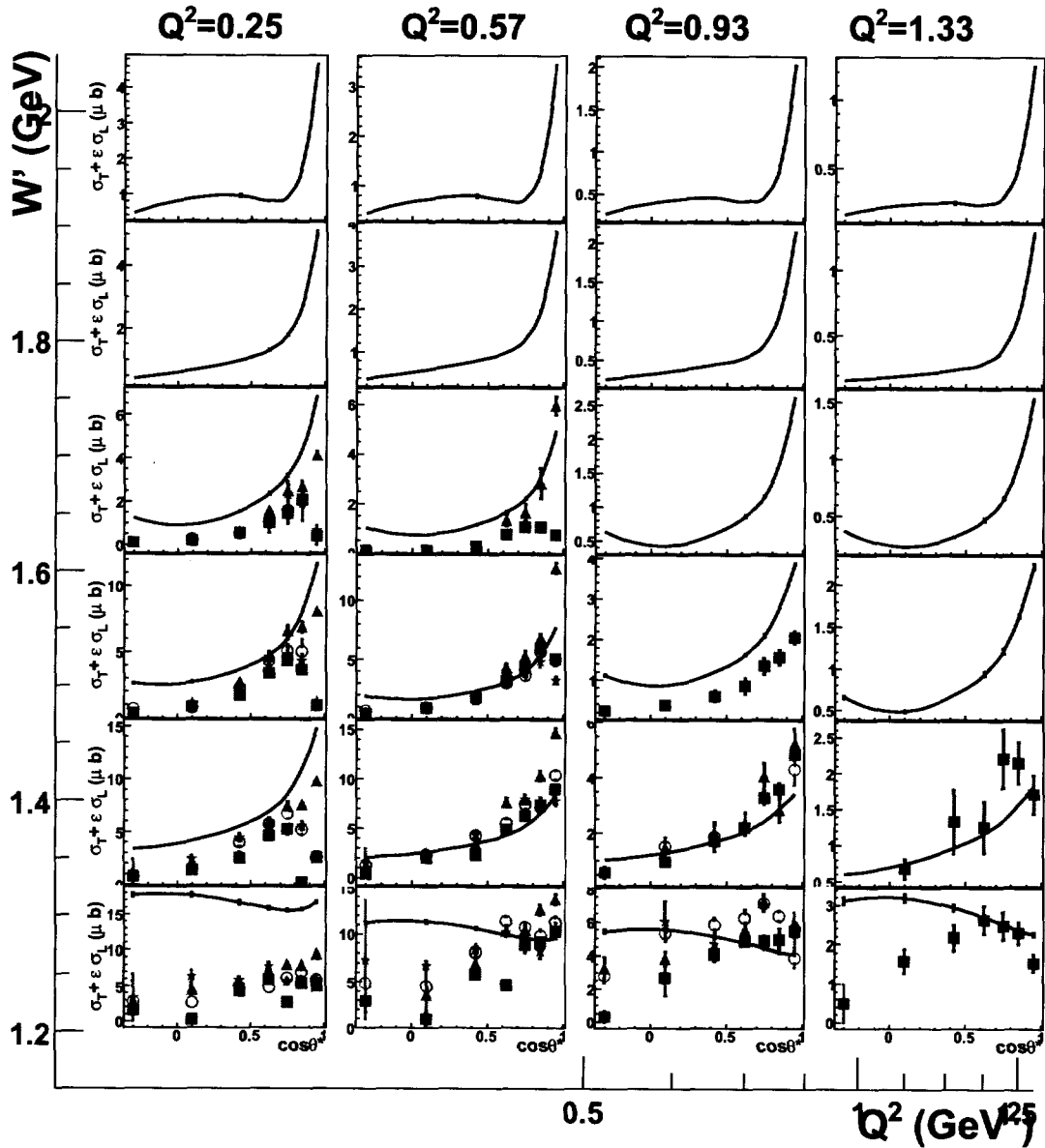


FIG. 159:  $\sigma_T + \epsilon\sigma_L$  vs.  $\cos\theta_\pi^*$  at various  $W'$  and  $Q^2$  bins for the 2 GeV data set. The central  $W'$  value of the panels from the bottom to the top are 1.230, 1.375, 1.525, 1.675, 1.825 and 1.975 GeV, respectively. The black solid curve is the MAID07 prediction. The red square, blue triangle, pink empty circle and green asterisk points are measurements of  $D(e, e'\pi^- p_{\text{CLAS}})p$ ,  $D(e, e'\pi^- p_{\text{RTPC}})p$ ,  $D(e, e'\pi^- p_{\text{CLAS}})p$  with VIP cut and  $D(e, e'\pi^- p_{\text{RTPC}})p$  with VIP cut, respectively.

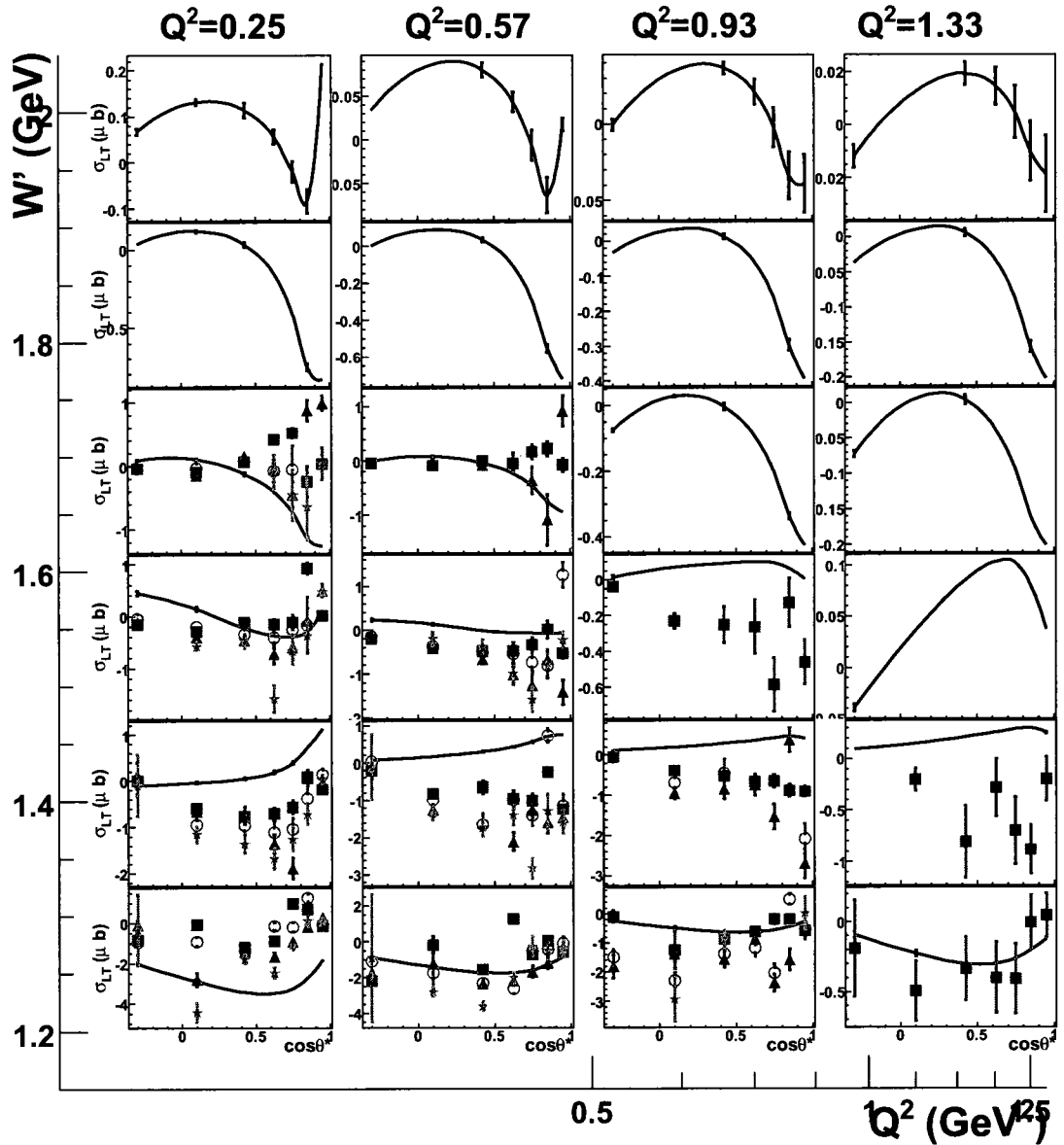


FIG. 160:  $\sigma_{LT}$  vs.  $\cos\theta_\pi^*$  at various  $W'$  and  $Q^2$  bins for the 2 GeV data set. The central  $W'$  value of the panels from the bottom to the top are 1.230, 1.375, 1.525, 1.675, 1.825 and 1.975 GeV, respectively. The black solid curve is the MAID07 prediction. The red square, blue triangle, pink empty circle and green asterisk points are measurements of  $D(e, e'\pi^- p_{CLAS})p$ ,  $D(e, e'\pi^- p_{RTPC})p$ ,  $D(e, e'\pi^- p_{CLAS})p$  with VIP cut and  $D(e, e'\pi^- p_{RTPC})p$  with VIP cut, respectively.

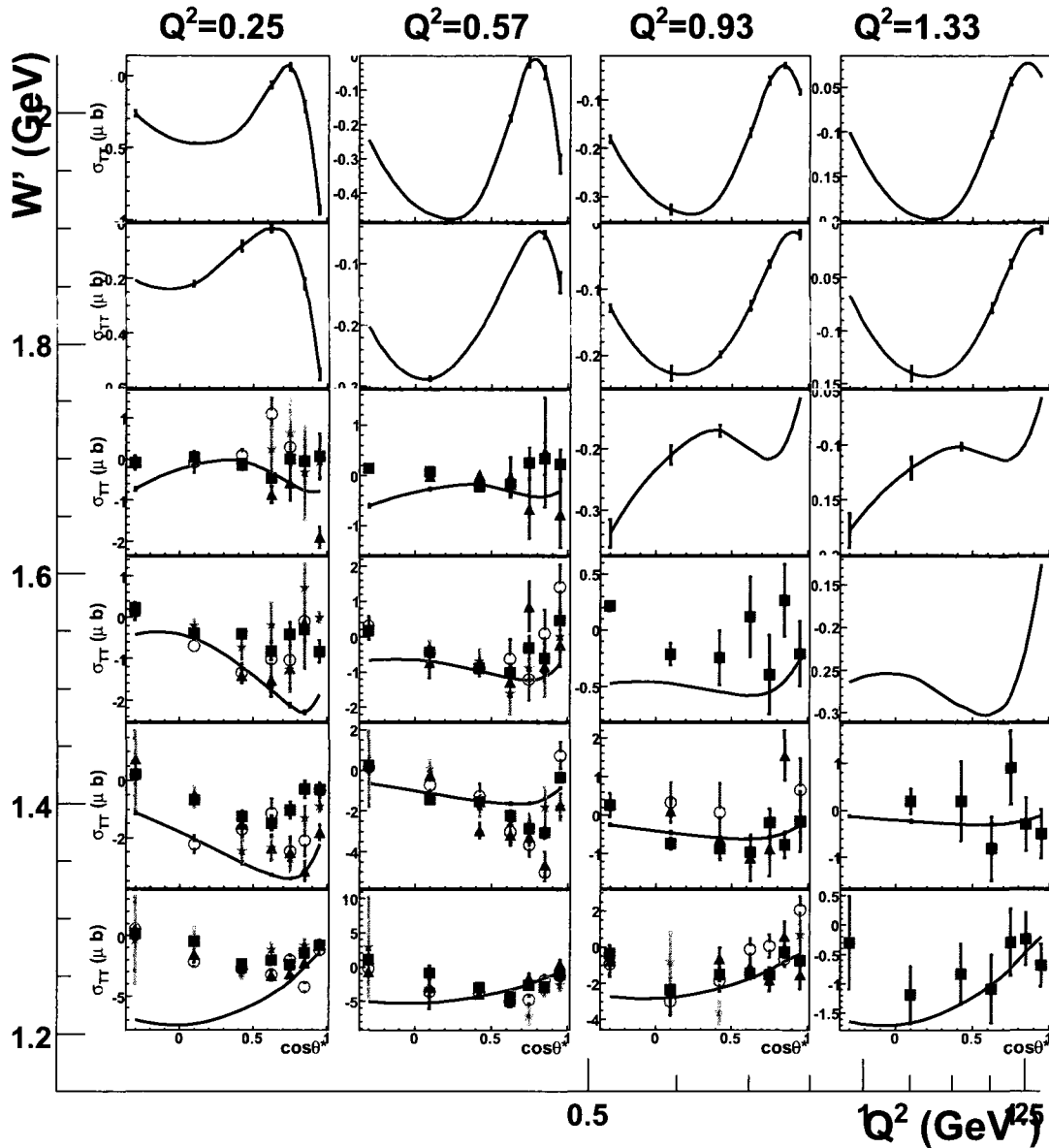


FIG. 161:  $\sigma_{\text{TT}}$  vs.  $\cos\theta_{\pi}^*$  at various  $W'$  and  $Q^2$  bins for the 2 GeV data set. The central  $W'$  value of the panels from the bottom to the top are 1.230, 1.375, 1.525, 1.675, 1.825 and 1.975 GeV, respectively. The black solid curve is the MAID07 prediction. The red square, blue triangle, pink empty circle and green asterisk points are measurements of  $D(e, e'\pi^- p_{\text{CLAS}})p$ ,  $D(e, e'\pi^- p_{\text{RTPC}})p$ ,  $D(e, e'\pi^- p_{\text{CLAS}})p$  with VIP cut and  $D(e, e'\pi^- p_{\text{RTPC}})p$  with VIP cut, respectively.



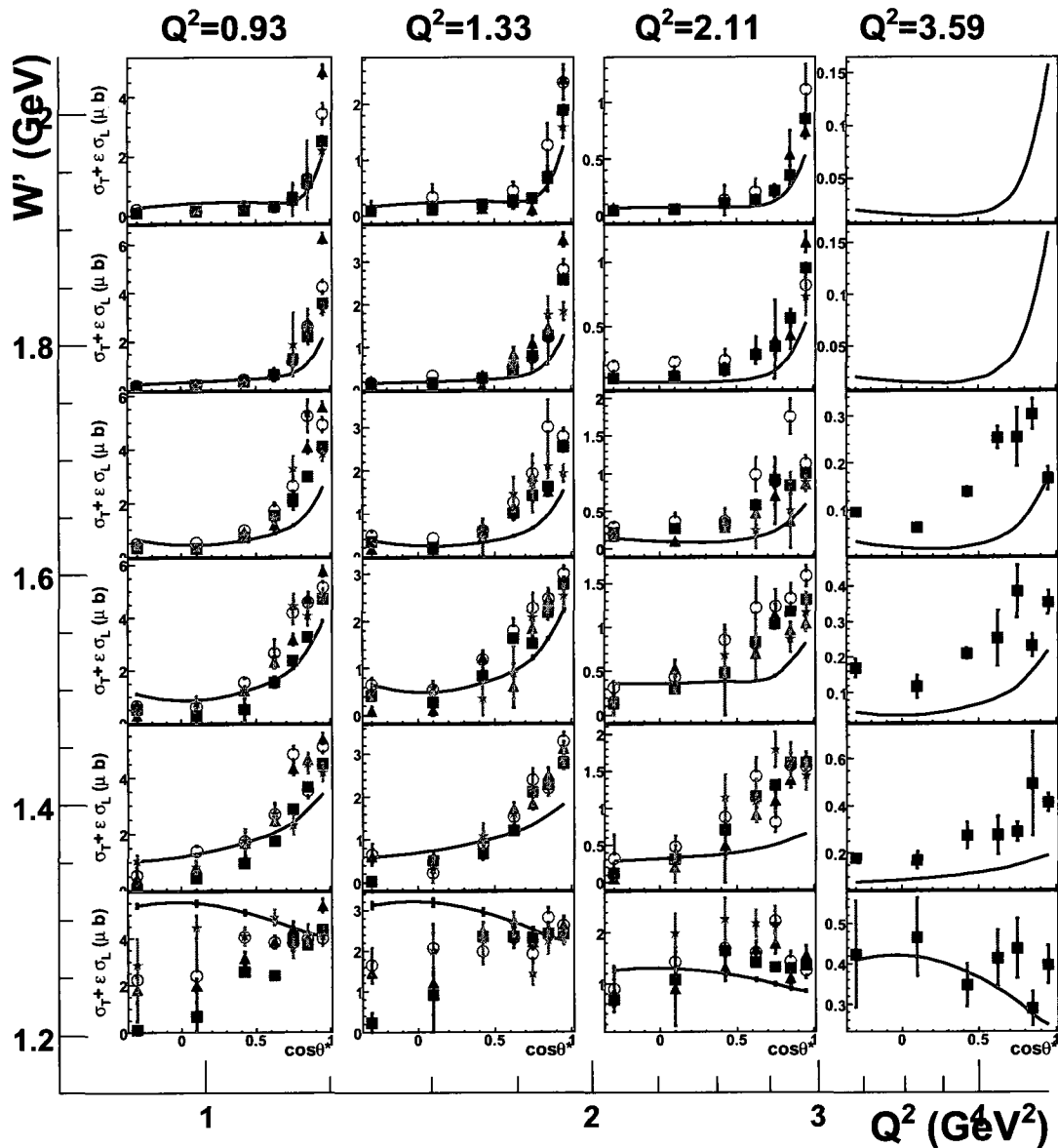


FIG. 162:  $\sigma_T + \epsilon\sigma_L$  vs.  $\cos\theta_\pi^*$  at various  $W'$  and  $Q^2$  bins for the 4 GeV data set. The central  $W'$  value of the panels from the bottom to the top are 1.230, 1.375, 1.525, 1.675, 1.825 and 1.975 GeV, respectively. The black solid curve is the MAID07 prediction. The red square, blue triangle, pink empty circle and green asterisk points are measurements of  $D(e, e'\pi^- p_{\text{CLAS}})p$ ,  $D(e, e'\pi^- p_{\text{RTPC}})p$ ,  $D(e, e'\pi^- p_{\text{CLAS}})p$  with VIP cut and  $D(e, e'\pi^- p_{\text{RTPC}})p$  with VIP cut, respectively.

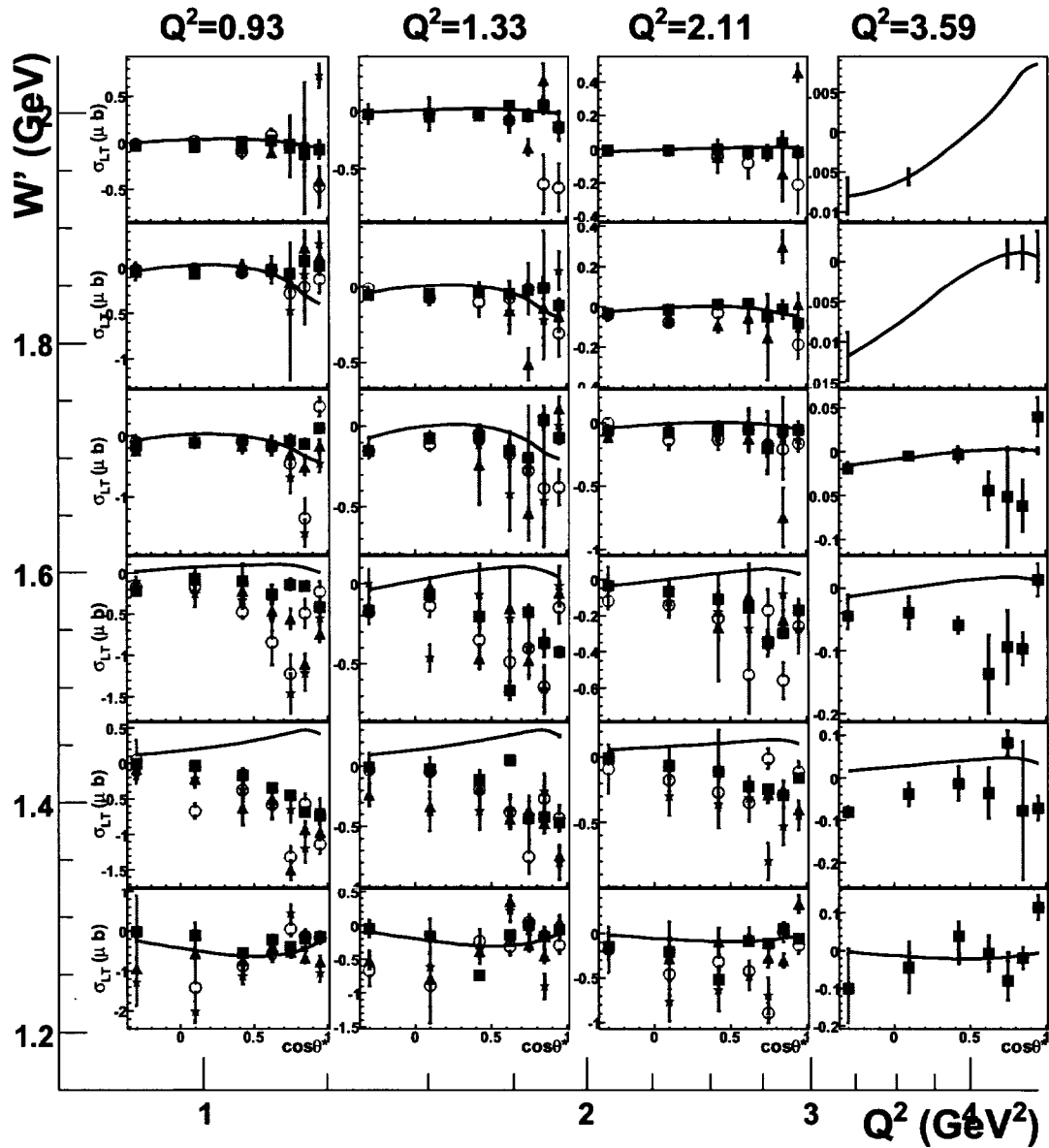


FIG. 163:  $\sigma_{LT}$  vs.  $\cos\theta_\pi^*$  at various  $W'$  and  $Q^2$  bins for the 4 GeV data set. The central  $W'$  value of the panels from the bottom to the top are 1.230, 1.375, 1.525, 1.675, 1.825 and 1.975 GeV, respectively. The black solid curve is the MAID07 prediction. The red square, blue triangle, pink empty circle and green asterisk points are measurements of  $D(e, e'\pi^- p_{CLAS})p$ ,  $D(e, e'\pi^- p_{RTFC})p$ ,  $D(e, e'\pi^- p_{CLAS})p$  with VIP cut and  $D(e, e'\pi^- p_{RTFC})p$  with VIP cut, respectively.

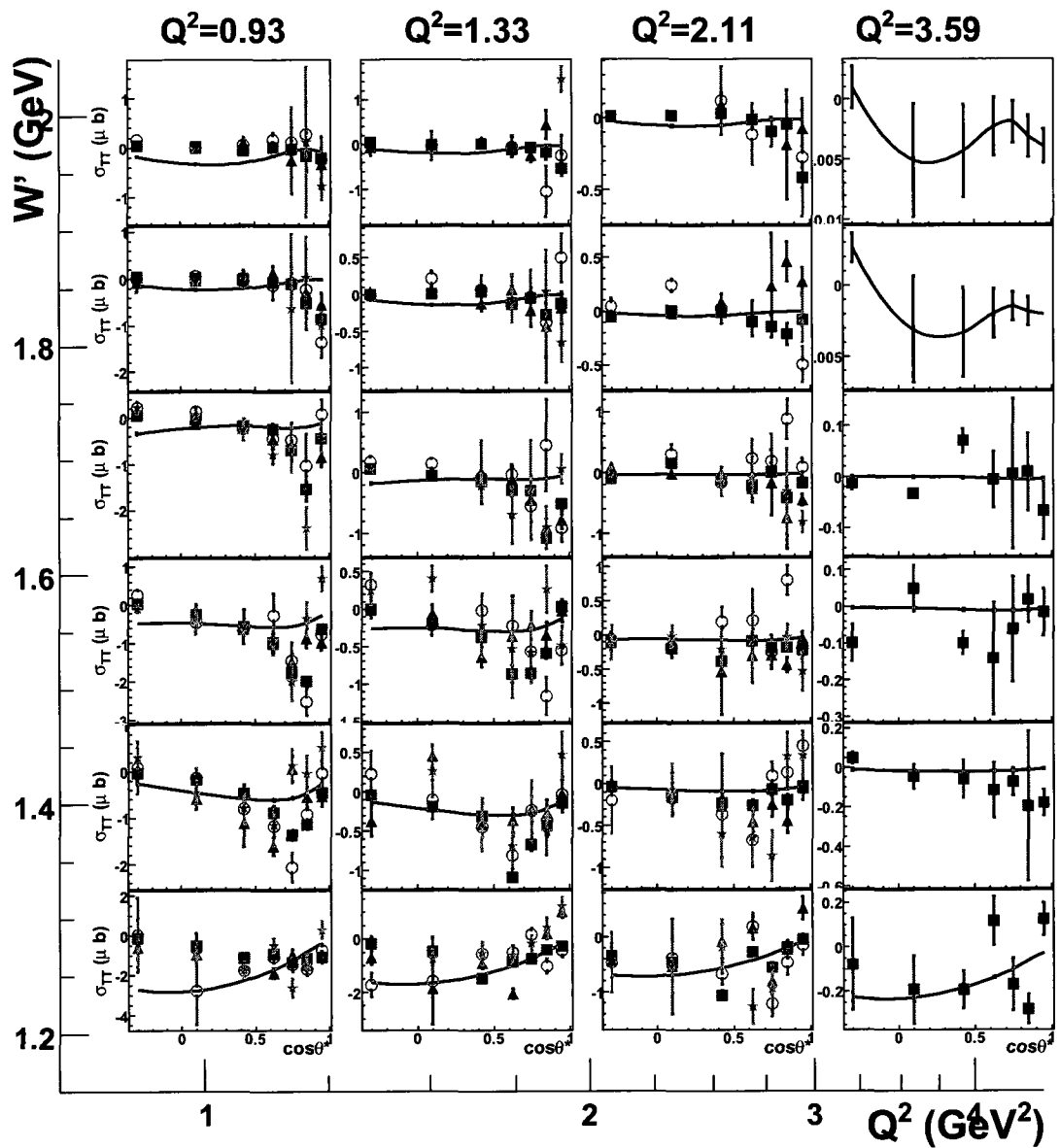


FIG. 164:  $\sigma_{TT}$  vs.  $\cos\theta_{\pi}^*$  at various  $W'$  and  $Q^2$  bins for the 4 GeV data set. The central  $W'$  value of the panels from the bottom to the top are 1.230, 1.375, 1.525, 1.675, 1.825 and 1.975 GeV, respectively. The black solid curve is the MAID07 prediction. The red square, blue triangle, pink empty circle and green asterisk points are measurements of  $D(e, e'\pi^- p_{CLAS})p$ ,  $D(e, e'\pi^- p_{RTPC})p$ ,  $D(e, e'\pi^- p_{CLAS})p$  with VIP cut and  $D(e, e'\pi^- p_{RTPC})p$  with VIP cut, respectively.

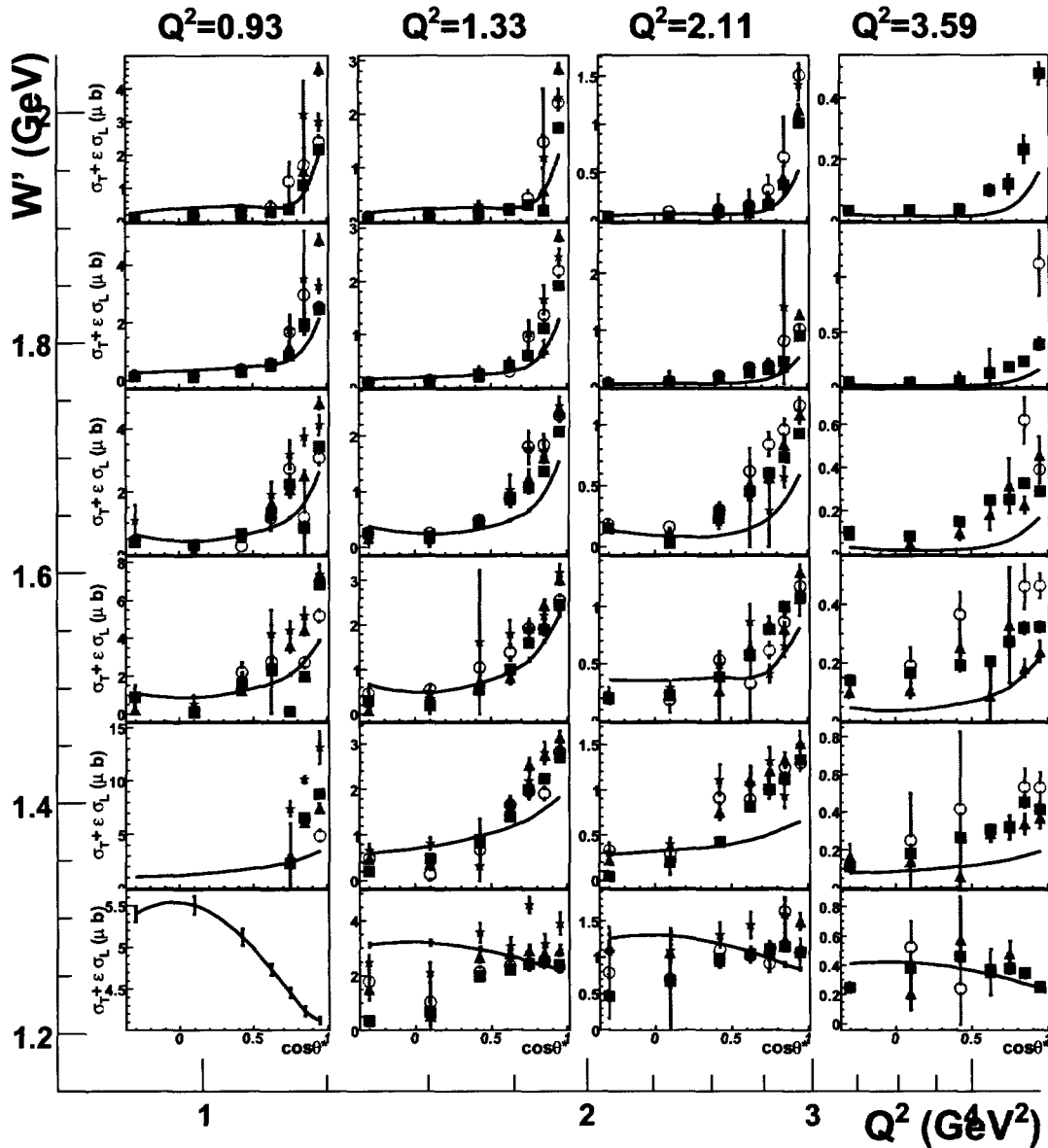


FIG. 165:  $\sigma_T + \epsilon\sigma_L$  vs.  $\cos\theta_\pi^*$  at various  $W'$  and  $Q^2$  bins for the 5 GeV data set. The central  $W'$  value of the panels from the bottom to the top are 1.230, 1.375, 1.525, 1.675, 1.825 and 1.975 GeV, respectively. The black solid curve is the MAID07 prediction. The red square, blue triangle, pink empty circle and green asterisk points are measurements of  $D(e, e'\pi^- p_{\text{CLAS}})p$ ,  $D(e, e'\pi^- p_{\text{RTPC}})p$ ,  $D(e, e'\pi^- p_{\text{CLAS}})p$  with VIP cut and  $D(e, e'\pi^- p_{\text{RTPC}})p$  with VIP cut, respectively.

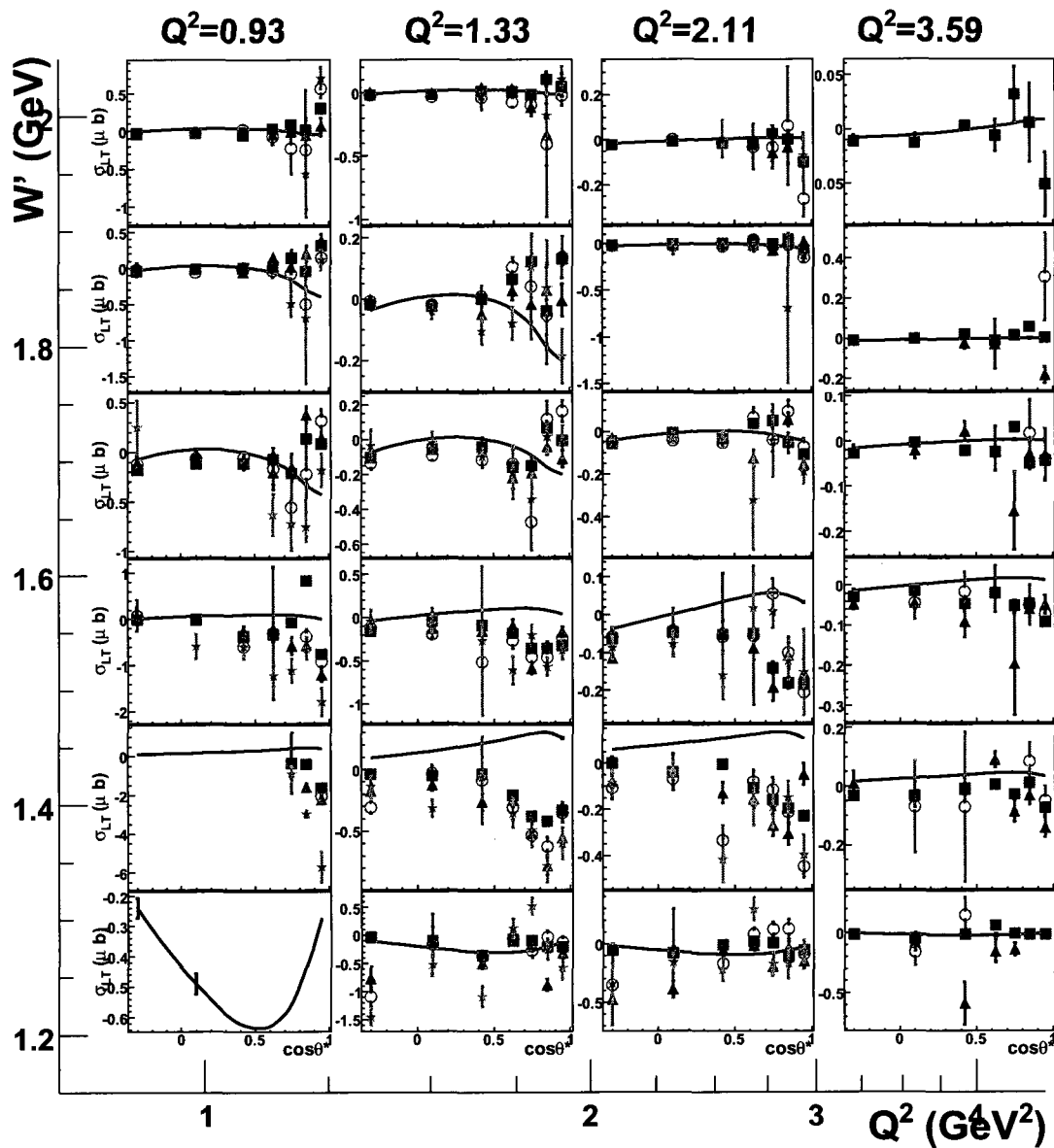


FIG. 166:  $\sigma_{LT}$  vs.  $\cos\theta_\pi^*$  at various  $W'$  and  $Q^2$  bins for the 5 GeV data set. The central  $W'$  value of the panels from the bottom to the top are 1.230, 1.375, 1.525, 1.675, 1.825 and 1.975 GeV, respectively. The black solid curve is the MAID07 prediction. The red square, blue triangle, pink empty circle and green asterisk points are measurements of  $D(e, e'\pi^- p_{CLAS})p$ ,  $D(e, e'\pi^- p_{RTPC})p$ ,  $D(e, e'\pi^- p_{CLAS})p$  with VIP cut and  $D(e, e'\pi^- p_{RTPC})p$  with VIP cut, respectively.

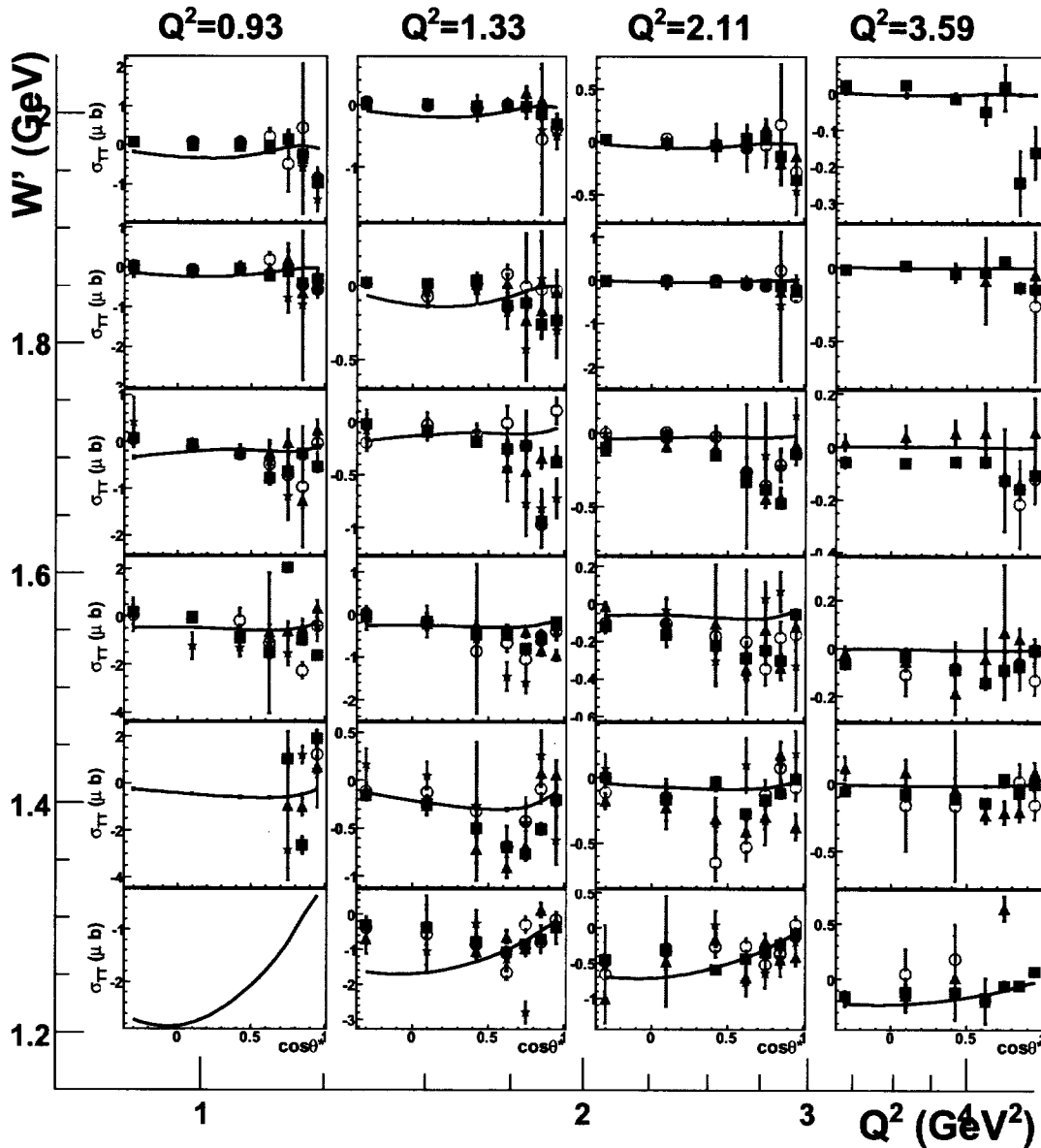


FIG. 167:  $\sigma_{TT}$  vs.  $\cos\theta_\pi^*$  at various  $W'$  and  $Q^2$  bins for the 5 GeV data set. The central  $W'$  value of the panels from the bottom to the top are 1.230, 1.375, 1.525, 1.675, 1.825 and 1.975 GeV, respectively. The black solid curve is the MAID07 prediction. The red square, blue triangle, pink empty circle and green asterisk points are measurements of  $D(e, e'\pi^- p_{CLAS})p$ ,  $D(e, e'\pi^- p_{RTFC})p$ ,  $D(e, e'\pi^- p_{CLAS})p$  with VIP cut and  $D(e, e'\pi^- p_{RTFC})p$  with VIP cut, respectively.

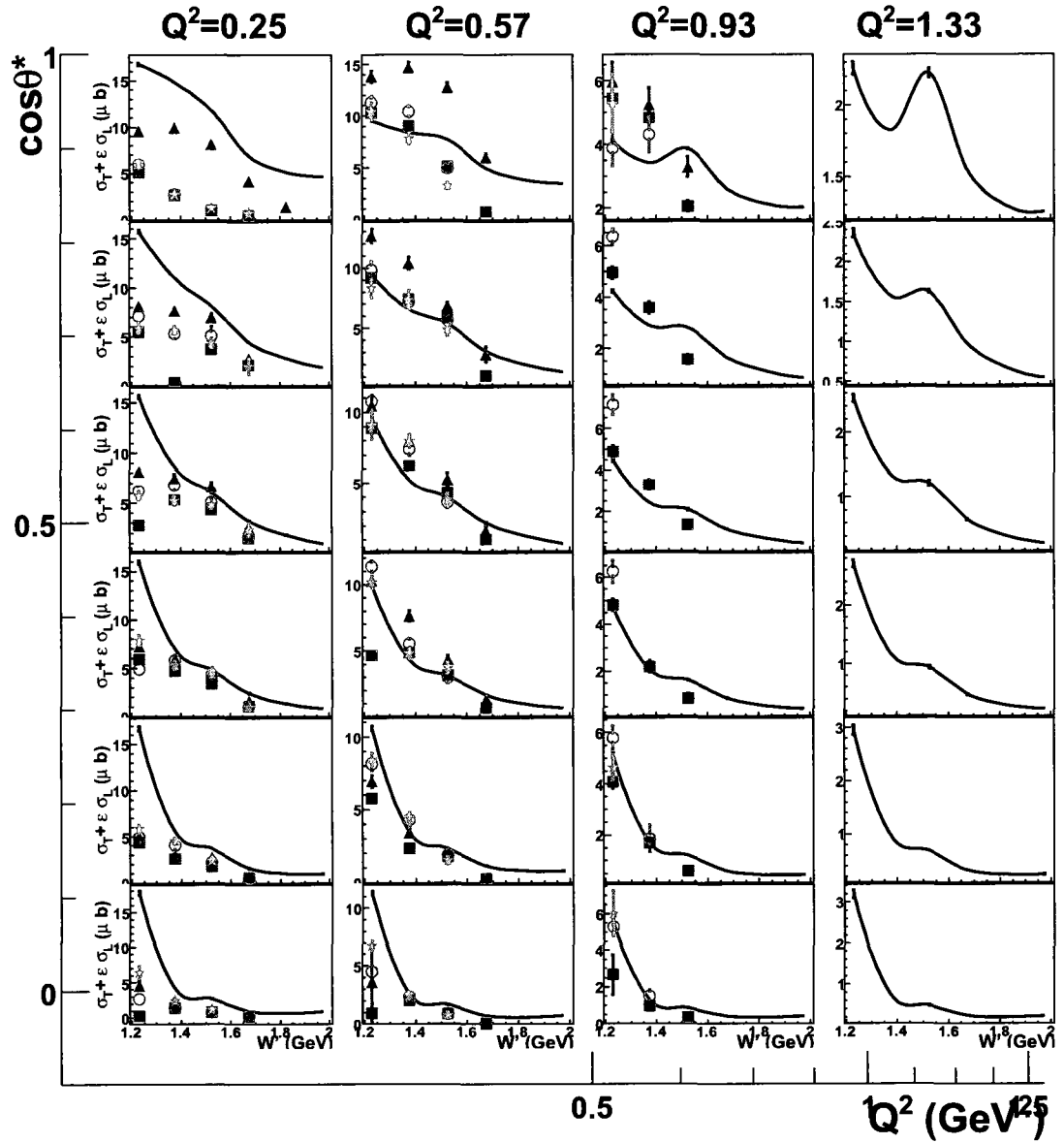


FIG. 168:  $\sigma_T + \epsilon\sigma_L$  vs.  $W'$  at various  $\cos\theta_\pi^*$  and  $Q^2$  bins for the 2 GeV data set. The black solid curve is the MAID07 prediction. The red square, blue triangle, purple empty circle and green asterisk points are measurements of  $D(e, e'\pi^- p_{\text{CLAS}})p$ ,  $D(e, e'\pi^- p_{\text{RTPC}})p$ ,  $D(e, e'\pi^- p_{\text{CLAS}})p$  with VIP cut and  $D(e, e'\pi^- p_{\text{RTPC}})p$  with VIP cut, respectively.

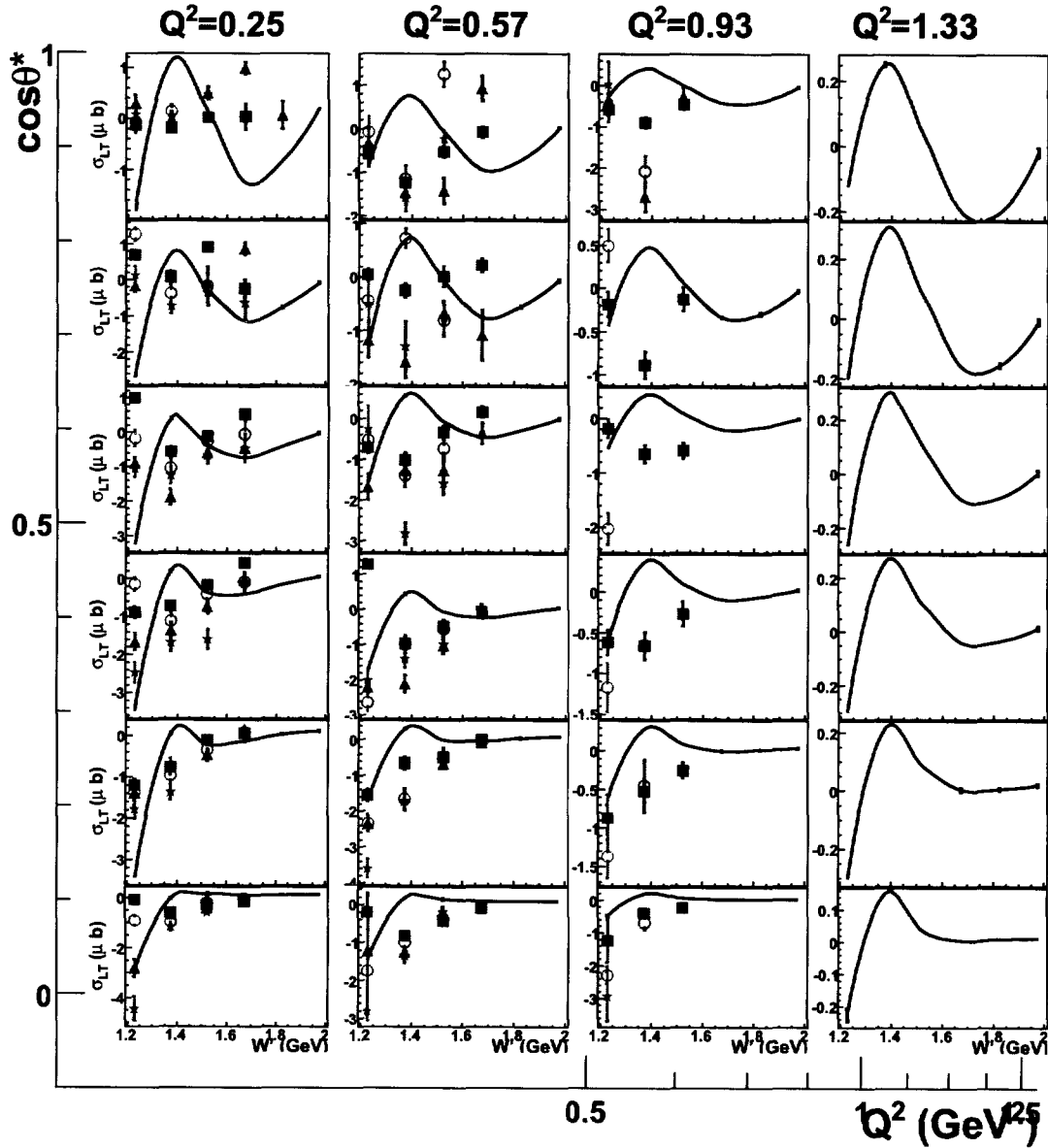


FIG. 169:  $\sigma_{LT}$  vs.  $W'$  at various  $\cos\theta_\pi^*$  and  $Q^2$  bins for the 2 GeV data set. The black solid curve is the MAID07 prediction. The red square, blue triangle, purple empty circle and green asterisk points are measurements of  $D(e, e'\pi^- p_{CLAS})p$ ,  $D(e, e'\pi^- p_{RTPC})p$ ,  $D(e, e'\pi^- p_{CLAS})p$  with VIP cut and  $D(e, e'\pi^- p_{RTPC})p$  with VIP cut, respectively.



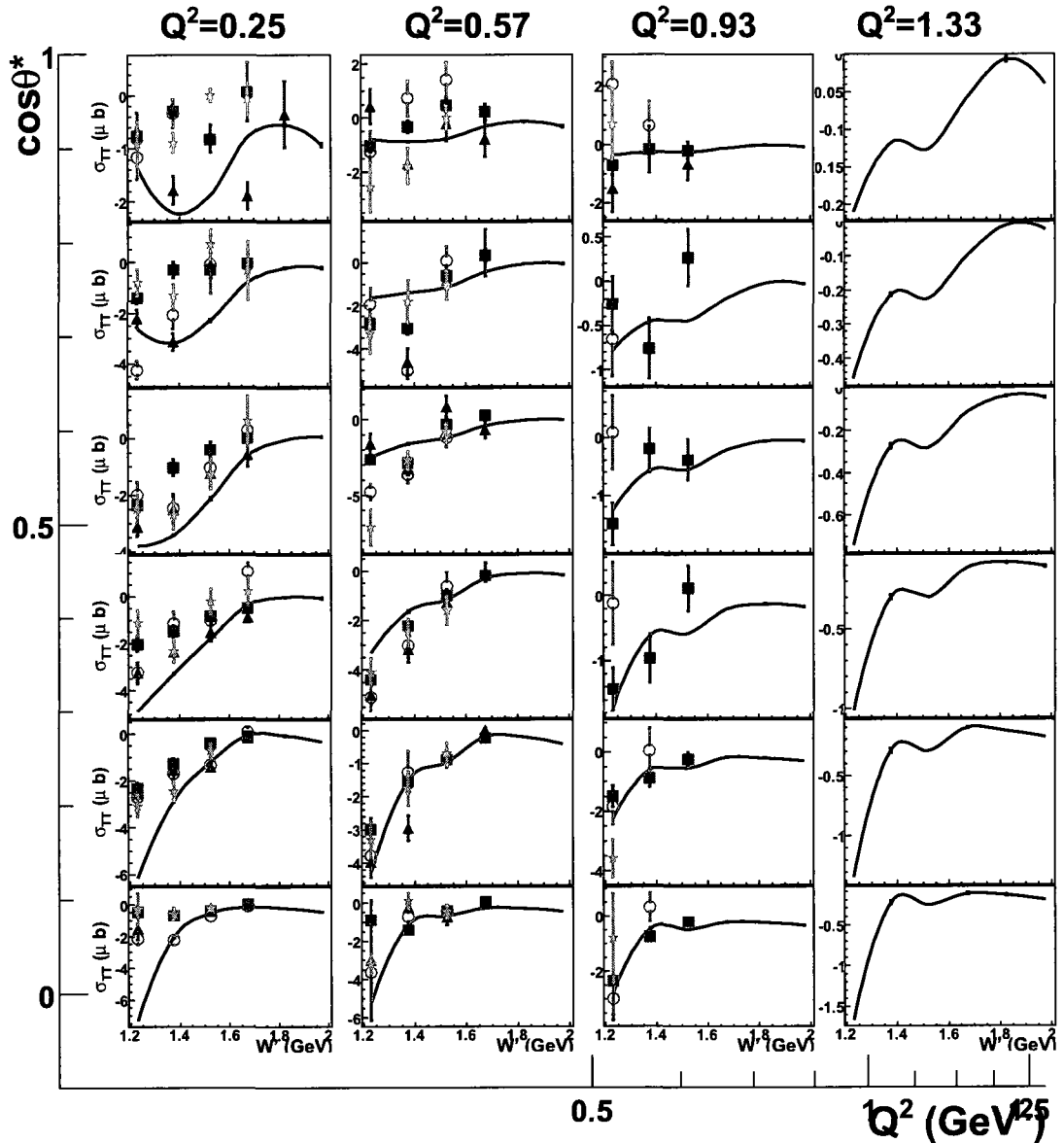


FIG. 170:  $\sigma_{TT}$  vs.  $W'$  at various  $\cos\theta_\pi^*$  and  $Q^2$  bins for the 2 GeV data set. The black solid curve is the MAID07 prediction. The red square, blue triangle, purple empty circle and green asterisk points are measurements of  $D(e, e'\pi^-p_{CLAS})p$ ,  $D(e, e'\pi^-p_{RTPC})p$ ,  $D(e, e'\pi^-p_{CLAS})p$  with VIP cut and  $D(e, e'\pi^-p_{RTPC})p$  with VIP cut, respectively.

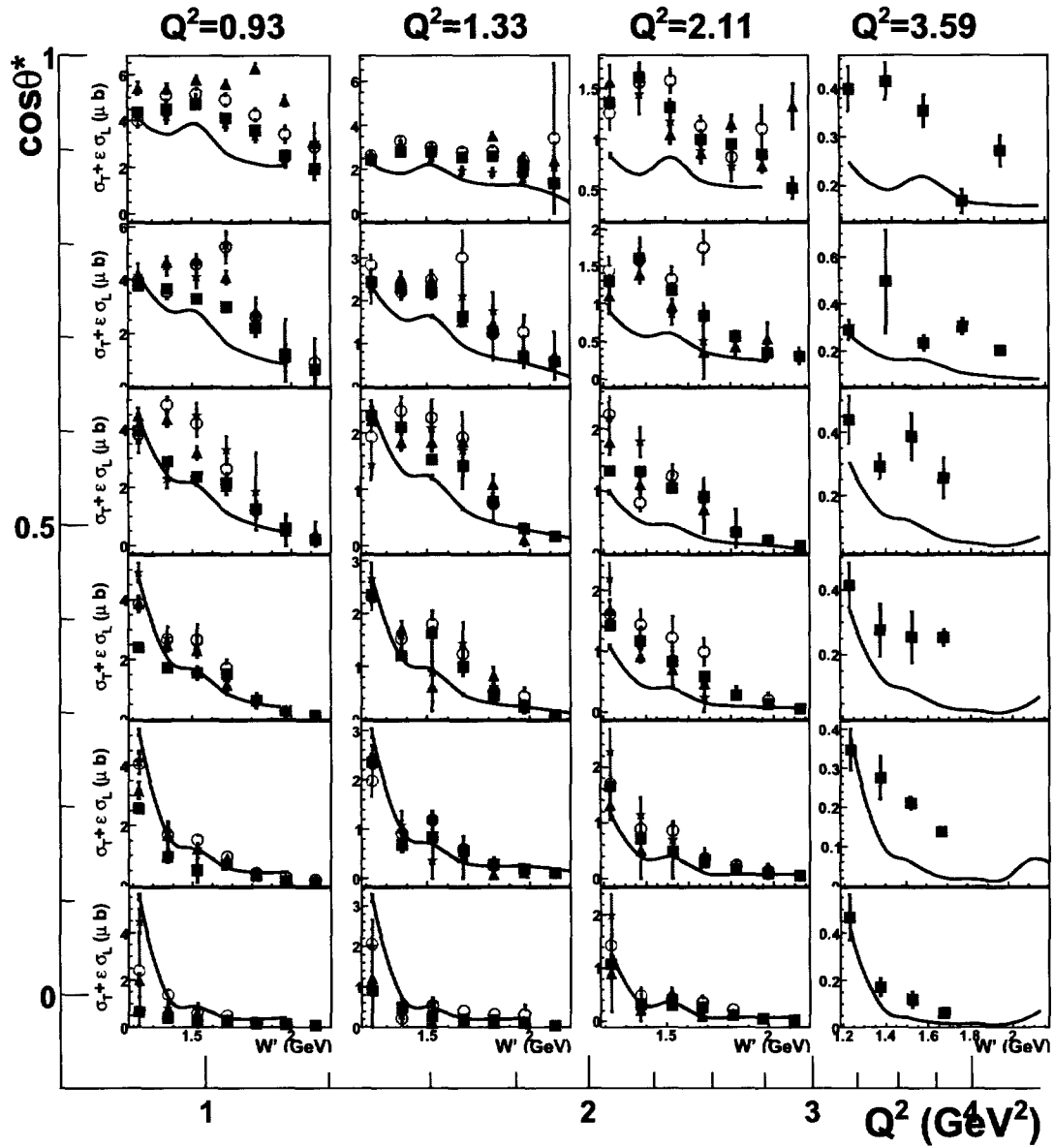


FIG. 171:  $\sigma_T + \epsilon\sigma_L$  vs.  $W'$  at various  $\cos\theta_\pi^*$  and  $Q^2$  bins for the 4 GeV data set. The black solid curve is the MAID07 prediction. The red square, blue triangle, purple empty circle and green asterisk points are measurements of  $D(e, e'\pi^- p_{\text{CLAS}})p$ ,  $D(e, e'\pi^- p_{\text{RTPC}})p$ ,  $D(e, e'\pi^- p_{\text{CLAS}})p$  with VIP cut and  $D(e, e'\pi^- p_{\text{RTPC}})p$  with VIP cut, respectively.

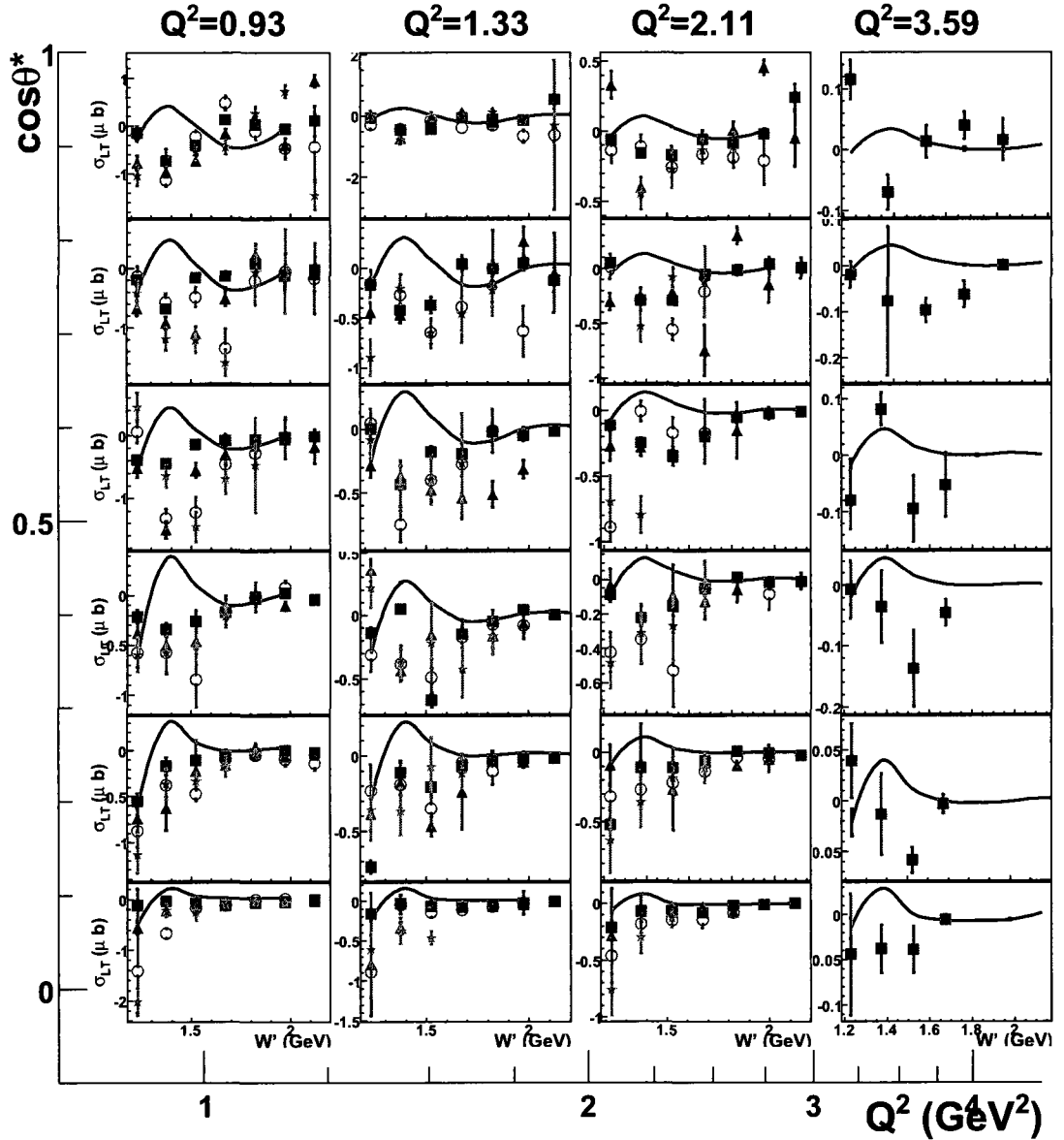


FIG. 172:  $\sigma_{LT}$  vs.  $W'$  at various  $\cos\theta^*$  and  $Q^2$  bins for the 4 GeV data set. The black solid curve is the MAID07 prediction. The red square, blue triangle, purple empty circle and green asterisk points are measurements of  $D(e, e'\pi^- p_{CLAS})p$ ,  $D(e, e'\pi^- p_{RTPC})p$ ,  $D(e, e'\pi^- p_{CLAS})p$  with VIP cut and  $D(e, e'\pi^- p_{RTPC})p$  with VIP cut, respectively.

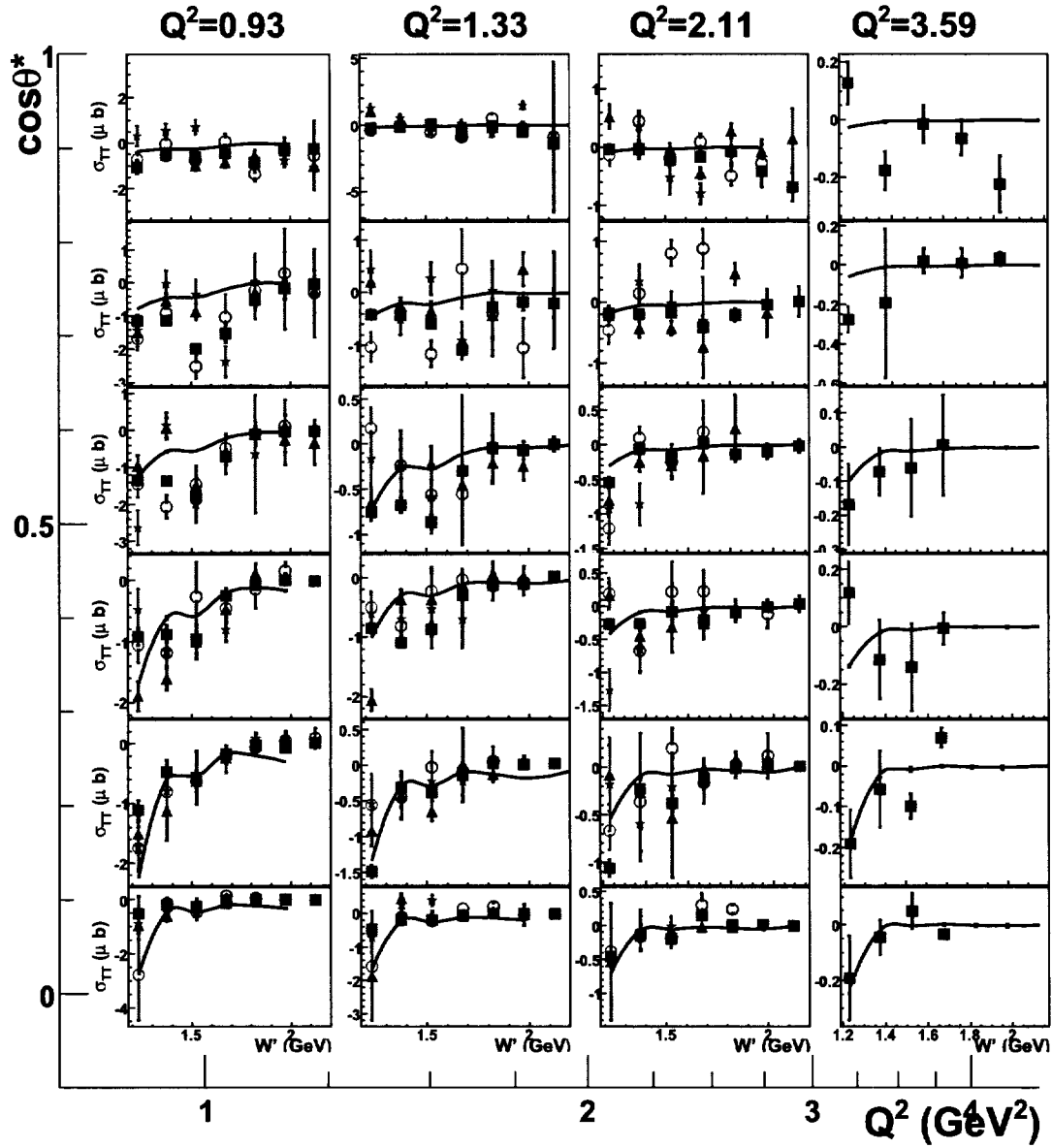


FIG. 173:  $\sigma_{TT}$  vs.  $W'$  at various  $\cos\theta_\pi^*$  and  $Q^2$  bins for the 4 GeV data set. The black solid curve is the MAID07 prediction. The red square, blue triangle, purple empty circle and green asterisk points are measurements of  $D(e, e'\pi^- p_{CLAS})p$ ,  $D(e, e'\pi^- p_{RTPC})p$ ,  $D(e, e'\pi^- p_{CLAS})p$  with VIP cut and  $D(e, e'\pi^- p_{RTPC})p$  with VIP cut, respectively.

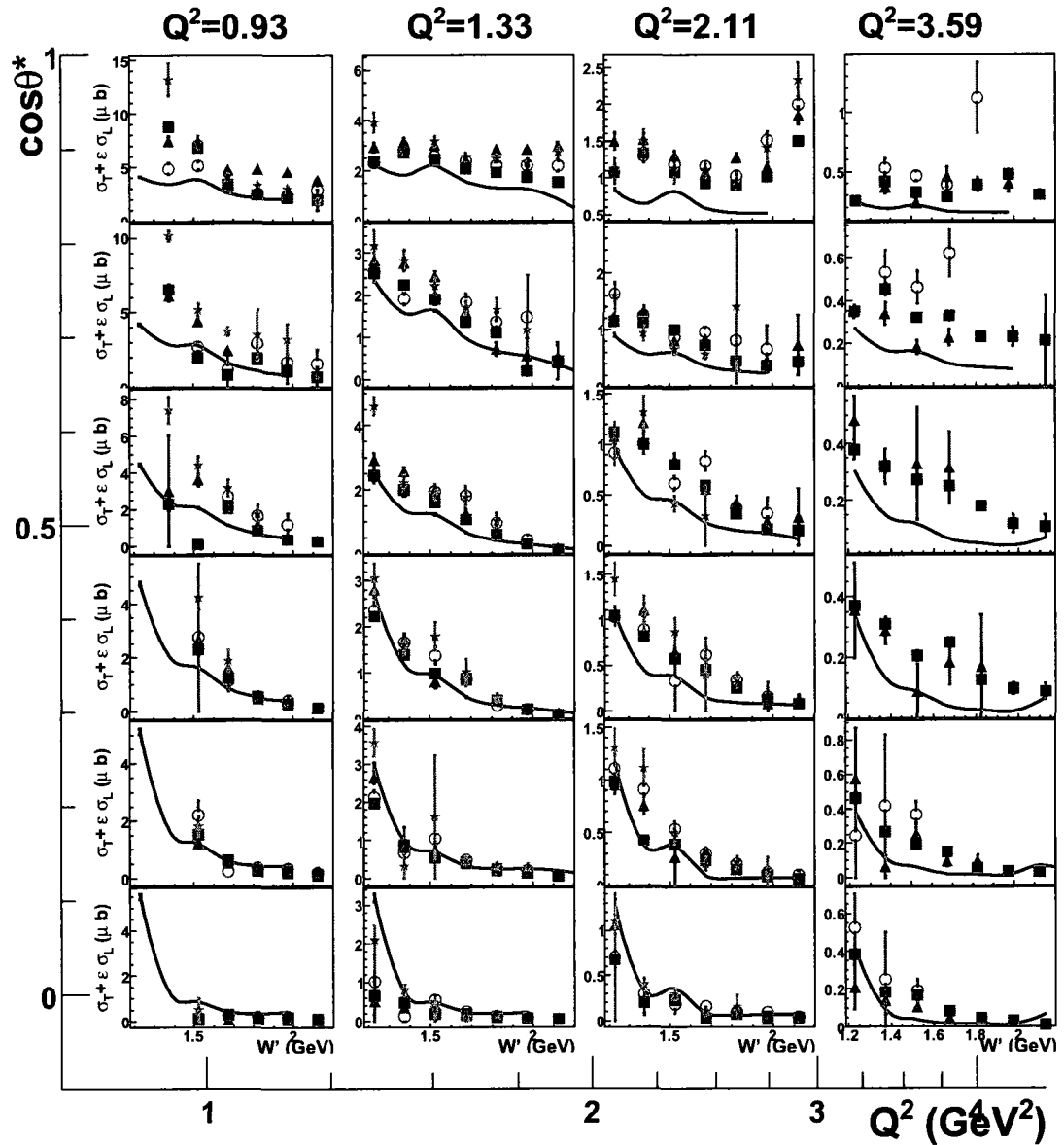


FIG. 174:  $\sigma_T + \epsilon\sigma_L$  vs.  $W'$  at various  $\cos\theta_\pi^*$  and  $Q^2$  bins for the 5 GeV data set. The black solid curve is the MAID07 prediction. The red square, blue triangle, purple empty circle and green asterisk points are measurements of  $D(e, e'\pi^- p_{\text{CLAS}})p$ ,  $D(e, e'\pi^- p_{\text{RTPC}})p$ ,  $D(e, e'\pi^- p_{\text{CLAS}})p$  with VIP cut and  $D(e, e'\pi^- p_{\text{RTPC}})p$  with VIP cut, respectively.

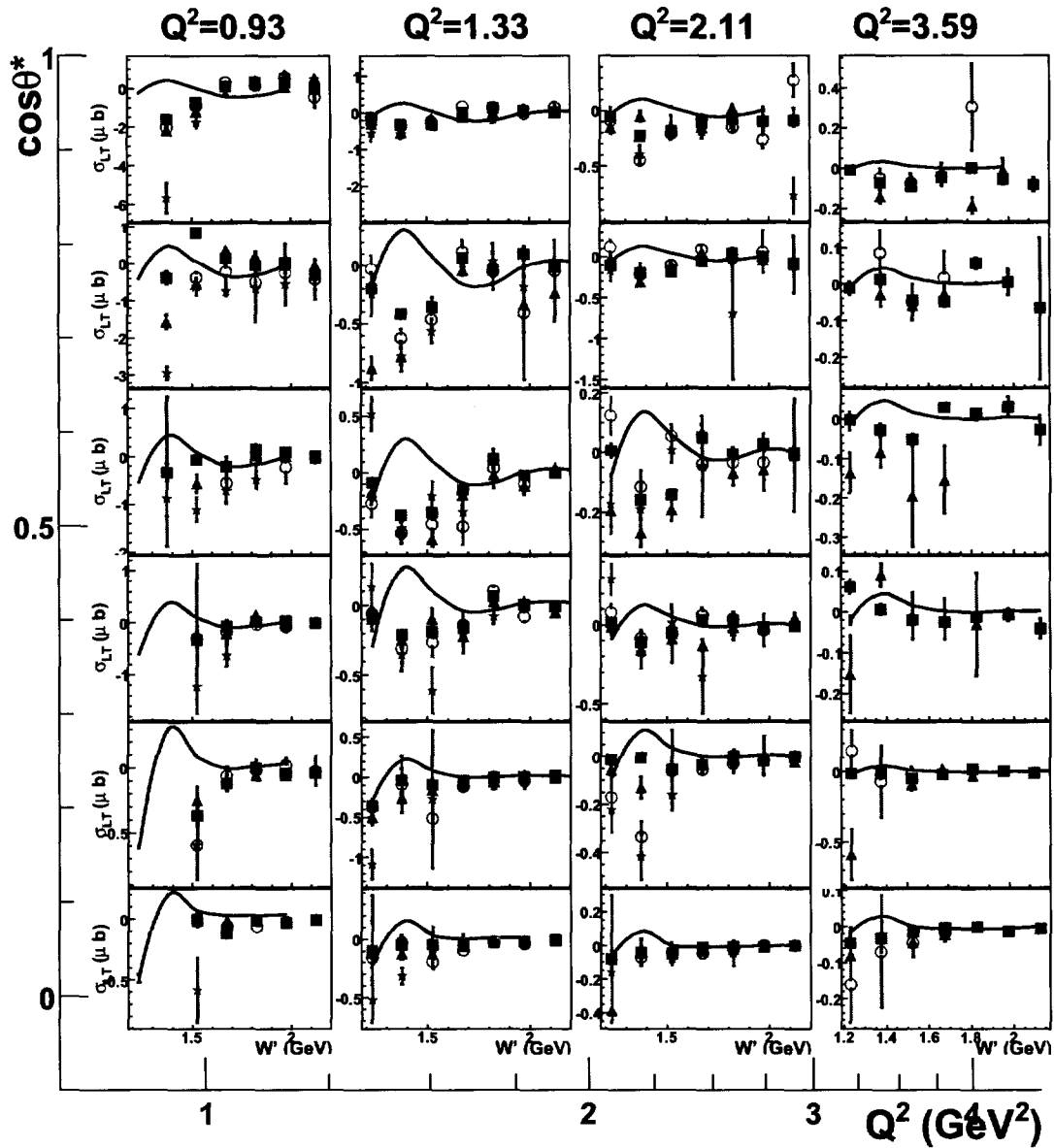


FIG. 175:  $\sigma_{LT}$  vs.  $W'$  at various  $\cos\theta_{\pi}^*$  and  $Q^2$  bins for the 5 GeV data set. The black solid curve is the MAID07 prediction. The red square, blue triangle, purple empty circle and green asterisk points are measurements of  $D(e, e'\pi^- p_{CLAS})p$ ,  $D(e, e'\pi^- p_{RTPC})p$ ,  $D(e, e'\pi^- p_{CLAS})p$  with VIP cut and  $D(e, e'\pi^- p_{RTPC})p$  with VIP cut, respectively.

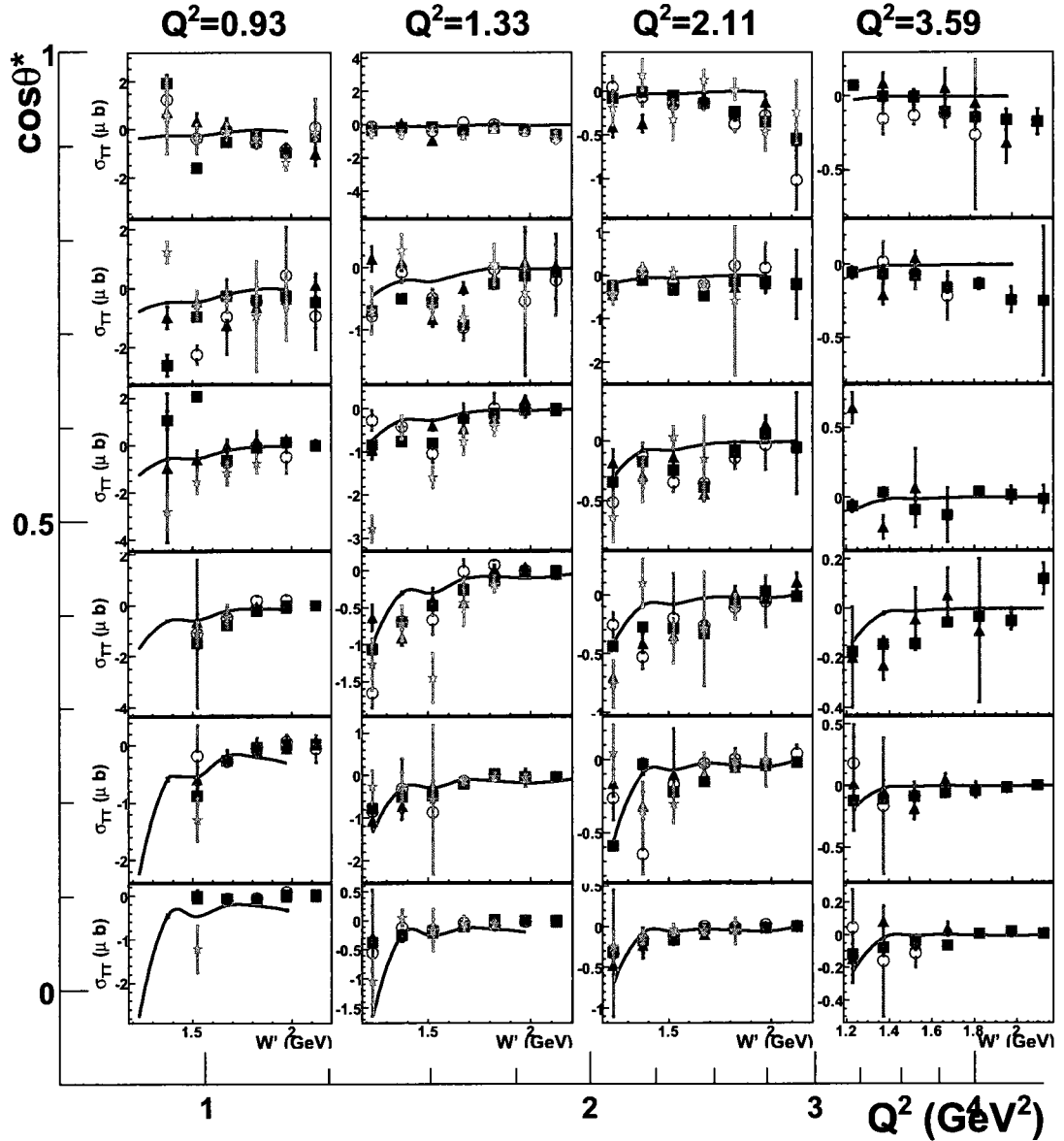


FIG. 176:  $\sigma_{TT}$  vs.  $W'$  at various  $\cos\theta_\pi^*$  and  $Q^2$  bins for the 5 GeV data set. The black solid curve is the MAID07 prediction. The red square, blue triangle, purple empty circle and green asterisk points are measurements of  $D(e, e'\pi^- p_{CLAS})p$ ,  $D(e, e'\pi^- p_{RTPC})p$ ,  $D(e, e'\pi^- p_{CLAS})p$  with VIP cut and  $D(e, e'\pi^- p_{RTPC})p$  with VIP cut, respectively.

## CHAPTER VII

### SUMMARY

The BoNuS experiment was performed with three electron beam energies of 2.1424, 4.2262 and 5.2681 GeV in Fall 2005 using the CLAS together with a newly built RTPC at JLab. A small amount of data with 1.1005 GeV beam energy were taken for calibration purposes. The data were collected on a 7 atmosphere gaseous deuterium target. The RTPC detector, using GEM technology, allowed us to measure the spectator proton with momenta from 67 to 250 MeV/c with a resolution of 18% [45], therefore providing two possible ways,  $D(e, e'\pi^- p_{\text{CLAS}})p$  and  $D(e, e'\pi^- p_{\text{RTPC}})p$ , for studying the exclusive  $\pi^-$  electro-production from the neutron. The  $D(e, e'\pi^- p_{\text{CLAS}}p_{\text{RTPC}})$  reaction was not considered in this analysis due to its extremely limited statistics.

The data were calibrated and corrected for beam line position and energy loss. Fiducial cuts for each detected particle were applied in order to eliminate regions where the detection efficiency is too low or unknown. More than 300 million  $D(e, e'\pi^- p_{\text{CLAS}}p_{\text{RTPC}})$  events were simulated for each beam energy in order to study the acceptance. To extract the cross section, corrections for the detection efficiency of trigger electrons, the fast proton measured by the CLAS and the spectator proton measured by the RTPC, as well as the acceptance of  $D(e, e'\pi^- p_{\text{CLAS}})p$  or  $D(e, e'\pi^- p_{\text{RTPC}})p$ , the radiative effects and the background determination were included.

A  $2\text{-}\sigma$  missing mass cut was used to select exclusive events. The cross sections were extracted as a function of  $W'$ ,  $Q^2$ ,  $\cos\theta_\pi^*$  and  $\phi_\pi^*$  using the 2, 4 and 5 GeV beam energy data sets over a large 4-D kinematic range. Although some limited measurements of pion production from the deuteron have been done in the past 50 years, by calculating the ratio of  $D(e, e'\pi^- p)p$  to  $D(e, e'\pi^+ n)n$ , this analysis for the first time directly measures the absolute cross section for  $D(e, e'\pi^- p)p$ .

The statistics of the  $D(e, e'\pi^- p_{\text{RTPC}})p$  channel was about one-fourth of that of the  $D(e, e'\pi^- p_{\text{CLAS}})p$  channel, and results for these two measurements were consistent in most bins. The structure functions  $\sigma_T + \varepsilon\sigma_L$ ,  $\sigma_{LT}$  and  $\sigma_{TT}$  were extracted by fitting the  $\phi_\pi^*$  dependence of the cross section. These structure functions were qualitatively in agreement with MAID and SAID models in most bins. However, we show some



significant disagreement, especially at low  $W'$  in the  $\Delta(1232)$  resonance region, and at  $\cos\theta_\pi^*$  close to 1. These regions require further study to make sure acceptance issues are not playing a role.

The off-shell and final state interactions effects were predicted to be as small as 20% under the VIP cut. Comparison of the data with and without the VIP cut have been done for both the  $D(e, e'\pi^- p_{\text{CLAS}})p$  and the  $D(e, e'\pi^- p_{\text{RTPC}})p$  cross sections. These measurements are consistent in most bins, except at regions of low  $W'$  ( $W' < 1.3$  GeV) or high  $\cos\theta_\pi^*$  ( $\cos\theta_\pi^* > 0.8$ ). These data are among the very few now available on the neutron, which is important for inclusion in new MAID and SAID fits. Ultimately, we hope these data will contribute to a better understanding of nucleon structure.

The statistics for both  $D(e, e'\pi^- p_{\text{CLAS}})p$  and  $D(e, e'\pi^- p_{\text{RTPC}})p$  channels are limited due to the short experiment time and low data acquisition rates of the RTPC. It may be interesting to repeat the  $D(e, e'\pi^- p_{\text{CLAS}})p$  analysis using other CLAS data. On the other hand, we can also calculate the ratio of  $D(e, e'\pi^- p)p$  to  $D(e, e'\pi^+ n)n$  using BoNuS and other CLAS data. These analyses may be undertaken in the future.

**BIBLIOGRAPHY**

- [1] M. Gell-Mann, Phys. Rev. **125**, 1067 (1962).
- [2] M. Gell-Mann, Phys. Lett. **8**, 214 (1964).
- [3] G. Zweig, CERN-8182-TH-401 (1964).
- [4] H. Anderson *et al.*, Phys. Rev. **85**, 936 (1952).
- [5] M. Han and Y. Nambu, Phys. Rev. B **138**, 1006 (1965).
- [6] O. Greenberg and D. Zwanziger, Phys. Rev. **150**, 1177 (1966).
- [7] D. Gross and F. Wilczek, Phys. Rev. D **8**, 3633 (1973).
- [8] H. D. Politzer, Phys. Rev. Lett. **30**, 1346 (1973).
- [9] H. D. Politzer, Phys. Rep. **14**, 129 (1974).
- [10] B. R. Martin and G. Shaw, *Particle physics*, **2nd** edition, p. 115, John Wiley & Sons Ltd. (1997).
- [11] <http://wwwkph.kph.uni-mainz.de/MAID/maid2007/maid2007.html>.
- [12] D. Drechsel, S. Kamalov, L. Tiator, Nucl. Phys. **A645**, 145 (1999).
- [13] D. Drechsel, S. Kamalov, L. Tiator, Eur. Phys. J. A **34**, 69 (2007).
- [14] <http://gwdac.phys.gwu.edu>.
- [15] R. Arndt, I. Strakovsky and R. Workman, Phys. Rev. C **62**, 034005 (2000).
- [16] C. Bebek *et al.*, Phys. Rev. D **13**, 25 (1976).
- [17] C. Bebek *et al.*, Phys. Rev. D **17**, 1693 (1978).
- [18] J. Morris *et al.*, Phys. Lett. B **73**, 495 (1978).
- [19] J. Morris *et al.*, Phys. Lett. B **86**, 211 (1979).
- [20] F. Foster and G. Hughes, Rep. Prog. Phys. **46**, 1445 (1983).
- [21] O. Varenikova *et al.*, Z. Phys. C **37**, 251 (1988).

- [22] J. Wright *et al.*, Nucl. Phys. **B181**, 403 (1981).
- [23] D. Gaskell *et al.*, Phys. Rev. Lett. **87**, 202301 (2001).
- [24] W. Melnitchouk, A. Schreiber, and A. Thomas, Phys. Lett. B **335**, 11 (1994).
- [25] W. Melnitchouk, Phys. Rev. D **49**, 1183 (1994).
- [26] I. Strakovsky, personal communications, in progress.
- [27] J. M. Laget, Phys. Rev. C **73**, 044003 (2006).
- [28] C. Ciofi degli Atti, L. Kaptari, and B. Kopeliovich, Eur. Phys. J. A **19**, 133–137 (2004).
- [29] H. Grunder *et al.*, *CEBAF Commissioning and Future Plans*, Proceedings of PAC95, p. 1.
- [30] C. Reece *et al.*, *Performance Experience with the CEBAF SRF Cavities*, Proceedings of PAC95, p. 1512.
- [31] G. Krafft *et al.*, *Measuring and controlling energy spread in CEBAF*, Proc. of LINAC 2000, p. 721.
- [32] C. Sinclair *et al.*, Nucl. Instr. Meth. **A318**, 410 (1992).
- [33] F. Gougnaud *et al.*, *Controls for high precision beam energy determination at CEBAF, Hall A: The ARC Project*, ICA LEPCS, 1999, Trieste, Italy.
- [34] C. Leemann *et al.*, *The continuous electron beam accelerator facility: CEBAF at the Jefferson Laboratory*, Annual review of nuclear and particle science, **51**, 413 (2001).
- [35] B. Mecking *et al.*, Nucl. Instr. Meth. **A503**, 513 (2003).
- [36] M. Mestayer *et al.*, Nucl. Instr. Meth. **A449**, 81 (2000).
- [37] L. Qin *et al.*, *Performance of a Region 2 drift chamber prototype and Region 2 drift chamber tracking*, CLAS-NOTE, **96-018** (1996).
- [38] G. Adams *et al.*, Nucl. Instr. and Meth. **A465**, 414 (2001).
- [39] V. Baturin *et al.*, Nucl. Instr. Meth. **A562**, 327 (2006).

- [40] E. Smith *et al.*, Nucl. Instr. Meth. **A432**, 265 (1999).
- [41] M. Amarian *et al.*, Nucl. Instr. Meth. **A460**, 239 (2001).
- [42] J. Zhang, <http://www.jlab.org/~jixie/meeting/BonusRunCharge.html>.
- [43] J. Zhang, <http://www.jlab.org/~jixie/meeting/BonusRunTrigger.html>.
- [44] K. Egiyan, *Determination of electron energy cut due to the CLAS EC threshold*, CLAS-NOTE, **99-007** (1999).
- [45] H. Fenker *et al.*, Nucl. Instr. Meth. **A592**, 273 (2008).
- [46] F. Sauli *et al.*, Nucl. Instr. Meth. **A386**, 531 (1997).
- [47] R. Veenhof, *GARFIELD CERN wire chamber field & transport computation program*, Version **6.33**.
- [48] A. Sharma *et al.*, Nucl. Instr. Meth. **A454**, 267 (2000).
- [49] S. Biagi, Nucl. Instr. Meth. **A421**, 234 (1999).
- [50] S. Agostinelli *et al.*, Nucl. Instr. Meth. **A506**, 250 (2003).
- [51] J. Allison *et al.*, IEEE Transactions on Nuclear Science, **53**, 270-278 (2006).
- [52] V. Blobel *et al.*, *The BOS System*, <http://www.desy.de/~blobel/bosman.pdf>, version **5** (2003).
- [53] D. Cords *et al.*, *CLAS event format with BOS - version 1.00*, CLAS-NOTE, **94-012** (1994).
- [54] <http://geant4.cern.ch>.
- [55] *GEANT4 users Guide*, version **8.0** (2006).
- [56] *GEANT4 Physics Reference Manual*, version **4.8** (2006).
- [57] N. Baillie, Ph.D. thesis, W&M (2009).
- [58] T. Zerguerras, *Simulation of the DVCS calorimeter With the GEANT4 toolkit*, CLAS-NOTE, **03-015** (2003).
- [59] K. Abe *et al.*, Phys. Lett. B **452**, 194 (1999).

- [60] A. Klimenko *et al.*, Phys. Rev. C **73**, 035212 (2006).
- [61] M. Lacombe *et al.*, Phys. Lett. B **101**, 139 (1981).
- [62] A. Klimenko, Ph.D. thesis, ODU (2004).
- [63] S. Tkachenko, Ph.D. thesis, ODU (2009).
- [64] S. Stepanyan, *fsgen package*, CLAS CVS, packages/fsgen.
- [65] T. Sjostrand, <http://home.thep.lu.se/~torbjorn/pythia/lutp0613man2.pdf>, FERMILAB-PUB-06-052-CD-T (2006).
- [66] <http://home.thep.lu.se/~torbjorn/Pythia.html>.
- [67] E. Smith *et al.*, *Calibration of the CLAS TOF system*, CLAS-NOTE, **99-011** (1999).
- [68] E. Smith *et al.*, *CLAS TOF online manual*, CLAS-NOTE, **01-019** (2001).
- [69] H. Baghdasaryan, Ph.D. thesis, ODU (2006).
- [70] D. Lawrence, M. D. Mestayer, *CLAS drift chamber calibration procedures*, CLAS-NOTE, **99-018** (1999)
- [71] R. Feuerbach, CLAS-NOTE, **01-022** (2001).
- [72] C. Smith, *EC energy calibration*, [http://www.jlab.org/~lcsmith/EC\\_Energy\\_Calibration.html](http://www.jlab.org/~lcsmith/EC_Energy_Calibration.html).
- [73] M. Guillo *EC time calibration procedure for photon runs in CLAS*, CLAS-NOTE, **01-004** (2001)
- [74] D. Protopopescu *et al.*, *Fiducial cuts for electrons in the CLAS/E2 data at 4.4 GeV*, CLAS-NOTE, **00-007** (2000).
- [75] R. Niyazov *et al.*, *Fiducial cuts for positive hadrons in CLAS/E2 data at 4.4 GeV*, CLAS-NOTE, **01-013** (2000).
- [76] S. Kuhn, A. Klimenko *Momentum corrections for E6*, CLAS-NOTE, **03-005** (2003).
- [77] J. Musolf *et al.*, Phys. Rep. **239**, 1 (1994).

[78] [http://en.wikipedia.org/wiki/Bethe\\_formula](http://en.wikipedia.org/wiki/Bethe_formula).

[79] A. Afanasev, radiative calculation, personal communications, in progress.

## APPENDIX A

### MATERIALS DEFINED IN THE RTPC GEANT4 SIMULATION

This list specifies all the materials defined in the RTPC GEANT4 simulation program (BONUS).

- Galactic: density = 0.000 kg/m<sup>3</sup>; temperature = 0.10 K; pressure = 0.00 atm;  
Radiation Length = 204727576.737 pc  
Element: Galactic (Vacuum); Z = 1.0; N = 1.0; A = 1.01 g/mole; Mass Fraction = 100.00 %; Abundance = 100.00 %
- Air: density = 1.290 mg/cm<sup>3</sup>; temperature = 273.15 K; pressure = 1.00 atm;  
Radiation Length = 285.161 m  
Element: Nitrogen (N); Z = 7.0; N = 14.0; A = 14.01 g/mole; Mass Fraction = 70.00%; Abundance = 72.71%  
Element: Oxygen (O); Z = 8.0; N = 16.0; A = 16.00 g/mole; Mass Fraction = 30.00%; Abundance = 27.29%
- Deuterium Gas: density = 1.227 mg/cm<sup>3</sup>; temperature = 300.00 K; pressure = 7.50 atm; Radiation Length = 1.027 km  
Element: Deuterium Gas ( ); Z = 1.0; N = 2.0; A = 2.01 g/mole; Mass Fraction = 100.00%; Abundance = 100.00%
- Kapton: density = 1.420 g/cm<sup>3</sup>; temperature = 273.15 K; pressure = 1.00 atm;  
Radiation Length = 28.576 cm  
Element: Hydrogen (H); Z = 1.0; N = 1.0; A = 1.01 g/mole; Mass Fraction = 2.64%; Abundance = 25.64%  
Element: Carbon (C); Z = 6.0; N = 12.0; A = 12.01 g/mole; Mass Fraction = 69.11%; Abundance = 56.41%  
Element: Oxygen (O); Z = 8.0; N = 16.0; A = 16.00 g/mole; Mass Fraction = 20.92%; Abundance = 12.82%  
Element: Nitrogen (N); Z = 7.0; N = 14.0; A = 14.01 g/mole; Mass Fraction = 7.33%; Abundance = 5.13%
- Ultem: density = 1.270 g/cm<sup>3</sup>; temperature = 273.15 K; pressure = 1.00 atm;  
Radiation Length = 32.528 cm

Element: Hydrogen (H);  $Z = 1.0$ ;  $N = 1.0$ ;  $A = 1.01$  g/mole; Mass Fraction = 8.31%; Abundance = 53.62%

Element: Carbon (C);  $Z = 6.0$ ;  $N = 12.0$ ;  $A = 12.01$  g/mole; Mass Fraction = 64.11%; Abundance = 34.78%

Element: Oxygen (O);  $Z = 8.0$ ;  $N = 16.0$ ;  $A = 16.00$  g/mole; Mass Fraction = 21.35%; Abundance = 8.70%

Element: Nitrogen (N);  $Z = 7.0$ ;  $N = 14.0$ ;  $A = 14.01$  g/mole; Mass Fraction = 6.23%; Abundance = 2.90%

- Fused-Quartz: density = 2.200 g/cm<sup>3</sup>; temperature = 273.15 K; pressure = 1.00 atm; Radiation Length = 12.295 cm

Element: Silicon (Si);  $Z = 14.0$ ;  $N = 28.1$ ;  $A = 28.09$  g/mole; Mass Fraction = 46.75%; Abundance = 33.33%

Element: Oxygen (O);  $Z = 8.0$ ;  $N = 16.0$ ;  $A = 16.00$  g/mole; Mass Fraction = 53.25%; Abundance = 66.67%

- Epoxy-Resin: density = 1.268 g/cm<sup>3</sup>; temperature = 273.15 K; pressure = 1.00 atm; Radiation Length = 32.338 cm

Element: Hydrogen (H);  $Z = 1.0$ ;  $N = 1.0$ ;  $A = 1.01$  g/mole; Mass Fraction = 6.30%; Abundance = 46.15%

Element: Carbon (C);  $Z = 6.0$ ;  $N = 12.0$ ;  $A = 12.01$  g/mole; Mass Fraction = 68.72%; Abundance = 42.31%

Element: Oxygen (O);  $Z = 8.0$ ;  $N = 16.0$ ;  $A = 16.00$  g/mole; Mass Fraction = 24.97%; Abundance = 11.54%

- G10FR4: density = 1.700 g/cm<sup>3</sup>; temperature = 273.15 K; pressure = 1.00 atm; Radiation Length = 18.418 cm

Element: Silicon (Si);  $Z = 14.0$ ;  $N = 28.1$ ;  $A = 28.09$  g/mole; Mass Fraction = 28.05%; Abundance = 11.88%

Element: Oxygen (O);  $Z = 8.0$ ;  $N = 16.0$ ;  $A = 16.00$  g/mole; Mass Fraction = 41.94%; Abundance = 31.18%

Element: Hydrogen (H);  $Z = 1.0$ ;  $N = 1.0$ ;  $A = 1.01$  g/mole; Mass Fraction = 2.52%; Abundance = 29.71%

Element: Carbon (C);  $Z = 6.0$ ;  $N = 12.0$ ;  $A = 12.01$  g/mole; Mass Fraction = 27.49%; Abundance = 27.23%



- Rohacel71: density = 750.000 mg/cm<sup>3</sup>; temperature = 273.15 K; pressure = 1.00 atm; Radiation Length = 59.713 cm  
Element: Hydrogen (H); Z = 1.0; N = 1.0; A = 1.01 g/mole; Mass Fraction = 14.40%; Abundance = 66.67%  
Element: Carbon (C); Z = 6.0; N = 12.0; A = 12.01 g/mole; Mass Fraction = 85.60%; Abundance = 33.33%
- Preamplifier-Chip: density = 2.310 g/cm<sup>3</sup>; temperature = 273.15 K; pressure = 1.00 atm; Radiation Length = 15.332 cm  
Element: Hydrogen (H); Z = 1.0; N = 1.0; A = 1.01 g/mole; Mass Fraction = 5.71%; Abundance = 45.26%  
Element: Carbon (C); Z = 6.0; N = 12.0; A = 12.01 g/mole; Mass Fraction = 61.69%; Abundance = 41.14%  
Element: Oxygen (O); Z = 8.0; N = 16.0; A = 16.00 g/mole; Mass Fraction = 24.65%; Abundance = 12.34%  
Element: Silicon (Si); Z = 14.0; N = 28.1; A = 28.09 g/mole; Mass Fraction = 1.57%; Abundance = 0.45%  
Element: Copper (Cu); Z = 29.0; N = 63.5; A = 63.55 g/mole; Mass Fraction = 6.39%; Abundance = 0.81%
- Cable: density = 3.520 g/cm<sup>3</sup>; temperature = 273.15 K; pressure = 1.00 atm; Radiation Length = 4.629 cm  
Element: Hydrogen (H); Z = 1.0; N = 1.0; A = 1.01 g/mole; Mass Fraction = 2.06%; Abundance = 40.91%  
Element: Carbon (C); Z = 6.0; N = 12.0; A = 12.01 g/mole; Mass Fraction = 16.31%; Abundance = 27.27%  
Element: Chlorine (Cl); Z = 17.0; N = 35.5; A = 35.45 g/mole; Mass Fraction = 24.08%; Abundance = 13.64%  
Element: Copper (Cu); Z = 29.0; N = 63.5; A = 63.55 g/mole; Mass Fraction = 57.55%; Abundance = 18.18%
- Helium-Gas: density = 0.163 kg/m<sup>3</sup>; temperature = 300.00 K; pressure = 1.00 atm; Radiation Length = 5.787 km  
Element: Helium Gas (He); Z = 2.0; N = 4.0; A = 4.00 g/mole; Mass Fraction = 100.00%; Abundance = 100.00%

- Mylar: density =  $1.390 \text{ g/cm}^3$ ; temperature =  $273.15 \text{ K}$ ; pressure =  $1.00 \text{ atm}$ ;  
Radiation Length =  $31.356 \text{ cm}$   
Element: Hydrogen (H);  $Z = 1.0$ ;  $N = 1.0$ ;  $A = 1.01 \text{ g/mole}$ ; Mass Fraction =  $6.30\%$ ; Abundance =  $44.44\%$   
Element: Carbon (C);  $Z = 6.0$ ;  $N = 12.0$ ;  $A = 12.01 \text{ g/mole}$ ; Mass Fraction =  $93.70\%$ ; Abundance =  $55.56\%$
- Aluminum: density =  $2.700 \text{ g/cm}^3$ ; temperature =  $273.15 \text{ K}$ ; pressure =  $1.00 \text{ atm}$ ;  
Radiation Length =  $8.893 \text{ cm}$   
Element: Aluminum (Al);  $Z = 13.0$ ;  $N = 27.0$ ;  $A = 26.98 \text{ g/mole}$ ; Mass Fraction =  $100.00\%$ ; Abundance =  $100.00\%$
- Stainless-Steel: density =  $7.850 \text{ g/cm}^3$ ; temperature =  $273.15 \text{ K}$ ; pressure =  $1.00 \text{ atm}$ ;  
Radiation Length =  $1.764 \text{ cm}$   
Element: Iron (Fe);  $Z = 26.0$ ;  $N = 55.8$ ;  $A = 55.84 \text{ g/mole}$ ; Mass Fraction =  $95.43\%$ ; Abundance =  $95.30\%$   
Element: Chromium (Cr);  $Z = 24.0$ ;  $N = 52.0$ ;  $A = 52.00 \text{ g/mole}$ ; Mass Fraction =  $3.25\%$ ; Abundance =  $3.49\%$   
Element: Nickel (Ni);  $Z = 28.0$ ;  $N = 58.7$ ;  $A = 58.69 \text{ g/mole}$ ; Mass Fraction =  $1.20\%$ ; Abundance =  $1.14\%$   
Element: Molydb (Mo);  $Z = 42.0$ ;  $N = 95.9$ ;  $A = 95.94 \text{ g/mole}$ ; Mass Fraction =  $0.12\%$ ; Abundance =  $0.07\%$
- DME-Gas: density =  $1.871 \text{ mg/cm}^3$ ; temperature =  $300.00 \text{ K}$ ; pressure =  $1.00 \text{ atm}$ ;  
Radiation Length =  $218.617 \text{ m}$   
Element: Hydrogen (H);  $Z = 1.0$ ;  $N = 1.0$ ;  $A = 1.01 \text{ g/mole}$ ; Mass Fraction =  $13.00\%$ ; Abundance =  $66.37\%$   
Element: Carbon (C);  $Z = 6.0$ ;  $N = 12.0$ ;  $A = 12.01 \text{ g/mole}$ ; Mass Fraction =  $52.20\%$ ; Abundance =  $22.41\%$   
Element: Oxygen (O);  $Z = 8.0$ ;  $N = 16.0$ ;  $A = 16.00 \text{ g/mole}$ ; Mass Fraction =  $34.80\%$ ; Abundance =  $11.22\%$
- Bonus-Gas: density =  $0.470 \text{ kg/m}^3$ ; temperature =  $300.00 \text{ K}$ ; pressure =  $1.00 \text{ atm}$ ;  
Radiation Length =  $1.036 \text{ km}$   
Element: Hydrogen (H);  $Z = 1.0$ ;  $N = 1.0$ ;  $A = 1.01 \text{ g/mole}$ ; Mass Fraction =  $9.31\%$ ; Abundance =  $43.96\%$

Element: Carbon (C);  $Z = 6.0$ ;  $N = 12.0$ ;  $A = 12.01$  g/mole; Mass Fraction = 37.40%; Abundance = 14.84%

Element: Oxygen (O);  $Z = 8.0$ ;  $N = 16.0$ ;  $A = 16.00$  g/mole; Mass Fraction = 24.93%; Abundance = 7.43%

Element: Helium Gas (He);  $Z = 2.0$ ;  $N = 4.0$ ;  $A = 4.00$  g/mole; Mass Fraction = 28.36%; Abundance = 33.77%

- Copper: density = 8.960 g/cm<sup>3</sup>; temperature = 273.15 K; pressure = 1.00 atm; Radiation Length = 1.436 cm

Element: Copper (Cu);  $Z = 29.0$ ;  $N = 63.5$ ;  $A = 63.55$  g/mole; Mass Fraction = 100.00%; Abundance = 100.00%

## APPENDIX B

### PHYSICS PROCESSES IN THE RTPC GEANT4 SIMULATION

In the RTPC simulation program, BONUS, the following physics processes have been registered:

- General Physics
- Ion Physics
- Electromagnetic Physics
- Muon Physics
- Hadron Physics

#### General Physics

Decay is a very general process for all particles. The decay process has been linked to all known particles, including baryons, bosons, ions, leptons, mesons, resonances and even all the quarks.

#### Ion Physics

In the Ion Physics process, I associated multiple scattering and ionization to the general ions. Some special processes have also been linked for the deuteron, triton, and alpha and  $^3\text{He}$  particles.

- General Ion: Multiple Scattering, Ionization
- Deuteron: Low Energy Elastic Scattering, Low Energy Inelastic Scattering, Multiple Scattering, Ionization;
- Triton: Low Energy Elastic Scattering, Low Energy Inelastic Scattering, Multiple Scattering, Ionization;
- Alpha: Low Energy Elastic Scattering, Low Energy Inelastic Scattering, Multiple Scattering, Ionization;
- $^3\text{He}$ : Low Energy Elastic Scattering, Low Energy Inelastic Scattering, Multiple Scattering, Ionization.

## Electromagnetic Physics

Electric-Magnetic physics usually relevant to photons ( $\gamma$ ), electrons and positrons. In this physics process, I registered the following:

- $\gamma$ : Gamma Conversion, Compton Scattering, Photo-Electric Effect, Low Energy Rayleigh Scattering, Low Energy Photo-Electric Effect, Low Energy Compton Scattering, Low Energy Gamma Conversion;
- $e^-$ : Multiple Scattering, Ionization, Bremsstrahlung, Low Energy Ionization, Low Energy Bremsstrahlung;
- $e^+$ : Multiple Scattering, Ionization, Bremsstrahlung, Annihilation, Low Energy Ionization, Low Energy Bremsstrahlung.

## Muon Physics

In the Muon Physics process, I associated the following processes to  $\mu^+$ ,  $\mu^-$ ,  $\tau^+$  and  $\tau^-$ :

- $\mu^+$ : Multiple Scattering, Ionization, Bremsstrahlung, Pair Production;
- $\mu^-$ : Multiple Scattering, Ionization, Bremsstrahlung, Pair Production;
- $\tau^+$ : Multiple Scattering, Ionization;
- $\tau^-$ : Multiple Scattering, Ionization.

## Hadron Physics

In the Hadron Physics process, I associated various physics processes to various hadrons, as described below.

- $\pi^+$  and  $\pi^-$ : Low Energy Elastic Scattering, Low Energy Inelastic Scattering, High Energy Inelastic Scattering, Multiple Scattering, Ionization;
- $K^+$  and  $K^-$ : Low Energy Elastic Scattering, Low Energy Inelastic Scattering, High Energy Inelastic Scattering, Multiple Scattering, Ionization;
- $K_L^0$  and  $K_S^0$ : Low Energy Elastic Scattering, Low Energy Inelastic Scattering, High Energy Inelastic Scattering;

- Proton and anti-proton: Low Energy Elastic Scattering, Low Energy Inelastic Scattering, High Energy Inelastic Scattering, Multiple Scattering, Ionization;
- Neutron: Low Energy Elastic Scattering, Low Energy Inelastic Scattering, High Energy Inelastic Scattering, Low Energy Fission Model, Low Energy Capture Model;
- anti-neutron: Low Energy Elastic Scattering, Low Energy Inelastic Scattering, High Energy Inelastic Scattering, Annihilation Model;
- $\Lambda$  and anti- $\Lambda$ : Low Energy Elastic Scattering, Low Energy Inelastic Scattering, High Energy Inelastic Scattering;
- $\Sigma^+$  and anti- $\Sigma^+$ : Low Energy Elastic Scattering, Low Energy Inelastic Scattering, High Energy Inelastic Scattering, Multiple Scattering, Ionization;
- $\Sigma^-$  and anti- $\Sigma^-$ : Low Energy Elastic Scattering, Low Energy Inelastic Scattering, High Energy Inelastic Scattering, Multiple Scattering, Ionization;
- $\Xi^0$  and anti- $\Xi^0$ : Low Energy Elastic Scattering, Low Energy Inelastic Scattering, High Energy Inelastic Scattering;
- $\Xi^-$  and anti- $\Xi^-$ : Low Energy Elastic Scattering, Low Energy Inelastic Scattering, High Energy Inelastic Scattering, Multiple Scattering, Ionization;
- $\Omega^-$  and anti- $\Omega^-$ : Low Energy Elastic Scattering, Low Energy Inelastic Scattering, High Energy Inelastic Scattering, Multiple Scattering, Ionization.

## VITA

Jixie Zhang  
 Department of Physics  
 Old Dominion University  
 Norfolk, VA 23529

### EDUCATION:

- Ph.D., Physics, Old Dominion University, Norfolk, VA, 2010  
 Dissertation: *Exclusive  $\pi^-$  Electro-production from the Neutron in the Resonance Region*  
 Advisor: Dr. Gail E. Dodge
- M.S., Physics, Old Dominion University, Norfolk, VA, 2005
- Bachelor, Engineering Physics, TsingHua University, BeiJing, China 2001

### ACADEMIC HONORS:

- 2009 Jefferson Science Associates (JSA) SURA Fellowship.
- 2008 1st prize, Jefferson Lab Users Group Poster Competition (2008).
- 2008 Jefferson Science Associates (JSA) SURA Fellowship.

### EXPERIENCE:

**5/2005 – present: Research Assistant, Old Dominion University**

- Developed the GEANT4 Simulation Program for BoNuS.
- Analyzed the  $D(e, e'\pi^- p_{\text{CLAS}})p$  and  $D(e, e'\pi^- p_{\text{RTPC}})p$  data for BoNuS.

### COMPUTER SKILLS:

Highly skilled in C++, SQL, Cshell, VBScript, JavaScript, ROOT and GEANT4.

Typeset using L<sup>A</sup>T<sub>E</sub>X.